

CRASHWORTHINESS OF SIDE IMPACT BEAMS

GLEN WILSON

PhD Thesis - Submitted 2002

Department of Mechanical Engineering

STRATHCLYDE UNIVERSITY



The following conference paper has been redacted for copyright reasons:

APPENDIX A1.1: Paper Presented at SAE Conference 200-01-0639

***'Predicting the Deformation of Automotive Beams'* G. Wilson, M Wheel, W K Lee. p. i-v;**

Copyright © 1998 Society of Automotive Engineers, Inc.

The place of useful learning

The University of Strathclyde is a charitable body registered in Scotland, number SC015263

THE LEADERSHIP & MANAGEMENT AWARDS 2017 | Winner Workplace of the Year

THE AWARDS 2016 | WINNER BUSINESS SCHOOL OF THE YEAR

THE | UK Entrepreneurial University of the Year 2012/13
UK University of the Year 2012/13

PAGE NUMBERING AS ORIGINAL

“The copyright of this thesis belongs to the author under the terms of the United Kingdom Copyright Acts as qualified by University of Strathclyde Regulation 3.49. Due acknowledgement must always be made of the use of any material contained in, or derived from, this thesis.”

ACKNOWLEDGEMENTS

Glen Wilson is an Associate of the Postgraduate Training Partnership (PTP) between the National Engineering Laboratory (NEL) and Strathclyde University. The PTP scheme is a joint initiative of the UK's Department of Trade and Industry (DTI) and the Engineering and Physical Sciences Research Council (EPSRC). The PTP scheme is supported by a grant from the DTI. Glen Wilson gratefully acknowledges grant support from both the EPSRC and NEL.

The project was sponsored by Ford Motor Co. Ltd. I wish to thank the company and, in particular, my contact at Ford: Roger Davis. I am grateful for the direct and in-kind support from Ford.

I wish to express my deep gratitude to both my academic supervisor, Dr Marcus Wheel, and my industrial supervisor, Dr Wai Kong Lee. I thank Dr Wheel for his great wisdom and level-headedness which often brought me back to reality. I thank Dr Lee for his inspiration, energy and practical guidance.

I thank the Mechanical Engineering Department of the University of Strathclyde for its support in various ways. In particular, I recognise the support of the University technicians. I gratefully acknowledge the contribution of Bjorn Auren who worked with me for his undergraduate project on the experimental testing of the composite material. This section of my thesis would have been significantly poorer without Bjorn's input.

I recognise the support of the National Engineering Laboratory for providing necessary facilities. In particular, I thank Dr Bob Dunlop for his interest and guidance.

Finally, I thank my wife, Linda Stirling, for her emotional and financial support, and for her patience when I felt the need to explain what I did for a living.

ABSTRACT

This thesis describes the investigations carried out into the crashworthiness of side impact beams. Two specific beams were investigated: a commercially used steel beam and a prospective composite beam made from a glass fibre weave within a polypropylene matrix. The components were simply supported and were subjected to quasi-static and impact loading, the latter experiments being performed using a Drop Weight Test (DWT) rig. Static and dynamic Finite Element Analysis (FEA) was used to model the behaviour observed during testing. Ansys v5.4 was used for the static FEA while LS-Dyna3D v940 was used for the dynamic FEA.

The objectives of the project were to assess and then model the behaviour of the steel and composite side impact beams. This behaviour is in terms of both the beams' static and impact response. The beams were tested to determine their elastic behaviour, when and how failure occurs and their post-failure response. Important factors in their performance were identified. The modelling offered insights into the beams' behaviour and could potentially be used as a predictive tool in design activity.

It was found that, for the loading conditions and material type used, both the static and dynamic FEA could provide accurate predictions of the behaviour of the beams although both types of FEA had their limitations.

THESIS CONTENTS

Chapter	Page
<i>Introduction</i>	
<i>Chapter One - Introduction</i>	1
1.1	Overview of the project 2
1.2	Brief history of safety 3
1.3	Background to the project 6
1.3.1	Previous commercial research 6
1.3.2	Conclusions of previous research 8
1.4	Methods used in the project 9
1.5	Beams and materials used in the project 11
<i>Literature Review</i>	
<i>Chapter Two - Literature review</i>	13
Overview of chapter	14
2.1	Plastic collapse of beams 16
2.1.1	Introduction to plastic collapse of beams 16
2.1.2	Plastic limit loads 20
2.1.3	Material elasticity 24
2.1.4	Transverse shear & finite deflections 26
2.1.5	Effect of strain rate sensitivity 27
2.1.6	Other related topics 30
2.2	Structural crashworthiness 31
2.3	Composite mechanics & failure 34
2.3.1	General description of composites 34
2.3.2	Thermoplastic composites 35
2.3.3	Co-mingled fibre composites 35
2.3.4	Composites in the automotive industry 36
2.3.5	Composite macromechanics 37
2.3.6	Composite failure 39
2.4	Testing methods 47
2.4.1	Introduction to testing methods 47
2.4.2	Drop weight testing 47
2.4.3	Composite coupon testing 49
2.4.4	Other issues 53
Summary of chapter	54
<i>Steel Work: Testing & FEA</i>	
<i>Chapter Three - Experimental testing of steel coupons & beams</i>	54
Overview of chapter	55
3.1	Tensile testing of steel coupons 57

3.1.1	Introduction to tensile coupon testing	57
3.1.2	Equipment used during testing	57
3.1.3	Testing procedure	57
3.1.4	Results of tensile testing	59
3.2	Static testing of beams	64
3.2.1	Introduction to static testing of beams	64
3.2.2	Equipment used during testing	64
3.2.3	Testing procedure	65
3.2.4	Results of tensile testing	66
3.3	Description of dynamic rig	69
3.3.1	Overview of the dynamic test rig	66
3.3.2	Drop weight facility	69
3.3.3	Striker head & load washer	71
3.3.4	Charge amplifier	72
3.3.5	Digital storage oscilloscope	72
3.3.6	Personal computer	72
3.3.7	High speed video camera	73
3.4	Load correction & calibration of dynamic rig	74
3.4.1	Correction of the measured force	74
3.4.2	Introduction to dynamic calibration	76
3.4.3	Calibration of charge amp & load washer	76
3.4.4	Calibration of test set up – method 1	76
3.4.5	Calibration of test set up – method 2	81
3.4.6	Discussion of all calibration methods	86
3.5	Impact testing of steel beams	87
3.5.1	Introduction to impact testing of beams	87
3.5.2	Equipment used during testing	87
3.5.3	Calculation of initial test conditions	88
3.5.4	Testing procedure	88
3.5.5	Results of impact tests	91
3.6	Comparison of static & impact results	98
3.7	Modal testing	100
3.7.1	Introduction to modal testing of beams	100
	Summary of chapter	102
	<i>Chapter Four - Quantitative analyses of steel beams</i>	103
	Overview of chapter	104
4.1	Static methods	106
4.1.1	Introduction to static methods	106
4.1.2	Elastic & plastic behaviour	107
4.1.3	Non-linear static FEA	111
4.1.4	Comparison of static methods & Experiment	116
4.1.5	Elastic buckling analysis	117
4.1.6	Elastic buckling FEA	120
4.2	Impact methods	122
4.2.1	Analytical methods	122
4.2.2	Dynamic FEA: Modelling of impact tests	123
4.2.3	Comparison of dynamic FEA & experiment	125
4.2.4	Dynamic FEA: effect of various parameters	126

4.3	Modal methods	130
4.3.1	Theoretical methods of vibration	130
4.3.2	Modal FEA	132
4.3.3	Comparison of all modal results	136
	Summary & Conclusions for all steel beam results	139

Composite Work: Testing & FEA

Chapter Five - Experimental testing of composite coupons 140

	Overview of chapter	141
5.1	Tensile coupon testing	143
5.1.1	Introduction to tensile coupon testing	143
5.1.2	Equipment used during testing with standard lay-up	143
5.1.3	Testing procedure	144
5.1.4	Results of testing of coupons with standard lay-up	145
5.1.5	Introduction to testing of coupons with laminate lay-up	152
5.1.6	Equipment & procedure used during testing	153
5.1.7	Results of testing with laminate lay-up	153
5.1.8	Comparison of both types of tensile testing	155
5.2	Compressive coupon testing	156
5.2.1	Introduction to compressive coupon testing	156
5.2.2	Equipment used during testing – original set-up	156
5.2.3	Testing procedure	157
5.2.4	Results of testing of coupons using original set-up	157
5.2.5	Introduction to testing using modified set-up	162
5.2.6	Equipment & procedure used during testing	163
5.2.7	Results of testing using modified set-up	163
5.2.8	Comparison of the testing set-ups and results	164
5.3	Shear coupon testing	166
5.3.1	Introduction to shear coupon testing	166
5.3.2	Equipment & procedure during $\pm 45^\circ$ tensile test	166
5.3.3	Results of shear testing: method 1	167
5.3.4	Introduction to shear testing using Iosipescu method	170
5.3.5	Equipment used during testing	171
5.3.6	Testing procedure	172
5.3.7	Results of shear testing: method 2	173
5.3.8	Comparison of both forms of shear testing	177
5.4	Flexural coupon testing	178
5.4.1	Introduction to flexural coupon testing	178
5.4.2	Equipment used during testing	178
5.4.3	Testing procedure	179
5.4.4	Results of flexural testing	181
5.5	Comparison of results of all coupon tests	184
	Summary of chapter	186

Chapter Six - Experimental testing of composite beams 189

	Overview of chapter	190
6.1	Static testing of beams	191

6.1.1	Introduction to static testing of beams	191
6.1.2	Equipment & procedure used during testing	191
6.1.3	Results of static testing	191
6.2	Impact testing of beams	196
6.2.1	Introduction to impact testing of beams	196
6.2.2	Equipment & procedure used during testing	196
6.2.3	Results of impact testing	197
6.3	Comparison of static & impact behaviour	203
	Summary of chapter	206
 <i>Chapter Seven - Quantitative methods for composites</i>		 207
	Overview of chapter	208
7.1	Analytical methods	210
7.1.1	Material properties from rule of mixtures	210
7.1.2	Flexural stresses	212
7.2	Static FEA of composite coupons	214
7.2.1	Introduction to static FEA of composite coupons	214
7.2.2	Failure criteria within static FEA	214
7.2.3	Static modelling of tensile & compressive coupons	215
7.2.4	Static modelling shear coupons	223
7.2.5	Static modelling of flexural coupons	227
7.3	Dynamic (quasi-static) FEA of static composite coupon tests	234
7.3.1	Introduction to dynamic FEA of composite coupons	234
7.3.2	Failure criteria within dynamic FEA	234
7.3.3	Dynamic modelling of tensile coupons	238
7.3.4	Dynamic modelling of compressive coupons	241
7.3.5	Dynamic modelling of shear coupons	243
7.3.6	Dynamic modelling of flexural coupons	245
7.4	Discussion of all coupon FEA	248
7.5	Static FEA of composite beam	250
7.5.1	Introduction to static FEA of composite beam	250
7.5.2	Static modelling of beam	250
7.6	Dynamic FEA of composite beam	259
7.6.1	Introduction to dynamic FEA of composite beam	259
7.6.2	Dynamic modelling of beam	259
 <i>Interpretation of Results</i>		
 <i>Chapter Eight - Discussion & Conclusions for all results</i>		 266
8.1	Discussion of all results	267
8.1.1	Discussion of all steel results	267
8.1.2	Discussion of all composite results	268
8.1.3	Comparison of steel & composite results	270
8.2	Conclusions from all results	273
8.3	Future work	274

Appendices**Page**

A1.1	Paper presented at SAE conference	i
A1.2	Composite material properties compiled by SACTAC	v
A1.3	Photograph of tooling used to produce composite beam	vi
A1.4	Nominal dimensions of composite beams	vii
A2.1	Review of literature on structural crashworthiness	ix
A3.1	Further details of test machine	xxv
A3.2	Certificate of calibration for test machine	xxvi
A3.3	Nominal & measured dimensions of steel coupons	xxviii
A3.4	Justification for selected value of proof stress	xxix
A3.5	Details of guide rails, base & support columns	xxx
A3.6	Diagrams of striker construction	xxxi
A3.7	Illustrations & technical data of load washer	xxxii
A3.8	Details of the digital storage oscilloscope	xxxiii
A3.9	Calculation of the force on the load cell	xxxiv
A3.10	Details of the high speed video camera	xxxv
A3.11	Calibration of the charge amplifier	xxxvi
A3.12	Calibration of the load cell	xli
A3.13	Calibration certificate for accelerometer & charge amplifier	xlvi
A3.14	Calculation of initial test conditions	xlviii
A3.15	Derivation of velocity & deflection data	l
A3.16	Signal filtering	lii
A3.17	Contact tests on beams	lvi
A3.18	Traces from the HSVC	lix
A3.19	Other values obtained from impact testing	lx
A3.20	Details of modal testing	lxi
A4.1	Determining the values of y_1 and y_2	lxix
A4.2	Stressed regions of plates & examples of different plates	lxxi
A4.3	Determining the buckling coefficient K	lxxii
A5.1	System & specimen bending during tensile testing	lxxiii
A5.2	Correlation of bending and material properties	lxxv
A5.3	Relationship between cross-head & mid-span deflection	lxxvii
A6.1	Effect of delamination on bending stiffness	lxxix

CHAPTER ONE

INTRODUCTION

1.1 OVERVIEW OF THE PROJECT

Automotive manufacturers are always keen to improve the safety of their vehicles during a side impact or maintain the same high performance using cheaper, easier to manufacture and fit, components. The side impact beam makes a major contribution to side impact protection and so it would be desirable to improve its performance.

Steel beams, made from high strength steel, come in a number of different geometries from hollow tubes to corrugated open sections. The manufacturers have considerable experience with these beams (even if little research literature on their performance exists in the public domain). Beams made from alternative materials, such as composites, offer many advantages such as weight savings, lower fabrication costs and parts integration. However, these novel beams are not as well understood, particularly their behaviour beyond failure and their energy absorption characteristics.

This thesis describes the investigations carried out into the *crashworthiness of side impact beams*. Two specific beams were investigated: a commercially used steel beam and a prospective composite beam made from a glass fibre weave within a polypropylene matrix. The project is a continuation of previous work carried out under the DTI 'LINK' project 'Structural Automotive Components using Thermoplastic Composites' (SACIAC) and is sponsored by Ford Motor Co. Ltd.

The objectives of the project were to assess and then model the behaviour of the steel and composite side impact beams. This behaviour is in terms of both the beams' static and impact response. The beams were tested to determine their elastic behaviour, when and how failure occurs and their post-failure response. Important factors in their performance were identified. Both beams were simply supported and loaded at mid-span. The modelling was, in the most part, performed using Finite Element Analysis. This offered insights into the beams' behaviour and could potentially be used as a predictive tool in design activity.

Side impact legislation covers whole vehicle tests. It is unrealistic to expect single components such as side impact beams to meet the regulations by themselves but it then becomes important to specify the contribution that the component makes to the performance of the

whole vehicle. A simple approach is to compare components, such as composite side impact beams, with existing parts used in commercial vehicles. If the new component compares as well as, or better than, the existing one then it can be reasonably expected that the whole vehicle will pass the legislation while utilising that component. The steel beam was also used as a benchmark for the development of testing procedures and modelling techniques to be transferred to the more complex composite beam.

1.2 A BRIEF HISTORY OF SAFETY

The automobile is just over a hundred years old and, in that time, over 25 million people have been killed in road accidents. Little was done in the first half century to make cars safer although laminated safety glass and closed bodies for occupant protection were introduced in the 1930s. However, car engines were becoming more and more powerful and the fatality rate continued to increase yearly [1.1].

By the 1950s cars had killed 5 million people yet no-one knew how. In the 1960s, accident investigators emerged and statistics began to be compiled. Also, experiments on human corpses built up a picture of human tolerance to injury and this led to the design of realistic dummies. Collapsible steering columns were soon introduced and, in 1959, Volvo patented the lap-shoulder seat belt and allowed other manufacturers to use the design free of charge.

Other manufacturers did not take up the design, nor did they make use of other safety devices such as head restraints and padded dashboards. Ford produced the first car with padded dashboards and lap belts in 1956 but pressure from the market leader, General Motors, led to the Ford campaign being scrapped. It was felt that these safety features would place too great an emphasis on what could go wrong rather than the style and romance associated with a car. The American lawyer Ralph Nader, author of 'Unsafe - at any speed' [1.2], was highly instrumental in opening the public's eyes and bringing about the first safety legislation in 1967. Europe soon followed and in the early '70s the death rate began to fall for the first time.

The seatbelt is widely regarded as the greatest safety device of all but people would not wear them. In the UK, a campaign which began in 1967 took until 1983 to make the wearing of seatbelts compulsory. There was no such campaign in America and airbags, which first

appeared on European cars in 1986, were seen as a substitute. However, American airbags have to be powerful enough to stop an unrestrained occupant and so can cause death or serious injury themselves [1.1].

In the new millennium, crumple zones and side impact beams are commonplace. More people survive car crashes than ever before and the current trend is on reducing the seriousness of injuries rather than survivability. Yet the rate of road accidents is still rising. Research indicates that drivers like to take risks: the safer we make our cars and roads, the faster and more dangerously we drive. Widen a lane by 1 foot and drivers will, on average, increase their speed by 3 mph. Make a road's edge markings clearer and the accident rate for that road will often rise [1.1]. It is clear that the psychological cause of accidents is still not understood however, even if there are many ways to reduce accidents, there is no reason to stop improving the safety of our cars by structural means.

Research into side impacts has always greatly lagged frontal collision research. Side impact legislation is problematic because of the proximity of the occupant to the side of the vehicle. There is little room to allow deformation but if the side is made too stiff then acceleration levels can become intolerably high. Typically, in a side impact there is just six inches of space between the driver and the impacting car which will be used up in about 20 milliseconds.

In the UK, some 30 % of occupant deaths (around 700 deaths a year) are caused during side impacts [1.3]. In about half the cases, impact is with another vehicle while, in the other half, it is with a fixed object such as roadside furniture [1.4]. The injuries are usually concerned with the head, chest, abdomen and pelvis and are caused by contact with the inner side structure and door of the vehicle.

European legislation for side impacts was only recently introduced in the form of European Union (EU) directive 96/27/EC. New and redesigned cars must meet the standard from 1998 and all cars by 2003. A European side impact test is shown in figure 1.1. Prior to this there was only the US Federal Motor Vehicle Standard 214 (FMVSS 214) which has been in effect since 1973. This is mainly a quasi-static regulation although a dynamic requirement was appended to the code in 1990.



Fig 1.1: European Side Impact Test

Quasi-static regulation involves a 305 mm diameter rigid cylindrical impactor penetrating 456 mm into the car with three different levels of force having to be met within three ranges of deformation and the levels of force depending on whether the seats are removed from the vehicle or not. With the seats removed, for instance, the average force must be at least 10 kN over the first 152 mm and then 15.57 kN over the first 305 mm and the peak force over the whole range of deformation must be at least 31.14 kN. A 1982 evaluation of the standard by the National Highway Traffic Safety Agency (NHTSA) concluded that it was effective in side impacts with fixed objects but provided little benefit for occupants in collisions with another vehicle [1.5].

The dynamic requirement involves the measurement of the acceleration of test dummies and then correlating the acceleration values with occupant injuries. A moving deformable barrier (MDB) of a mass of 1367 kg impacts the test vehicle at 24 kph (15 mph).

The European standard is similar to the dynamic requirement of the American Standard although there are some variations which reflect the different mass and geometry of cars in Europe. It also involves a different test dummy and different injury criteria.

The development of safety legislation is ongoing and is likely to become even more rigorous in the future. Safety laws are becoming standardised on a world-wide basis. There is an ever greater pressure on automotive manufacturers to continue meeting the imposed regulations.

1.3 BACKGROUND TO THE PROJECT

This thesis continues and expands previous work carried out under the DTI 'LINK' project 'SACTAC'. The project was carried out by a consortium of automotive companies, composite manufacturers and universities. SACTAC's objective was to develop new thermoplastic automotive components and two candidates were selected: a door cassette and a door side impact beam with both components to be designed initially for a Jaguar vehicle. The first component was selected to demonstrate Glass Mat Thermoplastics (GMT) and the second to exhibit the performance of *co-mingled fibre* composites. Separate sub-groups were formed for each of these components and it is the work of the Doorbeam Design Sub-Group that shall now be reviewed. All the information has been taken from the SACTAC Progress Reports [1.6].

1.3.1 Previous Commercial Research

The composite beam was made to differ from the traditional steel beam in a number of respects. Due to the composite material having a lower modulus of elasticity, and being more brittle, the beam's section was made deeper with the flanges thicker than the webs. This was, it was stated, to promote failure by local buckling as for the steel beam. The space within the door allowed a significant deepening of the beam's cross section. Towards both ends of the composite beam the section was reduced to maintain a more uniform bending stress distribution.

'Twintex' co-mingled glass/polypropylene material from Vetrotex was chosen with unidirectional fibres in the flanges and webs to maximise stiffness in the longitudinal direction.

The Motor Industry Research Association (MIRA) performed the initial Finite Element Analysis (FEA) on the steel and composite beams in a simply supported condition using data from Jaguar and Vetrotex. This latter data applied to a single layer of fabric. Results on the steel beams were compared with FEA models of the complete vehicle and this, according to the reports, provided an estimate of the door beam's contribution to load resistance. New FEA

models then used beams with one end fixed and the other incorporating spring elements to, supposedly, more closely represent the beam's conditions when fitted in the vehicle. Two types of model were used. The first involved an elastic-plastic material behaviour and the second is stated to be more complex though it is not described in any detail. The FEA showed the beam to be flattening rather than buckling and so values for wall thickness were altered. Reversing the beam so that it was loaded on the closed side also gave better results.

MIRA also performed the static tests on the door beams which were designed to simulate the FMVSS 214 standard. The beam specimens were made from wooden moulds using a variety of material combinations and thickness, some were closed sections, and four different beams were tested. A chain arrangement was used during the testing, as with the spring elements in the FEA, in an effort to represent the conditions of the beam within the vehicle.

The beams are said to have failed initially by compressive failure at the closed face through separation of individual layers of the Twintex material which then folded over one another. The zone of failure then spread to the side walls. It is stated that it is not known whether poor compressive strength or poor consolidation of layers was responsible. The modes of failure witnessed in the testing were not predicted by the FEA.

Impact tests were also performed using the Drop Weight Facility (DWF) at Strathclyde University. The impact mass was about 22 kg and the impact velocity up to 11 m/s according to the research reports. While these values lead to a much smaller level of impact energy, the pattern of failure of the beams was seen to be similar to the static tests.

Given the results of the tests it was decided to double the thickness of the beam over its whole length and to increase the draft angle to 15°. A new batch of beams was made and beams within this batch varied in terms of material lay-up, the method of consolidating material layers and their geometry. Differences in geometry involved the removal of flanges at mid-point, the inclusion of slots in the side walls or bottom face or all of the side walls removed.

The beams all still failed to meet expectations which was thought to be due to the material's low compressive strain to failure (only 46% of the tensile strength according to Vetrotex). Therefore a new beam was designed with only the beam's top flange increased in thickness to

shift the neutral axis towards the compressive face. Also, a $\pm 45^\circ$ lay-up was used to give a more gradual failure with only the additional layer on the beam's base being unidirectional.

In static tests the new beam showed an improvement in performance and its behaviour is described. The increase in load was linear over the first 50 mm of deflection and then reduced until 80 mm as the beam opened out. The load curve then fell rapidly as initial failure occurred. The load was then fairly constant up to 200 mm when the load again rose abruptly as the beam acted as a strap.

This new beam was also tested using the DWF with the tests being carried out by this author and these tests are described in detail in section 6.2. The SACTAC reports note a slightly higher deflection in these tests than in static tests but conclude that this can be accounted for by dynamic effects. The pattern of damage in both static and dynamic tests is stated to be very similar.

The composite beams are said to perform almost, but not quite, as well as the steel beams. Tests with a steel plate between the striker and beam showed around a 5 % greater failure load and this is thought to be due to the plate inhibiting crushing of the composite material. The average weight of the composite beams was about 5 % greater than the steel beams.

1.3.2 Conclusions of Previous Research

Five main conclusions were reached from all the work within the project:

- 1) A co-mingled fibre composite such as Twintex can be used to produce a satisfactory door beam despite its low failure strain.
- 2) There is little energy absorption that involved crushing of fractured edges or corners. The glass layers tended to peel apart with little energy dissipation.
- 3) A $\pm 45^\circ$ lay-up gave a more gradual failure in the beam.
- 4) The difference in failure stress in tension and compression must be given consideration.
- 5) FEA is only useful if the correct failure mode can be modelled.

A number of suggestions for future work were also given. The beam could still be improved in terms of its geometry, by further equalisation of tensile and compressive stresses, and its material properties, by using metal moulds. The beam could also be tested within the vehicle door or the whole door modelled. Finally, the material could be replaced by a three dimensional woven fabric.

1.4 THE METHODS USED IN THE PROJECT

It was from the background described above that the project of this thesis began. It was hoped that the project would provide a better understanding of the composite material and how it fails. It was also clear that there were limitations to the FEA work carried out and better modelling techniques could be developed. The performance of the composite beam could be compared with the commercial steel beam.

This thesis has been arranged into a number of sections: introduction, literature review, the work on the steel material and beam, the work on the composite material and beam and the discussion and conclusions. A block diagram of these general sections is shown below as figure 1.2 and includes the relevant chapter numbers.

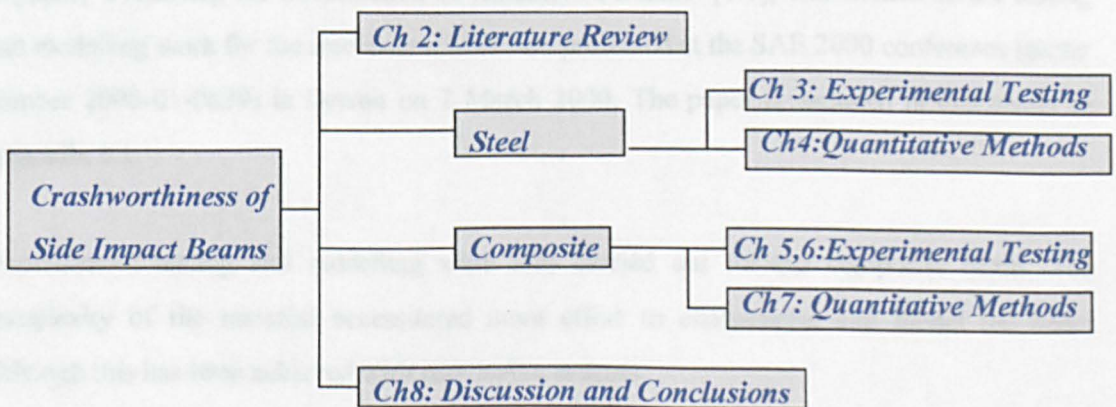


Fig 1.2: Block diagram of thesis structure

It should be realised, however, that the structure of this thesis has many more layers than the above figure suggests. For instance, both the testing and modelling were for static and impact conditions, coupons and beams were tested, a number of different types of coupon tests were

performed and the quantitative methods consisted of analytical approaches and FEA. To maintain clarity, further layers will be introduced within the respective chapters.

A number of fields have been reviewed which are relevant to the work of this project. These are: plastic analysis; structural crashworthiness; composite mechanics and failure; and testing methods.

Experimental testing on steel coupons and beams has ascertained the material's mechanical properties as well as the beam's static and impact behaviour. This behaviour is in terms of load response, deformation modes and energy absorption profiles. The beam is simply supported and loaded at mid-span. This does not represent the loading conditions of the beam within a vehicle where fixture to the vehicle structure would provide a complex end restraint. However, the simplified loading conditions can provide a benchmark with which an initial comparison of the performance of beams made from alternative materials can be made. The modal response of the beams has also been investigated.

Analytical methods have been used to predict a number of features of the beam's behaviour. Finite Element Analysis (FEA) models have been developed to represent the beam's static, impact and modal behaviour.

A paper, 'Predicting the Deformation of Automotive Beams' [1.7], was written on the testing and modelling work for the steel beam. This was presented at the SAE 2000 conference (paper number 2000-01-0639) in Detroit on 7 March 2000. The paper is included in this thesis as appendix 1.1.

Experimental testing and modelling were also carried out for the composite beam. The complexity of the material necessitated more effort to characterise and model the beam although this has been achieved with reasonable success.

This thesis makes a number of contributions to engineering knowledge. Experimental work on door beams of both material types provides information on the crashworthiness characteristics of structures (particularly automotive structures) in bending, something which is scarce at present. Also, coupon and whole beam tests provide much needed data on the behaviour of thermoplastics in a number of different conditions. FEA modelling techniques have been

developed, particularly for composite structures and accounting for delamination modes of failure. Further, the FEA modelling comprises a design tool for beam optimisation.

1.5 BEAMS AND MATERIALS USED IN PROJECT

The steel specimens are actual door beams used in commercial production by Ford. The steel is a press quenched material and a table of its properties is given in table 1.1 below.

Grade Name	Condition	Yield Strength MPa	Tensile Strength MPa
Boron 02	Press Quenched	950 (min)	1350 (min)

Table 1.1: Manufacturer's Values for Material Properties of Steel

The steel beam has a uniform cross section except for its ends which taper down to a flat plate. The dimensions of the beam's central section are shown below in figure 1.3 where all dimensions are in millimetres.

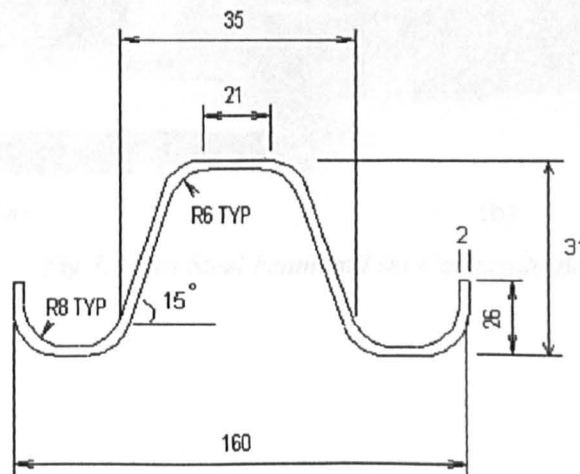


Fig 1.3: Dimensions of Steel Beam

The composite beams were handmade using material and wooden tooling supplied by Vetrotex. The material has the trade name 'Twintex PP60' and is a co-mingled glass/polypropylene mixture with 60% glass by weight. Most of the beams are the 'newer'

type i.e. the second design produced by the SACTAC group (see section 1.2.1). This has a $\pm 45^\circ$ lay-up with an additional unidirectional reinforcement in the central flange. The first type, the 'old' beam has a $0/90^\circ$ lay-up.

A table of material properties is given in appendix 1.2. Although the table was compiled by SACTAC, most of the property values listed are supplied by the material manufacturer. Photographs of the wooden tooling used to produce the composite beams are supplied in appendix 1.3 and nominal dimensions of the beams produced can be seen in appendix 1.4.

Photographs of the steel and composite beams are shown below in figure 1.4.

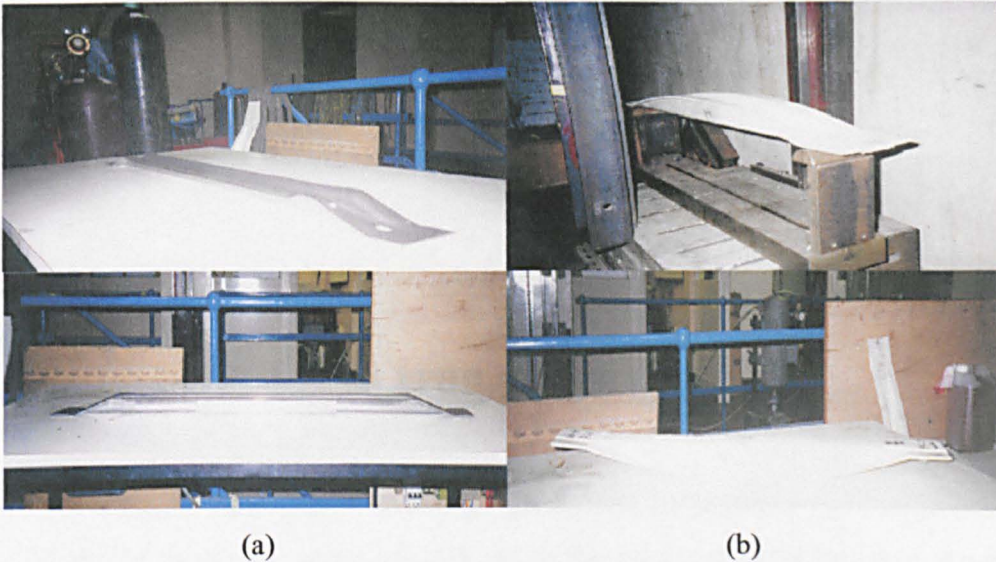


Fig 1.4: (a) Steel beam and (b) Composite Beam

CHAPTER TWO

LITERATURE REVIEW

OVERVIEW OF CHAPTER

There is a distinct lack of research into the crashworthiness of side impact beams. However, a number of fields do have some relevance to the context of this subject and it was decided to review these fields. The review may often be quite general, given the limited relevance of the subject, or it may specifically focus on the particular aspects of the subject that are more relevant. The subjects to be reviewed are shown below in figure 2.1, which includes the section numbers used in this thesis.

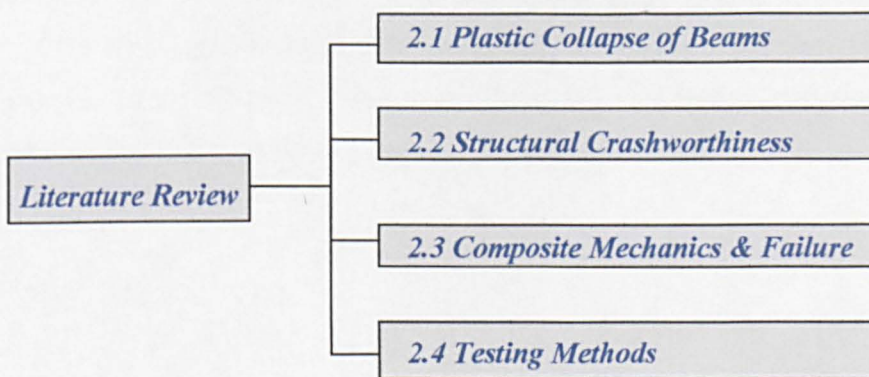


Fig 2.1: Block Diagram of Structure of Chapter

The loading of metal beams involving high stresses and strains may often produce a form of failure that is termed plastic collapse and so this subject shall be described. An exact plastic collapse loads can be derived for a simply supported beam subject to a mid-span load. Important factors are considered such as dynamic conditions, material elasticity, the effects of transverse shear and finite deflections, the strain rate and strain hardening.

Structural crashworthiness will be reviewed for metal and composite sections. While bending of structures is of the greatest relevance, the bulk of research has been on axial loading. However, due to a number of similarities, in methods and in material behaviour in particular, it is well worth looking at the whole subject.

Composite materials are, by nature, considerably more complex than metals. The complexity arises from their anisotropic behaviour and many modes of failure. Investigating the Macromechanics of the composite material of this research reveals that, for certain conditions, a small number of properties can define its elastic behaviour. Failure of the material is not as easy to characterise. A number of composite failure criteria exist however they all have their limitations.

This project requires considerable test-work on coupons and beams to determine material properties and the performance of side impact beams. A number of aspects concerning testing must be considered, particularly for the testing of composite coupons and the impact testing of beams.

2.1 PLASTIC COLLAPSE OF BEAMS

2.1.1 Introduction to Plastic Collapse of Beams

Structures, such as metal beams, may fail in a number of ways, most commonly through plastic collapse or elastic buckling. This section looks at research into the plastic collapse of beams and the theoretical methods that have been devised to approximate this collapse. However, it should be remembered that elastic buckling is a common failure mode for thin-walled open section beams.

The plastic analysis of structures is used when loading exceeds the elastic limit of the material. The well-known stress-strain curve given by a uniaxial tensile test on a typical mild steel specimen is shown below in figure 2.2. Tests on a specimen in uniaxial compression would produce a similar response curve (for low to medium strains).

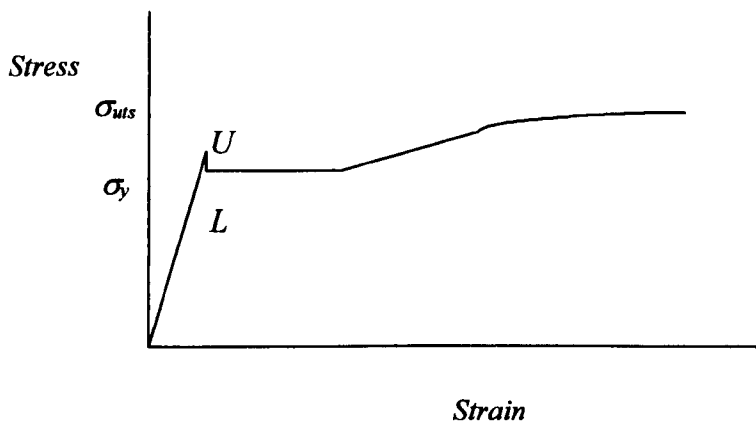


Fig 2.2: Stress-Strain Curve of Steel Specimen in Uniaxial Tension

The initial curve represents the elastic portion of the response and the gradient is the elastic modulus, E . When the stress reaches U , the upper yield point, there is a sudden drop to L and this value is known as the yield stress, σ_y . After this point is the plastic region where the stress remains constant until it begins to rise again due to strain hardening with a typical slope of $0.04 E$. The maximum value of stress reached is termed the ultimate tensile strength, σ_{uts} . Shortly after this fracture will occur.

The behaviour of steel may be idealised and Moy [2.1] describes steel as an almost perfect material for plastic analysis. These idealisations can neglect the elastic portion of the curve and strain hardening (thus giving a rigid-plastic analysis) or can include elastic behaviour but still ignore strain hardening (an elastic-perfectly plastic analysis). The upper yield point and the Bauschinger effect are also ignored but this will not usually cause significant error (the Bauschinger effect is a phenomenon caused by cyclic loading where the stress response deviates from expected behaviour when the load is reversed). These idealised responses of the material are shown below in figure 2.3.

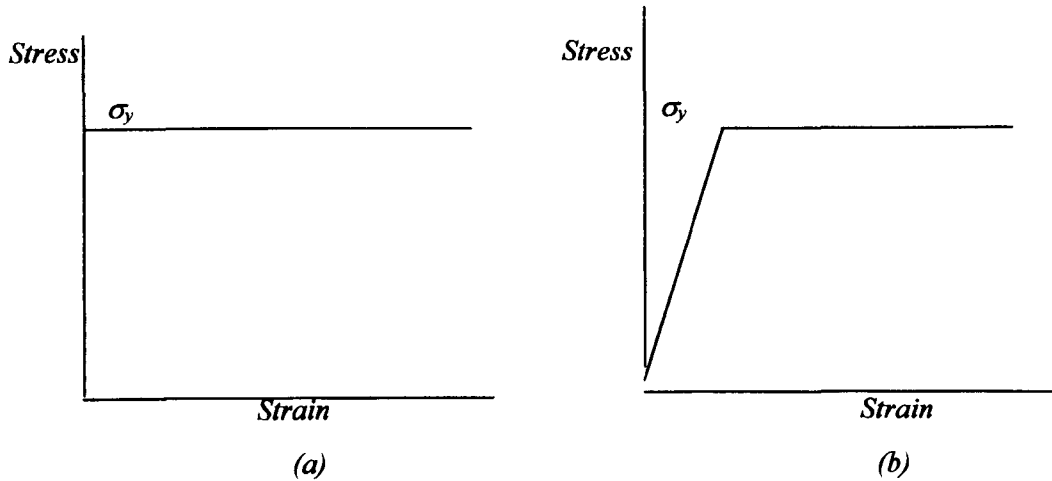


Fig 2.3: Idealised Analyses - (a) Rigid-plastic and (b) Elastic-perfectly plastic

For a beam subject to pure bending, simple bending theory gives a relationship for the bending moment, M , to the stress, σ , the second moment of area, I , and the distance from the neutral axis, y :

$$M = \frac{\sigma \cdot I}{y} \quad \text{Eq (2.1)}$$

As the bending moment is increased the stress will increase until the yield stress is reached. The bending moment at first yield is termed the yield moment, M_y :

$$M_y = \frac{\sigma_y \cdot I}{y} \quad \text{Eq (2.2)}$$

Due to the stress being dependent on the distance from the neutral axis for a given moment, yielding will occur initially at the outer surfaces of the beam and spread inwards as the bending moment is increased. For a beam loaded on the top surface, initially the top surface will yield in compression while the bottom surface yields in tension. This stress distribution is shown below in figure 2.4 (a) using the example of a beam with a solid rectangular cross-section.

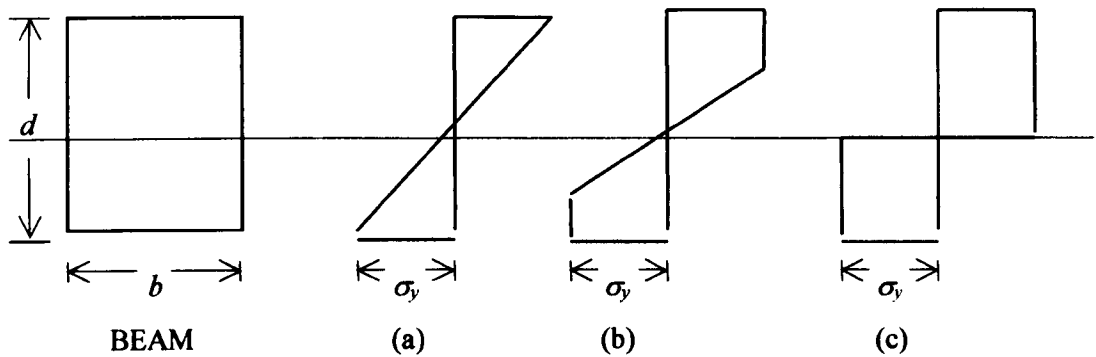


Fig 2.4: Stress Distribution of a Beam in Bending

In figure 2.4 (b) the bending moment has continued to increase beyond M_y and so yielding has spread inwards towards the core of the beam. When the condition shown in figure 2.4 (c) is achieved, there is effectively no elastic core remaining and the beam is incapable of sustaining any further increase in the bending moment. This value is therefore the ultimate moment carrying capacity of the beam and is termed the plastic moment, M_p .

When the plastic moment is reached, the total tensile force, T , will be equal to the product of the yield stress and the area above the neutral axis, A_1 , while the total compressive force, C , will equate to the product of the yield stress and the area below the neutral axis, A_2 . Therefore:

$$T = \sigma_y A_1$$

$$C = \sigma_y A_2$$

As the resultant force on the cross-section must be zero for equilibrium, T must equal C . Therefore:

$$A_1 = A_2 = \frac{A}{2}$$

where A is the total area for the cross-section. The neutral axis for the plastic moment therefore divides the cross-section into two equal areas and will differ from the neutral axis for elastic bending (unless the cross-section is doubly symmetric). The plastic moment can be found by taking moments about the neutral axis for T and C .

$$\begin{aligned} M_p &= T \cdot y_1 + C \cdot y_2 \\ &= \frac{\sigma_y \cdot A(y_1 + y_2)}{2} \end{aligned} \quad \text{Eq (2.3)}$$

where y_1 and y_2 are distances from the neutral axis to the centroids of areas A_1 and A_2 respectively. The geometric contribution to equation 2.3 is often collectively termed the plastic modulus, Z . Therefore:

$$M_p = \sigma_y \cdot Z \quad \text{Eq (2.4)}$$

For a beam of solid rectangular cross-section, for example:

$$\begin{aligned} M_y &= \frac{\sigma_y \cdot I}{y} \\ &= \frac{\left(\frac{\sigma_y \cdot b d^3}{12} \right)}{d/2} \\ &= \frac{\sigma_y \cdot b d^2}{6} \end{aligned}$$

$$M_p = \frac{\sigma_y \cdot A(y_1 + y_2)}{2}$$

$$= \frac{\sigma_y \cdot bd(d/4 + d/4)}{2}$$

$$= \frac{\sigma_y \cdot bd^2}{4}$$

$$\frac{M_p}{M_y} = 1.5$$

The ratio of the plastic moment to the yield moment is called the shape factor, f (i.e. $f = M_p / M_y$). It should be noted that open sections generally have lower shape factors and this includes the specimens used in this thesis (see section 4.1.2).

2.1.2 Plastic Limit Loads

The situation described above in section 2.1.1 is for the case of pure bending where all cross-sections of the beam would be fully plastic when M_p is reached. This is not the case for a simply supported beam of length L with a mid-span concentrated load, P , as shown in figure 2.5.

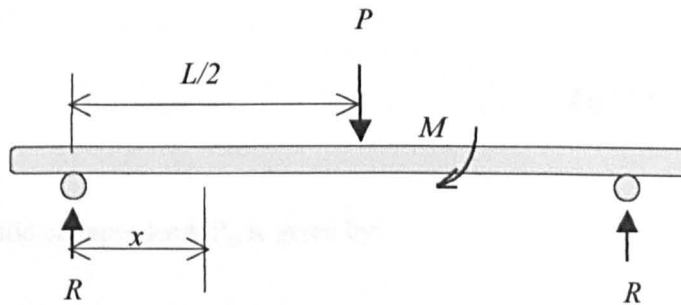


Fig 2.5: Loading and Support Conditions

where R is the reaction load at each support and x is an arbitrary distance along the beam. Given the symmetry of the above conditions and for static equilibrium of vertical forces:

$$R = \frac{P}{2} \tag{Eq (2.5)}$$

For equilibrium, the summation of moments must also be zero. Considering the moments to the right hand side of x and substitution of equation 2.5 gives:

$$M_x + P\left(\frac{L}{2} - x\right) - \frac{P}{2}(L - x) = 0$$

Considering values of x from 0 to L gives the bending moment diagram shown below in figure 2.6.

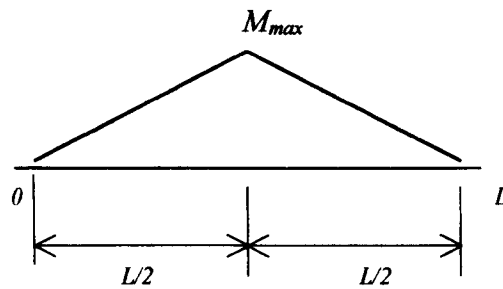


Fig 2.6: Bending Moment Diagram for Beam

Therefore, for such a beam and loading condition the bending moment varies across the span of the beam as shown in the above figure and reaches a maximum at $L/2$. For the case when $x = L/2$:

$$M_x = \frac{PL}{4} \qquad \text{Eq (2.6)}$$

Therefore the plastic collapse load, P_c , is given by:

$$P_c = \frac{4 \cdot M_p}{L} \qquad \text{Eq (2.7)}$$

Unlike the case of pure bending, the plastic moment is reached at only one cross-section of the beam (mid-span). When this happens a plastic hinge forms and the beam acts as a mechanism. Sustaining the applied loading results in lateral displacement of the beam through the plastic

hinge until failure of the beam. In static conditions, the plastic collapse load remains constant (at the value given by equation 2.7) thus no other cross-sections will become plastic.

Equations 2.6 and 2.7 implicitly assume equilibrium of all forces and moments and that yield conditions are satisfied. However, in plastic analyses, this represents only a lower bound to the true collapse load as a kinematically admissible collapse mechanism must develop. The collapse load can also be derived by considering the equilibrium and mechanism conditions, which may or may not be equal to the previously calculated collapse load. The collapse load derived in this manner will be an upper bound to the true collapse load. It has been proven [2.2] that these definitions of the lower and upper bound collapse loads will always remain valid for any structure and loading condition. If both methods produce the same value then this value is the true or exact collapse load. The upper bound collapse load is usually found using a virtual work or virtual velocities approach and the former is used below.

The virtual work method utilises the fact that the work done by the external loading will be equal to the work done by the beam in resisting bending. Therefore:

$$P \cdot \delta = \Sigma M \cdot \theta \quad \text{Eq (2.8)}$$

where δ is the beam's mid-span deflection and θ is the beam's rotation. Figure 2.7 below illustrates the relationship between the deflection and rotation of the beam.

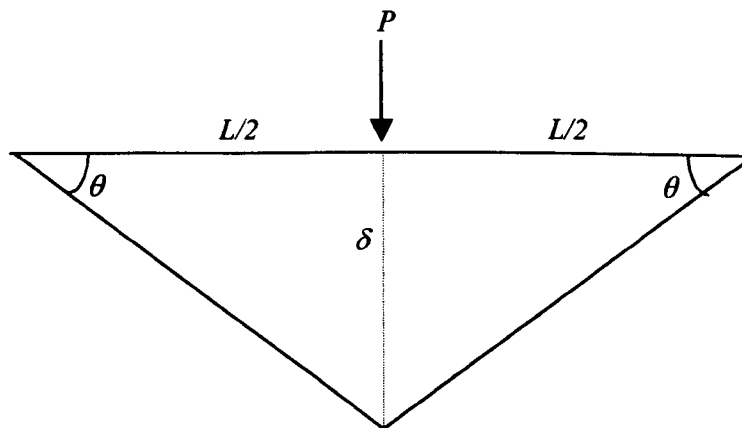


Fig 2.7: Deflection and Rotation of the Beam

It can be seen from figure 2.7 that $\theta = \tan^{-1} (\delta / L/2)$ and, for small rotations, $\theta = \delta / L/2$. Therefore $\delta = L\theta / 2$. Substituting this into equation 2.8, and since there is a rotation at both ends of the beam, equation 2.8 becomes:

$$\frac{PL\theta}{2} = 2. M\theta \quad \text{Eq (2.9)}$$

Therefore at collapse:

$$P_c = \frac{4. M_p}{L} \quad \text{Eq (2.10)}$$

As equations 2.7 and 2.10 both offer the same value for P_c it can be said that this value is the exact collapse load. It should be noted that a static loading case has been assumed and therefore it is the static plastic collapse load that has been obtained. Substituting equation 2.3 into equation 2.10 gives:

$$P_c = \frac{4\sigma_y A(y_1 + y_2)}{2L} \quad \text{Eq (2.11)}$$

Equation 2.11 is valid for any uniform beam undergoing small displacements with a cross-section that is symmetrical with respect to the vertical plane. Therefore, the geometry of the beams need not be considered at this stage though it shall be included in section 4.1.2 to determine the actual values of the collapse load. Note that the equation is not valid for analyses involving large displacements.

Haythornthwaite [2.3] investigated empirically solid rectangular cross-section beams to compare results with the static collapse load of equation 2.10. There was good agreement with beams having a length-to-depth ratio of between ten and twenty with the latter beam ratio being the closest to experimental results. However, for a beam with a ratio of forty the error between theory and testing was greater.

In the case of dynamic loading, the behaviour of the beam may change. The application of dynamic magnification factors to static plastic analyses generally lacks sufficient accuracy

[2.4]. This is because dynamic loading can result in different collapse modes from the static equivalent.

A rigid-plastic beam will remain rigid until its static plastic collapse load is reached. Static equilibrium is not possible for applied loads greater than the collapse load and, if this is the case, inertia forces will be generated. Displacements would be excessive if the loading was maintained for a substantial length of time but if the loading was a pulse the beam would deform until all the energy imparted by the load pulse had been absorbed.

Dynamic plastic analysis will usually involve a comparison of the static collapse load to the dynamic loading, P_o , to determine displacement and velocity profiles for the beam. Jones [2.5] showed using a theoretical analysis how these profiles can change during particular loading conditions when $P_o > 3.P_c$ to avoid yield violations (for different loading conditions, different dynamic factors apply). For dynamic loads less than three times the static collapse load, the displacement and velocity profiles are the same as for static loading and the static collapse load can be used.

2.1.3 Material Elasticity

It was observed in section 2.1.1 that both rigid-plastic and elastic-plastic models are possible. Both assume the same value of the collapse load but the pattern, or history, of deflection is different. It is desirable to determine which model is the most appropriate.

It is widely agreed that the influence of material elasticity on the permanent deflection of a structure is not great providing that the dynamic loading is large. To be more accurate, as long as the kinetic energy (*k.e.*) is much greater than the elastic strain energy (*s.e.*) that can be absorbed, elastic effects can be ignored. Thus, an energy ratio (E_r) is often defined which is the ratio of kinetic to strain energy and the condition set that this ratio be much greater than unity. Therefore:

$$E_r = \frac{k.e.}{s.e.} \gg 1$$

It is known that for a beam of volume V :

$$s.e. = \int \frac{\sigma_x^2 \cdot dV}{2 \cdot E}$$

where σ_x is the axial stress and E is Young's modulus. The strain energy is a maximum when the stress reaches the yield stress, σ_y , and so:

$$s.e._{\max} = \frac{\sigma_y^2 \cdot V}{2 \cdot E} \quad \text{Eq (2.12)}$$

The kinetic energy in an impact loading is given by:

$$k.e. = \frac{mv^2}{2}$$

where m and v are the mass and velocity of the impacting load respectively. The kinetic energy will reach a maximum ($k.e._{\max}$) at the impact velocity (v_i) and so:

$$k.e._{\max} = \frac{mv_i^2}{2}$$

Symonds [2.6] found that rigid-plastic models overestimated the permanent displacement by less than 10% when the energy ratio is greater than ten although the duration of the loading relative to the natural elastic period has an influence on the error. Yu [2.7] suggested that a ratio of five is generally acceptable although the mass ratio, rise time and pulse duration should all be considered.

Samuelides and Frieze [2.8] argued that there was a limit to the applicability of rigid-plastic analyses. The analyses of fully restrained beams subject to central impacts involving low energy ratios and not considering rate sensitivity could be in error by a factor of two to three [2.9]. The authors developed a numerical procedure that solves the partial differential equations governing large deflection transient response using the finite difference method. Results of this procedure were compared with analytical solutions. It was found that for rate-

insensitive beams the length-to-depth ratio of the beam had to be small (less than about 300) and the energy ratio not too small for analytical solutions to be valid. It was also noted that the applicability of analytical solutions reduces for rate-sensitive beams as the strain rate increases.

2.1.4 Transverse Shear and Finite Deflections

So far, only bending moments have been considered in the deformation of the beam but shear forces may also have a contribution. However, Hodge [2.10] concluded that, for beams, the influence of shear forces may be disregarded.

This said, Symonds [2.11] concluded that transverse shear effects are more important when the loading is dynamic. In addition, Nonaka [2.12] suggested, based on experiments and theory, that shear effects are greater when the beam has an open cross-section or when it is relatively short. To retain the influence of shear forces, a yield criterion is generally used. Shen and Jones [2.13] note that shear effects can be disregarded for low speed impacts. When the beams in question are not fully restrained it is again usually possible to neglect shear effects.

Until now, the influence of the change in the deformed beam's geometry on the collapse load has also not been considered. This change in geometry can be important as it results in a change in the internal forces of the beam.

Theoretical analyses that do not include the effect of finite displacements are often sufficient in the case of beams with no axial restraint. For beams with axial restraint, the importance of the applied moment and the shear force decreases as the beam deforms while a developing membrane force starts to dominate the beam's behaviour. Symonds and Mentel [2.14] developed a theoretical method for analysing axially restrained beams that can represent an upper bound theory. However, Symonds and Jones [2.15] presented an approximate method which includes the influence of finite displacements and which agrees much better with experimental data from authors such as Humphreys [2.16]. It seems to be the case that finite displacements become important in axially restrained beams when the deflection is greater than the beam's thickness.

No general theorems are available for plastic analyses that include the influence of finite displacements. This has led a number of researchers to develop approximate or bounding methods.

2.1.5 Effect of Strain Rate Sensitivity

When the plastic flow of a material is dependent on the strain rate ($d\varepsilon/dt$) then that material is known as strain rate sensitive. The sensitivity of a structure to strain rate is known to be a material property and independent of geometry [2.5]. It is widely agreed that mild steel is highly strain rate sensitive and an isometric projection of its stress-strain curve with varying strain rate in dynamic uniaxial compression is shown below in figure 2.8.

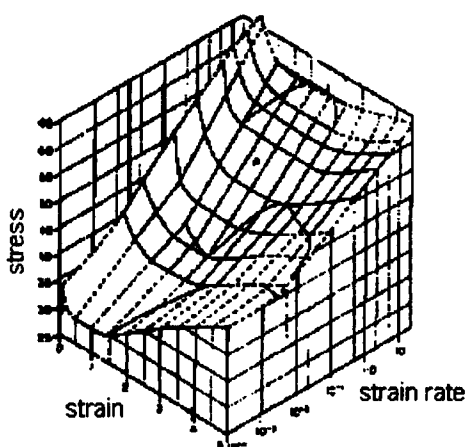


Fig 2.8: Stress-Strain-Strain Rate Curve for Mild Steel [2.17]

It can be seen in the above figure that the upper yield stress increases with strain rate. Also of interest, the material strain hardening appears to decrease with increasing strain rate. Tests of mild steel coupons in dynamic uniaxial tensile tests show similar characteristics and the findings of Campbell and Cooper [2.18] are represented below in figure 2.9.

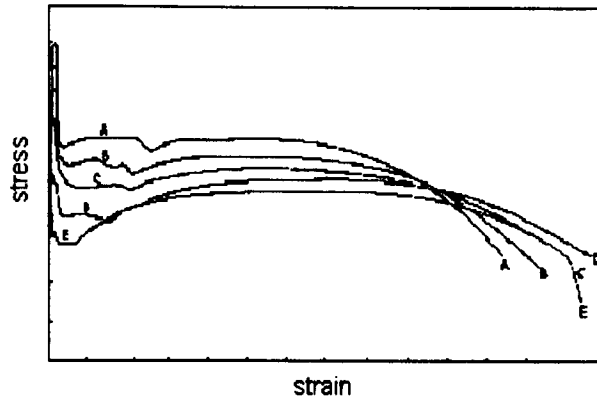


Fig 2.9: Tensile Stress-Strain curves at Strain Rates - A, 106; B, 55; C, 2;
D, 0.22; E, 0.001 [2.18]

The above figure shows other interesting points concerning the dynamic behaviour of mild steel. Both the upper and lower yield stresses increase with greater strain rates (Campbell and Cooper observed a 110% increase in the upper yield stress over a strain rate range of 10^{-3} to 10^2 sec^{-1}). The ultimate tensile stress also increases though less rapidly. Strain hardening effects again seem to diminish and the fracture strain decreases with increasing strain rate.

It is clear that mild steel is sensitive to the strain rate. However, it is widely recognised that the strain rate sensitivity is reduced as the strength of the steel is increased [2.19].

While aluminium is usually thought of as strain rate insensitive, the evidence is by no means conclusive [2.5]. It is clear, however, that it does not exhibit anything like the sensitivity of steel.

A number of researchers have formulated constitutive equations to represent the behaviour of different materials with the various coefficients determined empirically. By far the most widely used constitutive equation is that suggested by Cowper and Symonds [2.20] and it is shown below in equation 2.13.

$$\dot{\epsilon} = D \left[\frac{\sigma'_0}{\sigma_0} - 1 \right]^q \quad \sigma'_0 \gg \sigma_0 \quad \text{Eq (2.13)}$$

where σ_0' is the dynamic flow stress, σ_0 is the static flow stress and D and q are constants for a specific material. This can be rearranged to give equation 2.14:

$$\frac{\sigma_0'}{\sigma_0} = 1 + \left[\frac{\dot{\epsilon}}{D} \right]^{1/q} \quad \text{Eq (2.14)}$$

Thus the dynamic yield stress can be derived if the static yield stress is found from simple uniaxial static tests. Various researchers have determined values for D and q from experiments and these are given below in table 2.1. The values known for high strength steel are limited.

Material	D (s ⁻¹)	q
mild steel	40.4	5
aluminium alloy	6500	4
α-titanium (Ti 50A)	120	9
stainless steel	100	10

Table 2.1: Coefficients of D and q for Eq (2.12) - [2.5]

The Cowper-Symonds constitutive equation, sometimes modified for strain hardening, is used almost exclusively in engineering practice. Its validity, particularly at high strain rates and high strains, is in some cases questionable but its predictions have been found to be in excellent agreement with experimental results in the case of beams [2.21].

A number of researchers have examined the strain rate sensitivity of materials in bending. Rawlings [2.22] examined the dynamic behaviour of mild steel beams with rectangular cross-section in flexure and found that this behaviour agrees closely with the same material's behaviour in axial testing. However, the maximum strain rate they used was low at 1 s⁻¹.

Aspen and Campbell [2.23] looked at mild steel beams in bending at strain rates up to 20 s⁻¹. It was found that the increase in the yield stress in flexure due to strain rate was greater than that from axial testing.

2.1.6 Other Related Topics

There is a general consensus that the influence of material strain hardening is not great and can be ignored. Youngdahl used a modal approximation for beams with simple supports [2.24] and axial restraint [2.25].

Jones [2.26] considered the shape of the load pulse and stated that predictions involving impulsive loading were identical to those involving a rectangular pressure pulse of finite duration (since an impulsive load is simply a rectangular pulse of infinitesimal duration). Triangular pulses do, however, require special consideration. Symonds and Providence [2.27] also analysed the three types of load pulses mentioned and found only a variance of about ± 15 % for deformation arising from each of the loading types.

Seiler and Symonds [2.28] analysed rigid-plastic beams and examined the effect of concentrated loads in comparison to distributed loads. It was found that the final deflections for each type of load were very similar providing the distributed load was spread over up to about a third of the beam length.

2.2 STRUCTURAL CRASHWORTHINESS

2.2.1 Introduction to Structural Crashworthiness

The field of Structural Crashworthiness has, to date, been mostly concerned with the axial crushing of structures and, in particular, the axial crushing of axisymmetric tubes. This appears to be because the analysis is less complex and because the geometry and loading conditions represent the most efficient configuration for energy absorption. Yet in real life such configurations are not always possible and so alternatives must be used. An automotive collision, for example, will often be a side impact of structural members, i.e. beams, or a non-axial impact involving combined axial and bending loads. A number of researchers have recognised this and discussed the need for more research into bending response.

Structural crashworthiness for metal structures is often similar to plastic analysis, which was reviewed in section 2.1, due to the same plastic collapse mechanisms although crashworthiness will focus on energy absorption. The explicit study of the crashworthiness of beams is scarce though some work does exist on the subject and this is presented.

Axial crushing implies deformation modes quite different from lateral impact yet there is an overlap in the test methods and material behaviour. The same overall collapse mechanisms control the behaviour of beams and columns and are specific to the specimen material. For this reason, it was deemed important to review this area. Because the literature is more marginal to this thesis, full details of the literature review are provided in appendix 2.1. Only the main points are given below. As metal and composite sections behave quite distinctly, both must be considered.

For axially loaded metal structures, a progressive buckling mode gives the highest energy absorption. There is some dispute over the fundamental material property, the ultimate strength or the yield strength, involved in energy absorption.

Kecman [2.21] explained how the hinge behaviour of thin-walled beams may significantly differ from the predictions of plastic theory. Fully plastic moments may not develop, or the

moment may decrease following collapse (rather than remain constant) due to the elastic buckling of beam section walls. The maximum bending strength of thin-walled beams of rectangular and square section were calculated [2.28a] using the work of Rhodes and Harvey [2.28b] and then the possibility of elastic buckling considered. Theoretical models of the hinge collapse mechanism were developed. It was determined that fully plastic moments could only develop if the critical buckling stress was greater than 1.5 to 3 times the yield stress of the material. the bending collapse behaviour. Experiments at impact rates of up to 10 m/s showed that the dynamic collapse modes observed were very similar to the static collapse modes.

A number of researchers associated with Strathclyde University have investigated the collapse behaviour of thin-walled beams and columns. Authors such as Wah [2.28c] and Ho [2.28d] have also developed plastic mechanisms to help explain the behaviour of the structures.

Mamalis [2.29] has investigated the energy absorption of steel tubes in bending and the study does offer some information on the load response and deformation modes of these structures.

Composite tubes under axial crushing, unlike metals, absorb energy through a multiple microfracture processes. There are many more factors in a composite tube's degree of energy absorption than with metal tubes. These include the type, arrangement and nature of the fibre and resin, the manufacturing process used, the structural geometry, the method of triggering, material thickness, temperature and the rate of loading.

For composite components in bending, Mamalis looked at tubes of circular [2.30], rectangular [2.31] and hourglass geometry [2.32]. A common mode of failure was noticed for all these tubes although each had distinct differences in behaviour. Cheon *et al* [2.33] tested glass fibre-epoxy side impact beams of various cross sections in both static and dynamic three point bending. It was found that circular beams performed relatively poorly while square cross sectional beams could perform as well as steel impact beams.

Broughton *et al* [2.34] performed cantilever and three and four point static tests on U-channel and box section pultruded beams of various material types. Relatively simple theoretical analyses were presented for beam stiffness and failure loads which provided reasonably accurate predictions. Palmer *et al* [2.35] looked at the progressive failure of pultruded

rectangular composite beams during three point bending.. However, a particular mode of failure specific to the beam type tested was investigated. Failure was simulated using a Finite Element Analysis code, LS-Dyna.

2.3 COMPOSITE MECHANICS AND FAILURE

2.3.1 General Description of Composites

In this thesis the term ‘composite’ is used to refer only to fibre-reinforced polymer materials. Fibre-reinforced composites comprise of a large number of strong, stiff fibres (also known as the reinforcement) embedded in a second material called the matrix, which is most often a polymer. There are many possible types of fibre and types of matrix that can be utilised and so there are many more possible combinations.

In terms of orientation, fibres can be aligned (parallel), partially aligned or randomly oriented. This can lead to composites showing a high degree of orthotropy. The properties of an aligned composite, for instance, are highly anisotropic but significant improvements in strength are obtained if the stress is applied along the direction of the fibres.

The fibres are strong and stiff but, if the matrix was made solely of this material, it would be brittle. It could sustain a high stress but would fail in a catastrophic and unpredictable manner. The failure would result from surface flaws and crack propagation.

The matrix of the material serves to bind the fibres together and act as a medium for transmitting and distributing any applied stress to the fibres. It also protects the fibres from surface damage and, by keeping individual fibres separate, prevents any crack propagation from fibre to fibre. In addition, it should have good adhesive properties, an important factor in stress transfer. To achieve this stress transfer, the matrix must be relatively ductile so metals and polymers are most frequently used. Polymers, however, are chosen the most often due to their lightness and ease of fabrication. The polymer can be a thermoplastic or a thermosetting resin. Although thermoset composites make up the bulk of commercial composites, the type of material that shall be considered in this thesis is a thermoplastic. More specifically, the composite considered is a co-mingled glass/polypropylene material.

2.3.2 Thermoplastic Composites

Thermoplastic composites became more popular when traditional thermosets failed to provide sufficient damage tolerance. The thermoplastic matrix consists of long, closely packed molecules. Applying heat weakens the forces that hold these molecules together and the material softens until it reaches a viscous liquid state. Cooling the material will decrease its viscosity until it solidifies and returns to its original state. This is unlike thermosets which undergo a chemical reaction during processing which cannot be reversed by heating. The linear structure of the thermoplastic molecules allow substantial elongation before failure, 30 to 100 %, compared to thermosets, 1 to 2 %, with their rigid cross-linked structure.

Thermoplastic composites have a number of advantages over thermosets. They possess a higher toughness over the more brittle thermosets, which leads to good damage tolerance (impact resistance). They have considerable ability to resist delamination. In addition, the manufacturing of thermoplastic products tends to be quick and low-cost and the products themselves have a long shelf life. However, there are a number of problems specific to thermoplastics. Although the tensile properties are generally good, thermoplastics tend to have poor compressive strength. This can be due to yielding of the ductile matrix at high stresses causing premature fibre buckling. Other possible reasons for low compressive strength are poor fibre alignment and fibre waviness [2.36].

2.3.3 Co-mingled Fibre Composites

Glass mat thermoplastics (GMTs) found commercial applications, albeit mostly non-structural ones, from the 1970s. More recently, co-mingled E-glass and polypropylene materials have been produced which, while still aligned, are less expensive.

The process of co-mingling involves the production of multi-filament fibres from the thermoplastic material and then the blending together of these thermoplastic fibres with the reinforcing fibres. The co-mingled fibres are then used to produce a fabric using a standard weaving process. The Twintex fabric used within this thesis can be seen below in figure 2.10. By applying heat and pressure, the thermoplastic fibres melt and form the matrix for the reinforcing fibre. The commingling method entails a higher glass content which leads to a

higher strength and modulus and this makes them more suitable for structural applications. However, woven fabric has a low shear rigidity (their shear behaviour is dominated by the matrix) although this gives them good formability.



Fig 2.10: The Twintex Fabric

2.3.4 Composites in the Automotive Industry

There is a growing use of composites in the automotive industry though at present, for mass production volumes, their use is mainly in semi-structural or decorative applications. Composites offer the advantages of a weight reduction, design flexibility (in choice of materials and lay-up) and low fabrication costs. There is every reason to believe that an all composite car would equal or outperform a traditional steel car. The 1979 prototype car, Ford Graphite LTD, gave no difference in ride quality or vehicle dynamics and offered a 33% reduction in weight over standard production cars [2.37]. It is an important point, however, that if the application of composites leads to a lighter vehicle then the need for impact safety rises as statistics show that collisions of light vehicles with heavier ones are more severe for the lower mass vehicle.

Glass fibre composites are favoured by the automotive industry due to their being less expensive. In 1996 the Automotive Composites Consortium built and tested a car with a glass fibre front-end section, which went on to pass its crash tests [2.38].

The main limitations of composites are their processing time and cost. Even with Sheet Moulding Compounds (SMCs) which are the highest performance composite in general use within the automotive industry, the moulding time is around three to four minutes. The processes that offer the most promise for the future would seem to be resin transfer moulding (RTM) and structural-reaction injection moulding (SRIM) [2.38].

For smaller production rate vehicles composites often play a greater role. Lotus, for example, have been building cars with composite body structures since 1956.

2.3.5 Composite Macromechanics

(A) Constitutive Equations for Anisotropic Materials

Hooke's law for linear elastic behaviour can be generalised for the case of an anisotropic material as shown below in equation 2.15.

$$\begin{pmatrix} \varepsilon_1 \\ \varepsilon_2 \\ \varepsilon_3 \\ \gamma_{23} \\ \gamma_{31} \\ \gamma_{12} \end{pmatrix} = \begin{bmatrix} S_{11} & S_{12} & S_{13} & S_{14} & S_{15} & S_{16} \\ S_{12} & S_{22} & S_{23} & S_{24} & S_{25} & S_{26} \\ S_{13} & S_{23} & S_{33} & S_{34} & S_{35} & S_{36} \\ S_{14} & S_{24} & S_{34} & S_{44} & S_{45} & S_{46} \\ S_{15} & S_{25} & S_{35} & S_{45} & S_{55} & S_{56} \\ S_{16} & S_{26} & S_{36} & S_{46} & S_{56} & S_{66} \end{bmatrix} \begin{pmatrix} \sigma_1 \\ \sigma_2 \\ \sigma_3 \\ \tau_{23} \\ \tau_{31} \\ \tau_{12} \end{pmatrix} \quad Eq (2.15)$$

where the S matrix above is the compliance matrix which relates the stress (σ_i, τ_{ij} where i and j are integers representing the principal directions) in the material to its strain ($\varepsilon_i, \gamma_{ij}$). For an orthotropic material there is no interaction between shearing strains and normal stresses and equation 4.1 can be modified to give:

$$\begin{pmatrix} \varepsilon_1 \\ \varepsilon_2 \\ \varepsilon_3 \\ \gamma_{23} \\ \gamma_{31} \\ \gamma_{12} \end{pmatrix} = \begin{bmatrix} S_{11} & S_{12} & S_{13} & 0 & 0 & 0 \\ S_{12} & S_{22} & S_{23} & 0 & 0 & 0 \\ S_{13} & S_{23} & S_{33} & 0 & 0 & 0 \\ 0 & 0 & 0 & S_{44} & 0 & 0 \\ 0 & 0 & 0 & 0 & S_{55} & 0 \\ 0 & 0 & 0 & 0 & 0 & S_{66} \end{bmatrix} \begin{pmatrix} \sigma_1 \\ \sigma_2 \\ \sigma_3 \\ \tau_{23} \\ \tau_{31} \\ \tau_{12} \end{pmatrix} \quad \text{Eq (2.16)}$$

This equation can be simplified further if a state of plane stress is assumed:

$$\begin{pmatrix} \varepsilon_1 \\ \varepsilon_2 \\ \gamma_{12} \end{pmatrix} = \begin{bmatrix} S_{11} & S_{12} & 0 \\ S_{12} & S_{22} & 0 \\ 0 & 0 & S_{66} \end{bmatrix} \begin{pmatrix} \sigma_1 \\ \sigma_2 \\ \tau_{12} \end{pmatrix} \quad \text{Eq (2.17)}$$

It should be noted that equation 2.17 contains only four independent constants. The elements of the compliance matrix are noted below.

$$S_{11} = \frac{1}{E_1} \quad S_{22} = \frac{1}{E_2} \quad S_{12} = -\frac{\nu_{12}}{E_1} \quad S_{66} = \frac{1}{G_{12}}$$

It is assumed that the tensile elastic modulus is equal to the compressive elastic modulus. If it is further assumed, as for the composite weave material used in this thesis, that the longitudinal elastic modulus is equal to the transverse elastic modulus ($E_1 = E_2$) then only three constants are required to characterise the material. These are: E_1 , ν_{12} and G_{12} .

Rearranging equation 2.17 to express stress in terms of strain gives:

$$\begin{pmatrix} \sigma_1 \\ \sigma_2 \\ \tau_{12} \end{pmatrix} = \begin{bmatrix} Q_{11} & Q_{12} & 0 \\ Q_{12} & Q_{22} & 0 \\ 0 & 0 & Q_{66} \end{bmatrix} \begin{pmatrix} \varepsilon_1 \\ \varepsilon_2 \\ \gamma_{12} \end{pmatrix} \quad \text{Eq (2.18)}$$

where Q is the stiffness matrix and its elements are:

$$Q_{11} = \frac{E_1}{1 - \nu_{12}\nu_{21}} \quad Q_{12} = \frac{\nu_{12}E_2}{1 - \nu_{12}\nu_{21}} = \frac{\nu_{21}E_1}{1 - \nu_{12}\nu_{21}} \quad Q_{22} = \frac{E_2}{1 - \nu_{12}\nu_{21}} \quad Q_{66} = G_{12}$$

If the longitudinal elastic modulus is equal to the transverse elastic modulus then $\nu_{12} = \nu_{21}$.

(B) Transformation of Constitutive Equations

The above equations allow determination of principal stresses and strains. The principal values of an aligned fibrous material will always be in the direction of the fibres. Determining the stresses and strains in other directions can be achieved by transformation from the principal axes to some reference axes that represent the desired directions. If x , y and z represent the reference axes, transformation can be performed, for plane stress conditions, using equation 2.19 below.

$$\begin{pmatrix} \sigma_1 \\ \sigma_2 \\ \sigma_3 \end{pmatrix} = \begin{bmatrix} m^2 & n^2 & 2mn \\ n^2 & m^2 & -2mn \\ -mn & mn & m^2 - n^2 \end{bmatrix} \begin{pmatrix} \sigma_x \\ \sigma_y \\ \sigma_z \end{pmatrix} \quad \text{Eq (2.19)}$$

where $m = \cos \theta$ and $n = \sin \theta$. The angle θ is the rotation from the principal to the reference axes.

2.3.6 Composite Failure

(A) Introduction

There are many more modes of failure possible for a composite material than for an isotropic material such as steel. Strength will vary according to the type of loading (type and direction), constituent properties (and their relationship to each other) and failure will tend to be more localised than in other materials. Predicting how and when failure will occur in composite materials are recognised to be difficult to achieve.

(B) Failure of Unidirectional Composites Under Single Type of Loading

The failure modes for unidirectional composites subject to one type of loading in the material's principal material directions are now briefly discussed.

The axial tensile strength of a composite (the strength in the direction of the fibre) is generally a function of the strength of the fibres alone. Fibre strength is not easy to measure as it can vary. Single filaments are rarely used to determine strength. Instead, the fibres are impregnated with a low quality matrix and then tested. Strength will decrease as gauge length increases due to the increasing possibility of finding an imperfection [2.39]. A number of 'sub-modes' have even been identified for how the fibres fail. These include weakest-link failure, cumulative weakening failure and fibre break propagation failure among others.

In terms of the axial compressive strength of the composite, both strength and stability must be considered. An instability known as microbuckling is possible and two types are possible: the shear and the extension mode. Fibre diameter will affect material strength [2.39].

All other failure modes are collectively termed the matrix mode strength as they are all dominated by the properties of the matrix. Specifically, these modes are transverse tension, transverse compression and shear. Transverse tensile properties are generally the same as for the matrix [2.39]. For transverse compression, failure occurs through shearing along a surface parallel to the fibre axes, similar to a homogeneous material.

(C) Composite Failure Criteria

The above failure modes are concerned with unidirectional composites subject to one type of loading, however most structures are subject to combined stresses. This may be because of the structure's geometry, the type of loading or the use of laminates with varying ply orientations.

In this case, it has been common to construct failure criteria that predict when failure will occur. This is not an easy task given the complexity of the material and there is little consensus on which is the best criterion to use in any given situation.

The criteria all essentially describe a closed surface in stress space (the axes being the three principal stresses) with points inside the surface indicating no failure, points on the surface indicating failure and points outside the surface being stress-states that cannot be realised. More specifically, the criteria seek to identify when first failure will occur. In a laminate, for example, first failure describes when the first ply will fail although the laminate as a whole may be capable of sustaining far greater stresses.

The most simplistic criteria assume that failure will occur when some peak value of stress or strain is reached and these are the Maximum Stress (first developed by Stowell and Liu [2.40]) and the Maximum Strain (often attributed to Waddoups [2.41]) criteria respectively. There are five peak values, obtained from separate uniaxial tests, which correspond to five strength properties in the conditions of tension, compression (in both axial and transverse directions) and shear. For example, the maximum stress that the composite can sustain during an axial tensile test is assigned to be the axial tensile strength of the material. In the Maximum Stress criterion, failure is deemed to have occurred when any of the expressions given below in equation 2.20 are satisfied.

$$\frac{\sigma_1}{X^t} = 1 \quad \frac{-\sigma_1}{X^c} = 1 \quad \frac{\sigma_2}{Y^t} = 1 \quad \frac{-\sigma_2}{Y^c} = 1 \quad \frac{|\tau_{12}|}{S} = 1 \quad \text{Eq (2.20)}$$

where $X^{t,c}$ and $Y^{t,c}$ are the tensile and compressive strengths in the longitudinal and transverse directions respectively and S is the shear strength. Note that an expression for the Maximum Strain criterion would be similar to equation 2.20 but with the applied and failure stresses replaced with the appropriate applied and failure strains.

If the loading on a given composite is not in the material's principal directions then the principal stresses are calculated using equation 2.19. The failure surfaces in stress space of a composite subject to plane stress predicted by the Maximum Stress criterion are shown below in figure 2.12. The Maximum Stress or Strain criteria have been said to be appropriate only when one stress component is dominant [2.39]. Certainly both criteria disregard any interaction of the other stresses and tend to be non-conservative, particularly in the two tension-compression (shear) quadrants of stress space. For this reason, it is common to

truncate these quadrants to shear strain limits obtained from experiment. This truncation is also shown in figure 2.12.

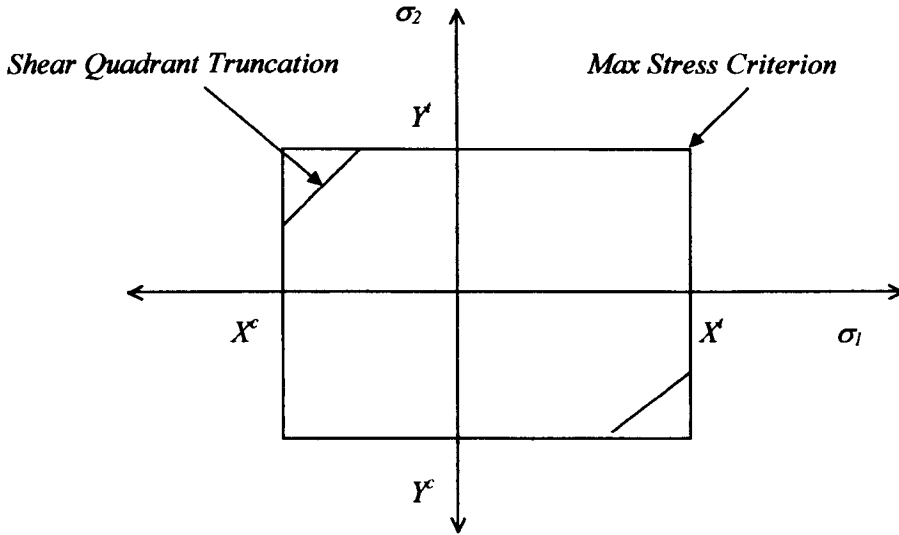


Fig 2.12: Failure Envelopes for Normal and Truncated Maximum Stress Criteria

A number of researchers have attempted to include stress interaction effects within their failure criteria. Some have based their work on yield criteria such as the Tresca or Von Mises criteria which have been generalised, for instance by Hill [2.42], for anisotropic materials. The most common criterion of this sort is by Tsai-Hill [2.43]. Yield strengths are replaced by the composite strengths as defined in the Maximum Stress or Strain criteria although no distinction is made between tensile and compressive loading. However, stress interaction terms are included within a continuous polynomial equation such as, for Tsai-Hill, in equation 2.21 below.

$$\left(\frac{\sigma_1}{X}\right)^2 + \left(\frac{\sigma_2}{Y}\right)^2 - \frac{\sigma_1\sigma_2}{X^2} + \left(\frac{\tau_{12}}{S}\right)^2 = 1 \quad \text{Eq (2.21)}$$

Note that X, Y and S are the failure strengths as in equation 2.20 except that no loading direction (tensile or compressive) is defined. Since tensile and compressive strengths are generally different in magnitude, this represents a serious limitation to the theory although in

practice the theory is applied using different strength values depending on the different quadrants in stress space. Thus, the sign of the normal stresses must be known *a priori*.

Other researchers have proposed yield-based methods that account for differing strengths in tension or compression. Yet, fundamentally, yield-based criteria do not attempt to describe the true physics of composite failure but rather only provide better correlation with empirical data. Other researchers have chosen to give no physical meaning to their methods at all, rather, they attempt mathematically to best fit the empirical data in a manner where the failure envelope is independent of orientation in stress space. Generally, tensor notation is used and these criteria are known collectively as Tensor Polynomial Criteria.

Perhaps the most well known example in this category is the Tsai-Wu criterion [2.44] which, in its most popular form, is expressed below in equation 2.22. This criterion is often referred to as the strength index.

$$F_1\sigma_1 + F_2\sigma_2 + F_{11}\sigma_1^2 + F_{22}\sigma_2^2 + F_{66}\tau_{12}^2 + 2F_{12}\sigma_1\sigma_2 = 1 \quad Eq (2.22)$$

The F_{ij} coefficients above are directly related to the material's failure strengths:

$$F_1 = \frac{1}{X^t} - \frac{1}{X^c} \quad F_{11} = \frac{1}{X^t X^c} \quad F_2 = \frac{1}{Y^t} - \frac{1}{Y^c} \quad F_{22} = \frac{1}{Y^t Y^c} \quad F_{66} = \frac{1}{S^2}$$

Another, less well known, version of the Tsai-Wu criterion is referred to as the strength ratio.

It should be noted that the F_{12} term in equation 2.22 is undefined as it cannot be determined in terms of ultimate stresses and there is no consensus on how the term should be determined. Biaxial tests are therefore often used to find the coefficient although this can often lead to unrealistic situations such as the compressive strength being considered in a biaxial tensile test. Some authors have proposed other empirical methods for determining F_{12} or expressions based on failure stresses that seem to correspond to empirical data. Others, such as Narayanaswami and Adelman [2.45], maintain that setting the term to zero will result in low errors (typically less than ten percent) but there seems little point in developing a tensor criterion and then ignoring the stress interaction.

In general, the polynomial criteria are all mathematical best fits and no explanations of the physical bases for failure are attempted. Indeed, they do not account for the various possible failure modes and a few researchers have attempted to correct this.

A popular criterion of this nature is by Hashin [2.46] who identifies the modes of tensile or compressive fibre failure and tensile or compressive matrix failure. Each mode is described separately by a quadratic polynomial.

For a tensile longitudinal stress, Tensile Fibre failure occurs when:

$$\left(\frac{\sigma_1}{X^t}\right)^2 + \left(\frac{\tau_{12}}{S}\right)^2 = 1$$

For a compressive longitudinal stress, Compressive Fibre failure occurs when:

$$\left(\frac{-\sigma_1}{X^c}\right)^2 = 1$$

For a tensile transverse stress, Tensile Matrix failure occurs when:

$$\left(\frac{\sigma_2}{Y^t}\right)^2 + \left(\frac{\tau_{12}}{S}\right)^2 = 1$$

For a compressive transverse stress, Compressive Matrix failure occurs when:

$$\left(\frac{\sigma_2}{2S}\right)^2 + \left[\left(\frac{Y^c}{2S}\right)^2 - 1\right] \frac{\sigma_2}{Y^c} + \left(\frac{\tau_{12}}{S}\right)^2 = 1$$

The shear strength is noted to be difficult to measure but can be taken to be the shear strength of the matrix. Whichever polynomial is satisfied first indicates the value and also the mode associated with first failure.

A failure criterion which is noticeably different from any discussed above is by Hart-Smith [2.47] and this is because the laminate is treated as a whole rather than individual plies. The theory only applies to fibre dominated failures and is based on the Tresca yield criterion. Failure occurs when the shear strain in the fibre reaches some maximum value.

A survey of composites designers, reported by Soni [2.48], showed that over ninety percent use either the Maximum Stress or Strain criteria or some form of polynomial criteria (usually Tsai-Wu).

(D) Ultimate Failure in Composites

How to consider the subsequent strength of the composite after first failure is unresolved although there is a common approach no matter which failure criterion is being used [2.39]. In the case of fibre failure the axial elastic modulus for the failed ply is reduced, often to zero as fibre failure tends to be catastrophic. For a matrix failure the transverse elastic modulus and the shear modulus are reduced though seldom to zero as uncracked regions even within a failed ply can remain bonded to adjacent layers. There is no specific guidance on how to treat failures in the modes of longitudinal compression or shear.

In the case of multiple laminates, another approach to modelling behaviour after first ply failure is to redistribute the load to the remaining plies and this is termed the Ply Discount method. It has been stated however that this method disregards the ability of the load to redistribute through ply interface bonding [2.39]. Yet another approach, as used by Petit and Waddoups [2.49] treats the failed ply as an elastic-plastic material though this method may not describe the true method of load redistribution.

(E) Related Issues

Residual thermal stresses, induced during the fabrication process are often included within failure criteria though there are good reasons for not including them. Firstly, the matrix will exhibit viscoelastic effects and residual stresses will be dissipated over time. Secondly, a limited amount of microcracking in the matrix during loading can reduce these stresses without significantly affecting the material properties [2.39].

None of the failure criteria described above account for a different mode of failure which is delamination (separation of the individual plies of a laminate). The mismatch of the material properties of two adjacent layers induces through-thickness stresses (interlaminar stresses) which can cause failure of the boundary between the two layers. Failure initiates, and is often confined to, any free edges of the structure where the interlaminar stresses can be singular.

Ebeling *et al* [2.50] examined delamination failure within a woven glass fibre composite. They found that crack growth was dominated by fibre-matrix debonding with the crack direction following the undulating pattern of the yarn. Any change in the crack path increased the delamination toughness. Crack jumps caused sharp load drops in the loading history of the specimen.

Recently, a comparison of twelve commonly used failure criteria was made by Hinton *et al* [2.51]. Predictions were made for initial and final failure stresses and deformations, by the originators of the various criteria, of a $(0/90)_2$ cross ply laminate which was regarded to be the simplest test case that could be set. Though all the originators were given the same information on processing and material properties many made different assumptions, such as whether to include residual stresses or whether lamina properties should be increased when considering a whole laminate. The predictions of initial and failure stresses and strains were generally poor with only two authors (Puck and Zinoviev) identifying an intermediate stage of failure seen in experiments.

It is clear that the field of composite failure prediction is far from being mature. A large number of very different approaches exist with little consensus on which particular criterion is the most appropriate for any given material type or loading condition. There is no true understanding of the physical basis for failure. A number of researches acknowledge this and offer only a mathematical best fit to empirical data.

2.4 TESTING METHODS

2.4.1 Introduction to Testing Methods

This section is concerned with a number of specific (and somewhat eclectic) aspects concerning experimental testing. The intentions of this section are to set the background for the testing procedures chosen within this thesis and also to highlight the problems and limitations of a number of test methods. It should be borne in mind that this thesis is concerned with two distinctly different types of testing: the static and impact beam tests and the coupon testing.

2.4.2 Drop Weight Testing

Birch and Jones [2.52] compared a laser Doppler velocimeter (LDV), accelerometer and load cell in the measurement of impact load during a drop test. Post-test numerical filtering was used rather than any electronic filtering to reduce the risk of signal distortion and pre-filtered signals showed three ranges of frequency content: low (<1 kHz), medium (1 - 4 kHz) and high (>10 kHz). High frequencies were explained by 'ringing' of the striker at impact and the medium range are explained by a spring and mass analogy in that the spring (beam specimen) would have a natural frequency of 2 - 4 kHz for the specimens used. Only the low frequency range is said to represent the true structural behaviour of the beams and so a 1 kHz cut-off frequency is used. Peak loads proved to be difficult to measure therefore no comparison was made.

Birch *et al* [2.53] discussed how energy loss could be used as a criterion for the performance of an impact rig. By their criterion, any energy not used to permanently deform the specimen should be considered a loss. It is suggested that the effectiveness of a rig can be established by measuring the impact energy dissipated by the anvil (support) and it was found that increasing the anvil-to-striker mass ratio reduced energy loss. It should be noted however that energy losses were still acceptable at loads of around 350 kN and only became unacceptable approaching loads of 800 kN.

Money and Sims [2.54] outlined a procedure for the calibration of load cells used in drop tests. They point out that the recommended procedure (by the load cell manufacturer) calibrates only the charge amplifier and neglects the load cell and its cable. They then offer an in-situ method that includes the whole set up including the striker (ensuring that all the impact load is transmitted to the load cell).

The output signal of a quartz load cell unavoidably drifts with time due to capacitive feedback (stray currents that build up in the capacitor within the amplifier's circuitry). Drifting cannot be eliminated and so the calibration procedure must account for it.

The procedure of Money and Sims involves applying a load to the striker and then removing it with the whole event captured by the oscilloscope. Force against time data is calculated, a least-squares first-order fit used to remove background noise and then the difference in force when the load is applied and when it is removed is calculated. This is illustrated below in figure 2.13.

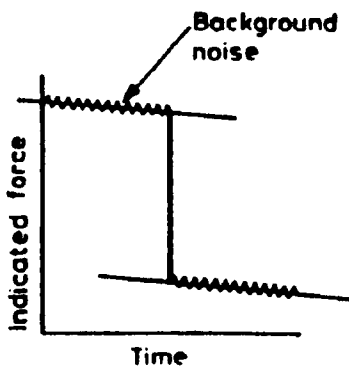


Fig. 4. Least-squares fit performed.

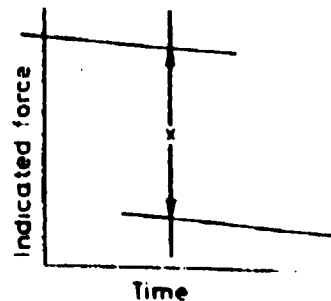


Fig. 5. Difference in force is calculated.

Fig 2.13: Illustration of Procedure of Money & Sims [2.54]

If the applied mass is known then the applied force can easily be ascertained. Thus, the measured load can be compared with the applied load and different applied loads can be used to check the linearity of the load cell/amplifier. This method is said to provide an error of considerably less than one percent.

2.4.3 Composite Coupon Testing

(A) Tensile Composite Coupon testing

The main concern within the tensile testing of composite coupons is that fibre direction should be correctly aligned with the loading direction. Even a small difference can lead to significant variations in the properties obtained in some materials. Composite laminates should also be balanced and symmetric with respect to the test direction. [2.39].

(B) Composite Compressive Coupon Testing

The testing of composite coupons in compression is widely known to be problematic leading to some sets of results being as much as twice the value of others. There are two main reasons for premature failure of coupons: stress concentrations and buckling. Localised stress concentrations can occur at the end of the gauge length. If buckling is allowed to occur then false failure modes such as gross shear or transverse splitting can occur rather than true modes characterised by crushing or shear of individual fibres [2.55].

A number of methods have been devised to combat these difficulties and many of the methods are used within the various standards that exist for compression testing of composite materials. Both of the above difficulties lead to premature failure and so a frequently used criterion for the suitability of a given standard is that 'the higher the results the better'. While this approach is often justified there are, as shall be seen, pitfalls associated with it.

The *ASTM D695* standard [2.56] uses dog-bone shape specimens subject to direct end loading however this often leads to crushing of the ends. An anti-buckling device is utilised. A version of this standard, the *Modified D695* method [2.57], is said to be simple to use, inexpensive to fabricate and produces results slightly higher than most other methods. It does however require separate specimens for the measurement of compressive modulus and strength. Care must also be taken with the bolt torque used to restrain the specimens. It has been found that increasing the torque proportionally increases the values of the results achieved but that these results are artificially high as they are produced by redundant load paths [2.55]. Finger-tight bolts are recommended.

ASTM D3410 [2.58] describes two methods which are known as the *Celanese test fixture* and the *IITRI* method. The Celanese method is rarely used today due to difficulties in grip alignment, which can cause redundant load paths [2.55]. The IITRI method is considered to be reliable although the large mass of the fixture and its high fabrication cost are recognised shortfalls [2.59]. The method involves shear loading via wedge grip interfaces with a short gauge length to avoid buckling.

The Modified D695 method and the IITRI method are the two most popular methods in industry although many others are used.

Curtis and Gates [2.60] suggest an approach similar to *ASTM D3410* but using tabbed specimens which are machined to particular radii to reduce stress concentrations. Finley and Adams [2.61] also used thickness-tapered specimens. While these methods seem to work well for thermosets, it is less effective for tougher materials such as thermoplastics.

A number of methods involve the use of sandwich beam specimens. These have a low modulus core material between two layers of the material of interest, which gives the coupon greater stability and therefore eliminates buckling. One drawback is that the two different types of material can debond due to mismatching of the values of Poisson's ratio. Crasto and Kim [2.62] believe this can be overcome using smaller sized specimens with better matched values of Poisson's ratio. However, the specimens remain harder to produce than conventional coupons.

Angle-ply laminates, with reference to the loading direction, provide an indirect method of determining material properties. Methods associated with this material type have less trouble with buckling since unidirectional materials are much more prone to the instability. This may not relate directly to woven fabrics though loading at 45° to the fibre direction (and allowing for fibre direction) may give different results.

The methods described above of thickness tapered, sandwich beam and angle-ply specimens have often given much higher (50 - 100%) results than the two most popular methods [2.55]. However each approach has its limitations.

Another method is by McKelvie et al [2.63]. A fixture was designed to test delamination in composites but can be, and has been, adapted for coupon testing. The fixture holds the coupon and transmits end loading when fitted into a standard testing machine. Results were compared with tests using a Celenese rig and were found to be higher.

Barker and Balasundaram [2.64] developed a compression rig to use on untabbed dog-bone specimens. The rig design entailed that about 20 % of the load was transferred through the side faces and 80 % through the ends of the specimen and this avoided end crushing.

Mathews and Häberle [2.59] used a rig similar to that devised by Barker and Balasundaram but with a modified specimen design. The specimen was rectangular rather than dog-bone shaped. End loading was applied yet tabs were still used to take up a portion of the load and thus avoid crushing. Their method (known as the *ICSTM* method) also incorporates weakly bonded areas near the gauge length of the specimens to eliminate stress concentrations. Thus the two main causes of premature failure are assumed to have been, at the least, minimised.

It should be noted that the literature is generally concerned with premature failure reducing the value of the compressive *strength* of the material. It can be seen in Mathews *et al* [2.65] that the compressive modulus is also subject to significant variation however no explanation for this is given.

Hsiao and Daniel [2.36] performed compression tests, at various strain rates, on unidirectional carbon/epoxy laminates. At higher rates, the behaviour was more linear (though the difference was small) and the strength and ultimate strain of the material were significantly higher.

(C) Composite Shear Coupon Testing

Shear testing of composites can often produce behaviour that is quite unexpected when considering their tensile characteristics. This shear behaviour may be non-linear, rather than elastic until failure, involving strains that are many times the tensile failure strain [2.39].

Hsiao and Daniel [2.36] also observed this non-linear behaviour during off-axis compression tests on unidirectional carbon/epoxy laminates. They also found that there was a significant increase in strength, and a small increase in the shear modulus, as the strain rate increased.

This was explained by the viscoelastic nature of the matrix and by time-dependent damage accumulation (at higher strain rates, damage does not have time to develop).

There are several methods of determining the shear properties of composites. These include tensile or compressive testing of off-axis (particularly $\pm 45^\circ$) laminates, rail shear tests, torsion of tubes and Iosipescu shear testing. Torsional testing is often seen as the most pure form of testing but it is limited to unidirectional materials and requires special procedures for fabrication. It cannot be used in the testing of flat coupons. For the other types of tests, there are problems associated with all of them such as they induce stress concentrations or they measure only the shear modulus or the shear strength but not both [2.66].

Rail shear testing involves fixing a rail to each longitudinal edge of a specimen and pulling each rail in opposite directions. However, failure is often caused by stress concentrations which form where the rail is fixed to the specimen [2.66].

Off-axis coupon testing is a popular method in the case of flat coupons requiring no special fixtures or specimens but there are some concerns that it does not accurately determine the shear strength [2.67]. Outer plies of the specimen may fail due to normal stresses rather than shear stress leading to an underestimated value of shear strength.

Another method, highly suitable for flat coupons is that originally devised for isotropic materials by Iosipescu [2.68], developed for composites by Walrath and Adams [2.66, 2.69] and eventually produced as an ASTM standard [2.70].

(D) Flexural Testing

A number of standards exist for the flexural testing of coupons; an example is *ASTM D790-96a* [2.71]. This standard offers two methods for calculating the flexural modulus and strength: three- and four-point bending tests. However, it has been observed that each of these tests results in different values of flexural strength being determined [2.72]. Also, strength is dependent on load span: strength decreases with increasing span. This is explained by different modes of failure (tensile, compressive or shear) being dominant at different spans and so affecting the flexural strength. It is stated that flexural strength is therefore not a material property. The flexural modulus, on the other hand, was not found to vary significantly.

In flexure, the flexural strength is dominated by the fibre tensile strength though it is influenced by the compressive strength [2.73].

2.4.4 Other Issues

(A) Strain Gauges

Strain gauges work on the principle that materials experience a small change in electric resistance when strained [2.74]. The gauge measures this change in resistance and converts it to values of strain. However, composite materials have poorer heat conduction than metallic materials and may be unable to dissipate the heat generated within the gauge. This can lead to measurement error.

There are two common methods of avoiding this problem. The first is to use higher resistance strain gauges. Since the power dissipated from the gauge is proportional to the voltage squared divided by the resistance, a higher resistance gauge will generate less heat. However, this type of strain gauge is expensive. The second method is to use a short burst data logger in conjunction with the gauges. The data logger uses discrete impulses with a short duration to measure the data and so very little heat is generated.

The strain gauges must also be of a sufficient size to avoid measuring only localised strain effects. For composite materials of weave construction, the basic repeating unit of the material should be represented.

SUMMARY OF CHAPTER

A number of relevant fields have been reviewed.

Plastic analysis uses idealisations to model the plastic collapse of metal structures. Plastic collapse loads have been derived for a simply supported beam subject to a mid-span load and, for such a loading condition, an exact collapse load is obtained.

The static collapse load is sufficient in dynamic conditions if the dynamic loading is less than three times higher than it. Material elasticity is important only at low energy ratios and the effects of transverse shear and finite deflections can be disregarded for non-axially restrained beams subject to low impact velocities. The effect of varying strain rate, however, can significantly alter a structure's response and this effect may be even greater for beams in flexure. Strain hardening can generally be ignored though the type of loading may be significant.

Structural crashworthiness research has primarily focused on the axial crushing of axisymmetric tubes. The same failure mechanisms govern the response of beams and columns and are dependent on the material type. Both steel and composite structures have been considered.

Descriptions have been given for composites and, in particular, co-mingled fibre thermoplastic composites. The Macromechanics and failure of composites has been briefly presented. The most popular failure criteria have been described.

Various aspects of testing have been considered, particularly concerning the testing of composite coupons and also drop weight testing.

CHAPTER THREE

EXPERIMENTAL TESTING OF STEEL COUPONS & BEAMS

OVERVIEW OF CHAPTER

The overall objective of this thesis is to assess and model the performance of two side impact beams; a particular type of composite beam is of interest as an alternative to the conventional choice of a steel beam. Both types of beam have been experimentally tested and modelled. Testing of steel beams has provided performance data with which to compare the composite beams and has helped to develop suitable testing procedures. Modelling of the steel beam has helped to develop appropriate modelling techniques to be used with the composite beam.

This chapter presents all of the experimental testing that has been performed on the steel side impact beam. The structure of the chapter is represented as a block diagram in figure 3.1 below.

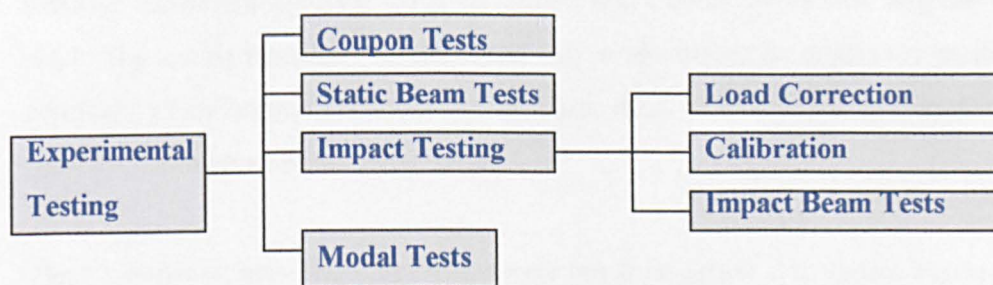


Fig 3.1: Block Diagram of Structure of Chapter

Coupon tests were used to characterise the properties of the material. Values for the elastic modulus and the strength (in terms of stress and strain) were derived. A yield stress was obtained using the principle of a proof stress.

The testing of beams has determined their behaviour in terms of load, deflection and energy absorption for static conditions. Elastic, collapse and post-collapse behaviour was clearly identified.

This can also be done for impact test conditions but dynamic effects are significant in the loading history for the beam. These effects are believed to be due to the dynamic properties of the beam and striker rather than to extraneous sources such as instrumentation noise.

There is a strong similarity between the beam's static and impact behaviour as seen in the beam's loading or energy absorption history.

Also, modal testing has assessed the beams' modal properties in an attempt to explain the beam's behaviour during impact tests. A number of resonant frequencies were obtained as well as the beam's damping characteristics. However, it is concluded that this modal testing cannot be used to predict impact behaviour though it can be used in the validation of a Finite Element model that may be able to predict the impact behaviour.

For all of the types of testing, the proper calibration of test equipment has been considered vital to achieving accurate results. For the impact testing of beams in particular, considerable work has gone into ensuring an adequate level of calibration.

3.1 TENSILE TESTING OF STEEL COUPONS

3.1.1 Introduction to Tensile Coupon Testing

A series of coupon tests were performed to determine the mechanical properties of the material used to produce the steel side impact beams. The manufacturer of the steel material describes it as a press quenched steel with the grade name 'Boron 02'. The tensile testing was designed to be in accordance with BS EN 10002-2:1992 which makes use of 'dog-bone' shaped specimens.

3.1.2 Equipment Used During Testing

The testing was carried out on a Tinius Olsen test machine. This is an electro-mechanical machine capable of applying loads up to 890 kN. Further details are supplied in appendix A3.1. The testing machine was calibrated only weeks before the tests were performed and a certificate of calibration is included as appendix A3.2. Displacement was measured using an extensometer with a 50 mm gauge length.

Three specimens were tested and these were cut from actual side impact beams as no other form of the material was available. Nominal dimensions were as specified in the fore-mentioned standard. These are illustrated in appendix A3.3, which also presents a table of the measured thickness and width of each coupon determined using Vernier callipers.

3.1.3 Testing Procedure

Coupons were first cut from the steel beams using a band saw. Each coupon was placed in the grips of the testing machine and the grips tightened. The tests were then performed at a displacement rate of 10 mm/min. The extensometer was connected to a plotter that produced graphs on paper of load against deflection for each coupon. Each value of load was listed with its associated deflection and then inputted into the spreadsheet package Microsoft Excel v7.0. This allowed much greater ease of manipulation and presentation.

The only source of test specimens was the actual side impact beams. This did ensure that the material being tested was consistent with the beam material. However, due to the required width of the coupons and the lesser width of the steel beam, it was observed that the coupons were not flat but rather were curved. The coupons were then pressed flat but this led to a slightly corrugated profile. Consequently, grip of the coupons in the testing machine was not evenly distributed but confined to certain regions of the coupons and, as a result, coupon test results may have been affected.

Load and deflection data were first offset so that each set began at zero and they were also converted from imperial to metric units. The data was then used to calculate engineering stress, σ_{eng} , and strain, ϵ_{eng} , values and the formulae used are given below as equations 3.1 and 3.2.

$$\sigma_{eng} = \frac{F_t}{A} \quad Eq (3.1)$$

$$\epsilon_{eng} = \frac{\Delta L}{L} = \frac{\delta}{L_G} \quad Eq (3.2)$$

Where F_t is the applied tensile force, A is the cross-sectional area of the coupon, ΔL is the change in length of the coupon, L is the original length, δ is the deflection and L_G is the gauge length. From these values the true stress, σ_{true} , and true strain, ϵ_{true} , could be derived using the formulae given below as equations 3.3 and 3.4.

$$\epsilon_{true} = \ln(1 + \epsilon_{eng}) \quad Eq (3.3)$$

$$\sigma_{true} = \sigma_{eng} (1 + \epsilon_{eng}) \quad Eq (3.4)$$

The relationship between stress and strain can now be plotted and a number of material properties can easily be derived from the data. Finally, small sections taken from a test coupon were polished and viewed under a microscope at a magnification factor of 400.

3.1.4 Results of Tensile Testing

A typical plot of stress against strain is shown below in figure 3.2, which also shows the proof stress line (defined below) and notes the values of the proof stress and the ultimate tensile stress, uts .

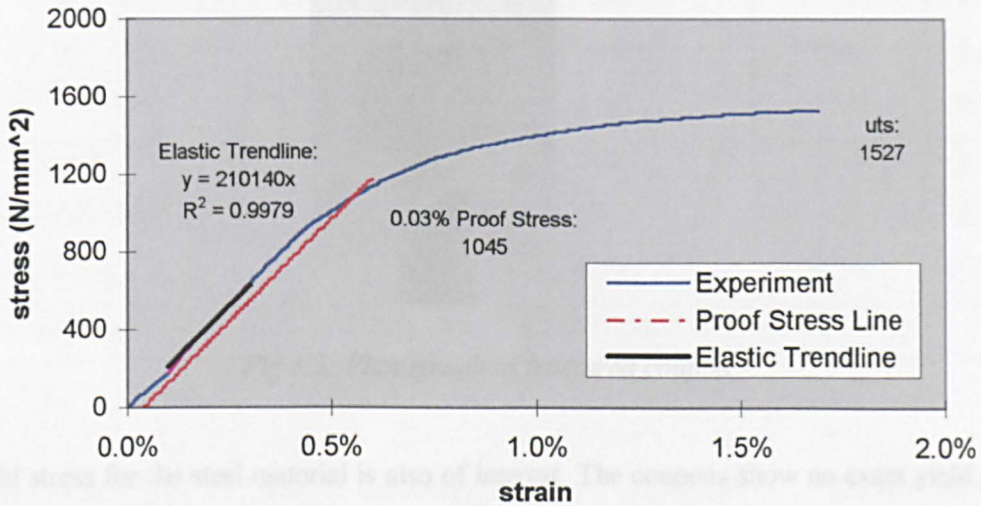


Fig 3.2: Typical Plot of Stress v Strain During Coupon Testing

The elastic modulus is the gradient of the curve for stress against strain within the elastic region. The standard recommends using the range of 0.1 to 0.3 % strain for calculating the elastic modulus. The data within this limit was selected and a trend line inserted. The gradient of the trend line was taken to be the elastic modulus.

The responses of the specimens are slightly non-linear at an early stage of the testing. However, this ‘settling period’ is common in many forms of coupon testing [3.1] and, although the warped profile may have had an additional effect, it is assumed that the effect is not particularly significant. Calculating the elastic modulus from 0.1 to 0.3 % strain is assumed to account for this early settling.

On each plot, the point where the curve ends represents the point of fracture of the specimen. Of interest are the values at this point both in terms of the stress and the strain. These values are the ultimate tensile strength, σ_{uts} , and the ultimate tensile strain, ϵ_{uts} , respectively. The

crack direction was always angled at about 45° in the plane of the specimen with fracture initiating at the fillet radius in two of the three tests. In the other test (coupon 2), the fracture was near the mid-span of the gauge section. Figure 3.3 below is a photograph of a fractured coupon.

	Force (kN)	Displacement (mm)	Force (kN)	Displacement (mm)
1	1043	1527	1.69	
2	985	1542	3.17	
3	929	1580	2.06	
Mean	983	1554	2.31	
Standard Deviation	61	27	0.80	
CV (%)	6.36	1.76	33.39	
Standard Error	20.4	13.5	0.25	

Fig 3.3: Photograph of fractured coupon

A yield stress for the steel material is also of interest. The coupons show no exact yield point but the non-linearity demonstrates that yielding is occurring. When no obvious yield point is exhibited it is common to use a proof stress. This method involves offsetting the gradient of the stress-strain curve (in the initial elastic region) by some value and the stress at which the offset line intersects the curve is termed the proof stress. Interpolation is required to find the point of intersection. In practice, this was performed by reading the intersection point off the stress-strain graph. By modifying the scale of each of the graph's axes, it was possible to 'zoom in' on the intersection point and identify the offset stress at the intersection to within 1 N/mm².

Although typical values for the offset strain are 0.1% and 0.2%, such values represent a level of strain where significant yielding has already occurred and so a much smaller value of 0.03% was chosen. This is explained in greater detail in appendix A3.4. The value of the proof stress is arbitrary but this should be borne in mind, for instance, if a value of yield stress is used in any calculations. A value of 0.1 % offset strain, for example, leads to a proof stress that is 16 % higher than the calculated proof stress.

Table 3.1 below lists the values of material properties determined from the testing as well as the mean, standard deviation and percentage coefficient of variation, *CV*(%), of these

properties. The standard specifies the reporting of these three statistical values. Also included in the table are the manufacturer's stated values, which are specified as minimum values.

Coupon	Elastic Modulus (N/mm ²)	0.03% Proof Stress (N/mm ²)	σ_{uts} (N/mm ²)	ϵ_{uts} (%)
1	210 140	1 045	1527	1.69
2	210 390	985	1542	3.17
3	210 280	920	1580	2.06
Mean	210 270	983	1554	2.31
Standard Deviation	125	63	27	0.80
CV (%)	0.06	6.36	1.76	33.39
<i>Manufact. values</i>	-	<i>950 (min)</i>	<i>1350 (min)</i>	-

Table 3.1: Material Properties from Coupon Tests

The statistical mean, \bar{x} , standard deviation, S_{n-1} , and coefficient of variation, $CV(\%)$ are calculated using equations 3.5 to 3.7 respectively.

$$\bar{x} = \frac{\left(\sum_{i=1}^n x_i \right)}{n} \quad \text{Eq (3.5)}$$

$$S_{n-1} = \sqrt{\left(\sum_{i=1}^n x_i^2 - n\bar{x}^2 \right) / (n-1)} \quad \text{Eq (3.6)}$$

$$CV(\%) = 100 \times \frac{S_{n-1}}{\bar{x}} \quad \text{Eq (3.7)}$$

where x_i is the measured value and n is the number of specimens.

The steel specimens, as expected, behave elastically up until a certain stress before demonstrating yielding and then, at a higher stress, fracture occurred. The fracture initiating at the fillet radius in two of the three tests may decrease confidence in the derived strength

properties although stress concentrations are difficult to remove completely. The coupon which failed near the mid-span of the gauge section showed medium ultimate tensile stress values though it exhibited the highest ultimate tensile strain. This suggests that the strength in terms of stress is not sensitive to small stress concentrations though it may be dependent on the ultimate strain. Figure 3.4 below shows two printouts of the material under a microscope where the sections are within the gauge section (but at a distance from the fractured cross section) and adjacent to the fractured cross section respectively. The micrograph of the specimen near the point of fracture shows a high degree of elongation, and thus strain, in the individual grains of the material.

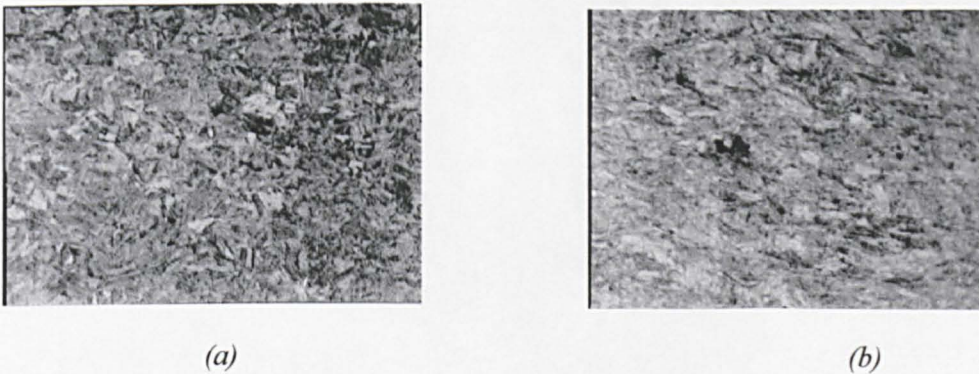


Fig 3.4: Micrographs - (a) General grain structure & (b) Structure 1 mm from Fracture

As table 3.1 indicates (particularly the values of the coefficient of variation), there is only a small degree of variation within test results for all properties excluding the ultimate tensile strain. This is especially true for the elastic modulus. Such findings are common for a steel material of good quality. The ultimate tensile strain for each of the specimens is very different in each case and the average value of this property is essentially meaningless. At this point of the test, the strain of the specimens is increasing while the load remains virtually constant. It seems likely that, at some value of strain, fracture will occur but, being dependent on small imperfections and cracks, the point when fracture occurs will vary widely from specimen to specimen.

The limited number of beams available meant that only three coupons could be prepared and tested. However, the lack of variability in test results gives greater confidence in the properties obtained albeit from a smaller sample size. The properties obtained from testing are in

approximate agreement with the manufacturer's stated values but direct comparison is not possible given that they are only minimum values.

3.2 STATIC TESTING OF BEAMS

3.2.1 Introduction to Static Testing of Beams

The test configuration for all the side impact beams was designed to replicate the standard simply supported, three point bending test as shown below in figure 3.4 (a). This is simulated using a test machine to displace an impactor at the mid-span of the beam as shown in figure 3.4 (b). Nominal dimensions for the striker and supports and the distance between the supports used in the tests are given in this latter figure.

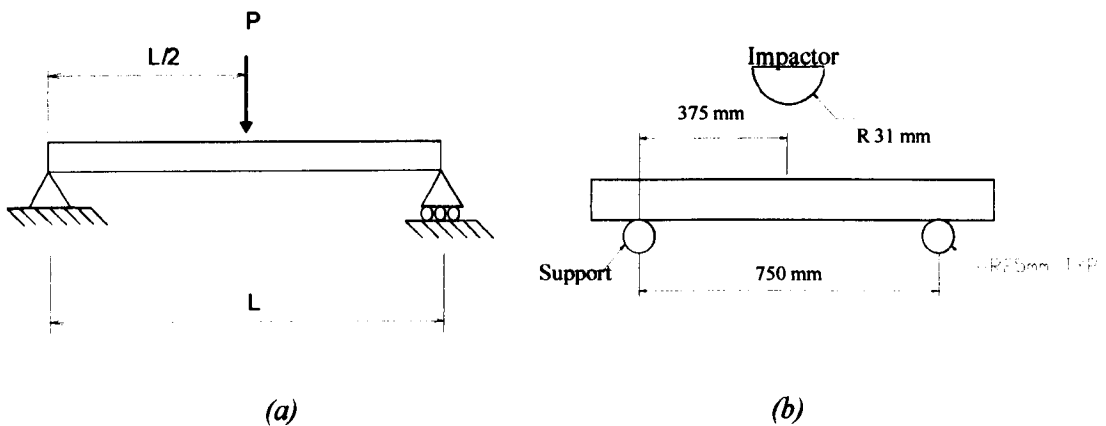


Fig 3.4: (a) Idealisation of Bending Tests and (b) Diagram of Set Up

Although this is a common test for structures in bending, there was no standard to follow. It was hoped that experience gained from other test work would ensure good practice. The purpose of the testing was to measure the static performance of the side impact beams in terms of load capacity, the degree of deformation and energy absorption. A further objective of the tests was to assess the repeatability of, or the variation in, the performance of the beams.

3.2.2 Equipment Used During Testing

Testing was once again performed on the Tinius Olsen test machine, details of which can be found in section 3.2. The impactor used was a steel cylindrical unit with a connected rod that could be gripped by the test machine.

3.2.2 Results of Static Testing

Below is figure 3.5, which is a photograph of a steel beam during testing. Two steel beam specimens were tested. Also visible in figure 3.5 is the supports unit that provides the support at each end of the beam. As can be seen, the unit is relatively rigid with the distance between the two supports fixed by a linkage. It is assumed that deflection of the supports in any direction is negligible.

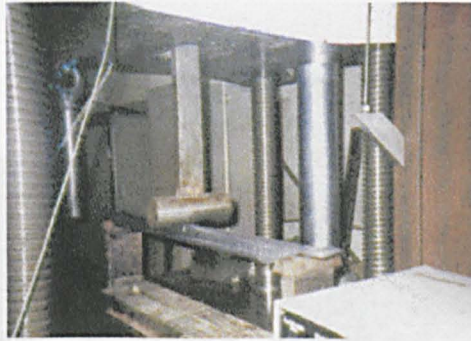


Figure 3.5: Steel Beam & Supports Unit During Testing

3.2.3 Testing Procedure

The supports unit was aligned on the test bed so that its midpoint was directly under the impactor, which had been placed in the grips of the test machine. Each beam was placed on the supports and aligned and then the test was performed. As with the coupon tests, the displacement rate of the test machine was 10 mm/min. Loading was continued until the collapsed beam was near the base of the supports unit.

The test machine produced traces of load against deflection using its connected plotter. The values from these traces were inputted into Excel. Load and deflection data were then offset so that each set began at zero and they were also converted from imperial to metric units. The data was now in the desirable form.

It was found that the beams could have continued to carry substantial load after the point at which the tests were terminated. Unfortunately, there was no simple means to increase the distance between the top and the base of the supports unit so that the testing could have been performed to even higher levels of deflection.

3.2.4 Results of Static Testing

The energy absorbed by the beam as a function of deflection, E_d , can be calculated by

Initially, the beam can be seen to behave in a global, elastic manner but, at a more advanced stage of testing, a significant change occurs. Figure 3.6 (a) and (b) below shows the deformation of the beam at such a stage. It can be seen that the deformation is predominately local with beam bending occurring through this local deformation, or hinge, at the mid-span.



Fig 3.6: (a) Beam at Advanced Stage of Static Testing & (b) Local deformation

Figure 3.7 below shows the results of the tests on the beams in terms of load against the deflection at mid-span. It can be seen that the beams behaved highly elastically up until a fairly well defined collapse load. After this the beams shed load although they were able to carry a substantial load for a great deal of subsequent deflection.

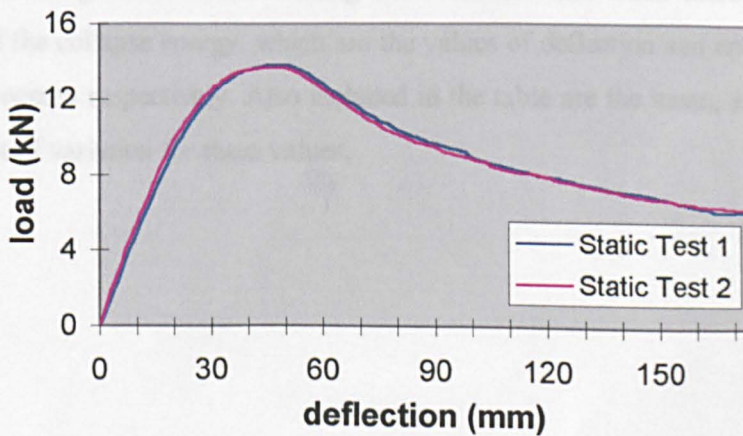


Fig 3.7: Load v Deflection for Beams During Static Testing

The energy absorbed by the beam as a function of deflection, EA , can be calculated by determining the area under the curve of load, P , against deflection, d . This is performed in Excel for each data point (up to the final value of $i+1$) using a Trapezoidal rule as shown in equation 3.8 below:

$$EA_{i+1} = EA_i + \left[\frac{P_i + P_{i+1}}{2} \times (\delta_{i+1} - \delta_i) \right] \quad \text{Eq (3.8)}$$

Figure 3.8 below shows the results of this calculation applied to each beam. Also noted is the point at which collapse occurs.

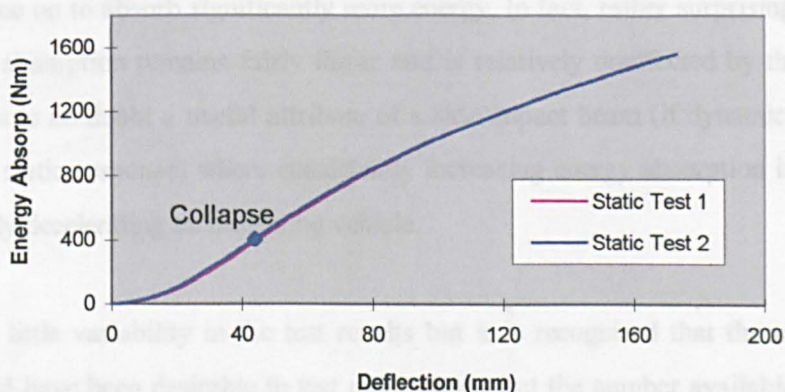


Fig 3.8: Energy Absorption v Deflection During Static Testing

A number of values of interest relating to collapse can be derived from the tests and these are given below in table 3.2. The first is the collapse load for each beam, which is defined as the point at which the gradient of the loading first becomes flat. Then there are the collapse deflection and the collapse energy, which are the values of deflection and energy at which the collapse load occurs respectively. Also included in the table are the mean, standard deviation and coefficient of variation for these values.

Specimen	Collapse Load (kN)	Collapse Deflection (mm)	Collapse Energy (J)
1	13.79	46	418
2	13.66	44	404
Mean	13.73	45	411
Stan Dev	0.09	1.41	9.90
CV (%)	0.67	3.14	2.41

Table 3.2: Values at Collapse for Beams During Static Testing

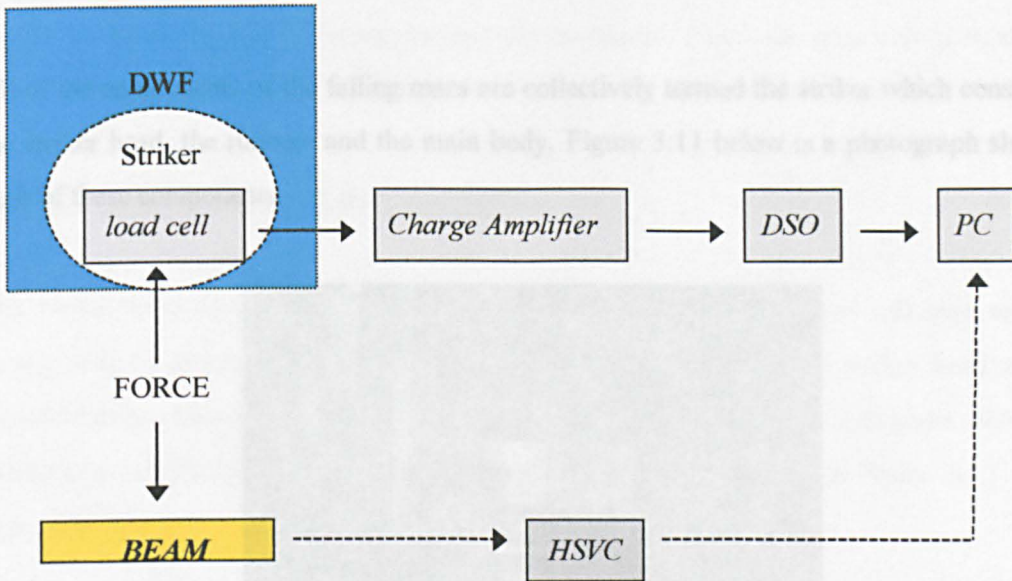
The post-failure load carrying capacity is implicit in the plot of energy absorption against deflection (figure 3.8). Although the beams collapse at a mean energy level of 411 J, they were able to continue to absorb energy up to a final measured value of around 1560 J and perhaps could have gone on to absorb significantly more energy. In fact, rather surprisingly, the curve of the energy absorption remains fairly linear and is relatively unaffected by the collapse of the beam. This is no doubt a useful attribute of a side impact beam (if dynamic behaviour is similar to the static response) where consistently increasing energy absorption is desirable to aid in gradually decelerating an impacting vehicle.

There is very little variability in the test results but it is recognised that the sample size is small. It would have been desirable to test more beams but the number available limited this. However, as with the coupon testing, the lack of variability in the results gives greater confidence that the true bending response of the beams has been ascertained.

3.3 DESCRIPTION OF DYNAMIC RIG

3.3.1 Overview of the Impact Test Rig

Impact tests were performed using the Drop Weight Facility (DWF) located at Strathclyde University. The test rig and associated instrumentation are schematically illustrated below in figure 3.9.



DWF = Drop Weight Facility

DSO = Digital Storage Oscilloscope

PC = Personal Computer

HSVC = High Speed Video Camera

Fig 3.9: Block Diagram of Dynamic Set Up

3.3.2 Drop Weight Facility (DWF)

Figure 3.10 (a) below shows a photograph of the guide rails and support columns of the DWF. The photograph was taken from the basement and shows the guide rails passing the first floor, where the test instrumentation is located, and up to the second floor. Also shown below is figure 3.10 (b), which is a photograph of the base of the guide rails and the support unit. Further details of the guide rails, base and columns can be found in appendix A3.5.



(a)



(b)

Figure 3.10: (a) Guide Rails & Support Columns and (b) Base & Supports Unit of DWF

All of the components of the falling mass are collectively termed the striker which consists of the striker head, the runners and the main body. Figure 3.11 below is a photograph showing each of these components.

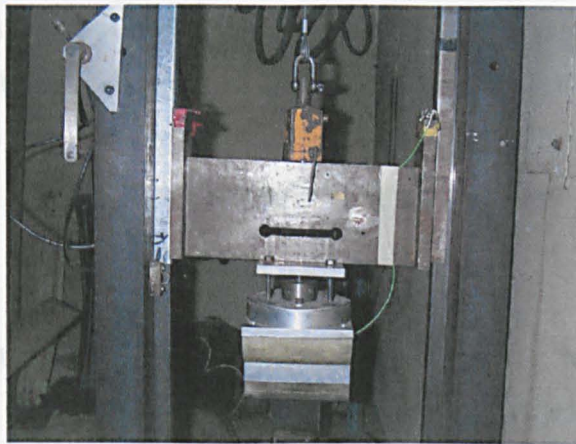


Fig 3.11: (a) Photograph of Striker

The runners fit into the guide rails to ensure the striker remains fixed in all degrees of freedom except, of course, for vertical movement where it is assumed at this time that there is no restraint (therefore friction between runners and guide rails is negligible). The main body is simply an assembly of thick metal plates, assumed to be rigid, which contributes the majority of the mass to the striker (14.1 kg including the runners which possess a relatively low mass). The striker head contains the load cell and is discussed in the next sub-section. The striker head has a weight of 7.6 kg and thus the striker has a total weight of 21.7 kg.

On the top of the striker is a rod with a wide groove around its circumference and onto this rod can fit the release mechanism, which was also shown in figure 3.11. This is a mechanical device and, when the lever of the device is turned 90° to either side, an internal part of the release mechanism fits into the groove of the rod so that the device and the striker are fixed. Attached to the release mechanism is a wire cable with a loop at the other end that can be placed over the hook of the gantry crane. By this means the whole striker can be raised to the required height. Moving the lever back to its original position will disengage the release mechanism allowing the striker to fall.

Sitting on the metal base is the support unit for the beams. This is the same unit as used in the static tests and details of this component were provided in section 3.7.

3.3.3 Striker head and Load Washer

The striker head was designed specifically to house the particular load cell used and this design was by Buckley [3.2]. Appendix A3.6 shows aspects of the striker head and all illustrations are taken from Buckley. The head is made out of nylon 66 with some sections of aluminium and there are six main parts bolted together as shown in figure A3.3 of the appendix.

The striker's impacting nose has a radius of 37.5 mm and has a vertical line marked on each side that indicates its impact point. The main design objective behind the construction of the striker head was to ensure that only the vertical component of the load on the striker head is measured. Ideally, the cylindrical supports and striker head give rise to a 'three load-line bending test' although this assumes the use of rigid bodies and the striker head in particular is not rigid. However, the test is seen as approximating the three point bending test with reasonable accuracy. Therefore, only vertical forces are of interest and figure A3.4 of appendix A3.6 indicates that only vertical forces will be measured.

The load cell used is a piezoelectric load washer, Type 9061A, by Kistler Instruments. Illustrations and technical data (from Buckley [3.2]) of the load washer are given in appendix A3.7. The calibration certificate for the load cell is given in the same appendix.

3.3.4 Charge Amplifier

The charge amplifier was a Kistler Type 5011 one channel microprocessor controlled amplifier. This unit proportionally converts its input charge from the load cell to its output voltage signal. The proportional factor, known as the sensitivity, for the input was set to 4.3 pC/N, which is the value specified by the manufacturer when using the 9061A load washer. The output voltage has a gain that was selected to be 10 kN/V. The maximum output of the amplifier is 10.5 V.

3.3.5 Digital Storage Oscilloscope (DSO)

The DSO is a Gould Datasys 740 oscilloscope, which is shown below in figure 3.12 (along with the PC and the charge amplifier). Its operators manual [3.3] describes it as a complete multidimensional waveform acquisition and analysis system. Further details are provided in appendix A3.8. This appendix explains, amongst other things, that there are eight vertical divisions with 30 subdivisions per division available to measure the magnitude of the input signal. This resolution represents a limit to the accuracy of the DSO. For the settings used in the dynamic beam tests, one distinct subdivision represents 225 N.



Fig 3.12: DSO, PC and Charge Amplifier

3.3.6 Personal Computer (PC)

Once the signal, or trace, generated from a test has been stored it is possible to manipulate the sampled data that comprises the trace using a PC. Using the software package 'Transition

Acquisition v2.09.02' the data points that have been stored are imported and then exported in an ASCII format. The converted data is then imported into the spreadsheet package 'Microsoft Excel v7.0'. Each data point is then a numerical value and the relationship between this value and the force on the load cell is given by the manufacturer [3.3]. How the load cell force is derived is given in appendix 3.9. The constant sampling time between each value can be derived from the DSO settings, thus the load cell force against time relationship for each beam can be calculated.

3.3.7 High Speed Video Camera (HSVC)

A High Speed Video Camera (HSVC) was also used during the beam tests. The HSVC system used was a Kodak Ektrapro 1000, which allows recording at up to 1000 frames per second (fps). Further details of the HSVC are provided in appendix A3.10. High-powered lamps provided the lighting required for the camera system.

3.4 LOAD CORRECTION AND CALIBRATION OF DYNAMIC RIG

3.4.1 Correction of the Measured Force

Before calibration work on the dynamic rig is presented, an important point must be made. It may not always be appreciated that, during an impact event, a load measuring device will not experience the total mass of the striker but only the proportion of mass that is acting upon it from above. Therefore, for a striker assembly where the load measurement is not at the point of impact, the measured load will not be the load experienced by the impacted structure. This fact is shown to be the case below and how to determine the total force acting on the beam (the only force of real interest) is also shown.

Figure 3.13 below shows a free body diagram of two masses, m_1 and m_2 , and a load cell (of negligible mass) with the masses in motion towards a beam at their respective accelerations, a_1 and a_2 . Such a system is a representation of the striker in terms of the masses above, m_1 , and below, m_2 , the load cell. Also shown are the forces experienced by the load cell, F_{lc} , and by the beam, F_{beam} , and it will be shown that these two forces are not identical.

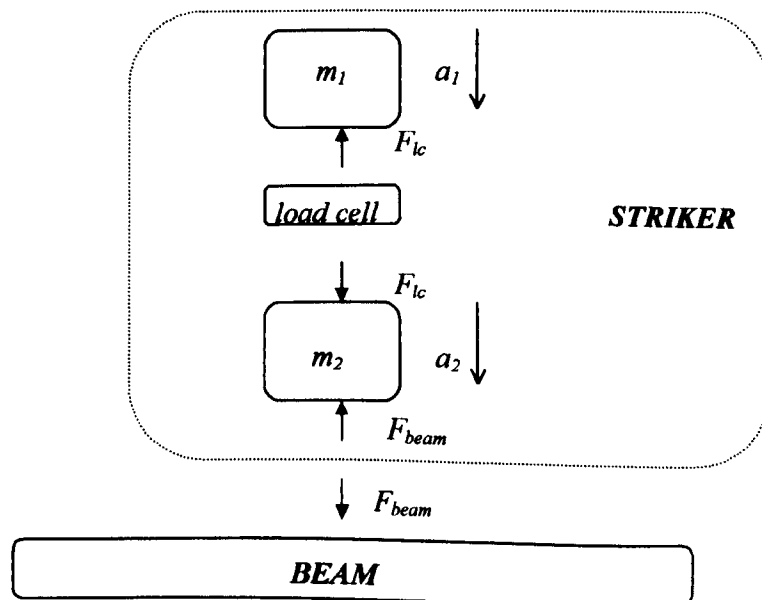


Fig 3.13: Free Body Diagram of Striker Masses

Let the upward forces and accelerations be positive. Considering only the forces involving the upper mass:

$$F_{lc} = -m_1 a_1 \quad \text{Eq (3.9)}$$

Considering only the forces involving the lower mass:

$$F_{beam} - F_{lc} = -m_2 a_2 \quad \text{Eq (3.10)}$$

Substituting equation 3.9 into equation 3.10 gives:

$$F_{beam} = -m_2 a_2 - m_1 a_1$$

If the three bodies of the masses and the load cell are in contact and are accelerating at the same rate, a , as in the case of the striker, then:

$$F_{beam} = -(m_1 + m_2)a \quad \text{Eq (3.11)}$$

Thus the force on the beam involves the total mass of the striker as expected whereas the force on the load cell involves only the upper mass. The relationship of the force on the beam to the load cell force can be expressed by dividing equation 3.11 by equation 3.9:

$$\frac{F_{beam}}{F_{lc}} = \frac{-(m_1 + m_2)a}{-m_1 a}$$

$$F_{beam} = F_{lc} \left(\frac{m_1 + m_2}{m_1} \right) \quad \text{Eq (3.12)}$$

The ratio of masses within equation 3.12 can be termed the correction factor.

Considering an impact using the test rig described in section 3.3: the main body acts upon the striker's top plate, which then exerts force on the striker head's central column, which in turn

acts upon the load cell. The rest of the striker head can be considered to be below the load cell. Therefore, the mass above the load cell consists of the main body (14.1 kg), the top plate (0.2 kg) and the central column (1.8 kg) and is equal to 16.1 kg. The mass below the load cell is the striker head (7.6 kg) with the mass of the top plate and central column subtracted which equals 5.6 kg. Inserting these values into equation 3.9 gives a calibration factor of 1.35.

3.4.2 Introduction to Dynamic Calibration

Before reliable dynamic experiments could be carried out it was deemed necessary to calibrate the dynamic test instrumentation. A number of approaches were used: calibration of the load cell and charge amplifier separately and then checks on the overall performance of the set up. Two types of checks were carried out because the results of the first were unsatisfactory.

3.4.3 Calibration of the Charge Amplifier and Load Washer

The charge amplifier and the load washer were calibrated individually. Detailed descriptions of this work are provided in appendices A3.11 and A3.12 respectively. In order to be concise, only the general findings of the work are presented below.

The output of the charge amplifier was found to be highly accurate and linearly proportional to its input over a wide voltage range. The amplifier's filters appear to be functioning correctly. There is noise due to an ac electrical source but this is deemed insignificant.

The accuracy of the load washer was found to be within five or six percent of its correct operation. It may be higher given that the accelerometer or its charge amplifier may be in error but this is not known. There may be a slight decrease in accuracy at frequencies lower than about 100 Hz but the evidence is inconclusive.

3.4.4 Calibration of Test Set Up - Method 1

This method involved full drop tests on beams. Along with force measurement using the load cell, an accelerometer was fixed to the striker and its measured signal converted to force data. It was hoped that the two sets of data could be compared and an assessment made of the load

cell's accuracy while situated within the striker. While it is understood that the comparison would not be more revealing than the method of section 3.4.3 in terms of individual components, it would determine whether there was any loss of accuracy due to situating the load cell within the striker. Such a loss of accuracy could come about by poor design of the striker leading to false load paths.

(A) Equipment and Procedure

The equipment and procedure used for the load cell will be detailed in sections 3.5.2 to 3.5.4 for beam tests and so are not described here. Also used were the same accelerometer and charge amplifier as described in section 3.13. The beams tested were of a steel material and, though they were similar, they were not the same geometry as the beams that have been considered within this thesis (a greater number of these beams were available).

The accelerometer was bonded to the horizontal top plate that forms part of the striker's construction (part 3 in appendix A3.6). The signal from this component was inputted to a separate channel of the DSO and, along with the load cell signal, both traces were saved for each beam. Three tests were performed and then the test results were transferred to spreadsheet software for analysis.

When these beam tests were conducted, modifications had been made on the striker assembly, mainly so that the impact mass could be increased. One aspect of these modifications was to remove a plate that formed part of the mass of the striker's main body. This allowed an additional mass to be fixed to the main body and because the plate was positioned to one side of the main body which may have caused slight asymmetric loading. Consequently, the striker's mass, and thus the calibration factor used to obtain the force on the beam from load cell force data, as defined in section A3.9, was slightly different.

The total striker mass was measured on two separate scales. The total mass was 19.9 ± 0.1 kg, still with 5.6 kg below the load cell and so 14.3 kg was acting upon the load cell. This latter figure represented 72% of the total mass and gave a calibration factor of 1.39.

The accelerometer measures the acceleration of the whole mass of the striker and so no calibration of data is required. The measured acceleration data is simply multiplied by the total mass to give the load as a function of time.

(B) Results

Figure 3.14 below shows a typical graph of test results for the loading, from the load cell and derived from accelerometer data, as a function of time. The load cell force has been calibrated using the factor of 1.39.

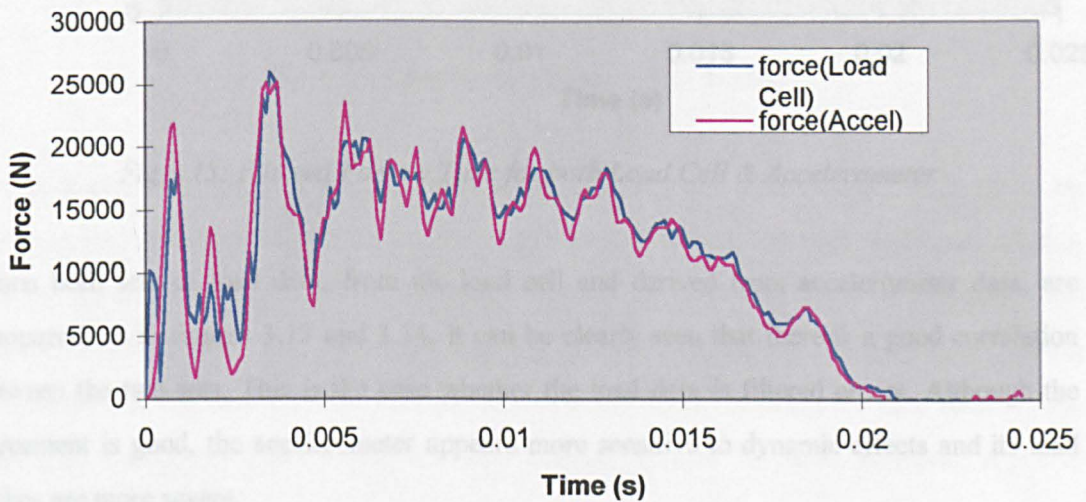


Fig 3.14: Unfiltered Force v Time for both Load Cell & Accelerometer

Each data set can be filtered and this has been performed using an exponential smoothing function within Excel. To obtain each smoothed value, $f_{smooth(i+1)}$, the function adds only a proportion of the unfiltered load value, $f_{(i+1)}$, to a proportion of the previous smoothed value, $f_{smooth(i)}$, so that effectively a more 'steady-state' load trace is produced. The function has the form:

$$f_{smooth(i+1)} = a(f_{(i+1)}) + b(f_{smooth(i)})$$

Where a and b are constants selected arbitrarily but such that $a + b = 1$. Decreasing the value of a and increasing the value of b will increase the degree of smoothing. Values of 0.15 and 0.85 were selected for a and b respectively. A graph of the filtered force is shown below as figure 3.15.

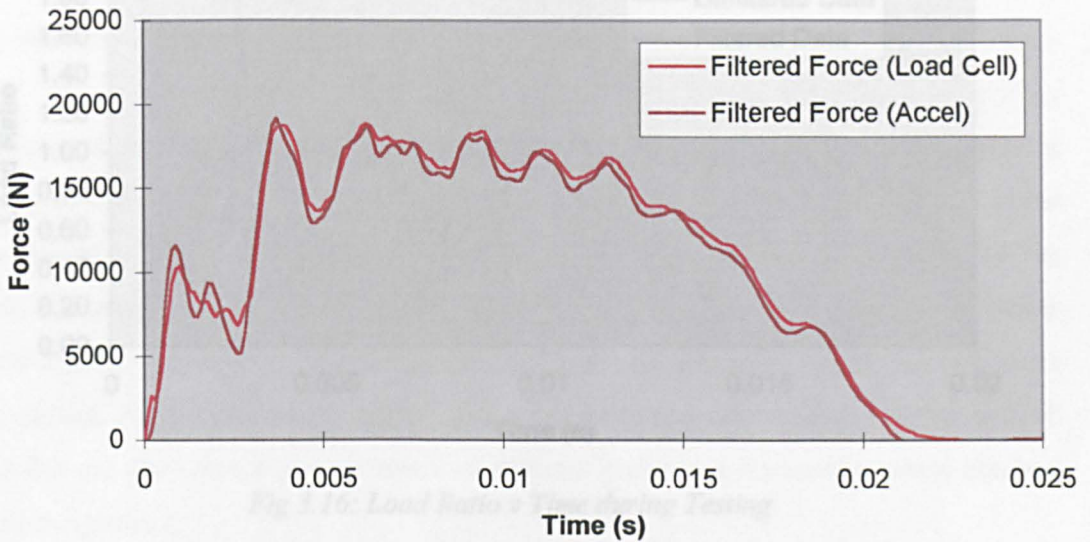


Fig 3.15: Filtered Force v Time for both Load Cell & Accelerometer

When both sets of load data, from the load cell and derived from accelerometer data, are compared, as in figures 3.13 and 3.14, it can be clearly seen that there is a good correlation between the two sets. This is the case whether the load data is filtered or not. Although the agreement is good, the accelerometer appears more sensitive to dynamic effects and its load spikes are more severe.

A load ratio, which is the ratio of the force derived from accelerometer readings to the force from the load cell, can be defined. A typical graph of this ratio for both filtered and unfiltered load data as a function of time is shown below in figure 3.16 and a baseline at a ratio value of one is also shown. The time range selected for the graph omits the initial period of large load oscillations because the load ratio also shows such large oscillations that would obscure the pattern of the ratio during later stages of the test.

Time (s)	Mean Load Ratio (Filtered)	Mean Load Ratio (Unfiltered)
0.005	0.96	0.96
0.010	0.95	0.95
0.015	0.98	0.98

Table 3.3: Collected Mean Load Ratios for each Test

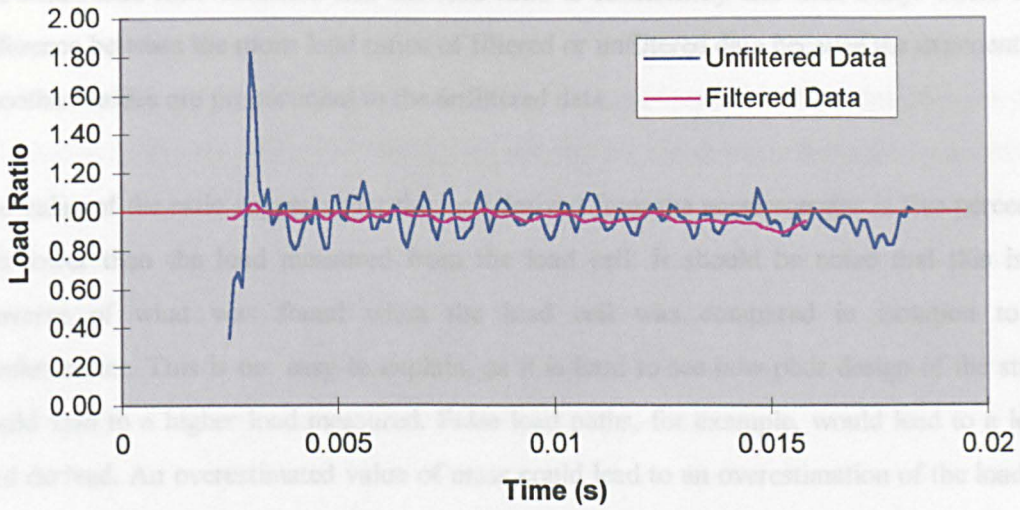


Fig 3.16: Load Ratio v Time during Testing

It was hoped that the good correlation between load cell and accelerometer data could be demonstrated quantitatively by the load ratio. For unfiltered data, however, such a ratio, being a more instantaneous measure of correlation throughout each test, tends to exaggerate the difference between each set. This is because it is strongly dependent on the load spikes, which are greater for the data derived from the accelerometer data. Filtering the data removes the load spikes and, consequently, the load ratio is more constant in nature. However, it is still clearly less than unity.

A mean load ratio can be calculated. A medium time range of 5 to 15 ms was used for the calculation. Other ranges were tried but it was found that the resulting mean value was not particularly sensitive to the range used so long as the initial period of the test was omitted. Table 3.3 below lists the mean load ratios for both filtered and unfiltered load data that were calculated for each test.

Test Number	Mean Load Ratio (Unfiltered)	Mean Load Ratio (Filtered)
1	0.96	0.96
2	0.95	0.95
3	0.98	0.98

Table 3.3: Calculated Mean Load Ratios for each Test

The mean load ratio confirms that the load ratio is consistently less than unity. There is no difference between the mean load ratios of filtered or unfiltered data because the exponentially smoothed values are proportional to the unfiltered data.

The value of the ratio suggests that the load derived from the accelerometer is five percent or less lower than the load measured from the load cell. It should be noted that this is the converse of what was found when the load cell was compared in isolation to the accelerometer. This is not easy to explain, as it is hard to see how poor design of the striker would lead to a higher load measured. False load paths, for example, would lead to a lesser load derived. An overestimated value of mass could lead to an overestimation of the load cell force but the mass was measured twice on different scales and the measurements obtained within two percent.

It is more likely that, once again, the calibration method only allows an assessment of accuracy up to a certain point. It can at least be posited, with some confidence, that the load cell within the striker is accurate to within five percent or so and that the striker arrangement does not lead to any wildly erroneous results.

3.4.5 Calibration of Test Set Up - Method 2

Method two of the test set up calibration involved the in-situ procedure of Money and Sims [2.73] that was reviewed in section 2.4. Briefly, this was a quasi-static procedure that involved applying and then removing a known mass to the striker. The output signal of the load cell within the striker (after conversion and amplification by the charge amplifier) was used to derive a relationship between the applied load and the measured signal. This relationship should correspond to the settings of the charge amplifier selected.

(A) Equipment

This method involved a number of components of the DWF to achieve the set up of Money and Sims including the DSO, striker, guide rails and release mechanism (and associated wire cable). Also used were a wooden fixture to support the striker and four steel plates used as additional mass.

(B) Procedure

The wooden fixture was designed so that, when tightened, it could be fixed between the guide rails and support the striker. The striker was inverted so that the impacting nose was pointing upwards and around this was looped the cable of the release mechanism. The main body of the striker, with or without additional plates, was used for the applied mass. For safety reasons, this arrangement was set at such a height so that the main body was suspended only about 100 mm above the base and a wooden plank was placed on the base to cushion any accidental fall. A photograph of the arrangement is shown below as figure 3.17.



Fig 3.17: Photograph of Calibration Set Up

A time base of 1 s was chosen for the DSO so that a total of 10 s would be captured. On the charge amplifier, the long time constant was selected to minimise drift (see section 2.4) and the sensitivity was set to the manufacturer's recommended value of 4.3 pC/N. Initially, a gain of 10 000 was used (this value will be used in the beam tests) but early tests indicated that the measured signal contained excessive noise and so the gain was decreased to 100.

Six tests were performed consisting of two tests at three different applied masses. Loading involved the conventional arrangement as described while unloading involved a person taking the weight of the applied mass so that none acted upon the striker.

The test was started by initiating data storage and then the charge amplifier was quickly reset to eliminate drift. After about three seconds the load was removed and data was stored in the unloaded condition for a further three seconds or so and then the load was reapplied. After another three seconds the load was once again removed and this condition continued to the end of data storage. The trace was saved and the next test was then performed.

Because it was the difference in the measured signal in the loaded and unloaded condition that was being calculated, none of the components of the striker should be considered in the applied mass as they were present in both conditions. The applied mass consisted of the main body of 12.3 kg, the plates when used of 4.13 kg each and also the release mechanism of 2 kg. Table 3.4 below lists the masses, m , used and the resulting applied forces, f_{app} which is calculated using:

$$f_{app} = mg$$

Where g is the gravitational constant equal to 9.81 m/s^2 .

Test No.	Applied Mass (kg)	Description	Applied Force (N)
1	14.3	Main body & Release Mech	140
2	14.3	Main body & Release Mech	140
3	22.6	Additional 2 plates	221
4	22.6	Additional 2 plates	221
5	30.7	Additional 4 plates	302
6	30.7	Additional 4 plates	302

Table 3.4: Applied Mass and Force Used During Testing

Once all the tests had been performed the stored data was transferred to Excel for analysis. Within Excel a trend line was fitted through each of the two slopes in the traces that represent the loaded and unloaded conditions and equations of the trend lines were generated. These equations are in the form:

$$y = ax + b$$

where the constants a and b are given. A value of x was selected such that it was approximately at the mid-point of the two loaded conditions and a value of y was obtained for each trend line.

The difference between the two y values was calculated which represented the difference in the measured signal, S_{meas} , when the striker was loaded or unloaded. This was converted to the measured force, f_{meas} , using the charge amplifier settings in the following manner:

$$f_{meas} (N) = \frac{S_{meas} (V)}{Gain (V/N)}$$

A load ratio was then defined which was the ratio of the applied force to the measured force.

(C) Results

Figure 3.18 below is a typical graph of the signal measured during the testing against time. Also shown are the two trend lines and the equations of the lines. The load spike seen in the figure was a frequent occurrence when the load was applied. This is due to dynamic effects but it is assumed that the measured load was not affected. No spike occurred when the loading was removed.

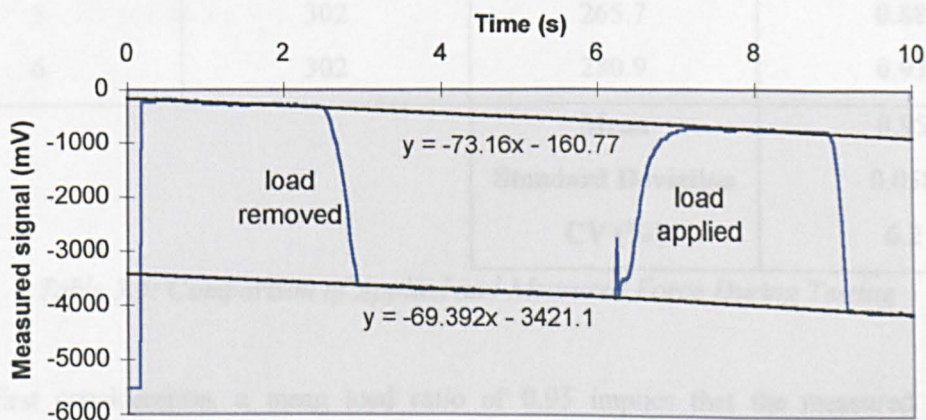


Fig 3.18: Graph of Measured Signal v Time During Testing

The two equations of the lines in figure 3.18 show that the lines have different gradients and this is common for all the calibration tests. To minimise error, the difference between the two lines was taken at approximately the mid-point of the two loaded conditions. The difference in gradients suggests that the charge amplifier drift is not strictly linear throughout the test but the procedure of Money and Sims relies on this assumption. The effect of drift may be small but, considering the relatively small loads that are being measured, it may be significant.

In fact, discussions with the load cell manufacturer, Kistler [3.4], confirm that the use of low load ranges for calibration may be problematic for another reason. While the load cell accuracy is stated to be $\pm 1\%$ (see appendix A3.7), this is over the load range of 0 to 20 kN which means the error could be as great as 200 N. Such an error may not be too significant in dynamic beam tests but would have a dramatic effect on low load range calibration tests.

Table 3.5 below lists the applied force, the derived measured force and the load ratio for each test. Also shown are statistical values for all the samples.

Test No.	Applied Force	Measured Force	Load Ratio
1	140	133.0	0.95
2	140	130.1	0.93
3	221	232.1	1.05
4	221	201.1	0.91
5	302	265.7	0.88
6	302	280.9	0.93
		Mean	0.95
		Standard Deviation	0.058
		CV (%)	6.2

Table 3.5: Comparison of Applied and Measured Force During Testing

Upon first consideration, a mean load ratio of 0.95 implies that the measured force is generally five percent less than the applied force and so the error in the dynamic equipment, the systematic error, is of the same magnitude. However, the variation in the load ratio is far higher than would be expected in calibration tests of this nature. Since the applied force is known with a high degree of certainty, it would be expected that the systematic error would be

fairly constant yet the error appears more random. This could be explained by random changes in the drift and inadequate measurement accuracy for low load ranges.

3.4.6 Discussion of All Calibration Methods

The charge amplifier has been shown to be highly accurate and the load cell appears to be accurate to within five percent. The accelerometer method also suggests that the load cell within the striker is accurate to within five percent. However, a number of difficulties are encountered when dynamic methods are used to calibrate the load cell (such as the accuracy of accelerometers) whether in isolation or within the striker.

Static calibration methods have their own problems. The procedure of Money and Sims relies on the assumption of linear charge amplifier drift and may be less accurate because of this. It should be noted that any static method would have to make the same assumption. However, the effect of drift could be minimised if far higher loads are applied and this would also suit the accuracy of the load cell. Unfortunately, this would require the use of static test machines as well as special apparatus if the load cell is to be tested within the striker.

Although none of the calibration methods were ideal, there are reasonable grounds to state that the dynamic rig can provide a measurement of force that is accurate to within around five percent. This seems to be a sufficient accuracy with which to carry out beam tests and assess crashworthy characteristics.

3.5 IMPACT TESTING OF STEEL BEAMS

3.5.1 Introduction to Impact Testing of Beams

A series of impact tests were performed on the steel beam specimens to determine their impact behaviour. As with the static tests, the impact tests were designed to replicate the three point bending of a simply supported beam. In fact, in all aspects other than loading rate, the impact tests should resemble the static tests.

3.5.2 Equipment Used During Testing

The impact tests were performed using the Drop Weight Facility (DWF) and a description of the equipment used was given in section 3.3. For the Digital Storage Oscilloscope (DSO), initial testing of steel specimens revealed the optimum settings. In fact, many of these settings have been mentioned, as they are the ones used as examples in appendix A3.8. These settings are restated below along with other relevant settings:

DSO settings

Number of Samples	=	500	
Time Base	=	5	ms
Number of Volts per Division	=	0.5	V/div
Trigger	=	+, PRE, 20 %	
Bandwidth	=	FULL	
Probe Gain	=	1	
Impedance	=	1	M Ω

As a consequence of using the settings listed above, a number of other values of interest can be derived which were also given in appendix A3.8 and how they were derived can be found in that section. These values of interest are listed below. Note that the force on the beam must be determined using a correction factor as discussed in section 3.4.1.

Values Derived from DSO Settings

Total time captured	=	50	ms
Time Size	=	0.1	ms
Force on Beam	=	Load Cell Force x Correction Factor	N
	=	Load Cell Force x 1.35	

The charge amplifier had an input gain of 4.3 pC/N as specified by the manufacturer. Initial tests revealed that a suitable output gain was 10 kN/V.

Four steel beams were tested with two at an impact velocity of 8 m/s and the other two at 9.75 m/s.

3.5.3 Calculation of Initial Test Conditions

Appendix A3.14 details how the initial conditions in terms of velocities, energy and drop heights were derived. These two sets of conditions are summarised in table 3.6 below.

Condition Set	Velocity (m/s)	Mass (kg)	Impact Energy (J)	Drop Height (m)
1	8.0	21.7	695	3.25
2	9.75	21.7	1035	4.85

Table 3.6: Initial Conditions for Beam Tests

3.5.4 Testing Procedure

(A) Procedure Used During Testing

Each beam specimen was first labelled for future identification. It was also marked at six 25 mm intervals starting at the beam's mid-span and in the direction of one end. This aided in calculating the displacement derived from the video recording as well as giving some qualitative assessment of any local deformation.

Due to the support for one of the guide rails being in front of the beam's midpoint, the camera had to be positioned at an angle to the beam's side wall for the beam's midpoint to be visible.

Once the HSV was satisfactorily adjusted the settings would not be changed to ensure a constant view scale factor. The highest frames-per-second (fps) setting of 1000 fps was used.

With the striker raised slightly, both the supports unit and each beam were placed so that their mid-point were directly under the striker's centre. The striker was then raised to the required drop height using the gantry crane.

The DSO was then armed so that it was awaiting a suitably high signal to trigger data storage. The lamps were switched on for video recording. The signal from the charge amplifier slowly drifts with time due to capacitive feedback when it is in RUN mode however this effect was virtually eliminated by pressing the amplifier's reset button shortly before a test. The release mechanism was then disengaged allowing the striker to fall and, at the same moment, video recording was initiated.

Once the impact event was over, video recording was terminated and the DSO trace was saved to file. Finally, the specimen was inspected for any visible deformation. This procedure was then repeated for each of the beams.

(B) Procedure Used for Data Analysis

All of the saved data was transferred to ASCII format using the Transition Acquisition software so that it was now ready for analysis within the Excel environment. The file for each beam consisted of a list of data values. The relationship of these values to the force is known (see appendix A3.9) and so they could be converted to load data.

The data values did not begin at zero for the no-load condition due probably to noise or a small level of drift in the charge amplifier and so the values were first offset to begin at zero. Due to the pre-triggering function of the DSO, there were a number of values at the start of each data set that represented a no-load condition (pre-impact condition). All but the last of the values relating to zero load were deleted so that values started from the moment of impact. Starting at zero and incrementing by the time size gave the time associated with each force value. The level of force as it changed with time could now be plotted.

It is desirable that the value of force associated with each increment of deflection be known. This is also necessary to compare results with static test results. The deflection of the beam can be determined from the data and from the physical relationships governing the beam and this is done in appendix A3.15. Briefly, since the ratio of the corrected force data to the mass of the striker gives its acceleration, integration of this ratio over time (using the trapezoidal rule) provides the velocity of the striker. Further integration of this velocity data, as a function of time, leads to the striker's displacement. As the striker is in contact with the beam for virtually the whole of the impact event, the striker's displacement is taken to be the beam's deflection at mid-span.

Hence a plot of force against displacement could now be made and the level of displacement as it changed with time could also be plotted. These plots were made from the moment of impact up to the maximum displacement of the beam and therefore the maximum energy absorption. This point could be identified as when the beam's velocity reached zero. During the tests the beams would reach a maximum displacement and then stored elastic energy would start to be released causing the striker to rebound. However, it is assumed that, from a crashworthiness point of view, force and deflection values have no real relevance beyond this stage.

It will be seen, in section 3.5.5, that there are considerable dynamic effects within the load trace over the entire impact event and so it was deemed necessary to filter the data obtained. Dynamic effects are often due to the noise induced by instrumentation and load cell vibrations that are at a higher frequency than the response of the specimen. This makes filtering a much simpler and reliable process if it is carried out in the frequency domain.

A conventional and powerful method of filtering in the frequency domain is using the Fast Fourier Transform (FFT). This method was used and is discussed in appendix A3.16. Briefly, the appendix explains why a cut-off frequency of 1 kHz was chosen even though filtering at this frequency does not remove the large fluctuations seen in load data. Also, certain frequency components are highly dominant in the load data, which are mainly responsible for the load fluctuations. These frequencies may be a function of the contact stiffness of the beam and striker or of vibrational modes of the beam under impact test conditions but this requires verification.

Pre-filtering of the force on the load cell could have been performed (using the charge amplifier's filters) but it was considered a better methodology to obtain all the data and identify the physical causes of the higher frequencies to justify their removal.

Relationships for force-time, force-displacement and displacement-time were now available for both filtered and unfiltered data. Beam displacements over time could also be derived from video recording of the impact tests and compared with load cell generated values. Full details of the procedure used to do this are given in appendix A3.18.

Perhaps the most important feature of the specimens' behaviour, from an automotive point of view, could also be derived from the test results and this was the degree of energy absorption. Values for this factor, as a function of deflection were derived in the same manner as was used for static results (refer to section 3.9).

3.5.5 Results of Impact Tests

(A) Video Playback

The HSV system allowed replaying of the beam tests at a rate where the beams' response could be appreciated. The steel beams appeared to behave in a global and elastic manner however, when the striker separated from the beam during rebound, there was a visible deformation of the beams. They had deformed about their mid-point to take on a shallow 'V' shape. There appeared to be a brief loss of contact (less than 2 ms) between the striker and the beam just after the initial impact. There was no noticeable difference between the responses of beams at different impact velocities other than the fact that the whole impact event took longer at the higher velocity.

(B) Load Results for the Beams

Figure 3.19 below is a typical plot in terms of filtered and unfiltered load against time for beams at both impact velocities.

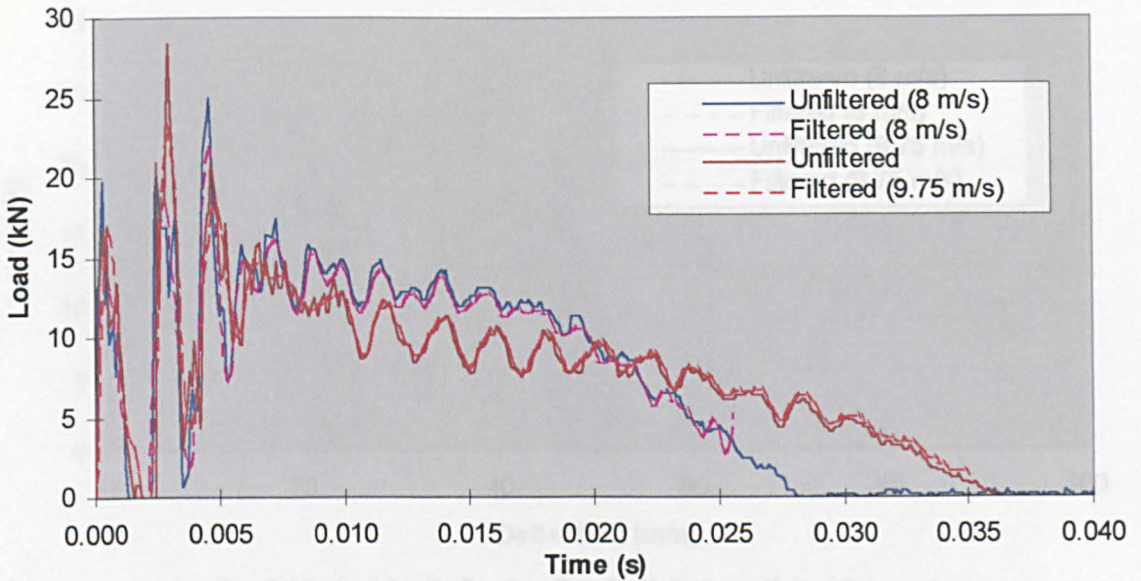


Fig 3.19: Load v Time For Both Impact Velocities

Results of the beam tests show a general pattern. In each case the load trace exhibits strong fluctuations within the first 10 ms or so before becoming more settled. At about this time the load seems to reach a 'steady-state' maximum (any peak loads are ignored). After this point the fluctuations are more modest and, once the maximum deflection has been reached, the load begins to fall. The point at which the load fluctuations become more modest may be termed the collapse load though it is not well defined given the degree of load fluctuation. Although a discrete value cannot be assigned for the collapse load, as was possible for the results of static beam tests, an approximate value could be identified.

Beam tests at both velocities are fairly similar except that at the higher velocity the load falls to a lower level after reaching the collapse load and it also takes longer to fall to zero. For both impact velocities, there are always three transient peak loads and always at around the same time in each test. The zero load that can be seen after the first peak load is confirmation of the brief loss of contact between the striker and the beam that appeared to occur during video playback.

Figure 3.20 below shows the filtered and unfiltered loading at both impact rates as a function of deflection.

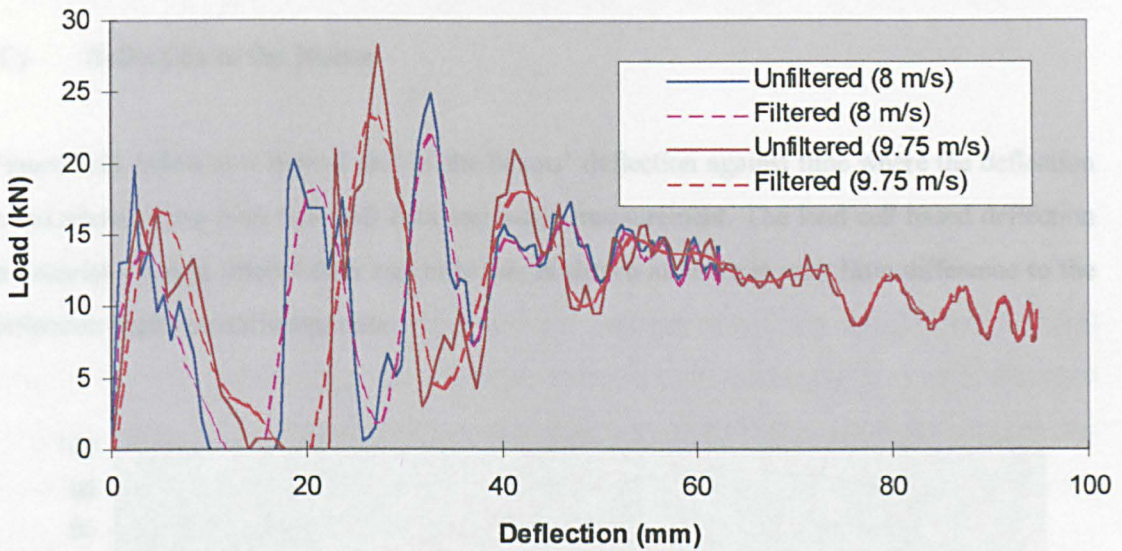


Fig 3.20: Load v Deflection For Both Impact Velocities

The load at which collapse occurs is the collapse deflection. Again, this value is not well defined and an approximation must be used.

It would be desirable to be able to explain the dynamic behaviour of the side impact beam. It could be hypothesised that there is a steadily rising load that reaches a maximum at beam collapse and then load is shed. Finally the load falls to zero as all of the impact energy has been absorbed. Superimposed upon this 'steady-state' load is an oscillating but decaying signal due, perhaps, to the contact stiffness of the beam and striker or to the modal properties of the beam. The magnitude of the vibration is relatively large while the beam is straight and behaving elastically but, as the beam collapses, the v-shape of the beam and the plastic material response limit the magnitude.

However, much of this description is speculative and more evidence is required. Appendix 3.17 presents impact tests carried out to investigate the effect of the contact stiffness on the load data. Section 3.6 presents the modal testing that has been carried out to determine the modal properties of the beam.

Filtering at 1kHz improves the load trace while retaining signal integrity but load fluctuations have not been removed. These oscillations still persist after more excessive filtering even when the integrity of the signal has been lost. This is evidence that the load fluctuations are indeed a dynamic response of the beam and striker rather than caused by instrumentation noise.

(C) Deflection of the Beams

Figure 3.21 below is a typical plot of the beams' deflection against time where the deflection is calculated using both load cell data and video measurement. The load cell based deflection is calculated using filtered data and only this is shown as there is very little difference to the deflection based on unfiltered data.

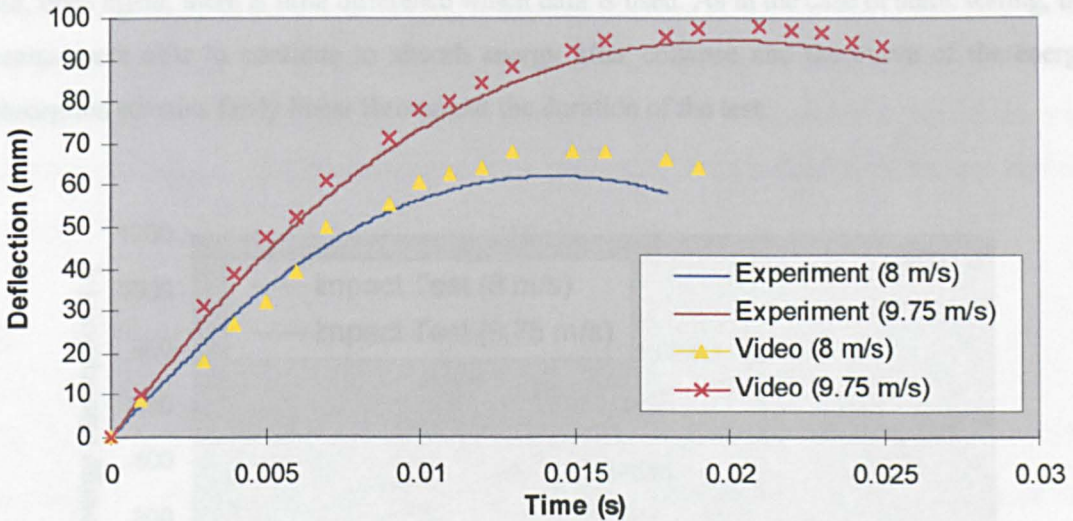


Fig 3.21: Deflection v Time For Both Impact Velocities

The deflection measured from the video correlates reasonably well with load cell based deflection but it is generally a little higher. There is perhaps closer agreement up until around 10 ms. While video deflection upon first consideration may be thought to be the more accurate, there are a number of factors that must be considered. Measurements from video recording were made by eye using a rule and so accuracy may only be around ± 1 mm. Also, the measurements were then multiplied by a view scale factor, which involved the apparent distance (on the monitor) between marks on the beam. The beam not being normal to the camera's view angle and the resolution of the recording and monitor may have introduced error into the video deflection, perhaps as great as 10%. These two sources of error are cumulative. Any error from measurements by the rule would have been multiplied by the view scale factor that may also have contained error. However, these two factors could only lead to a maximum error of less than 2 mm. Perhaps the greatest factor was that as the beams

deflected they ceased to be level with the camera and this would have had implications for the view scale.

Impact Velocity (m/s)	Impact Energy (J)	Final Energy Absorption (J)	Percentage Error (%)
8	64	694	6.2
9.75	1031	1031	0.0

Table 3.7: Impact and absorbed Energy in beam tests

Figure 3.22 below shows the calculated energy absorption as a function of the deflection. Also shown are the final values of absorbed energy for each impact velocity and the (approximate) point at which beam collapse occurs. Filtered data was used to calculate the energy absorbed but, once again, there is little difference which data is used. As in the case of static testing, the beams were able to continue to absorb energy after collapse and the curve of the energy absorption remains fairly linear throughout the duration of the test.

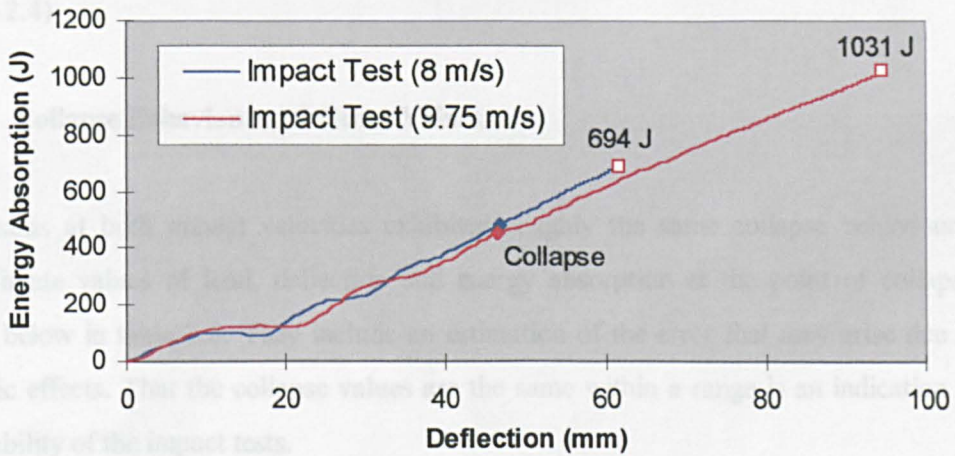


Fig 3.22: Energy Absorption v Deflection For Both Impact Velocities

Table 3.7 below lists the impact energy (IE) and the calculated maximum energy absorption (EA_{max}) for each impact velocity. The percentage error is also included which is defined below in equation 3.12.

$$Error \text{ (\%)} = \frac{EA_{max} - IE}{IE} \times 100\% \quad Eq \text{ (3.12)}$$

Impact Velocity (m/s)	IE (J)	Ea _{max} (J)	Error (%)
8	695	694	0.1
9.75	1035	1031	0.4

Table 3.7: Impact and Absorbed Energy in Beam Tests

Table 3.7 shows that the absorbed energy is similar to but less than (by under one percent) the impact energy. This is what would be expected, as a small fraction of the impact energy would be dissipated in the form of heat (during impact and friction of the runners in the guide rails) and sound (at impact). This seems to offer validation to the data calculation procedures since the final procedure is the calculation of energy absorbed and it is dependent on the accuracy of the other procedures. Also, the low error is an indication of the suitability of the test rig (see section 2.4)

(E) Collapse Behaviour and Other Values

The beams at both impact velocities exhibited roughly the same collapse behaviour. The approximate values of load, deflection and energy absorption at the point of collapse are shown below in table 3.8. They include an estimation of the error that may arise due to the dynamic effects. That the collapse values are the same within a range is an indication of the repeatability of the impact tests.

Specimen	Collapse Load (kN)	Collapse Deflection (mm)	Collapse Energy (J)
ALL	14.5 ± 1	45 ± 2	450 ± 20

Table 3.8: Approximate Values from Impact Tests

A number of other values of a more minor interest could be derived from test results such as the values of peak loads, maximum deflections and the total duration of the impact event. These values can be found in appendix A3.19. It is felt that the value of the peak loads are not particularly informative, especially given the effect of filtering on their magnitude. If the peak loads are influenced by dynamic properties of the test rig then their significance to the behaviour of the beam is questionable. However, it should be noted that there is considerable consistency in the magnitudes of the peaks that occur at three different stages of the tests,

whether the data is filtered or not, and this is another indication of the repeatability of the dynamic tests.

(F) Inspection of the Impacted Beams

After each test the specimen was inspected for any visible deformation and this confirmed what was seen on HSV recording. There was permanent deformation of the steel beams with all beams being deformed in the same manner and to the same extent for each impact velocity. A photograph of the typical deformation is shown below in figure 3.23. It can be seen that the deformation is restricted to one location: the mid-line. The beam has developed an angle from the horizontal that shall be termed the bend angle. All the steel beams possessed a similar bend angle of about 22° for the lower impact velocity and about 27° for the higher impact velocity. This is a further indication of the repeatability of the tests.

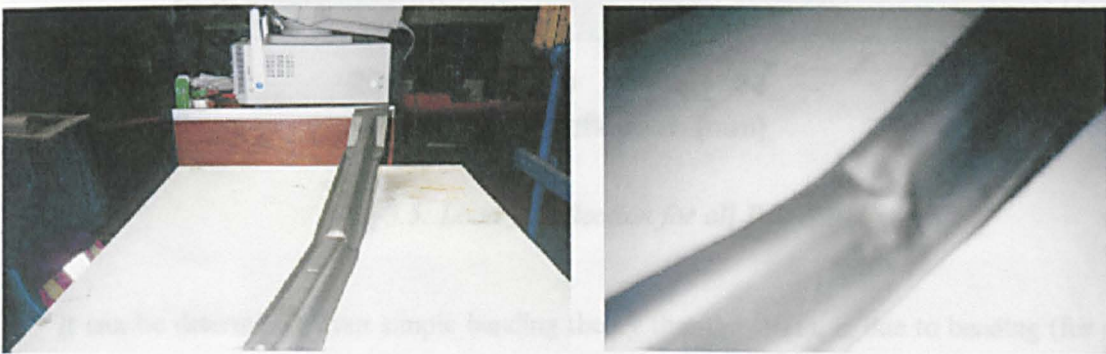


Fig 3.23: Typical Deformation of Steel Beam

The steel beams all possessed local and permanent deformation after the testing acting as if a plastic hinge had developed. The test arrangement was designed to measure only the beam's global deflection. Any local deformation is not measured though it may be an important parameter and it is still unclear what is the mode of collapse. This point is related to the effect of another parameter, which is the geometry of the supports and striker head. The effect of this parameter is also unknown since the geometry remained fixed. It would be informative if future testing incorporated changes in striker and supports geometry.

3.6 COMPARISON OF STATIC AND IMPACT RESULTS

Figure 5.5 is a comparison of static and impact test results. Impact behaviour appears very like a static response with an oscillating but decaying response superimposed. This suggests that the dynamic failure mode is much the same as the static case. The similarity in damage profile of post-tested beams in each situation also supports this view.

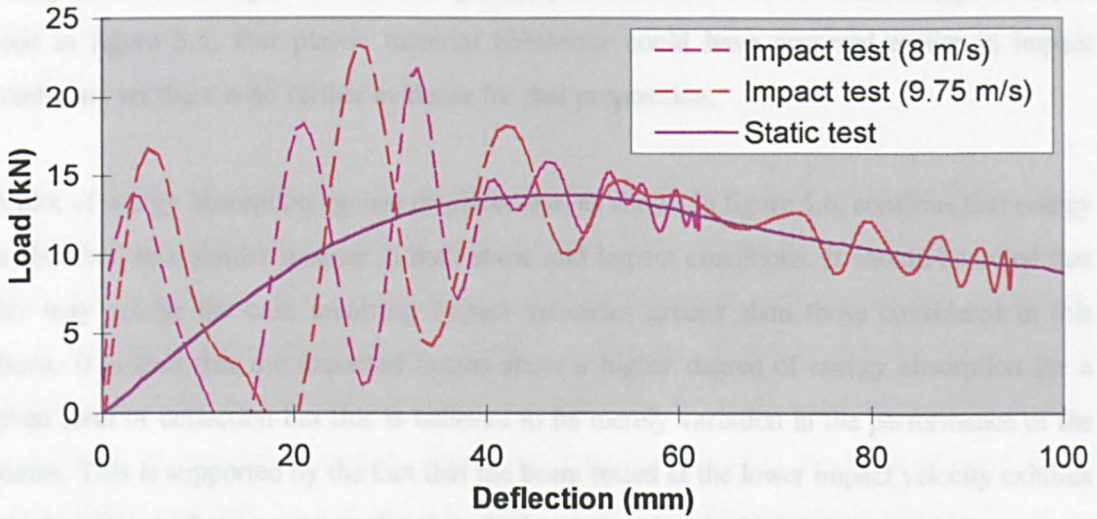


Fig 5.5: Load v Deflection for all Test Results

It can be determined from simple bending theory that the strain, ϵ , due to bending (for small deflections of the beam) is given by:

$$\epsilon = \frac{My}{EI}$$

By substituting equation 2.6, the strain rate, $\dot{\epsilon}$, is given by:

$$\dot{\epsilon} = \frac{Ly}{4EI} \dot{P}$$

The load over time may be readily calculated in Excel as the change in load data divided by the time step. It was found that it was necessary to use filtered load data or the resulting strain rate data would be highly fluctuating. Using values obtained from experiment gave a

plots of strain rate against time that were similar in pattern to those of load against time. This is to be expected, however, the values of strain rate obtained are surprisingly low with a maximum strain rate of around 0.07 sec^{-1} . It is known [2.19] that, for such a strain rate, there is a negligible increase in the yield stress of a high strength steel material. Therefore, because of the impact velocity used, and because the beam is made from high strength steel, there is little difference in the static and the impact response of the beam.

It may have been thought that because dynamic peak loads are well above the collapse load, as seen in figure 5.5, that plastic material behaviour could have occurred earlier in impact conditions yet there is no further evidence for that proposition.

A plot of energy absorption against displacement, as shown in figure 5.6, confirms that energy is absorbed in a similar manner in both static and impact conditions. It should be noted that this may not be the case involving impact velocities greater than those considered in this thesis. It is true that the impacted beams show a higher degree of energy absorption for a given level of deflection but this is believed to be merely variation in the performance of the beams. This is supported by the fact that the beam tested at the lower impact velocity exhibits a higher degree of energy absorption than the beam tested at the higher impact velocity.

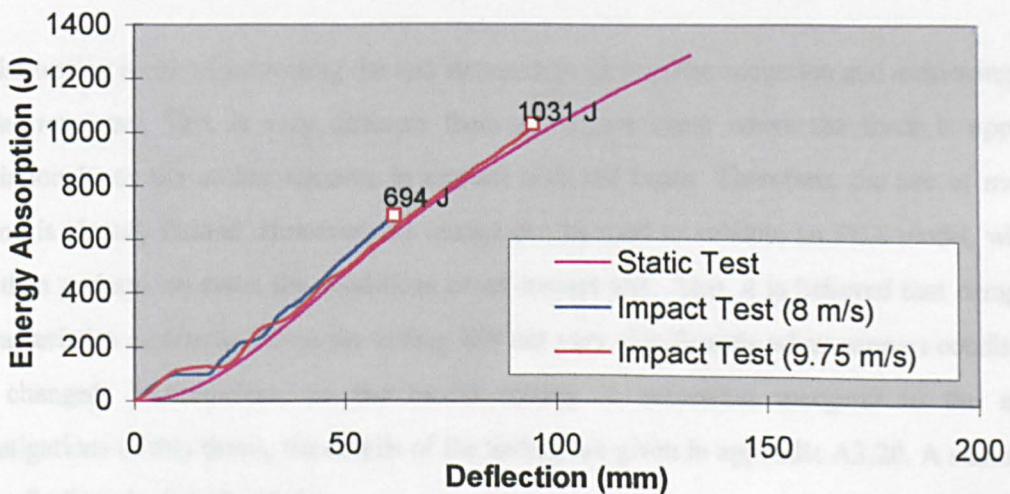


Fig 5.6: Energy v Deflection for all Test Results

3.6 MODAL TESTING

3.6.1 Introduction to Modal Testing of Beams

The primary reason for investigating the modal properties of the side impact beam was to assess whether modal behaviour of the beam, in terms of frequency response, damping and modes of deformation could explain any aspects of the results of impact tests. Perhaps the modal behaviour of the beams could even be superimposed onto their static response in bending to give their dynamic response.

It was discussed in appendix A3.16 how certain frequencies, and one in particular, were dominant in the load data from beam tests. It can be hypothesised that, during an impact, the beam will behave as it does statically but will also vibrate at particular modes, each mode having varying degrees of deflection associated with them. It may be that the deflections of these modes decrease with time due to structural damping or for other reasons such as changes in geometry or material properties. Therefore, if modal properties can be determined and if modal deflections can be related to a given force, then the hypothesis can be tested by comparison with the load traces obtained from impact tests.

Modal testing involves subjecting the test structure to an impulse excitation and measuring the modal response. This is very different from an impact event where the force is applied continuously as the striker remains in contact with the beam. Therefore, the use of modal testing is already limited. However, the testing can be used to validate an FEA model, which can then perhaps be given the conditions of an impact test. Also, it is believed that damping characteristics determined from the testing will not vary significantly when support conditions are changed. Nevertheless, as the modal testing is somewhat marginal to the main investigations of this thesis, the details of the testing are given in appendix A3.20. A summary of the findings is described below.

The modal analyses were performed using virtually unsupported beams, a standard steel beam and a post-impact beam, with an excitation force provided by impact by a hammer. This force, and the beams' response to it, was measured using accelerometers. The system response was analysed using an FFT analyser, which generated the Frequency Response Function

(FRF) for each point along the beam. This data could be used to determine the resonant frequencies of the beams and give some indication of each mode shape.

It is believed that the vibrational modes of the beam have been determined to a reasonable accuracy. Bending mode shapes are clearly defined but other types of modes are not, as the test set up only allowed the measurement of linear displacements. An approximate damping factor of 0.6 % has been determined.

The post-impact beam displayed modes that had often shifted in frequency, compared to the standard beam. As FRF data is calculated from an output response normalised to the input force, true deflections from a particular input force cannot be determined from modal testing. This means that no comparison can be made of the deflections of the standard and the post-impacted beam, though there is some evidence that the V-shape of the post-impact beam inhibits the magnitude of deflections. Furthermore, the magnitude of force oscillations during an impact test could not be derived from modal data even if support conditions were the same.

In conclusion, modal testing cannot be used, in conjunction with static behaviour, as a simple means of predicting dynamic behaviour. This is mainly because the loading conditions are not the same and because true deflections cannot be derived from test data. However, resonant frequencies have been predicted with reasonable accuracy and bending modes are known. This can be used to validate an FEA model that may perhaps be able to predict modal behaviour during the conditions of an impact test.

SUMMARY OF CHAPTER

A number of different types of experiments have been carried out to determine the behaviour of the beam and the properties of the steel material.

Coupon tests have provided values such as the elastic modulus and the yield stress (proof stress). Static beam tests have shown that the beam behaves highly elastically up until a well defined collapse load after which the beams shed load though they are still able to carry a substantial load. Energy absorption is relatively unaffected by the collapse of the beam

A number of methods were used to calibrate the dynamic test equipment but calibration of the load cell was found to be problematic. However, it is believed that the accuracy of the load cell is within about five percent. As in the case of static testing, the energy absorption of the impacted beams is relatively unaffected by beam collapse. The impact behaviour of the steel beam is very similar to its static response.

Impact testing of beams shows large fluctuations in the loading on the beams, which may be due to either the contact stiffness of the beam and striker or the modal behaviour of the beam. Contact tests support the former reason while modal tests, by themselves, cannot be used to provide an explanation. The modal testing has determined vibrational modes of the beam and the damping factor of the material. Though it cannot be used as a simple means of predicting dynamic behaviour, it could be used in the validation of an FEA model.

It is recognised that, in a number of cases, the number of specimens used in the tests was small due to a lack of availability. However, it has been seen that there is low variability in all of the test results. Therefore, it is believed that realistic assessments have been made for the material's properties and the beam's behaviour.

CHAPTER FOUR

QUANTITATIVE ANALYSES OF STEEL BEAMS

OVERVIEW OF CHAPTER

Experimental testing of the steel beam has provided performance data with which to compare the composite beam. Modelling of the steel beam can help to develop appropriate modelling techniques to be used with the composite beam. The modelling is achieved using quantitative methods.

This chapter uses quantitative methods in an attempt to predict a number of features of the beam's behaviour. The two methods used are analytical methods and Finite Element Analysis (FEA). The structure of the chapter is represented as a block diagram in figure 4.1 below.

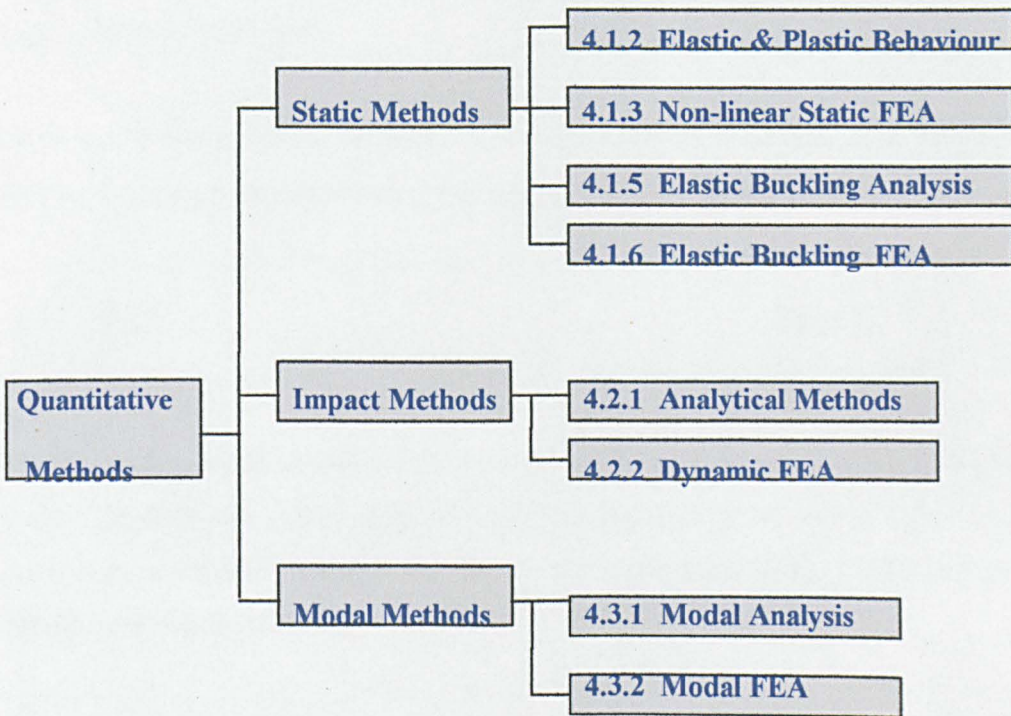


Fig 4.1: Block Diagram of Structure of Chapter

For the analytical methods, simple elastic theory predicts the elastic bending for the beam while plastic analysis forecasts the load at which collapse will occur due to plastic material behaviour. The beam may fail due to elastic buckling, however, buckling analysis has found to be inappropriate due to the dominance of plastic behaviour. Modal theory predicts natural frequencies for the beam that is subject to a range of support conditions. However the theory does involve making a number of simplifications concerning beam geometry and the response of the beam (and striker) during an impact test.

For the FEA, non-linear static analysis predicts the stresses in the beam and its deformation as it is loaded. Elastic, collapse and post-collapse behaviour are predicted. Elastic buckling FEA predicts buckling loads far higher than the load that causes collapse of the beam and this confirms that elastic buckling is not a realistic failure mode for the beam. Modal FEA gives a number of estimates of the natural frequencies of the beam for a range of support conditions. This can be used as a validation of the FEA model. Both shell and beam element models are used although the latter model may oversimplify the geometry of the beam. Dynamic FEA predicts the impact behaviour of the beam and can be used to help understand the effect of a number of parameters within an impact test.

4.1 STATIC METHODS

4.1.1 Introduction to Static Methods

A number of methods can be used to provide predictions of the beam's static behaviour. This behaviour is in terms of both its elastic and plastic response under the loading conditions considered and at what point global elastic buckling would occur. Each of these methods is examined below.

4.1.2 Elastic and Plastic Behaviour

(A) Elastic Behaviour

From simple elastic theory, the load, P_e , causing a certain deflection, δ , of the beam due to bending in a simply supported beam with concentrated mid-span load is given by:

$$P_e = \frac{\delta.48.EI}{L^3} \quad \text{Eq (4.1)}$$

Where E is the elastic modulus, I the second moment of area and L the support span of the beam. The deflection due to shear is usually negligible in metal beams unless the span-to-depth ratio is extremely small [4.1]. Thus a plot of the load against deflection during static conditions is readily obtained.

(B) Plastic Collapse Loads

Section 2.1 derived a relationship for the yield moment. It was seen in the same section that the plastic moment, M_p , is related to the yield stress and the section modulus. For a simply supported beam subject to a mid-span concentrated load, the bending moment varies across the span of the beam with a maximum at mid-span. At the plastic moment the beam's mid-span cross section is fully plastic and the plastic collapse load, P_c , is given by:

$$P_c = \frac{4\sigma_y A(y_1 + y_2)}{2L} \quad \text{Eq (4.2)}$$

This load is the exact static plastic collapse load and, when it is reached, a plastic hinge forms and the beam acts as a mechanism. Sustaining the applied loading results in lateral displacement of the beam through the plastic hinge until failure of the beam. In static conditions, the plastic collapse load remains constant thus no other cross-sections will become plastic. This analysis assumes that the material behaves in a perfectly plastic manner.

The shape factor is the ratio of the plastic moment to the yield moment.

The steel beam has a length-to-depth ratio of approximately fifteen (750/50). Haythornthwaite [2.3] found good agreement between experimental results and the static collapse load for beams having a length-to-depth ratio of between ten and twenty (refer to section 2.1.2).

The effects of shear and finite deflections are not being considered since the beam is unrestrained and subjected to quasi-static loading. Strain hardening is also neglected.

The static collapse load may even be appropriate for dynamic conditions. This is discussed in section 4.2.

(C) Determination of Material and Sectional Properties

In order to calculate specific values for the beam's elastic and plastic behaviour, a number of material and sectional properties had to be determined. Given the complex geometry of the beam, a number of methods were required, namely computer modelling and an analytical approach as well as using material properties obtained from the coupon testing.

(I) Computer Modelling

The geometry of the beam was modelled using the solid modelling package, Pro-Engineer v20.0, to obtain the cross-sectional area, the location of the neutral axis and the second moment of area (all at mid-span). The location of the neutral axis is in terms of the distance from the base or extreme faces of the beam's bottom flanges (refer to figure 1.3).

The procedure was to model the beam, define a cross-section and then use the facilities within the software to calculate the sectional values. Since only mid-span values were required, it was not necessary to model the beam's ends. Any slots were also ignored. Table 4.1 below lists the values that the software produced.

Property	Value	Units
Area	248.14	mm ²
Location of Neutral Axis	13.82	mm
Second Moment of Area	2.99 x10 ⁴	mm ⁴

Table 4.1: Sectional Properties Obtained from Computer Modelling

(II) Analytical approach

A method was required to calculate the values of y_1 and y_2 which are the distances from the neutral axis to the centroids of areas A_1 and A_2 respectively as defined in section 2.1. This was done by simplifying the geometry somewhat and then splitting the geometry into a number of separate areas representing fillets and flat plates. It is known that:

$$A_1 \cdot y_1 = \int_{A_1} D_i \cdot dA_1$$

$$A_2 \cdot y_2 = \int_{A_2} D_i \cdot dA_2$$

where D_i are the distances from the neutral axis to the centroids of each separate area. As these distances are known, y_1 and y_2 can be derived. A diagram of this and more detailed calculations are shown in appendix A4.1 and the results are listed below.

$$y_1 = 13.05 \text{ mm}$$

$$y_2 = 6.10 \text{ mm}$$

(III) *Material Properties Obtained from Coupon Testing*

The elastic modulus and the yield stress (0.03% proof stress) were assigned the mean values obtained from the tensile coupon testing, which are listed again below.

$$E = 210.3 \text{ kN/mm}^2$$

$$\sigma_y = 983 \text{ N/mm}^2$$

(D) *Elastic and Plastic Predictions*

Employing the values obtained using the methods described above, analytical predictions of elastic and plastic behaviour could be made. Table 4.2 below lists values of a number of relevant properties.

Property	Value	Units
Yield Moment	2127	Nm
Section Modulus	2.38×10^{-6}	m^3
Plastic Moment	2335	Nm
Static Plastic Collapse Load	12.45	kN
Shape Factor	1.10	-

Table 4.2: Values of Some Elastic and Plastic Properties

Inputting values into equation 4.1, the beam's response during elastic loading is obtained. The static load is related to the deflection (in millimetres) of the beam as follows:

$$P_e = 715.4 \cdot \delta \quad (\text{N/mm}) \quad \text{Eq (4.3)}$$

Equation 4.3 produces a straight line with a gradient of 715.4 (N/mm). An analysis that combines elastic and plastic behaviour uses equation 4.3 but, once the load reaches 12.45 kN, the load remains constant for any increase in deflection. This is termed an elastic-plastic analysis.

4.1.3 Non-linear static FEA

(A) Modelling Procedure

Static beam tests were modelled using an implicit Finite Element Analysis (FEA) code, namely ANSYS 5.4. A quarter model of the beam with symmetrical boundary conditions was used to reduce the size of the model. The symmetry was applied about vertical planes at mid-span and also mid-width

of the beam. The complex end of the beam was modelled in case it was significant in overall behaviour. To represent the simply supported condition, the nodes at a distance of 375 mm from the mid-span, the support location, were constrained only in the vertical axis; rotation was still permitted. These boundary conditions are shown below in figure 4.2.

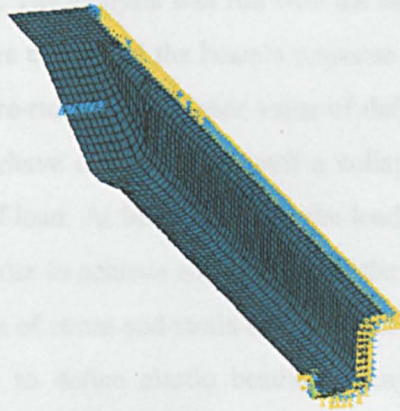


Fig 4.2: Element plot with boundary conditions

Although the side impact beam has a number of small slots, none of these are located at the beam's mid-span and so will not influence the beam's local failure. It is assumed that the slots do not have any significant effect on the beam's elastic response at the cross-section where they are located. Therefore, they are not included in the FEA model.

The results of the coupon tests in terms of stress against strain were inputted into the analysis. This was by entering eleven pairs of values of strain and the relevant stress in the form of a table. Only three pairs were needed to define the material's elastic response while five pairs

were used to define the point at which yield occurs and the remainder of pairs were sufficient to describe the material's plastic behaviour. Thus, the complete range of material behaviour was represented within the FEA.

Shell elements of type 'shell 43' or 'shell 181' are the two possible options for shell elements with plastic material behaviour and both are four-noded elements. The latter element is recommended for non-linear and/or large strain responses. The model consisted of 1926 nodes and 1832 elements.

The isotropic material option was selected. Although the elastic modulus was inputted, material behaviour was determined within the software by the stress-strain table. Other material properties specified were the density of the material and Poisson's ratio.

Only one node on the top flange at mid-span was assigned a value of deflection (the node at mid-width). This was so the beam was not constrained in such a manner as to impose an unrealistic deformation profile. The analysis was run with the user-defined value of deflection (the time step) and the software calculated the beam's response. The magnitude of force was noted. The analysis was then re-run using a higher value of deflection. Initial trials indicated the beam model did indeed behave elastically up until a collapse load after which it could sustain a smaller magnitude of load. At beam collapse, the loading on the beam behaves in a more non-linear manner. In order to achieve convergence of the solution, the time step had to be decreased. As with the pairs of stress and strain used to describe material behaviour, only a few analyses were sufficient to define elastic bending, many analyses were required to characterise the behaviour during collapse and an intermediary number of analyses could classify the beam's post-collapse behaviour.

A number of different mesh densities were attempted during initial analysis runs to justify the element mesh used. In particular, regions of high stress were checked to ensure that the refinement was adequate. For practical mesh densities, there was reasonable convergence in results at a medium level of refinement. This level was selected to keep analysis times as short as possible.

Instead of specifying a particular value of deflection, it is possible to define forces on the beam and the software will calculate the corresponding deflection (the time step is now force).

However, given the non-linear nature of the load, using deflection allows greater control, and easier convergence, of the analysis. Nevertheless, in order to confirm that the method chosen had no influence on the results, separate analyses were performed using force as the controlling parameter. Force was applied as a line force to nodes of the top flange at mid-span. However, when the beam began to deform locally, the force was applied only to the highest nodes (in the y-axis) of the top flange. This would be more representative of the loading during a static beam test.

In order to verify that the type of elements used, in terms of material behaviour permitted and the number of nodes, did not significantly affect the results, other elements were tried in the analyses. These elements were 'shell 63' and shell '93' which are four-noded and eight-noded elements respectively. They are both elastic elements and so comparisons could only be made in the initial elastic region.

(B) Results of the Analysis

The software allows stress plots to be generated for each analysis at a particular magnitude of deflection. As the material is isotropic, the Von Mises stress perhaps best illustrates the reaction of the beam. Figure 4.3 (a) and (b) show the beam at a deflection of 10 and 20 mm respectively. Both of these states are before beam collapse has occurred. To maintain clarity, no legend for stress values is shown in figure 4.3 but these values are known.

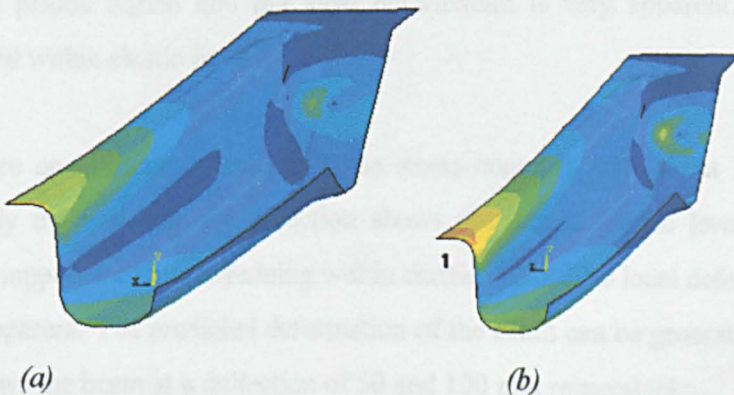


Fig 4.3: FEA Prediction of Beam at a Deflection of (a) 10 mm and (b) 20 mm

At a deflection of 10 mm all the stresses are within elastic limits and are as expected. Figure 4.3 qualitatively shows that the stresses increase as the distance from the neutral axis, in either

vertical direction, increases and also as the distance from the beam end increases reaching a maximum at mid-span. There is a local region of higher stress at the location of the support.

At a deflection of 20 mm it is known that the compressive stresses are just beginning to reach the plastic region (of inputted stress values taken from coupon testing) at the top flange at mid-span (point 1 in figure 4.3 (b)). Figure 4.4 (a) and (b) show the beam at a deflection of 30 and 40 mm respectively. These values of deflection represent points during and immediately following beam collapse.

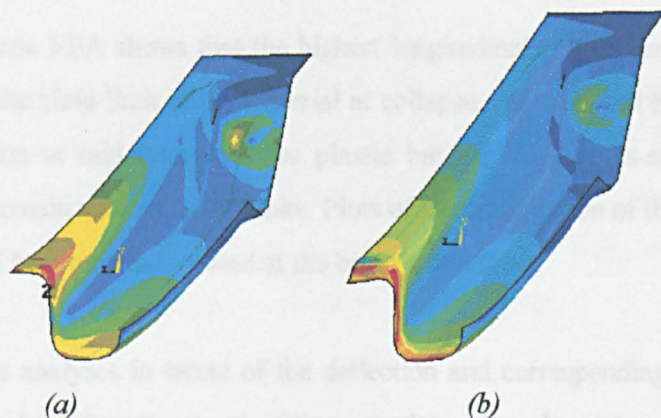


Fig 4.4: FEA Prediction of Beam at a Deflection of (a) 30 mm and (b) 40 mm

At a deflection of 30 mm the plastic stresses at the top flange have developed further and spread to the corner fillet (point 2 in figure 4.4 (a)). Tensile stresses at the bottom flange are just ceasing to be elastic. At 40 mm the whole cross-section of the beam at mid-span has stresses in the plastic region and the local deformation is very apparent. Stresses at the supports are still within elastic limits.

The beam more or less continues with these stress contours throughout higher values of deflection. Only the mid-span cross-section shows stresses at plastic levels with even the stresses at the support location remaining within elastic limits. The local deformation becomes increasingly apparent. The predicted deformation of the beam can be generated and figure 4.5 (a) and (b) shows the beam at a deflection of 50 and 100 mm respectively.

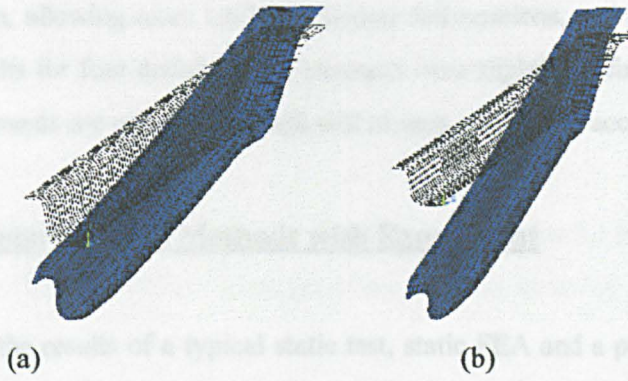


Fig 4.5: FEA Prediction of Beam Deformation at a Deflection of (a) 50 mm and (b) 100 mm

The non-linear static FEA shows that the highest longitudinal stresses are indeed at the mid-span and exceed the yield limit of the material at collapse. As predicted by plastic theory, the whole cross-section at mid-span becomes plastic but all other cross-sections, even at the support location remain within elastic limits. Plots of the deformation of the beam confirm that the failure is local in nature and located at the beam's mid-span.

The results of the analyses in terms of the deflection and corresponding load were inputted into Excel. Figure 4.6 below is a graph of these results with each point representing a separate analysis (for each load step). Results for elastic elements, or where force was the controlling parameter, are not included as no difference could be seen at this scale.

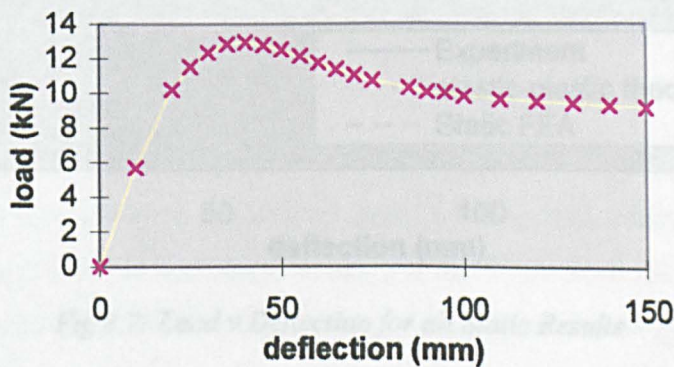


Fig 4.6: Load v Deflection Predicted by Non-linear Static FEA

There was little difference in the results of different elements in the elastic region. The results for the four-noded elements were a little stiffer than for the eight-noded elements (slightly higher gradient). This is to be expected as eight-noded elements possess a higher number of

degrees of freedom, allowing more realistic element deformations, and so are generally more accurate. The results for four-noded plastic elements were slightly stiffer again. This suggests that the plastic elements are over-stiff though still of very reasonable accuracy.

4.1.4 Comparison of Static Methods with Experiment

Figure 4.7 shows the results of a typical static test, static FEA and a prediction from elastic-plastic theory. The theoretical prediction was produced using Equation 4.3 up until the static collapse load was reached, and after this point the load was assumed to remain constant.

Static test results show that the beam behaves linearly up to a reasonably well-defined collapse load (of about 13.5 kN) after which the beam sheds load. The FEA prediction correlates well with this behaviour. It is highly accurate in the elastic region though possibly slightly over-stiff due to the use of plastic elements. The FEA is fairly accurate in predicting collapse although it is not so accurate in the post-collapse region.

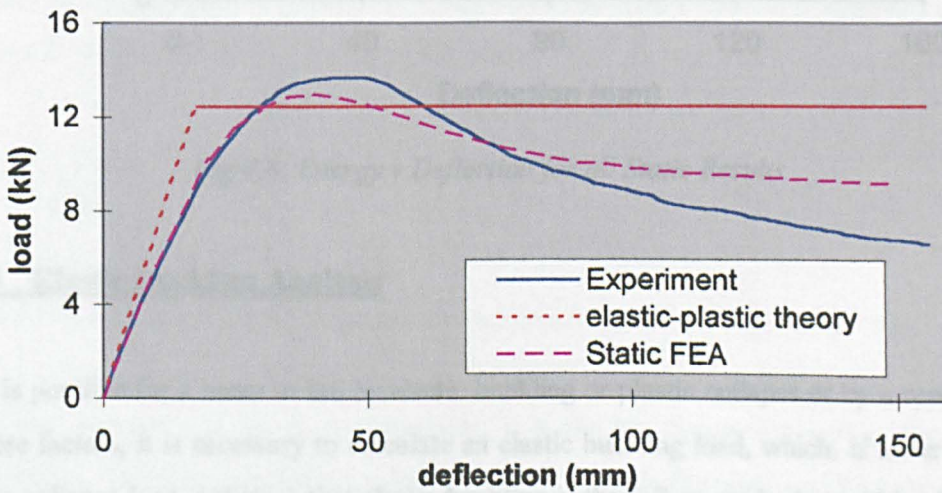


Fig 4.7: Load v Deflection for all Static Results

The theoretical prediction is over-stiff in the elastic region, perhaps because it does not consider finite displacements. The collapse load is underestimated however, given the arbitrary nature of the proof stress selected, an exact prediction is not possible. Plastic theory offers a first approximation of load response but, with the assumption of constant strain after yield, it does not accurately predict the post-collapse behaviour.

The profile of local deformation at mid-span of the beams predicted by the non-linear static FEA corresponds to that seen following the static testing.

Figure 4.8 shows the energy absorbed as a function of deflection for experimental, FEA and theoretical results. The same trends in accuracy are apparent as stated above for load against deflection.

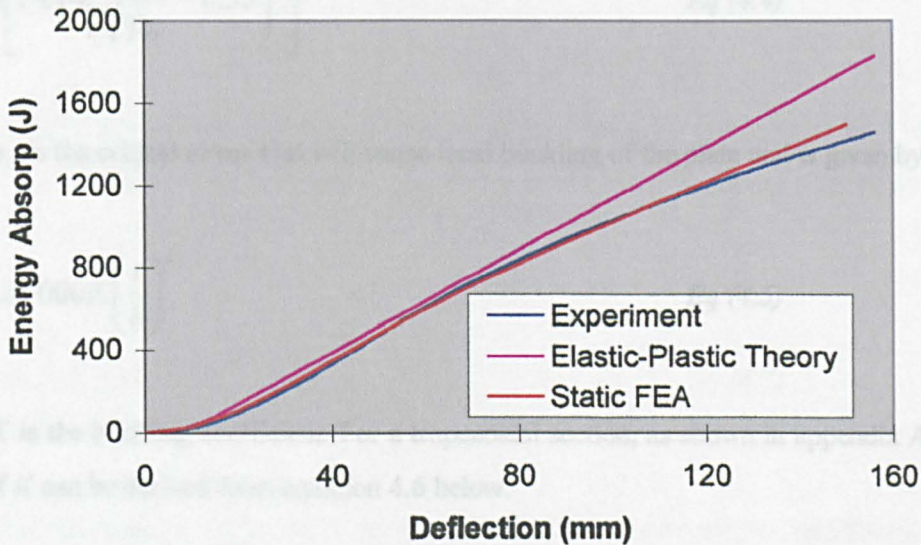


Fig 4.8: Energy v Deflection for all Static Results

4.1.5 Elastic Buckling Analysis

As it is possible for a beam to fail by elastic buckling or plastic collapse or by a combination of these factors, it is necessary to calculate an elastic buckling load, which, if lower than the plastic collapse load, indicates that elastic buckling is the failure mode that will be dominant. A common approach is the Finite Width method, which forms the design approach within BS5950: part5 [4.2].

Briefly, a thin-walled structure is idealised as an assembly of plates or elements. Attention is given to any plates under compression where local buckling may occur. Under compressive loading, each plate will have regions that are lightly and heavily stressed and lightly stressed regions are ignored when determining sectional properties. This can be seen in appendix A4.2.

The effective width of a plate will depend on the magnitude of the applied stress, f_c , the plate's width-to-thickness ratio, b/t , and whether the plate is stiffened or not. A stiffened plate is a plate supported by webs at both its longitudinal edges while an unstiffened plate has only one web for support. This is also illustrated in appendix A4.2.

For a stiffened plate, the effective width, b_{eff} , is stated in the standard to be:

$$b_{eff} = b \left[1 + 14 \left(\sqrt{\frac{f_c}{p_{cr}}} - 0.35 \right)^4 \right]^{-0.2} \quad Eq (4.4)$$

where p_{cr} is the critical stress that will cause local buckling of the plate and is given by:

$$p_{cr} = 185\,000 K \left(\frac{t}{b} \right)^2 \quad Eq (4.5)$$

where K is the buckling coefficient. For a trapezoidal section, as shown in appendix A4.3, the value of K can be derived from equation 4.6 below.

$$K = 7 - \frac{1.8h}{0.15 + h} - 0.091h^3 \quad Eq (4.6)$$

where h is the inverse ratio of the plate's width to the length of the supporting web.

When the beam of this thesis is considered, it is the top flange that will be the plate in compression. The fillets are neglected in assigning a value to the plate's width given that they have a far higher resistance to buckling than a flat plate. Therefore:

$$h = \frac{13}{11} = 1.2$$

Substituting this value of h into equation 4.6 gives $K = 5.24$. Putting this value of K into equation 4.5 gives $p_{cr} = 32\,046 \text{ N/mm}^2$.

The applied stress, f_c , cannot be greater than the yield stress, σ_y , of the material and so is set to 983 N/mm^2 . Substitution of these values for the applied and the critical stress into equation 4.4 gives an effective width of 10.97 mm , which is approximately equal to the actual width. Thus, there should be no reduction in sectional properties. This is due mainly to the short width of the plate relative to its thickness. In fact, the standard recommends, for a stiffened plate, that fully plastic principles should be used when:

$$\frac{b}{t} < 25 \sqrt{\frac{280}{\sigma_y}}$$

Substituting in appropriate values in both sides of the inequality gives $5.5 < 13.3$ indicating that plastic principles should be used. The stress in the webs, p_{web} , can also be considered using equation 4.7 below.

$$p_{web} = \sigma_y \left[1.13 - 0.0019 \frac{D}{t} \sqrt{\frac{\sigma_y}{280}} \right] \quad \text{Eq (4.7)}$$

where D is the depth of the beam. If the web stress is found to be greater than the yield stress then the yield stress should be used. Inserting the appropriate values into equation 4.7 gives $p_{web} = 1057 \text{ N/mm}^2$ which is higher than the yield stress. This is further indication that the whole section should be analysed using fully plastic principles.

In the standard, the moment capacity, M_{ult} , of the beam is calculated using:

$$M_{ult} = Z_c f_c$$

where Z_c is the effective compression sectional modulus based on the effective width of the top flange. Since there has been no reduction in sectional properties, and setting the applied stress to the yield stress gives:

$$M_{ult} = Z_c \sigma_y = M_p$$

Therefore, the plastic moment can be derived using the procedure of section 4.1.2.

The analytical method for predicting elastic behaviour has been found to be inappropriate due to the dominance of plastic material behaviour.

4.1.6 Elastic buckling FEA

(A) Modelling Procedure

The buckling analysis used the same shell model and boundary condition as the non-linear static analysis. In fact, an (elastic) static analysis is performed prior to the buckling analysis. The buckling analysis assumes only elastic material behaviour and so only elastic properties were inputted. A vertical force of 83.3 N ($250/3$ N) was applied to three nodes of the top flange at mid-span. Given the quarter symmetry used, this meant a total vertical force of 1 kN was applied.

(B) Results of the Analysis

The analysis predicted the critical values when various buckling modes occur. These values represent factors of the applied loading and, given a total force of 1 kN, are also the buckling load. The values are shown in table 4.3.

Mode	Buckling Load (kN)
1	79.0
2	103.5
3	109.6
4	114.7
5	118.3

Table 4.3: Buckling Modes Predicted by FEA

The software can generate plots indicating the beam's buckling during each mode. Figure 4.9 below shows the first two modes of buckling.

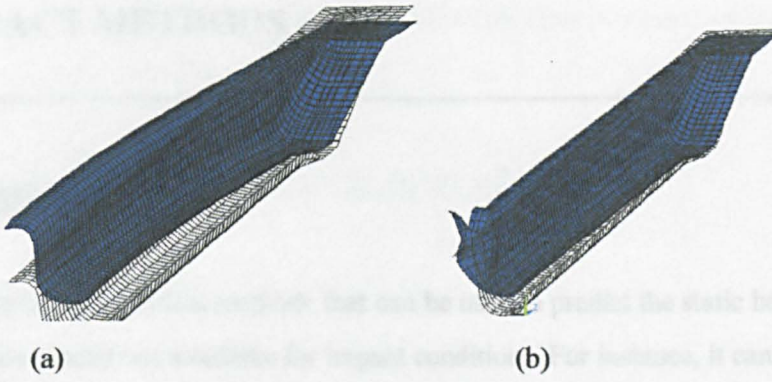


Fig 4.9: (a) Mode 1 and (b) Mode 2 of Buckling Predicted by FEA

The buckling analysis predicted a number of modes and many more could have been identified. At lower modes the buckling is more global in nature while, at higher modes, buckling is associated with increasingly complex patterns of local buckling always at the mid-span. It is really only the first mode that is of any interest as, in normal conditions, this will be the first and only mode to occur. Yet even this mode does not occur until the relatively high load of 79 kN. The buckling analysis considers only elastic behaviour but it has been seen that plastic material behaviour will cause beam collapse at a much more modest load. Thus it can be said from these results that the failure mode of the beam is by plastic collapse with little or no influence of elastic buckling.

4.2 IMPACT METHODS

4.2.1 Analytical Methods

Section 4.2 presented analytical methods that can be used to predict the static behaviour of the beam. There are predictions available for impact conditions. For instance, it can be shown that the maximum deflection of a beam, δ_{\max} , produced by a mass falling on to the mid-span of a simply supported beam is related to the static deflection, δ_s , that would be caused by the same mass resting on the beam, and the drop height, h . This relationship is shown below in equation 4.8.

$$\delta_{\max} = \delta_s + (\delta_s^2 + 2h\delta_s)^{1/2} \quad \text{Eq (4.8)}$$

However, such predictions make a number of assumptions, one of them being that the beam behaves only in a linearly elastic manner. As this assumption is clearly false for the beam being considered within this thesis, these predictions will not be considered further.

The static collapse load can often be appropriate for dynamic conditions. The results of impact tests (see section 3.5.5) show that even the highest (unfiltered) peak loads are only around twice the magnitude of the collapse load. Since the dynamic loading is less than three times the static collapse load, then it is appropriate (as shown by Jones [2.5]) to use an analysis that uses the static collapse load.

Section 2.1.3 described how elastic material behaviour could be ignored when the energy ratio (the ratio of the kinetic energy to the strain energy) is much greater than unity. A value for the energy ratio has been determined (based on maximum values of the kinetic and strain energy during impact) and is equal to approximately 1.6 (at the lower impact velocity) and 2.4 (at the higher impact velocity). The literature suggests a minimum value of perhaps five and so it is not appropriate to ignore elastic material behaviour.

It may be that the effect of the strain rate is important but the constants of the constitutive equations (see section 2.1.5) are unknown. An analysis that does not consider the strain rate

will still be appropriate if the impact velocity is sufficiently low or since the high strength steel may be less strain rate sensitive.

4.2.2 Dynamic FEA: Modelling of the Impact Tests

(A) Modelling Procedure

The dynamic FEA was performed using LS-Dyna v940. Once again, two planes of symmetry were utilised and the beam was modelled using shell elements where plastic material behaviour was inputted using results of coupon tests. Material model of type 24 was used which allows elastic-plastic behaviour and an optional strain rate dependency. Other input parameters were the density of the material, the elastic modulus and Poisson's ratio.

In this case the striker was also modelled, using solid elements. These elements were given the material properties of nylon 66, apart from the density of the material, which was used to control the overall mass of the striker. Initial velocities of 8 or 9.75 m/s were specified for each node of the striker. Surface-to-surface contact elements were selected for the interface between striker and beam and the load against time was determined using the contact force between contact elements. Figure 4.10 below shows the model of the beam and striker (LS-Dyna produces poorer quality bitmaps that can be misleading when examining the element mesh).

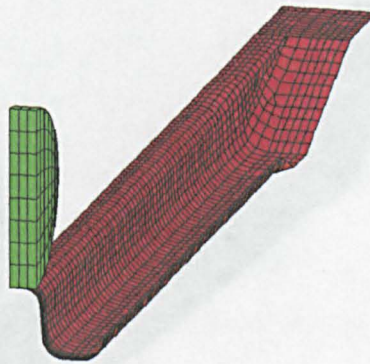


Fig 4.10: Dynamic FEA Model of Beam and Striker

There are material model options within LS-Dyna to specify parameters that correspond to the Cowper-Symonds equations and thus represent the influence of strain rate. However, these options were not selected.

Unlike the static analyses, LS-Dyna, because it is an explicit code, allows one analysis to determine beam's behaviour during the entire loading history. The software allows the output of results in a number of forms and load or energy absorbed against time or deflection are all possible. The results could be exported to Excel for easier manipulation.

(B) Results of the Analysis

Examination of the stresses obtained using LS-Dyna show a number of similarities to the non-linear static analysis. Before collapse, they are within elastic limits and are as expected for a simply supported beam in bending (in terms of how they vary from the beam end to mid-span and from the neutral axis to the top and bottom flanges). The stresses reach the plastic region at the top flange, spread to the corner fillet and continue to develop until the whole cross-section at mid-span becomes plastic. Throughout the rest of the impact event the stresses at all other cross-sections, even at the support location, remain within elastic limits. To avoid unnecessary repetition, only the stresses during collapse are shown below in figure 4.11. It can be seen that, at this point, the top flange at mid-span has deformed considerably and high stresses have developed in the corner fillet.

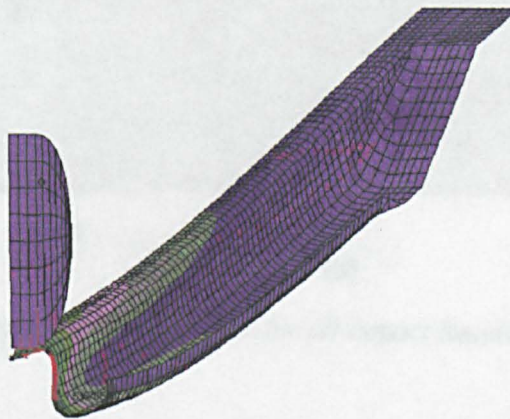


Fig 4.11: Dynamic FEA Prediction of Stresses at Collapse

4.2.3 Comparison of Dynamic FEA with Experiment

The behaviour of the beam predicted by the dynamic FEA is the same seen in the video playback of the impact test. Even the loss of contact between beam and striker can be seen happening within the FEA model.

The typical results of impact tests and FEA at both impact speeds are shown in Figure 4.11a. It can be seen that both the test and FEA results all show large initial oscillations in load. This may be due to the contact between beam and striker or to the impact of the striker causing the beam to vibrate as well as deform. Both features are represented in the FEA. Certainly, other features, such as instrumentation noise, are not represented in the FEA and this is strong evidence that they are not causes of the dynamic effects seen in test results. The load fluctuations decay with time and this decay seems to occur as the plastic collapse load is reached. The beam will deform in a similar manner at the higher impact speed as at the lower although the maximum deflection will be greater given the greater energy. The post-collapse load is also a little lower at the higher impact speed and this is predicted by the dynamic FEA.

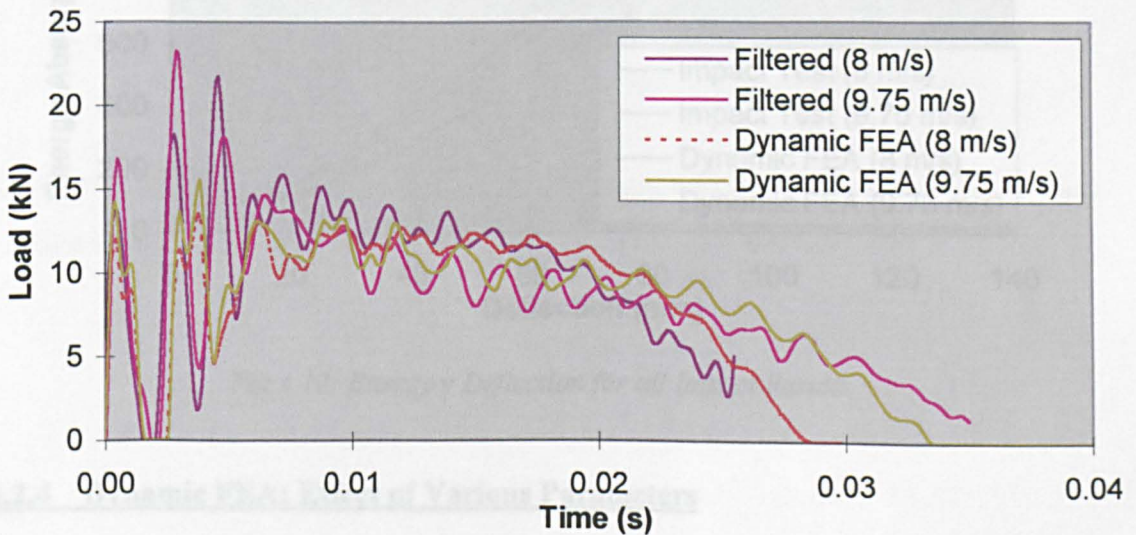


Fig 4.11a: Load v Time for all Impact Results

The predictions of the FEA model are in good agreement with actual behaviour; initial load fluctuations, the rate of decay of these load fluctuations and the later mean load are all predicted with good accuracy. It is therefore believed that a suitable model has been developed. The model does not include any strain rate effects (such as the Cowper-Symonds

equations discussed in section 2.1) which appear to be unnecessary at the impact velocities being considered.

The decay in initial load fluctuations could be the result of two interacting factors: damping in the material or the change in the beam's stiffness due to its deformation. Once the plastic collapse load has been reached, the beam will form a plastic hinge and become increasingly 'v-shaped'. Such a structure will have very different modal properties and it may be that the deformed beam exhibits lesser load oscillations.

Figure 4.12 shows the derived energy absorption as a function of deflection from experimental and FEA results. It can be seen that there is a difference in each set of experimental and FEA results and this is because the FEA tends to overestimate the deflection of the beam for a given impact speed.

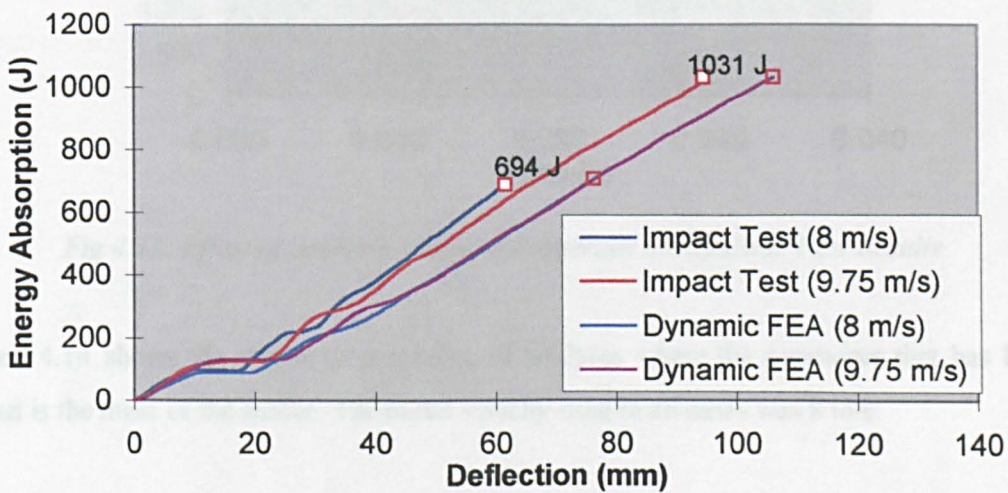


Fig 4.12: Energy v Deflection for all Impact Results

4.2.4 Dynamic FEA: Effect of Various Parameters

(A) Modelling Procedure

The dynamic modelling of the impact test included modelling of the striker and defining its mass and initial velocity unlike for static analyses where force is applied directly to the beam. It then becomes a straightforward task to assess the effects of a number of input parameters

such as the striker's material properties or its mass or velocity.

(B) Results of the Analysis

Figure 4.13 shows the results of two analyses that vary only in the material properties of the striker. This would be expected to alter the contact stiffness of the beam and striker. Values for a typical steel material were used and the results compared with those from a conventional analysis using the properties of nylon 66.

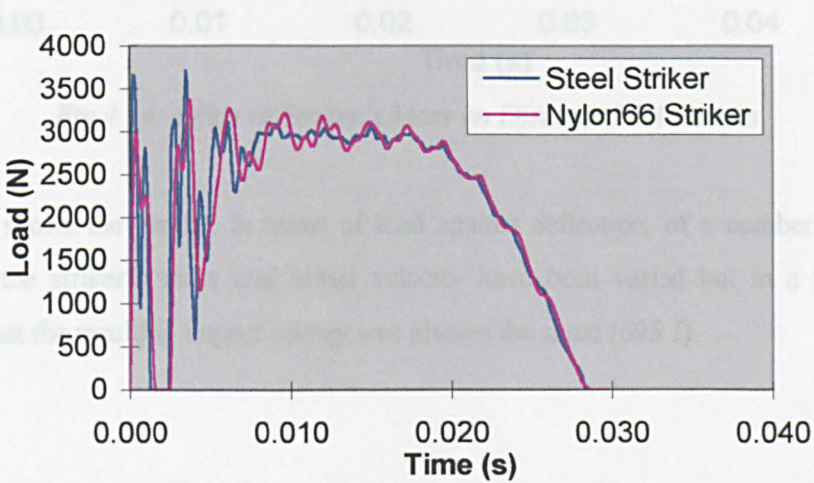


Fig 4.13: Effect of Striker's Material Properties on Dynamic FEA Results

Figure 4.14 shows the results of a number of analyses where the parameter that has been varied is the mass of the striker. The initial velocity used in all cases was 8 m/s.

Deflection (mm)

Fig 4.14: Effect of Varying Striker's Mass & Velocity on Dynamic FEA Results

Varying the material properties of the striker has little effect except that the load spikes are sharper using the properties of steel though they seem to decay faster (the damping coefficient for the nylon material is unknown). Increasing the mass of the striker does not alter the collapse load and the behaviour up until collapse is remarkably similar. The magnitude of the post-collapse load is affected, as has been seen already for the analysis of impact tests at two different impact velocities, and obviously it will be sustained for longer as the mass is

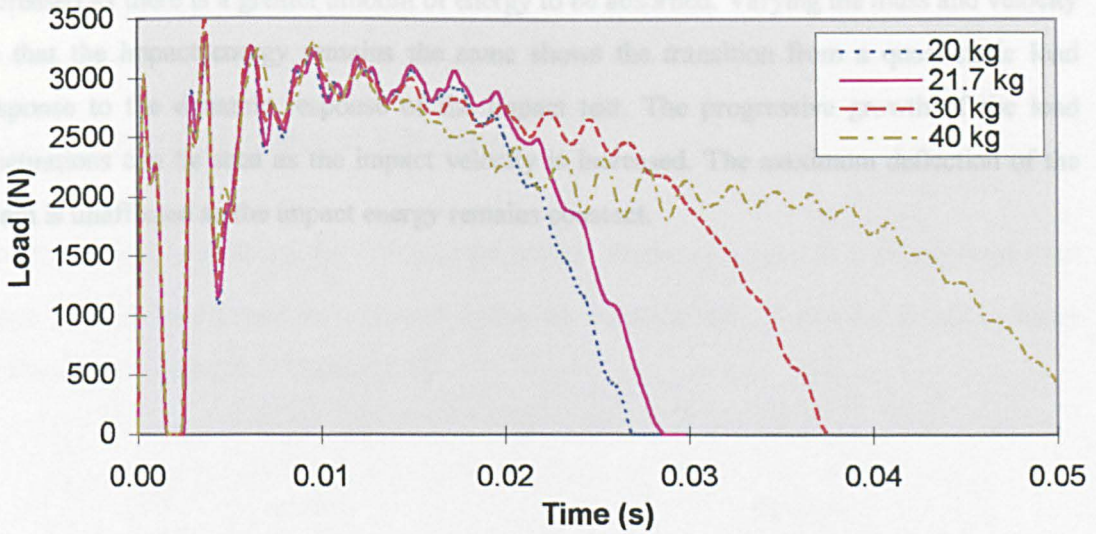


Fig 4.14: Effect of Striker's Mass on Dynamic FEA Results

Figure 4.15 shows the results, in terms of load against deflection, of a number of analyses where both the striker's mass and initial velocity have been varied but in a proportional manner so that the resulting impact energy was always the same (695 J).

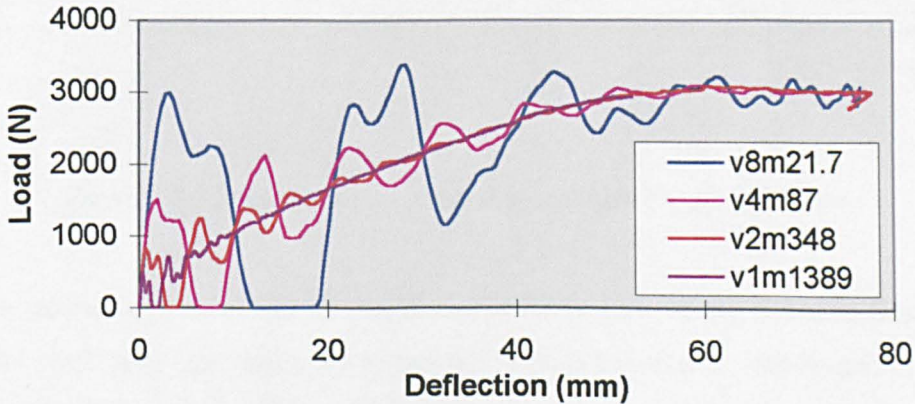


Fig 4.15: Effect of Varying Striker's Mass & Velocity on Dynamic FEA Results

Varying the material properties of the striker has little effect except that the load spikes are sharper using the properties of steel though they seem to decay faster (the damping coefficient for the nylon material is unknown). Increasing the mass of the striker does not alter the collapse load and the behaviour up until collapse is remarkably similar. The magnitude of the post-collapse load is affected, as has been seen already for the analyses of impact tests at two different impact velocities, and obviously it will be sustained for longer as the mass is

increased as there is a greater amount of energy to be absorbed. Varying the mass and velocity so that the impact energy remains the same shows the transition from a quasi-static load response to the dynamic response of the impact test. The progressive growth of the load fluctuations can be seen as the impact velocity is increased. The maximum deflection of the beam is unaffected as the impact energy remains constant.

4.3 MODAL METHODS

4.3.1 Theoretical Modes of Vibration

The theoretical formulation for deriving the natural frequencies, ω_i , of a simply supported beam is well known and is presented below as equation 4.9. It can be found in many textbooks; one example is Beards [4.3].

$$\omega_i = \left(\frac{i\pi}{L}\right)^2 \sqrt{\frac{EI}{A\rho}} \quad \text{rad/s} \quad \text{Eq (4.9)}$$

where i is the mode number from 1 to n , ρ is the density of the material and all other variables are as previously defined. Figure 4.10 (a) and (b) illustrate the first two modes of the beam respectively.

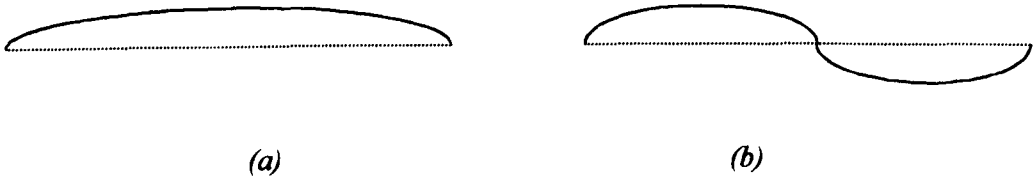


Fig 4.10 (a) Mode 1 and (b) Mode 2 of a Simply Supported Beam

It may be the case that neither of the two modes of figure 4.10, or any higher modes, will be dominant in their own right during an impact test. This is because, as with the modal testing, the loading conditions of the striker on the beam are not represented.

It is highly likely that the striker does influence the beam's modal behaviour. The impact event could be idealised as a simply supported beam with a lumped mass at mid-span. It is known that such a system will vibrate at the lowest natural frequency given by equation 4.10 below [4.3].

$$\omega^2 = \frac{EI \left(\frac{\pi}{L}\right)^4 \left(\frac{L}{2}\right)}{\left(m_1 + \frac{m_2}{2}\right)} \quad \text{Eq (4.10)}$$

where m_1 is the mass on the beam, which has a mass m_2 . Other material properties are for the beam.

It is also desirable to determine the modes of the beam in an unsupported condition to compare them with the modal test results. The modes are given by equation 4.11 below [4.3].

$$\omega_i = \left(\frac{(i + \frac{1}{2})\pi}{L}\right)^2 \sqrt{\frac{EI}{A\rho}} \quad \text{rad/s} \quad \text{Eq (4.11)}$$

Table 4.4 below lists the frequencies and periods for the conditions discussed above applied to the beam considered within this thesis.

Support	Mode	Length (mm)	Frequency (Hz)
Simply Supported	1	750 (L)	159
Simply Supported	2	750 (L)	638
Simp Supp + Mass	1	750 (L)	28
Unsupported	1	750 (L)	362
Unsupported	2	750 (L)	997

Table 4.4: Period & Frequency of Various Modes & Support Conditions

Vibrational modes have been given for a beam that is subject to a range of support conditions including those used in the modal testing. Predicting these modes does involve making a number of simplifications concerning beam geometry and the behaviour of the beam (and striker) during an impact test.

4.3.2 Modal FEA

(A) Modelling Procedure

The modal FEA was carried out using two different models: a beam element and a shell element model. The reason for this was, as will be seen, to confirm both the analytical method and the experimental testing. For both models, a number of different support conditions were imposed: freely supported, simply supported, and simply supported with a lumped mass at mid-span.

It was hoped that modal testing could validate the FEA model, which could then be used to simulate the conditions of an impact test. However, the complex dynamic loading of the striker on the beam cannot be represented in an implicit FEA code. It was hoped that, by modelling the beam using a number of support and loading conditions, the frequencies seen in impact tests could be derived.

A beam element model provided quick and easy predictions of modal behaviour with the whole of the beam modelled, given its simplicity. A number of idealisations were implicit in the model such as uniform cross-section with no portion of the beam overlapping the supports and so, in this respect, the model has a number of similarities to the theoretical approach of section 4.3.1.

For the unsupported condition, the span specified was kept at 750 mm as with the simply supported beam. This was to 'average out' the tapered ends of the beam in a model which assumes constant cross-section. The freely supported condition was modelled in two ways. The first was with no constraints on the elements but this method generated a warning message and it was thought possible that results may have been affected. Therefore, springs with a very low stiffness coefficient were attached to each end to provide constraint in a manner similar to that used in modal testing. However, it was found that there was no difference in the results of the analyses using the two methods.

A simply supported beam with a lumped mass was modelled to represent the striker on the beam. A mass element ('mass21') was created at mid-span which provides a point mass at one node.

A shell element model was also used. This was the same model as used in the non-linear static analysis except, as with the beam element model, the model was of the complete beam. This was because models employing symmetry would have missed any asymmetric modes such as even the second bending mode. For the greatest accuracy, the accelerometer was modelled for the freely supported condition to fully represent the modal testing. This was done using a mass element at the appropriate location. However, it was found that the addition of the accelerometer only affected modal results by 1 to 2 Hz.

FEA models are idealisations of structures and the geometry of the beam had to be slightly simplified, particularly at the beam ends where corner fillets taper to become a flat plate. This is seldom significant but, for modal FEA, the mass, along with the stiffness, of the model is of some importance. ANSYS calculates the total mass during the solution and it was found to be approximately 2% greater than for the actual beam. Therefore it was deemed necessary to calibrate the density of the material so that the correct mass results. The density was reduced by about 2% and the analyses rerun. However, it was found that results only varied by 2 to 3 Hz (higher for the model with reduced density).

(B) Results of the Analysis

Figure 4.11 below is an element and deformation plot of the first mode of the simply supported with a fixed support at mid-span. It is provided as an example of a beam element model and exhibits the main features of all the models. Only one line is meshed leading to a model of only thirty elements. In figure 4.11 the nodes at both ends have been constrained in the y-axis and the nodes at mid-span have been fully constrained.



Fig 4.11: Example of Beam Element Model and Predicted Displacement

Table 4.5 below lists the results of the beam and shell element models for the freely supported beam. Analyses involving beam elements predict only bending modes. The shell element model, however, can predict bending and torsional modes, as well as modes that involve local

regions of the beam such as its ends. These latter modes have been termed ‘local’. The mode is easily identified by examining the predicted deformation of the beam.. The analyses were run until a sufficiently high frequency was reached.

Beam Element: Frequency (Hz)	Shell Element: Frequency (Hz)	Description
	103	torsional
359	227	bending mode 1
	305	torsional
983	474	bending mode 2
	602	local
	637	torsional
	695	local
	707	local
	829	local

Table 4.5: FEA Prediction of Modal Behaviour for Unsupported Beam

Figure 4.12 (a) and (b) below show the first and second bending modes respectively for the shell element model of the freely supported beam.

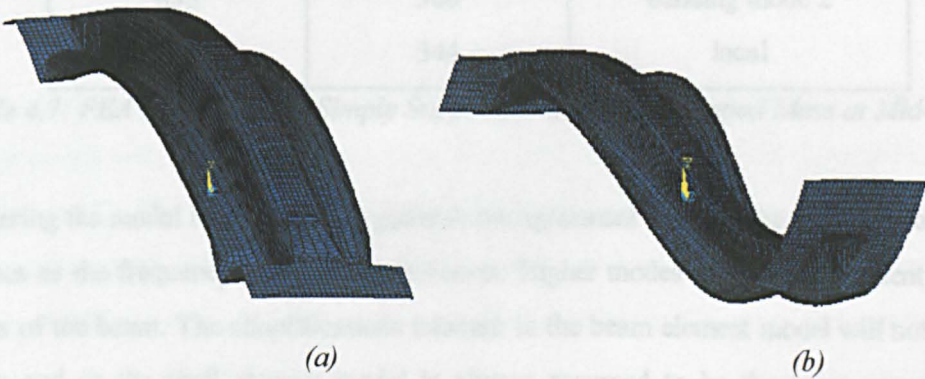


Fig 4.12: (a) First and (b) Second Bending Modes for Freely Supported Beam.

Table 4.6 below lists the results of both models for the simply supported beam.

Beam Element: Frequency (Hz)	Shell Element: Frequency (Hz)	Description
159	157	bending mode 1
	207	torsional
634	511	bending mode 2
	514	local
	523	local
	583	torsional
	654	local

Table 4.6: FEA Prediction of Modal Behaviour for Simply Supported Beam

Table 4.7 below lists the results of both models for the simply supported beam with a lumped mass at mid-span.

Beam Element: Frequency (Hz)	Shell Element: Frequency (Hz)	Description
28	28	bending mode 1
	171	torsional
655	506	bending mode 2
	544	local

Table 4.7: FEA Prediction for Simply Supported Beam with Lumped Mass at Mid-Span

Considering the modal FEA results, in general, the agreement between the two types of models decreases as the frequency of the mode increases. Higher modes are more dependent on local sections of the beam. The simplifications inherent in the beam element model will not account for this and so the shell element model is always assumed to be the more accurate. The agreement between the two models also depends on the support conditions. For instance, in the unsupported condition, there is a considerable difference in the predictions for even the first bending mode.

4.3.3 Comparison of All Modal Results

Modal results are compared, where appropriate, from the modal testing, the impact testing, analytical methods and the modal FEA (beam and shell element models) for a range of loading and support conditions. Table 4.8 below lists results, up to 1 kHz, from the analytical method (theory), the modal FEA and modal testing (of the standard beam) for the freely supported beam.

Theory Frequency (Hz)	Beam FEA: Frequency (Hz)	Shell FEA: Frequency (Hz)	Modal Test Frequency (Hz)
		103	104
362	359	227	232
		305	280
997	983	474	464
		602	548
		637	584
		695	680
		707	696
		829	808

Table 4.8: All Modal Results for Unsupported Beam

It can be seen from the above table that the theory and the beam element FEA results are in good agreement with each other for bending modes but not with the shell element FEA or the modal test results. The divergence in results seems to increase as the frequency increases. This must be because of features that they both neglect, such as the ends of the beam, being relatively significant in the true modal response. This invalidates the use of these methods.

Table 4.9 below lists results from the analytical method (theory) and the modal FEA for the simply supported beam.

Theory Frequency (Hz)	Beam FEA: Frequency (Hz)	Shell FEA: Frequency (Hz)
159	159	157
		207
638	634	511
		514
		523
		583
		654

Table 4.9: All Modal Results for Simply Supported Beam

Once again, the theory and the beam element FEA results are in good agreement with each other. Although the first mode for the shell element FEA results correlates well with other results, there is little correlation for the second bending mode. Perhaps the poorer agreement at higher frequencies is because higher modes are more dependent on local sections of the beam such as its ends and only the shell element FEA incorporates these features.

Table 4.10 below lists the results for the simply supported beam with a lumped mass at mid-span. As this could be said to represent the conditions of an impact test, the frequencies seen in impact test data (refer to appendix 3.16) are also included.

Theory Frequency (Hz)	Beam FEA: Frequency (Hz)	Shell FEA: Frequency (Hz)	Impact Test Frequency (Hz)
28	28	28	
		171	
	655	506	469
		523	547
	1031	856	703

Table 4.10: All Modal Results for Simply Supported Beam with Lumped Mass

The theory and FEA results are in agreement for the first mode but, as before, the shell element FEA results are divergent for higher modes. There is no real correlation between any

of these three sets of results and the frequencies from impact tests. This suggests that the beam and lumped mass is an inappropriate description of physical behaviour during impact.

None of the analyses presented above have been able to predict the most dominant frequency seen in impact test data. The closest frequencies are usually associated with the second bending mode of the beam but during an impact test the force is both applied and measured at the mid-span of the beam. As this location is a stationary node of the second bending mode, the mode should not be excited. Even if the impact was not perfectly at mid-span, the mode should not be excited to the degree that it is the most dominant in the test data. Rather, it is believed that an adequate description of dynamic behaviour has not been found.

The description with the striker as a lumped mass was thought the most likely but the predictions of this description bear no relation to impact frequencies. It was then hypothesised that the striker possessed so much energy that it was less affected by the vibration of the beam than the beam and lumped mass description supposed. In which case, the striker would act more like a support. However, this description is also weak and some other physical description is probably necessary to account for the dynamic effects seen in test results.

There may be a striker/beam interaction present during an impact test that requires a more complex analysis. Impact tests, presented in appendix 3.17, suggest that dynamic effects may be a function of the contact stiffness of the beam and striker. Further work in this area is required.

SUMMARY AND CONCLUSIONS FOR ALL STEEL BEAM RESULTS

Static and impact tests involving a simply supported beam loaded at mid-span were carried out on a particular steel side impact beam. Static and dynamic FEA were performed and compared with experiments to determine the accuracy of the analyses.

Successful modelling of both static and dynamic beam behaviour is possible using FEA. Theoretical predictions using plastic analysis can provide a first approximation of static elastic behaviour and the collapse load. It has been shown that the beam fails by plastic collapse with little or no influence of elastic buckling. The impact behaviour of the beam includes complex dynamic effects that cannot simply be explained by the beam's modal properties.

There is now a basis from which to go on to beams of alternative material types. Simple test procedures, while they do not represent the loading conditions of the beam within the vehicle, can evaluate static behaviour under certain conditions and assess the importance of dynamic loading rates. FEA models could perhaps be adapted for these alternative materials.

CHAPTER FIVE

EXPERIMENTAL TESTING OF COMPOSITE COUPONS

OVERVIEW OF CHAPTER

The mechanical properties of the thermoplastic composite material must be known if modelling, using Finite Element Analysis, of the composite beam is to be performed. Although a number of material properties have been obtained within the SACTAC project, the information required for modelling is incomplete. They are also, in most cases, the manufacturer's stated values and so it was considered prudent to carry out further testing. Furthermore, the testing provided a better understanding of the composite material's behaviour under various types of loading.

Due to the anisotropy of the material and the number of possible failure modes (see section 2.3), a considerable amount of testing was required to characterise the material. This chapter presents the coupon testing that has been performed and the structure of the chapter is represented as a block diagram in figure 5.1 below. Section numbers for this thesis are included in the figure. For all of this test-work, an undergraduate student, Bjorn Auren, aided the author.

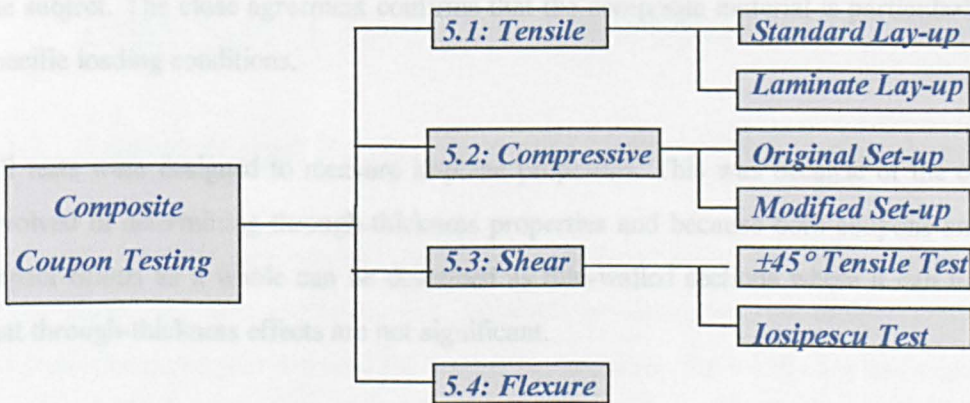


Fig 5.1: Block Diagram of Structure of Chapter

Tensile coupon testing has been performed on two types of coupons. The first was made from material all at the same orientation of 0/90° and the second was cut from an actual side impact beam and is comprised of two layers of material with different lay-ups. The first type of coupon established properties such as the tensile elastic modulus, Poisson's ratio and tensile failure stresses and strains. The second type was used to assess qualitatively the behaviour of an important part of the beam.

Compressive coupon testing has determined the compressive elastic modulus and compressive failure stresses and strains. Concerns over the test set-up led to modifications being made. However, the quality of the results of the modified set-up did not improve and may even have been poorer.

Shear testing was carried out using a tensile test of coupons with $\pm 45^\circ$ fibre orientation. Although the shear modulus could be evaluated, the testing seemed unsatisfactory for determining the shear strength of the material and so another type of shear test, using the Iosipescu method, was also performed. However, the same shear behaviour was witnessed and specifying the shear strength remains problematic.

Flexure testing involved the four-point bending test on coupons. The testing provided a comparison of the elastic modulus and information on the material's failure in bending.

Comparisons are made of all the test results with values obtained within the SACTAC project (see section 1.4). Generally, there is good agreement between the two sets of results. On the few occasions where the correlation is not as strong, reasons can be found in the literature on the subject. The close agreement confirms that the composite material is particularly weak in specific loading conditions.

All tests were designed to measure in-plane properties. This was because of the complexity involved in determining through-thickness properties and because both coupons and the side impact beams as a whole can be described as thin-walled sections where it can be assumed that through-thickness effects are not significant.

5.1 TENSILE COUPON TESTING

5.1.1 Introduction to Tensile Coupon Testing

The tensile coupon testing was carried out in accordance with *ASTM D3039/D3039M-95a* [5.1]. This standard involves flat, straight coupons and gives recommended coupon dimensions. The number of specimens that should be tested is specified (a minimum of five).

Tensile testing was also performed on specimens cut from actual side impact beams. The coupons were taken from the top flange of the beam, which is comprised of two layers of material with different lay-ups. This testing was performed to assess qualitatively the behaviour of the two layers and of an important part of the beam.

Both forms of tensile testing are presented separately and are described as standard lay-up and laminate lay-up. Comparisons are then made between the two forms of tests.

Tensile Coupon Testing Using Standard Lay-up

5.1.2 Equipment Used During Testing of Coupons with Standard Lay-up

The testing machine used was an Instron Model 1342 and the calibration certificate number is 88285 (NAMAS). Five specimens were prepared, nominally with the dimensions 250 x 25 x 3.5 mm. Strain gauges were used for measuring extension; three 120 ohm strain gauges, with a gauge factor 2.15, were bonded onto each specimen. This allowed both lateral and longitudinal strains of the coupon to be measured. Also, the longitudinal strain on both sides of the coupon could be measured and this could be used to evaluate the degree of bending of the specimen. These two gauges are termed back-to-back gauges. Figure 5.2 below shows a specimen within the cross-heads of the test machine.

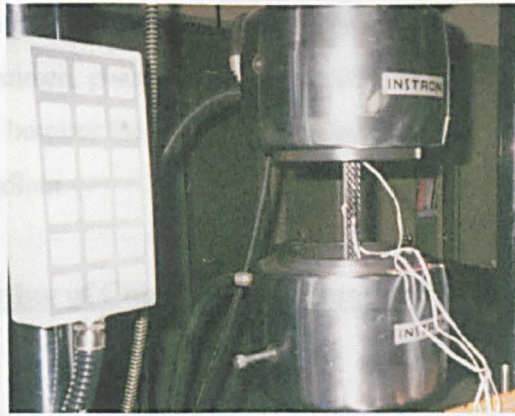


Fig 5.2: Tensile Specimen During Testing

The strain gauges were standard gauges as used with steel specimens. Error could arise caused by the composite material being unable to dissipate the heat generated within the gauge (see section 2.4). To avoid this, a short burst data logger, in conjunction with a PC, was used. A balancing resistor of $120\ \Omega$ was used for the data logging.

5.1.3 Testing Procedure

Rectangular coupons were cut from plates of co-mingled woven glass reinforced polypropylene. This material was provided by Nottingham University. The plates are made from eight plies of material all of the same orientation of $0/90^\circ$. They were of the correct length, approximately 250 mm, and of suitable thickness and so only required cutting to the correct width of 25 mm. Care was taken to ensure that the longer edge of the coupon was parallel to the fibre direction. Final dimensions of the thickness and width of specimens were checked at three points (near each end and at mid-point) with a micrometer and the values noted. The mean of these dimensions was calculated. Aluminium tabs ($40 \times 25 \times 3$ mm) were then bonded onto both sides and at both ends of each specimen to prevent the grips from crushing the specimens. *Loctite 406* was used for all bonding after the surface had been primed with *Loctite 770* polyolefin primer. Then the strain gauges were bonded to the specimens.

Each specimen was then tested, at a cross-head rate of 2 mm/min, and the results were recorded in terms of load, cross-head displacement, and the three sets of strain. Due to equipment error during the first test, the specimen was destroyed and the results for only four

coupons could therefore be taken. In many cases, the strain gauges would cease to function before failure of the specimen, possibly due to the difficulty of bonding on to polypropylene. This difficulty can arise because the polypropylene has a higher elongation to failure than the strain gauge bonding medium.

5.1.4 Results of Testing of Coupons with Standard Lay-up

(A) Failure Modes

The types of failure for each specimen and the failure loads are shown in table 5.1 below. Also shown are the specimens' cross sectional area and any remarks about each specimen test.

Specimen	Area (mm²)	Failure Description	Failure Load (kN)	Remarks
1	88.92	Equipment error.	-	Tabs came off.
2	87.98	Angled failure at upper grip	25.0	Tabs came off.
3	90.36	Lateral failure at upper grip	25.6	-
4	89.67	Angled failure at upper grip	29.7	-
5	89.04	Angled failure more than one width from upper grip	27.7	-

Table 5.1: Types of Failure & Failure Loads During Tensile Testing

All of the specimens behaved in a manner expected during tensile testing of composites. The specimens appeared to be elastic until failure, which was a catastrophic event dominated by fibre breakage. With regards to the type of failure, three of the four specimens had initial failure at the upper grip and this may often cast doubt on the validity of results. It should be said that, for these three specimens, both the highest (higher than for the specimen which had failure away from the grips) and lowest failure loads were recorded. This suggests that the location of initial failure was not critical. Whether the crack direction was lateral or angular did not seem to affect the failure load either. Although the tabs came off the specimen with the lowest recorded failure load (specimen 2), the difference is small and easily accounted for by the lesser cross sectional area.

(B) Strain Results

All strain data was converted from engineering to true strain which is the most accurate measurement of strain as it allows for changes in the coupons' cross sectional area due to deflection. The standard does not specify its use; no doubt it assumes engineering values are sufficiently accurate. While this may be true, it was felt that the conversion would only increase accuracy.

Two values required from the testing were the maximum stress and strain for each specimen but this was often not directly possible given the premature failure of many of the strain gauges. Therefore, it was decided to use (modified) strain data based on the cross-head displacement to obtain these values. This is explained in detail below.

Figure 5.3 below is a typical graph of strain against time derived from both the back-to-back gauges and from the cross-head displacement (divided by the length of the coupon). Time during testing, being of no intrinsic interest, was not directly measured and the units in figure 5.3 are in terms of data logger steps. Only the strain results up to 0.5 % strain are shown to clarify the gauges' initial response.

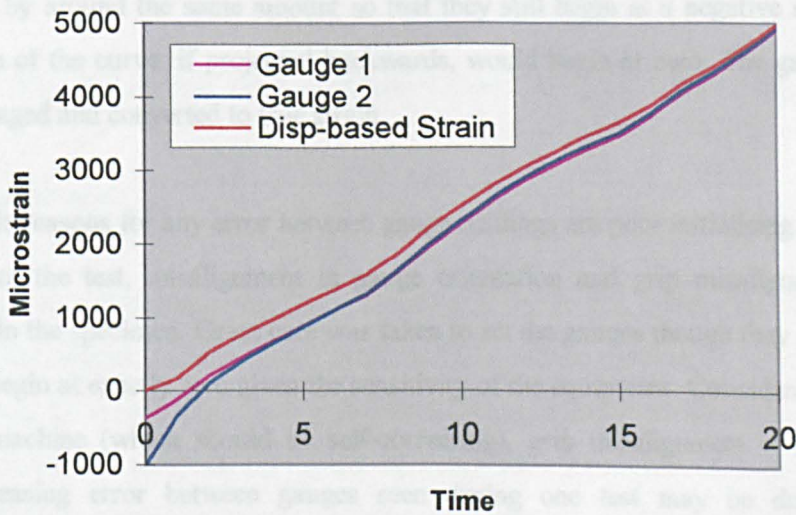


Fig 5.3: Graph of Strain v Time from Gauges and Extensometer During Tensile Testing

The above figure shows two types of error in the measurement of strain: the initial error between strain gauges and the error between the gauges and the displacement-based strain. Both types of error are discussed below.

The initial error between gauges, or 'settling period', can be seen from figure 5.3. Neither gauge begins at zero strain. Also, one of the gauges begins at a greater negative strain and shows a non-linear response until it becomes collinear with the other gauge's values. This is the case in two of the tests although, in another, the error between the gauges was linearly increasing throughout the test. In the fourth test one of the gauges failed from the outset and so the gauges cannot be compared. It is thought that this initial error between gauge readings is due mainly to initial curvature of the specimens (the plates from which the coupons were cut are not perfectly flat). This would explain why one or more of the gauges would exhibit a brief, initial non-linear response starting at a higher (positive or negative) strain. The specimen is experiencing a decreasing bending strain as the specimen straightens out as well as the increasing tensile strain.

It is common to see this constant difference in strain gauge readings and a 'settling period' during tensile or compressive testing [3.1]. Removing this 'settling period' and setting the strains to begin at zero at the data processing stage can overcome the problem. Each set of gauge measurements is adjusted so that its linear response would pass through zero. Therefore 'gauge 1' readings in figure 5.3 are adjusted so that they begin at zero and 'gauge 2' results are modified by around the same amount so that they still begin at a negative strain but the linear portion of the curve, if projected backwards, would begin at zero. The gauge readings are then averaged and converted to true strain.

Other possible reasons for any error between gauge readings are poor initialising of the strains at the start of the test, misalignment in gauge orientation and grip misalignment causing bending within the specimen. Great care was taken to set the gauges though they should not be expected to begin at exactly zero given the sensitivity of the equipment. Considering the design of the test machine (which should be self-correcting), grip misalignment is unlikely. The linearly increasing error between gauges seen during one test may be due to serious misalignment in the orientation of one of the gauges but, for the other tests, the effect of gauge misalignment is believed to be marginal.

The second type of error is a larger, linearly increasing difference between gauge readings and the displacement-based strain. This is assumed to be due to the lesser accuracy of the test machine's measurement of cross-head displacement. Therefore, to derive maximum strains,

the displacement-based strain is factored so that it is collinear with the average of the gauge results. The factor used ranged from 0.95 to 1.05. No reason can be given why the strain derived from the cross-head displacement should be, in some cases, lower than strain gauge readings and, at other times, higher. One such calibrated data set is shown in figure 5.4 below, which also shows the derived engineering and true strain for one test. It can be seen that there is little difference between the engineering and the true strain and that the calibrated displacement-based strain corresponds closely to the engineering and the true strain.

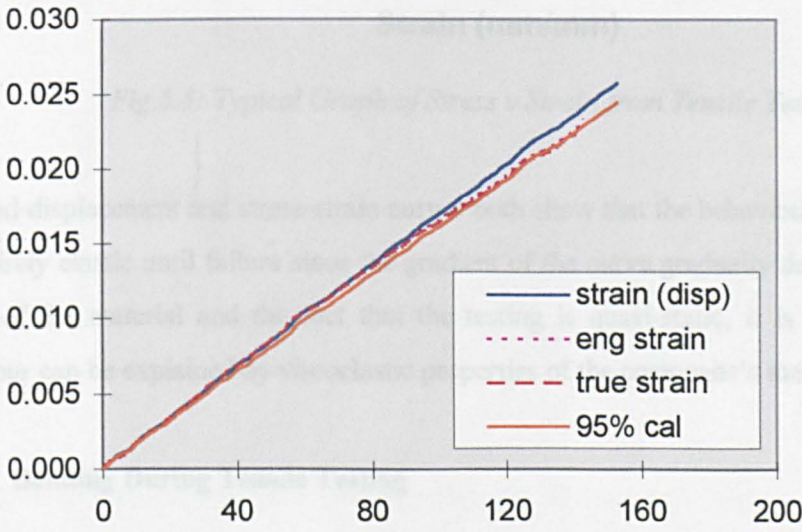


Fig 5.4: Graph of Derived Strains v Time During Tensile Testing

(C) Stress Results

The true stress was calculated from the load data and the known cross sectional area of the specimen. Stress against strain data was now available and the gradient of the curve gave the elastic modulus. To ensure only elastic conditions, the modulus was calculated by taking the gradient only over the range of 0.1 to 0.3 % strain where the curve shows a good linear behaviour. This is the strain range recommended within the standard for materials that fail at a strain greater than 0.6 %. A typical curve of stress against strain is shown below in figure 5.5.

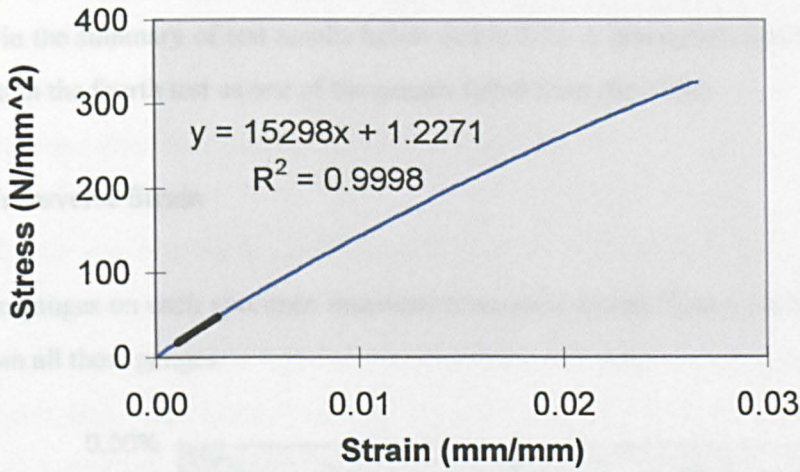


Fig 5.5: Typical Graph of Stress v Strain from Tensile Tests

The load-displacement and stress-strain curves both show that the behaviour of the coupons is not entirely elastic until failure since the gradient of the curve gradually decreases. Given the nature of the material and the fact that the testing is quasi-static, it is assumed that this behaviour can be explained by viscoelastic properties of the composite's matrix.

(D) Bending During Tensile Testing

The ASTM standard recommends that an evaluation of the degree of bending is made and an upper limit of five percent is set before the bending becomes unacceptable. Both system-induced bending and specimen bending are defined in the standard and equations for each are given. However, it has been noticed that these equations are actually the same. This is shown in appendix A5.1. The standard appears to be in error and there is no difference between specimen and system-induced bending as defined.

Perhaps more importantly, degrees of bending are calculated only from the relationships of the readings of the two longitudinal gauges on each specimen yet a number of other reasons why differences in readings can occur have been given. Therefore, the bending equations are considered questionable although excessive values (though not necessarily greater than the five percent that the standard recommends) would still be a cause for concern.

Nevertheless, the percentage bending was calculated for each specimen and the results are presented in the summary of test results below (table 5.2). A percentage bending could not be determined in the fourth test as one of the gauges failed from the outset.

(E) Transverse Strain

One of the gauges on each specimen measured transverse strain. Figure 5.6 below shows the results from all these gauges.

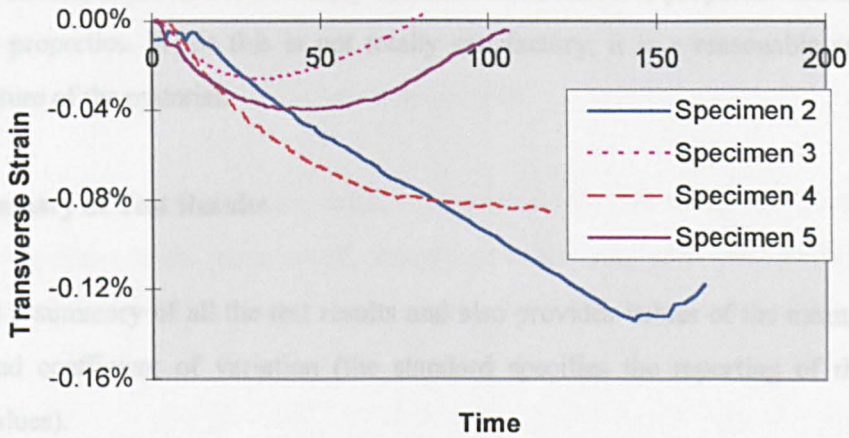


Fig 5.6: Graph of Transverse Strains v Time for all Specimens During Tensile Testing

Figure 5.6 above shows that the transverse strain does not remain linear, even within the range of 0.1 % to 0.3% and so this range could not be used to calculate Poisson's ratio, which is the ratio of transverse to longitudinal strain. In fact, each specimen shows some linearity within different strain ranges and so, to determine Poisson's ratio, different ranges had to be used for each specimen based on judgement. The difference between upper and lower values of the strain range selected were used to give one absolute value for both transverse and longitudinal strain and their ratio gave the Poisson's ratio.

The results of the transverse strain for all the specimens are very surprising. The specimens behaved in a non-linear manner almost from the outset. There was no elastic behaviour up until some failure strain and there is significant variation between specimens. Why this should be the case is not fully understood. However, the transverse contraction of the specimen will have affected the material's transverse fibres and matrix to different degrees. This presumably produced a complex interaction between fibres and matrix. This point requires greater

investigation. However, it shall be seen that Poisson's ratio for the material is relatively small (the transverse strain is more than one order of magnitude smaller than the longitudinal strain) and so transverse effects are assumed to be less significant.

The results for the transverse strain seem typical of viscoelastic behaviour though such behaviour is not so severe for the longitudinal strain. Shear effects or out-of-plane stresses may also influence transverse behaviour. Given the difficulties associated with transverse stresses and strains, it has had to be simply assumed that transverse properties are identical to longitudinal properties. While this is not totally satisfactory, it is a reasonable assumption given the nature of the material.

(F) Summary of Test Results

Table 5.2 is a summary of all the test results and also provides values of the mean, standard deviation and coefficient of variation (the standard specifies the reporting of these three statistical values).

Material Property	Specimen				Mean	SD	CV(%)
	2	3	4	5			
Elastic Mod (MPa)	14192	14752	15083	15298	14831	481.7	3.25
Poisson's Ratio	0.08	0.05	0.08	0.06	0.08*	-	-
UT Stress long (MPa)	294.3	298.6	353.5	325.9	318.1	27.45	8.63
UT Stress tran (MPa)	-	-	-	-	-	-	-
UT Strain long (%)	2.40	2.56	3.02	2.66	2.66	0.26	9.88
UT Strain tran (%)	-0.13	-	-	-	-0.13	-	-
Bending (%)	8.4	2.1	0.3	-	-	-	-
Area	87.98	90.36	89.67	89.04	89.26	1.01	1.13

* Value shown is average of only specimens 2 & 4.

Table 5.2: Material Properties Derived from Tensile Testing

In two of the three cases where bending could be ascertained, the values were relatively low. In the third case the bending was about eight percent but this is the second specimen where, as has been noted, the difference in gauge readings increases linearly during the test. This is thought to be due to poor gauge alignment and so it is believed that this has caused the apparently high degree of bending.

It was found to be difficult to select a strain range of any length for specimens three and five in which the transverse strain remained linear. For this reason the calculated Poisson's ratio for these specimens is artificially low and it was decided not to include them in the calculation of the mean. However, this decreases confidence in the statistical mean as it is based on a smaller sample size.

There is good agreement in the results for the elastic modulus of all the specimens (the coefficient of variation is only around three percent). There is greater variability in the strength values (expressed as an ultimate stress or strain) however this is expected since strength values are dependent on a fracture process (and since it is a composite material that is being considered) and the variation still seems acceptable.

It is unfortunate that one of the tests could not be performed due to equipment error. This does affect confidence in the mean results though, given the relatively low variability in the other four tests, it is believed that the testing has provided a realistic measure of the material's properties.

Tensile Coupon Testing Using Laminate Lay-up

5.1.5 Introduction to Tensile Coupon Testing with Laminate Lay-up

In this case, test specimens were cut from actual side impact beams. The coupons were taken from the top flange of the beam which, as was shown in appendix 1.4, is made up of a nominally six millimetre layer of $\pm 45^\circ$ Twintex and a nominally four millimetre layer of unidirectional Twintex. It is therefore important to realise that testing of these coupons will not provide any meaningful material properties of the composite material in any given direction. For instance, the $\pm 45^\circ$ Twintex layer is expected to be less stiff in tension than the unidirectional layer leading to lower values of the elastic modulus. Though realistic material properties cannot be obtained, these coupon tests were deemed useful as an investigation of the behaviour of an important part of the side impact beam. The top flange of the composite beam is important because it is the only part that is a true laminate (it consists of two layers of different material orientation) and also because, as will be seen later, the top flange is the location of initial failure in the beam. It was hoped that the coupon tests would reveal

characteristics such as the dominance of any particular layer in the coupon's behaviour or whether delamination occurred between the two layers or not.

As this was a more qualitative investigation, and due to the limited number of beams available, only two specimens were tested and these are listed below in table 5.3 with the measured thickness and width of each coupon.

Specimen	Thickness (mm)	Width (mm)	Cross-sectional Area (mm ²)
1	10.7	25	268
2	11.2	25	280

Table 5.3: Dimensions of Laminate Coupons

5.1.6 Equipment and Procedure Used During Testing

The testing in this case was performed along with the steel coupons that were described in chapter three. Therefore, the testing equipment and procedure used were exactly as previously described and further details can be found in sections 3.2 and 3.3.

5.1.7 Results of Tensile Coupon Testing with Laminate Lay-up

Once again, the composite coupons were more or less elastic until failure. When failure did occur, it was catastrophic as it involved fibre breakage across a complete cross-section. This cross-section was close to the mid-span of the coupon. What distinguishes these specimens is that there is clearly visible delamination between the two layers of differing material orientation at the failed cross-section, which spreads towards the ends of the coupon though it ceases well before the grips.

Unfortunately, during the testing this delamination was not so obvious given that the tensile loading held the delaminated layers in-plane. Almost surprisingly, the results of stress against strain for the coupons are linear up until failure despite the occurrence of delamination. Therefore, it is not known when (at what stress or strain) this delamination was initiated.

The true stress was calculated from the load data and the gradient of the curve gave the elastic modulus. The range of 0.1 to 0.3 % was used to calculate the modulus as recommended by the standard. Figure 5.7 below shows a typical plot of the stress against strain from the testing.

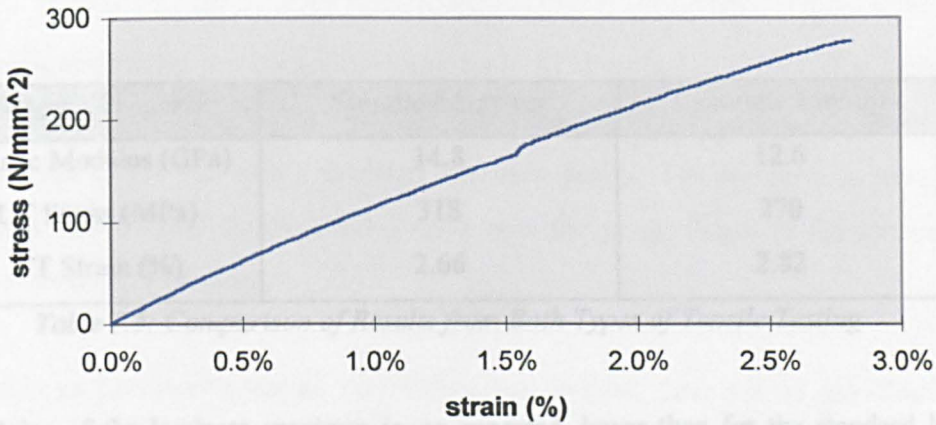


Fig 5.7: Stress v Strain During Tensile Testing (Laminate Lay-up)

Table 5.4 below lists the values of material properties determined from the testing. Although only two specimens were tested, table 5.4 still provides averages of the results. Standard deviations and the coefficients of variance are not included as they would be essentially meaningless for such a small sample size.

Coupon	Elastic Modulus (MPa)	UT Stress (long) (MPa)	UT Strain (long) (%)
1	13 058	278	2.81
2	12 134	261	2.83
Mean	12 596	270	2.82

Table 5.4: Material Properties from Tensile Testing (Laminate Lay-up)

It is interesting that the ultimate tensile strain for both composite coupons are very similar however, given the small number of specimens, this may be a coincidence and no conclusions drawn from this fact are possible.

5.1.8 Comparison of Both Types of Tensile Coupon Testing

Table 5.5 below lists some of the mean material properties derived from both the standard and the laminate lay-up testing.

Material Property	Standard Lay-up	Laminate Lay-up
Elastic Modulus (GPa)	14.8	12.6
UT Stress (MPa)	318	270
UT Strain (%)	2.66	2.82

Table 5.5: Comparison of Results from Both Types of Tensile Testing

The modulus of the laminate specimen is, as expected, lower than for the standard lay-up material yet the difference is not particularly large. This suggests that the unidirectional layer of the laminate coupon is dominant in providing the stiffness of the material for these loading conditions. There is insufficient information to explain why the failure stress of the laminate coupon should be lower or the failure strain higher than the standard coupon. It is thought likely that the shear failure of one layer of the laminate coupon has a significant effect on the overall results. Delamination may also have been an influence on the magnitudes of the ultimate stress and strain.

Although both types of coupons ultimately fail by fibre breakage, the laminate coupon also delaminates during the testing. However, the delamination could not be physically seen during the testing or inferred from test results. It could be argued that delamination has little effect on the coupon's elastic response or its mode of failure. However, even if this is true, it may only be specific to tensile testing where delaminated layers are held together in tension and the overall stiffness of the coupon remains the same. Also, as has been noted, the magnitude of the failure stress and strain may have been affected.

5.2 COMPRESSIVE COUPON TESTING

5.2.1 Introduction to Compressive Coupon Testing

The compressive testing was carried out using the ICSTM method as discussed in section 2.4. Briefly, Mathews and Häberle [2.56] used a rig similar to that devised by Barker and Balasundaram [2.61] but with a modified specimen design. The specimen is rectangular, tabbed and incorporates weakly bonded areas near the gauge length of the specimens to eliminate stress concentrations.

As there is no particular standard that utilises this method, there are no specifications or recommendations to follow other than those given in the literature (such as Mathews and Häberle). However, using the literature, and the experience gained from other forms of coupon tests, it was hoped that reliable results could be obtained.

Initially, five specimens were tested but, as shall be explained, it was considered necessary to carry out further testing. Therefore, modifications were made to the test rig and then another six tests were performed. This chapter has been divided into descriptions of the original set-up, the modified set-up and a comparison of the results of each approach.

Compressive Testing Using Original Set-up

5.2.2 Equipment Used During Testing

Given the relative simplicity of the fixture design, drawings were made up and the fixture manufactured at Strathclyde University. Two identical steel blocks were made; each is comprised of two parts with a slot for the specimen. The parts are connected together by two large screws and the specimen is clamped within the blocks by an internal component that is pushed against the specimen using separate screws. It was believed that, with sufficient care in aligning the specimens in the test machine, the die set used by Imperial College could be avoided.

The test machine used was a Zwick REL 2061. The nominal specimen dimensions were 90 x 10 x 2 mm. With 40 mm length tabs at each end of the specimen, this gives a gauge length of only 10 mm and so smaller gauges (with a gauge length of 3.5 mm) than used in the tensile test were required. Back-to-back gauges were once again used on the specimens in order to evaluate bending but, due to limited space, no transverse gauge was used to measure the transverse strain. A short burst data logger connected to a PC was again used for capturing the strain data.

5.2.3 Testing Procedure

Coupons were cut from the composite plates provided by Nottingham University. The edges of the specimens were ground flat and aluminium tabs were bonded to the specimens using the *Loctite 406* adhesive and *Loctite 770* primer. Following the recommendation of Mathews and Häberle, PTFE-tape was used to produce a debonded zone at the inward edge of each tab. Final dimensions of the thickness and width of the specimens were recorded at three points (near each end and at mid-point) using a micrometer and an average calculated. Strain gauges were then bonded to the specimens.

Each specimen was then tested. This was at a low cross-head speed of 0.2 mm/mm due to the short gauge section entailing relatively small values of deflection. The results were recorded in terms of load, cross-head displacement and the two sets of strain.

5.2.4 Results of Testing Using Original Set-up

(A) Failure Modes

All of the specimens failed in a very similar manner, which is illustrated in figure 5.8 below. The specimens were elastic up until failure, which was a catastrophic event that consisted of fibre breakage and matrix cracking. The failure mode was one of crack initiation near the mid-length of the specimen, which spread laterally. No global buckling was ever evident. The crack was angled at about 45° in the through-thickness direction.

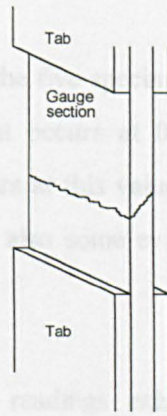


Fig 5.8: Failure Mode During Compressive Testing (Illustration by Auren [5.2])

It was encouraging that the failures for all the specimens occurred in the gauge section and not near the tabs. The crack direction was angular (through the thickness) and this may be explained by small out-of-plane shear effects driving the direction of the propagating crack. As with the tensile testing, all of the tabs could be peeled off after testing due to inadequate bonding.

(B) Strain Results

Due to the fact that failure in compression was at considerably lower strains than in tension, all of the gauges functioned correctly up until specimen failure. Therefore, it was never necessary to use a strain based on the cross-head displacement. Figure 5.9 shows a typical graph of strain against ‘time’ where time is simply the data logger steps. As before, the strain results have been modified at the data processing stage so that they begin at zero.

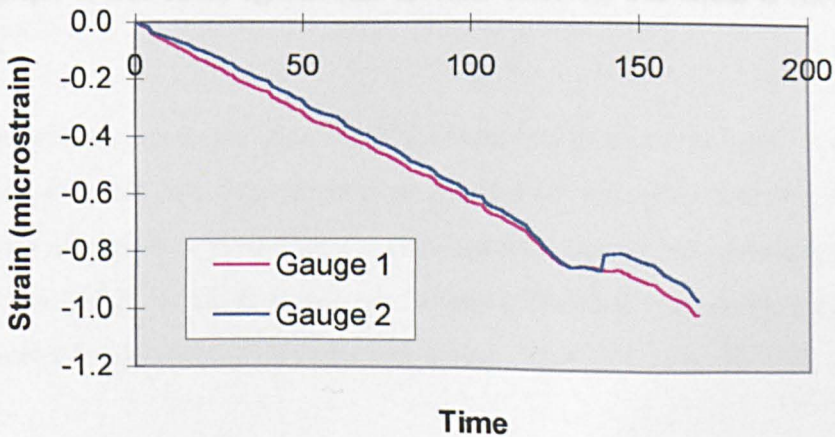


Fig 5.9: Strain v Time During Compression Testing (Original Set-up)

Figure 5.9 is 'typical' in that three of the five specimens showed a similar strain-time history. The anomaly in elastic behaviour that occurs at 0.9 % strain can be seen in two of the specimens and, in a third, failure occurs at this value of strain. The other two specimens did not reach a strain of 0.9 %. There is also some evidence (two specimens) of a decrease in stiffness from about 0.75 % strain.

For the third specimen, the gauge readings exhibited a linearly increasing difference throughout the test, perhaps due to misalignment of the two longitudinal gauges. Results for the first specimen were very unusual, whether in terms of load, displacement, stress or strain. The loading linearly increased then dramatically decreased and this happened a number of times. This phenomenon can also be seen in the strain against time plot yet, when stress is plotted against strain, the graph appears similar to the other tests.

The unusual results for the first specimen may be explained by specimen slippage. This was the first time the compression blocks were used and poor insertion of the specimen and insufficient tightening of the bolts on the compression block led to a significant amount of slack uptake during the test. The linearly increasing difference in the gauge readings of the third specimen may be due to misalignment of one of the strain gauges. It cannot be dismissed, however, that these anomalies are due to an inadequate test set-up.

(C) Stress Results

A typical graph of true stress against (the absolute value of) true strain is shown below in figure 5.10.

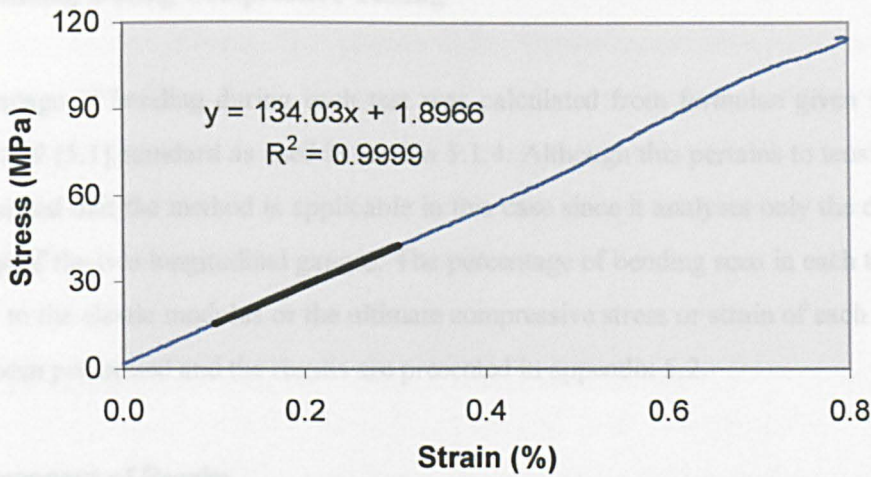


Fig 5.10: Stress v Strain During Compression Testing (Original Set-up)

It can be seen that the stress curve is highly linear even though the strain (against time) does not exhibit this linearity. This is because the loading, and thus the stress, as a function of time shows the same pattern as the strain and the consequence of this is a straight curve for stress against strain. Therefore, it is surely acceptable to describe the coupons as being elastic until failure. Nevertheless, the strain does appear to have a dependency on time, suggesting a cause such as viscoelastic effects.

Although a displacement-based strain was never necessary, as the gauges did not fail during the testing, such a strain was derived to investigate whether it would produce more linear results. However, both the strain against time plots and particularly the stress against strain plots always decreased in their linearity. This may be because any specimen slippage will be measured as an increased displacement whereas there will be no change or a decrease in the measured strain.

The gradient of each curve (the equation of the trend line as shown in figure 5.10) gives the compressive elastic modulus. Since there is no standard for this series of testing, and since the literature does not specify a strain range to calculate the modulus, the same range of 0.1 % to 0.3 % strain as used in the tensile testing was selected. The final value on the curve represents both the ultimate compressive (UC) stress and strain.

(D) Bending During Compressive Testing

The percentage of bending during each test was calculated from formulae given within the *ASTM D3039* [5.1] standard as used in section 5.1.4. Although this pertains to tensile testing, it was assumed that the method is applicable in this case since it analyses only the differences in readings of the two longitudinal gauges. The percentage of bending seen in each test can be correlated to the elastic modulus or the ultimate compressive stress or strain of each specimen. This has been performed and the results are presented in appendix 5.2.

(E) Summary of Results

Table 5.6 below lists the material properties derived from the results for all the specimens. Also shown are the cross sectional areas of each specimen and the percentage of bending for each test.

Material Property	Specimen					Mean	SD	CV(%)
	1	2	3	4	5			
Elastic Mod (<i>MPa</i>)	14779	13545	13403	12769	12730	13445	831	6.2
UC Stress (<i>MPa</i>)	116.9	130.9	115.0	123.2	128.4	123.5	7.9	6.4
UC Strain (%)	0.77	0.98	0.79	1.06	0.92	0.90	0.12	13.7
Bending (%)	35.1	9.5	17.1	3.0	3.2	-	-	-
Area (mm^2)	36.57	36.04	35.25	35.40	34.68	35.59	0.73	2.1

Table 5.6: Results of Compressive Coupon Tests

Referring to appendix 5.2, there is no conclusive evidence of a relationship between bending and the elastic modulus or the ultimate compressive stress or strain. The closest correlation is between bending and the elastic modulus but the relationship, if it existed, would suggest that the measured modulus increases as the bending increases. Such a relationship seems fairly unlikely. Bending may have no effect on the material's properties due to the inadequacies in the method of how it is calculated that have previously been described. However, the magnitude of bending in two or three of the tests is cause for concern. It could be that the test set-up was causing bending (though there may have been other reasons such as the specimens' lack of straightness). The upper compression block was not fixed to the upper cross-head of the test machine or connected to a die set, as used by Imperial College. The weight of the block, therefore, may have bent the specimens before the test commenced causing the specimen to be out of alignment in the plane of loading.

Results for the ultimate compressive stress show acceptable variation given that they are dependant on a fracture process. The variation in the ultimate compressive strain seems a little high and it is believed that this is due to a number of competing failure mechanisms being present within the specimen. A coefficient of variation of six percent for the elastic modulus values may be a little high. The variation in values may arise from a poor set-up generating errors, such as bending that varies from specimen to specimen.

Compressive Testing Using Modified Set-up

5.2.5 Introduction to Compressive Coupon Testing with Modified Set-up

It was noted in section 5.2.4 that bending and specimen slippage might be a concern due to the test set-up. This concern arises mainly from the magnitudes of bending in some of the tests and the anomalies and lack of linearity seen in test results. Therefore, an attempt was made to improve the set-up and this was done by tightening the specimen within the compression block and fixing the upper block to the upper cross-head of the test machine. This latter modification could be achieved quite simply by using a couple of clamping plates and screwed rod that utilised the existing hole in the upper cross-head. An illustration of these components can be found in figure 5.11 below.

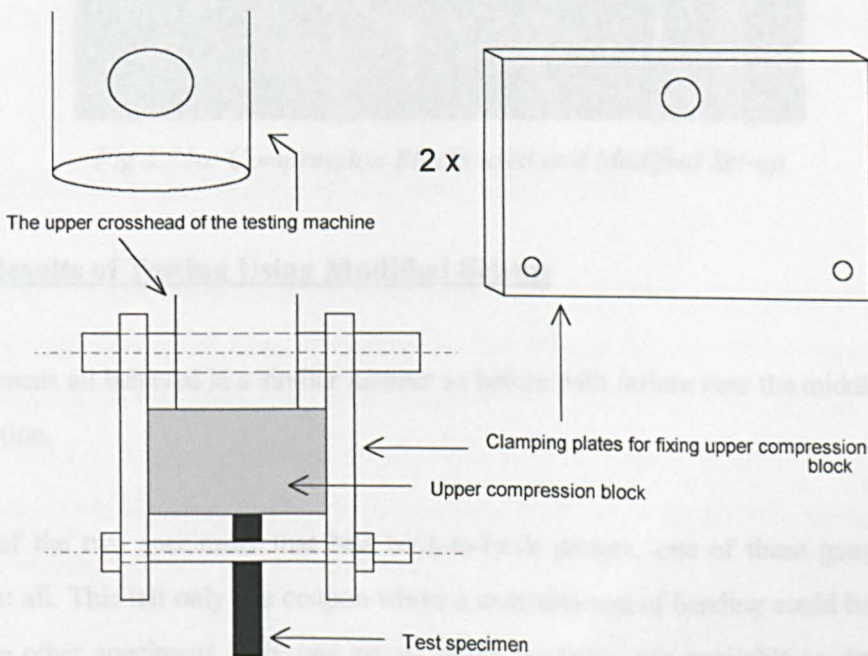


Fig 5.11: Drawing of Components Used to Modify Test Set-Up (Illustration by Auren [5.2])

These components were designed and the drawings given to the university technicians for manufacturing. Once produced, a new batch of tests was performed.

5.2.6 Equipment and Procedure Used During Testing

Six specimens were tested this time, which were cut and prepared from a new plaque. However, due to a shortage of strain gauges, only two of the specimens had back-to-back gauges. Apart from the modifications, the same equipment and procedure were used as with the original set-up. Figure 5.11a below shows the compression blocks used and the modified set-up.

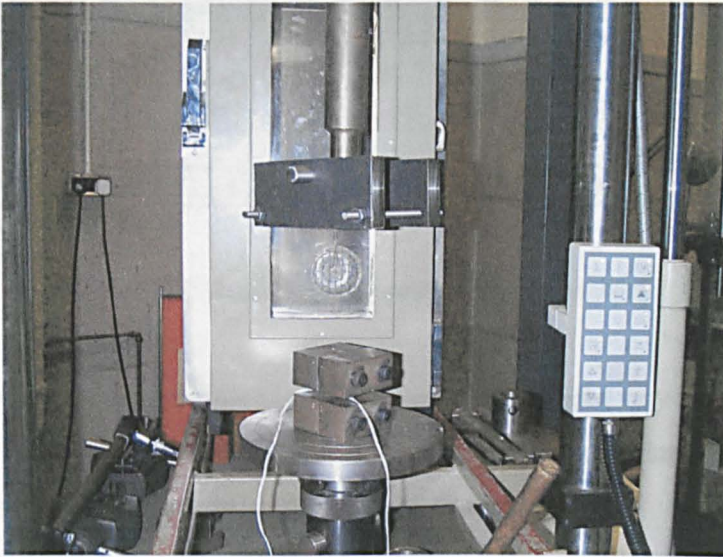


Fig 5.11a: Compression Blocks used and Modified Set-up

5.2.7 Results of Testing Using Modified Set-up

The specimens all behaved in a similar manner as before with failure near the middle of the gauge section.

For one of the two specimens that had back-to-back gauges, one of these gauges did not function at all. This left only one coupon where a measurement of bending could be made and, for all the other specimens, only one set of gauge readings was available to determine the strain.

The strain-time history results were similar to the previous batch of tests. For the first specimen, a small spike in its stress against strain curve (at 0.4 % strain) can be seen after which there is a decrease in linearity. The second specimen exhibits a similar phenomenon early on (at 0.05 % strain) although the response after this is highly linear.

The same range of 0.1 % to 0.3 % strain was used to calculate the modulus. The percentage of bending was calculated for the fifth specimen, which was the only coupon with working back-to-back gauges. Table 5.7 lists the material properties derived from the results for testing using the modified set-up.

Material Property	Specimen						Mean	SD	CV(%)
	1	2	3	4	5	6			
Elastic Mod (<i>MPa</i>)	18288	15661	17668	10264	17917	17705	17448*	1029	5.9
UC Stress (<i>MPa</i>)	131.9	119.4	125.9	101.7	116.9	123.8	123.6*	5.9	4.7
UC Strain (%)	0.72	0.76	0.66	1.09	0.55	0.71	0.68*	0.08	11.9
Bending (%)	-	-	-	-	26	-	-	-	-
Area	47.63	43.34	44.27	48.38	48.26	44.90	46.13	2.15	4.7

*Values do not include test 4

UC=Ultimate Compressive

Table 5.7: Results of Compressive Coupon Tests

It can be seen in the above table that the fourth specimen produced very atypical results. It is not known why this should be; there was nothing unusual noticed during the test. Results for this specimen have not been included in the statistical values.

5.2.8 Comparison of the Testing Set-ups and Results

The variation in results was about the same within each test set-up but results from the two set-ups are very different in terms of the elastic modulus and the ultimate compressive strain. Such differences are not easy to explain although it is known (see section 2.4) that variation in modulus values is common between many forms of compression testing. Thus, composite materials are often highly sensitivity to test parameters. Comparing the two set-ups, only the ultimate compressive stress seems unaffected.

Certainly, the thickness of the test specimens is greater for the modified set-up (about 33% higher). Thicker specimens could lead to higher bending strains since the distance from the neutral axis to the outer surface is greater. In the one test where bending could be quantified, it was found to be relatively high.

The modifications to the test set-up appear to have failed in improving the test results. The results are no more linear than for the original set-up and there are still a number of anomalies present. In fact, it was found that, when the upper compression block was fixed to the upper cross-head of the test machine, inserting the specimen was more difficult. This may have induced poor alignment.

It must be concluded that the compressive test set-up is not yet satisfactory. In fact, the modification to the rig may have contributed in producing poorer results. While all of the results are by no means worthless, their sensitivity to test parameters does limit their accuracy. Compression testing of composites is notoriously problematic and the high variation in results is not unexpected.

It is assumed that the results from the first test set-up are more reliable and this is for three reasons. The specimens were thinner which may reduce bending; more information is known about the specimens' strain and bending (since back-to-back gauges were used for all the coupons); the modifications to the test set-up produced no apparent benefit and may even have been detrimental to the accuracy of results. Therefore, the results from the first test set-up are taken to be the properties of the material.

5.3 SHEAR COUPON TESTING

5.3.1 Introduction to Shear Coupon Testing

In-plane shear testing was carried out in accordance with the standard *ASTM D3518/D3518M-94* [5.3]. The test is a uniaxial tensile test using material with a $\pm 45^\circ$ fibre orientation and this method was discussed briefly in section 2.4. It was noted in that section that there are often difficulties with the method in determining the shear strength. This was found to be true for the testing performed and so another type of shear test was also carried out. This was the Iosipescu shear test that was also discussed in section 2.4. The testing using each method is presented separately and then their results compared.

Shear Testing - Method 1 ($\pm 45^\circ$ Tensile Testing)

5.3.2 Equipment and Procedure Used During Testing Using $\pm 45^\circ$ Tensile Test

All equipment, materials and procedures were the same as used for the tensile testing with two exceptions. The plates, again supplied by Nottingham University, that were used to make up the specimens had a fibre orientation of $\pm 45^\circ$. Also, two of the specimens were tested at higher rates of cross-head displacement to investigate the influence of strain rate on load response. Specimen four was tested at 6 mm/min and specimen five was tested at 20 mm/min. All other specimens were tested at a rate of 2 mm/min.

The standard specifies how the in-plane shear stress, τ_{12} , and shear strain, γ_{12} , should be calculated. The equations given in the standard are represented below as equations 5.1 and 5.2 respectively.

$$\tau_{12} = \frac{P}{2A} \quad \text{Eq (5.1)}$$

$$\gamma_{12} = \varepsilon_x - \varepsilon_y \quad \text{Eq (5.2)}$$

where P is the measured load, A is the cross-sectional area of the coupon and ε_x and ε_y are the measured longitudinal and transverse strains respectively.

5.3.3 Results of Shear Testing (Method 1)

(A) Failure Modes

The specimens' behaviour during the testing was very different to that seen during the other forms of coupon tests. There was substantial elongation of the coupons with a corresponding highly reduced cross-section. In latter stages of the tests, there was significant delamination at the free edges of the coupons. There was no ultimate fracture in any of the specimens.

(B) Stress and Strain Results

When there was premature failure of strain gauges the method of calibrated displacement-based strain, as described in section 5.1.4, was used. A typical graph of shear stress against shear strain is given below in figure 5.12. Also shown are the shear modulus and two values for the shear strength. As per the standard, the shear modulus was calculated over the 0.2 to 0.6 % range of strain. Since ultimate failure did not occur within 5 % strain then the value at 5 % was taken to be the shear strength. An alternative method within the standard is to determine an offset shear strength in a similar manner to calculating a proof stress and, for this method, a 0.2 % offset strain is recommended. Both methods were used to calculate shear strength since the values that they give are very different.

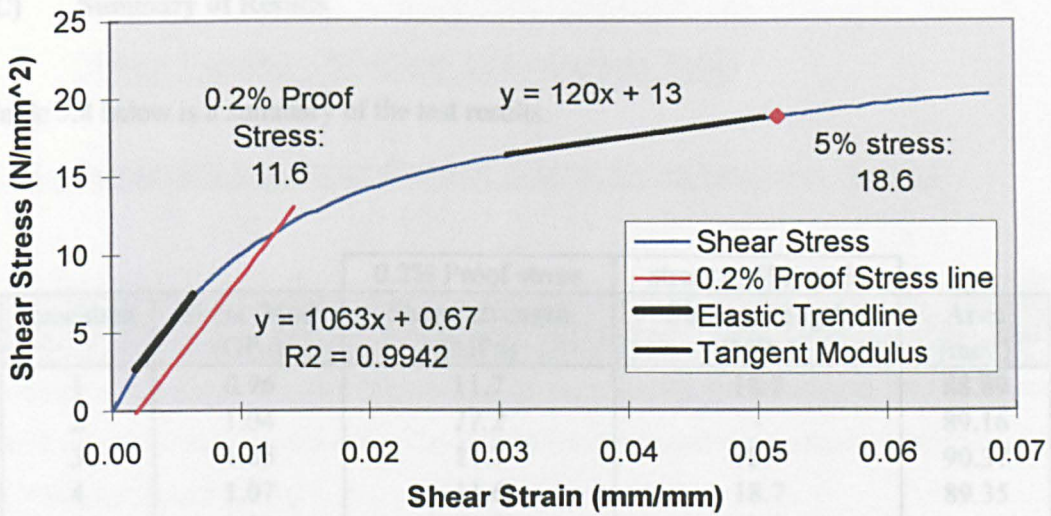


Fig 5.12: Plot of Shear Stress v Shear Strain During $\pm 45^\circ$ Tensile Test

The stress-strain curves are characterised by their non-linearity and by the very large strains involved. Shear properties are relatively low: a mean shear modulus of 1.05 GPa is only about 10 % higher than the shear modulus of the matrix material (refer to appendix 1.4). It seems likely that the composite's shear behaviour is dominated by the matrix properties with little reinforcement provided by the fibres in this mode.

Figure 5.12 includes, along with the initial shear modulus, a trend line showing a typical gradient of the curve in a latter stage of the testing. It can be seen that the behaviour of the coupon rapidly deviates from the initial modulus and decreases until it is in the region of 10 % of the shear modulus. It is believed that the behaviour at this stage is mainly due to viscoelastic yielding which is more severe during shear testing because of the dominance of the matrix in shear behaviour. It can be hypothesised that, if viscoelastic yielding was removed, the high degree of straining would be removed. Yet the specimen would still not experience ultimate failure. The non-linear response may also be due to geometrical factors such as a rearrangement of the fibres within the matrix. There may even be a material/structure interaction. Whatever the reason, this type of shear behaviour is not uncommon and was described in section 2.4.3.

(C) Summary of Results

Table 5.8 below is a summary of the test results.

Specimen	Shear Mod (GPa)	0.2% Proof stress	stress at 5% strain	Area (mm ²)
		Shear strength (MPa)	Shear strength (MPa)	
1	<i>0.96</i>	11.7	18.7	88.89
2	1.04	<i>11.2</i>	-	89.16
3	1.05	11.7	18.7	90.37
4	1.07	11.6	18.7	89.35
5	1.03	11.8	19.2	89.10
Mean	1.05	11.7	18.8	89.40
Stan Dev	0.02	0.08	0.25	0.58
CV (%)	1.63	0.70	1.33	0.65

values in italics not included in statistical calculations

Table 5.8: Results of Shear Testing ($\pm 45^\circ$ Tensile Test)

There was a discontinuity in the load trace of the first specimen perhaps due to slippage in the grips of the test machine or some other similar phenomenon. This led to an artificially low shear modulus and so this value was not included in the calculation of the sample mean or variation. The second specimen behaved in an atypical manner after the initial elastic response and this is attributed to the poor quality of this specimen. There was also premature failure of a strain gauge. For these reasons, the specimen was not included in either calculation of mean strength although it was included for determining the mean modulus.

The two methods of calculating the shear strength gave very different results. At which point the specimens can be said to have failed is a somewhat subjective matter. It was known from the literature (see section 2.4) that there is concern that off-axis testing may underestimate the shear strength. However, it was not known beforehand that the shear strength would be difficult to quantify. Therefore, it was deemed necessary to carry out further shear tests.

While there is some evidence that higher strain rates may lead to a higher initial strain and a higher strength, there is insufficient data to be conclusive. In fact, it is assumed that the strain rate up to the highest magnitude used (the limit of the testing machine) had little influence on response and so all specimens were included in determining sample means and variations.

Shear Testing - Method 2 (Iosipescu Test)

5.3.4 Introduction to Shear Coupon Testing Using Iosipescu Method

It has been noted that the previous form of shear testing seemed unsatisfactory for determining the shear strength of the material. It was therefore decided to carry out further testing and the Iosipescu method was chosen. This method of shear testing was discussed briefly in section 2.4. It was noted in that section that the method has developed into a standard, which is *ASTM D5379/D5379M-93* [2.67].

Figure 5.13 below is an illustration of the Iosipescu test rig.

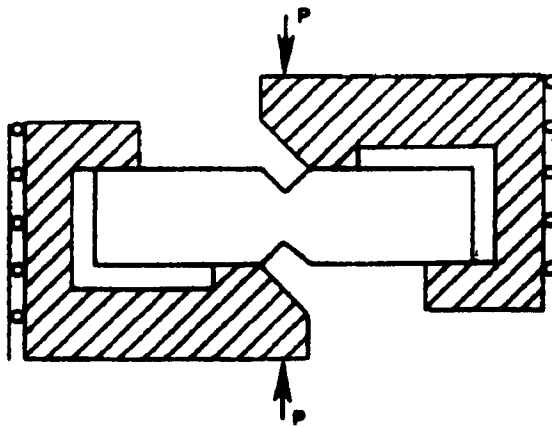


Fig 5.13: Illustration of Iosipescu Test Rig

The Iosipescu method utilises two force couples that produce two counteracting moments in such a way that the moment at the mid-section is zero while the shear force is constant and equal to the applied load due to the inclusion of two 90° notches on each edge of the specimen. This is illustrated in figure 5.14 below. Exact force distributions and the dimensions a and b in figure 5.14 cannot be directly determined for the test fixture but they are not required.

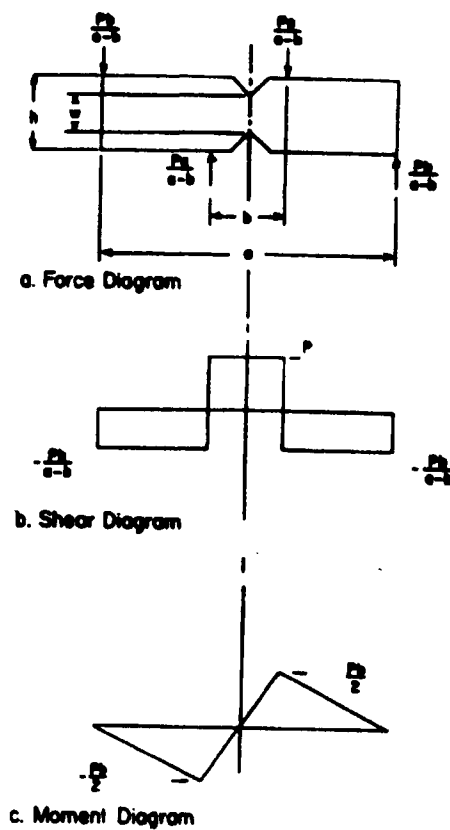


Fig 5.14: Forces and Moments During Iosipescu Shear Testing

5.3.5 Equipment Used During Testing

The testing machine used was the Zwick REL 2061 that was also used for the compression testing and details can be found in section 5.2.2. The cross-head rate was 2 mm/min.

A special test fixture was used in conjunction with the testing machine. A drawing of the test fixture was procured from the American Society for Testing and Materials (ASTM) and the fixture produced by university technicians. One half of the fixture displaces vertically down a bearing post when under loading and this creates shear stresses in the gauge section of the specimen.

Specimens were cut from the composite plates. The standard advocates that at least five specimens be tested and it gives recommendations for the specimen geometry, which are shown below in figure 5.15.

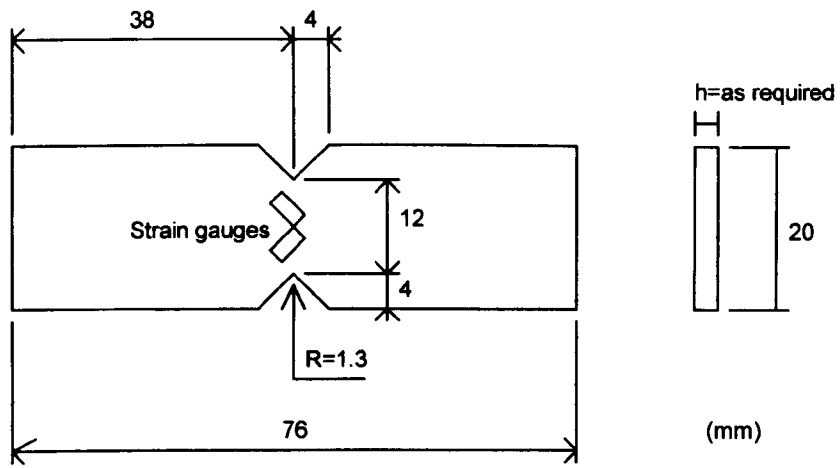


Fig 5.15: Specimen Geometry During Shear Testing Using Iosipescu Method

Strain gauges were bonded to the specimens in such a way that they were at an angle of 45° to the loading direction. The short burst data logger was again used. Tabs were bonded to each end and to each side of the specimen.

5.3.6 Testing Procedure

The specimen was placed in the test fixture and carefully aligned so that the loading was in the centre of the gauge section. The testing machine then applied load to the fixture. Results were recorded in terms of load, displacement and the two sets of strain.

The shear strain, γ , is equal to the sum of the absolute values of the two strain gauges (ϵ_1 and ϵ_2) as shown in equation 5.3 below.

$$\gamma = |\epsilon_1| + |\epsilon_2| \quad \text{Eq (5.3)}$$

Since the test arrangement entails that the shear force in the gauge section of the specimen is equal to the applied load, the shear stress, τ , is simply the applied load, P , divided by the cross-sectional area of the gauge section, A_{gauge} . This is shown below in equation 5.4.

$$\tau = \frac{P}{A_{gauge}} \quad \text{Eq (5.4)}$$

During the first test, after considerable deflection, the specimen made contact with the test fixture and the test had to be terminated. The standard recognises that this is a common problem for a number of materials and 0/90° lay-ups are mentioned specifically. In these cases the failure stress should be taken as the offset stress or the stress at 5 % strain as with the $\pm 45^\circ$ tensile testing. Although 5 % strain had easily been reached, it was considered desirable to test the specimens until ultimate failure. To that end, the fixture was modified by incorporating a couple of plates between the fixture and the specimen to extend the allowable deflection of the specimen. However, even with this modification, there was no ultimate failure of the specimen in subsequent tests.

5.3.7 Results of Shear Testing (Method 2)

(A) Failure Modes

Although there was no ultimate failure of the specimens, the fibres within the notched section were highly deformed though they remained parallel. The standard describes this as an acceptable failure mode.

(B) Strain Results

A number of the strain gauges failed during the tests. One of the gauges failed during the first and the fifth test and the shear strain had to be calculated using twice the absolute value of the remaining gauge's measurements. No strain data could be derived for the second test where both gauges failed. Figure 5.16 below shows the strain against time (data logger steps) for one of the two tests where both gauges remained functional.

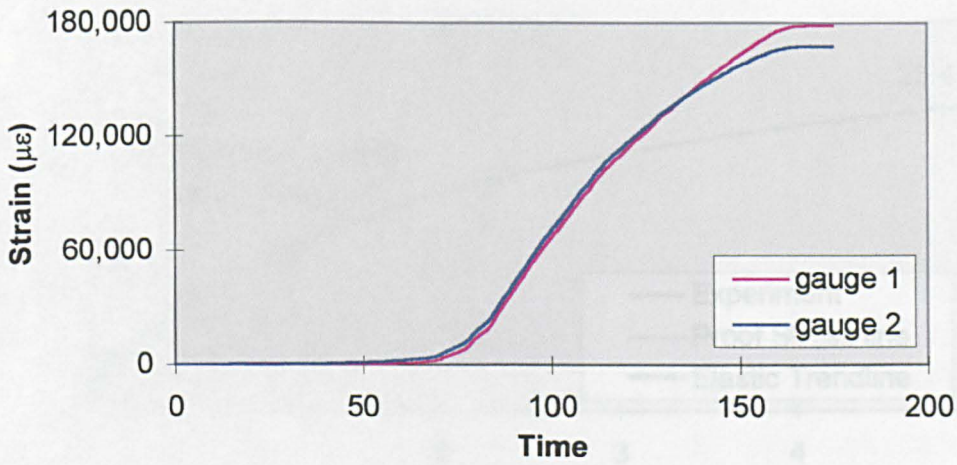


Fig 5.16: Strain v Time During Testing using Iosipescu Method

Once again, the strain of the material seems to show a time dependency. The readings of the strain gauges are in good agreement at least up until the latter stages of the tests. This period easily encompasses the range of most interest: up to and beyond 5 % strain. However, the small number of functioning gauges decreases confidence in test results.

(C) Stress Results

Figure 5.17 is a typical plot of the shear stress against the shear strain only up to 5 % strain. The full range of results (which exhibits the same typical behaviour) is in excess of 30 % strain. Noted in the figure below is the elastic trend line used to calculate the modulus over a strain range of 0.1 to 0.6 % strain. Also shown are the 0.2 % proof stress line and the value at 5 % strain.

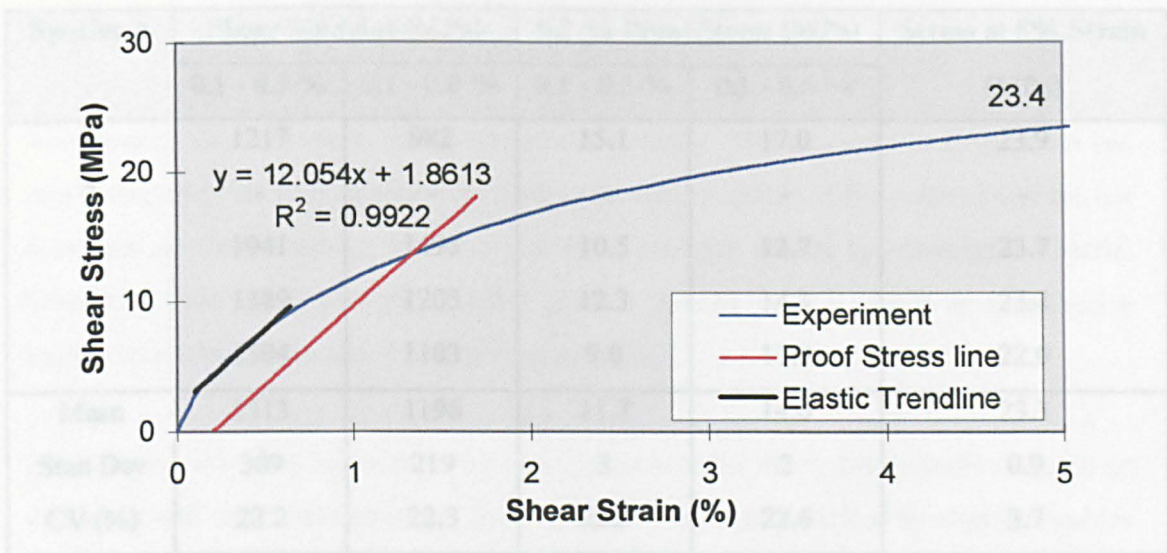


Fig 5.17: Shear Stress v Shear Strain During Testing Using Iosipescu Method

The standard recommends that a range of 0.1 to 0.6 % strain be used for materials that fail at a strain greater than 1.2 %. However, even within this early strain range, the material is behaving quite non-linearly. It would be desirable to use a smaller range to produce a more accurate elastic modulus and the next range the standard recommends is from 0.1 to 0.3 % strain for materials that fail between 0.6 and 1.2 % strain. Both ranges were used to calculate the elastic modulus.

As with the previous shear testing, there are two possible ways to determine the shear strength: a proof stress line or the stress at 5 % strain. Both methods were employed; a value of 0.2 % offset strain was used for the proof stress line.

(D) Summary of Results

Table 5.9 below lists the results of the testing and includes statistical derivations of these results.

Specimen	Shear Modulus (MPa)		0.2 % Proof Stress (MPa)		Stress at 5% Strain (MPa)
	0.1 - 0.3 %	0.1 - 0.6 %	0.1 - 0.3 %	0.1 - 0.6 %	
1	1217	982	15.1	17.0	23.9
2	-	-	-	-	-
3	1941	1495	10.5	12.7	23.7
4	1389	1205	12.3	14.3	23.4
5	1504	1103	9.0	11.9	22.0
Mean	1513	1196	11.7	14.0	23.3
Stan Dev	309	219	3	2	0.9
CV (%)	22.2	22.3	22.5	22.6	3.7

Table 5.9: Results of Testing Using Iosipescu Method

Plots of shear stress against shear strain exhibit a gradual non-linearity throughout the test. This causes the shear modulus to be generally inconsistent and highly dependent on the strain range used for the calculation. It also affects the consistency of the shear strength using an offset stress, as this strength value is dependent on the shear modulus. Both properties show excessive variation in their values. The situation is not improved by the fact that both strain gauges remained functional in only two of the tests.

The main purpose of carrying out the Iosipescu testing was to determine the value of stress that best represents the shear strength of the material. Clearly, it has not provided that solution. Yet a value for the shear strength must still be assigned in any Finite Element Analyses, at least when the softwares' predefined failure criteria are used. There are two arguments concerning this point. Looking at results as a whole, 5 % strain does seem to represent a point on the curve when the non-linearity is clear but not too advanced. However, this is considering a strain range much larger than experienced by the beam. Even 5 % is probably more than the shear strains for the beam during impact. Yet the strain at 5 % will also include viscoelastic yielding. The values of strain measured (over 30 %) are probably dominated by the viscoelastic yielding of the material that would not occur in an impact event.

5.3.8 Comparison of Both Forms of Shear Testing

Non-linearity can be seen in both types of shear testing. The similarity in form of the test results suggests that they represent the true static shear response of the material and are not dependent on the test set-up. The non-linearity is probably caused by viscoelastic material behaviour, which is considerably greater in shear loading than in tensile or compressive loading due to the dominance of the matrix properties.

Shear failure, therefore, seems to be a gradual process rather than a linear elastic response up until some well defined failure stress. Such a response has been described by other researchers (see section 2.4). With this in mind, it seems almost inappropriate to define a particular value of shear strength and yet one is required in the Finite Element Analysis of the material.

The $\pm 45^\circ$ tensile test does at least have a better defined elastic region. This makes it easier to specify an elastic modulus with low variation between tests. Therefore, this form of testing is used to specify the value of the elastic modulus.

Both forms of testing are in rough agreement for the shear strength based on an offset stress. The Iosipescu method produces higher (by about 25 %) values of shear strength at 5 % strain. This may be because the strain rate was higher and viscoelastic yielding less during the Iosipescu testing. Generally, in both tests, a cross-head rate of 2 mm/min was used but the strain rate for the Iosipescu specimen will have been significantly higher due to the smaller specimen geometry. Since higher values are generally favourable, the Iosipescu method could be used to specify the shear strength when the value at 5 % is used. However, no decision about which method should be used is made at this point.

5.4 FLEXURAL COUPON TESTING

5.4.1 Introduction to Flexural Coupon Testing

Flexural testing does not determine any new material properties. Flexural behaviour is a combination of the tensile and compressive response of the material. However, the testing can be used to evaluate the bending response of the material and identify dominant failure mechanisms. It can also be used to confirm the results from the tensile and compressive coupon tests.

The standard used for the flexural testing of coupons was *ASTM D790-96a* [2.68], which offers two methods for calculating the flexural modulus and strength: three- and four-point tests. The three-point test involves loading at mid-span of the specimen. For the four-point testing, the two loading noses are equally spaced from their adjacent supports with twice the distance between them (therefore, the load span is the support span divided by two). Testing is to be performed until breakage occurs in the outer fibres or until 5 % strain is reached. A minimum of five specimens should be tested. Strain and deflection data can be derived from either a strain gauge at mid-span of the specimen or using the cross-head displacement.

5.4.2 Equipment Used During Testing

The testing machine used was a Zwick REL 2061 and details of the machine were given in section 6.11. The testing machine measured the load and cross-head displacement during the tests and these parameters were used to derive deflection, stress and strain values. A graphical plotter was connected to the testing machine and so the applied load against specimen deflection could be seen during each test.

The four-point bending test was selected as this provides a constant bending moment between the loading noses. The standard gives recommendations on the dimensions of the specimens and on load and support spans according to the thickness of the specimens. The closest thickness listed in the standard is 3.2 mm. This entailed other specimen dimensions of 127 mm length and 25 mm width. The support span was 102 mm and the load span 51 mm (102/2).

A test fixture was available that could be modified to meet requirements. The fixture consists of a top and a bottom part that provide the loading and support respectively. The radii of the noses were 5 mm. Figure 5.16 below is a photograph of the test fixture.

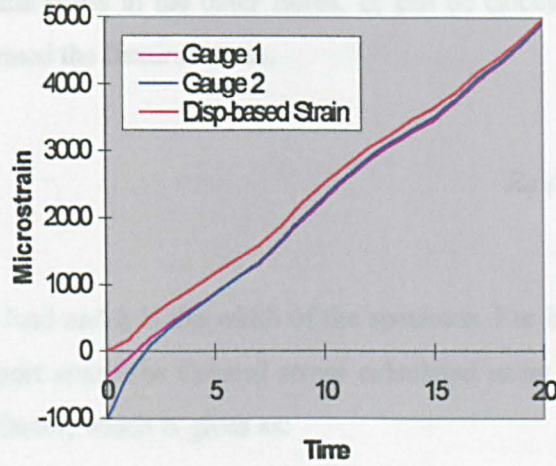


Fig 5.16: Test Fixture Used During Flexure Testing

5.4.3 Testing Procedure

The coupons were cut from plates and final dimensions of the thickness and width were checked at three points. Testing was carried out at a cross-head rate of 5 mm/min. Five specimens were tested.

It was found during the first test that the deflecting specimen eventually made contact with the part of the fixture that held the loading nose. This was avoided in subsequent tests by supporting the nose within the fixture at a higher point.

The standard provides equations to calculate the values of a number of parameters. The strain at the outer fibres, ϵ , is related to the mid-span deflection, δ_{mid} , the specimen's thickness, t , and the support length, L , as follows:

$$\epsilon = \frac{4.35 \cdot \delta_{mid} \cdot t}{L^2} \quad Eq (5.5)$$

The strain evaluated using equation 5.5 is termed the flexural strain. No relationship is given to calculate the flexural strain using the cross-head displacement. However it can be shown that the mid-span deflection is simply equal to the cross-head displacement multiplied by a factor of 1.375. Further details of this are provided in appendix 5.3.

For small deflections, the stress in the outer fibres, σ , can be calculated using equation 5.6 below. This stress is termed the flexural stress.

$$\sigma = \frac{3PL}{4bt^2} \quad \text{Eq (5.6)}$$

where P is the applied load and b is the width of the specimen. For large deflections (greater than 10 % of the support span) the flexural stress calculated using equation 5.6 should be subject to a correction factor, which is given as:

$$\left[1 - \frac{10.91\delta \cdot t}{L^2} \right]$$

The flexural strength of the material is taken to be the maximum value obtained from equation 5.6, which is then multiplied by the correction factor.

The flexural modulus, E , is calculated using a portion of the gradient of the curve of load against deflection, m . This is shown in equation 5.7 below. The standard does not specify a deflection range to use other than that it should be the initial straight-line portion of the curve.

$$E = \frac{0.17 \cdot L^3 m}{bt^3} \quad \text{Eq (5.7)}$$

5.4.4 Results of Flexural Testing

(A) Test Behaviour

Figure 5.17 below is a graph of the flexural stress against the flexural strain. Both the stresses for small deflections and for large deflections (using the correction factor) are shown. A plot of the load against deflection would have the same appearance.

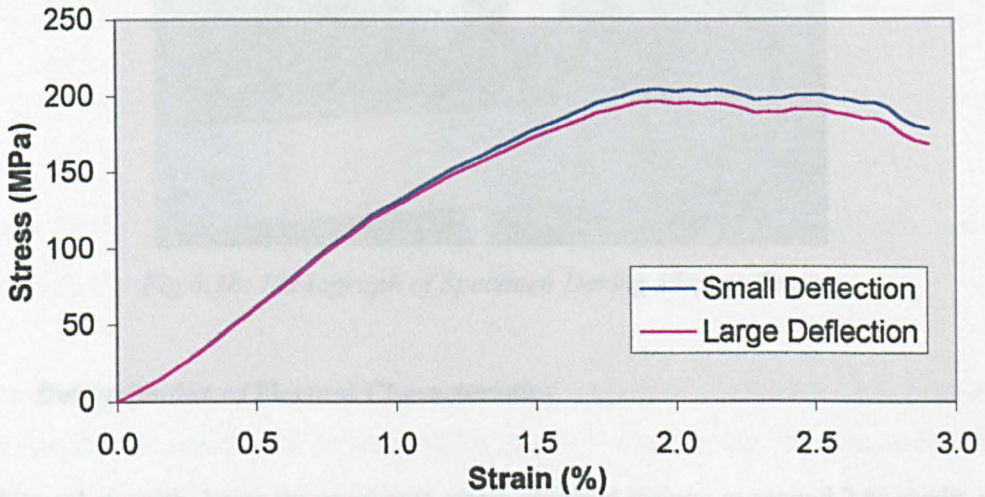


Fig 5.17: Flexural Stress v Flexural Strain

As the testing machine was connected to a graphical plotter, specimen behaviour could be identified with the loading (against deflection) response. The specimen behaved elastically up until a load of about 0.45 kN, after which cracking could be heard and there was a change in the specimen's stiffness. Such a load represents a stress of around 120 MPa and it can be hypothesised that compressive failure occurred on the top face of the coupon. This can often reduce the effective cross-section of the specimen and cause bending stresses to increase. However, the specimen was able to sustain substantial increases in the loading. This may be because a compressive crack, while reducing the flexural stiffness, would tend to be held closed by flexural loading and crack propagation would be inhibited.

Table 5.10 below shows the results of all the tests. Also shown is the width and thickness of

The maximum stress is reached at a load of about 0.75 kN or a stress of 200 MPa. By this point the gradient of the loading or stress suggests a stiffness of around 0.4 of its original value. There was no catastrophic failure of the specimens. Inspection after testing reveals only

minor damage on the compressive face at the point of loading. Thus, it is assumed that the stresses in the material did not reach values where tensile failure would occur. Figure 5.18 shows a specimen at an advanced stage of bending.



Fig 5.18: Photograph of Specimen During Flexure Testing

(B) Determination of Flexural Characteristics

The flexural strength, being the maximum stress obtained, occurs at around 2 % strain, which represents a deflection of around 10 mm. Such a value is approximately 10 % of the support span (of 102 mm) and so it is appropriate to use the large deflection stress to determine the flexural strength.

It was considered important, to achieve consistency, that the same deflection range be used in each test for calculating the flexural modulus even though each test varied slightly in which range was the most linear. A deflection range of 1.3 - 4 mm was used as these minima and maxima are the most extreme values that still represent linear regions in all of the tests.

(C) Summary of Results

Table 5.10 below lists the results of all the tests. Also shown is the width and thickness of each specimen and statistical values based on the results.

Specimen	Width (mm)	Thickness (mm)	Flexural Modulus (MPa)	Flexural Strength (MPa)
1	24.99	3.44	14870	215.1
2	25.14	3.45	14863	210.7
3	25.10	3.40	14223	196.2
4	25.15	3.43	14292	202.9
5	25.09	3.42	15261	203.4
Mean	25.09	3.43	14702	204.3
Stan Dev	0.06	0.02	598.2	5.72
CV (%)	0.25	0.56	4.2	2.9

Table 5.10: Results Obtained During Flexure Testing

Variation in the results is low which suggests flexural tests are highly repeatable and gives considerable confidence in the results.

The flexural testing allows comparison with properties obtained from other types of tests such as the (tensile or compressive) elastic modulus and, to a lesser extent, the compressive failure stress. An evaluation of bending performance is also possible. It would seem likely that any structure made from this material and lay-up would fail in a compressive mode although the structure may be able to sustain considerably more loading.

5.5 COMPARISON OF RESULTS OF ALL COUPON TESTS

The material properties derived from all of the coupon testing that has been presented are listed again in table 5.11 below. They are compared, where possible, with those already obtained within the SACTAC project. Also shown is the percentage difference between the two sets of results.

Property	Units	Testing	SACTAC	Difference (%)
Tensile Modulus	GPa	14.8	13.6	8.1
UT Strength	MPa	318	315	0.9
UT strain	%	2.66	-	-
Poisson's Ratio	-	0.08	0.08	0.0
Compressive Modulus	GPa	13.4	-	-
UC Strength	MPa	123.5	125	1.2
UC Strain	%	0.90	-	-
Shear Modulus	GPa	1.05	1.2	6.7
Shear Strength (Offset)	MPa	11.7	-	-
Shear Strength (5 %)	MPa	23.3	22.5	3.4
Flexural Modulus	GPa	14.7	13	11.6
Flexural Strength	MPa	204	280	37.3

Table 5.11: Material Properties Obtained from Coupon Testing

In general, there is good agreement between both sets of results. This gives greater confidence when the properties are used in models of the composite beam. The tensile modulus obtained by SACTAC is noticeably less than tensile test results and more similar to compressive test results.

Almost surprisingly, it is strength values that show the best agreement in all of the tests except for the flexural testing. It has been noted in the literature that 3- or 4-point flexural testing, and tests at different spans, can lead to different values of the flexural strength (though not the modulus).

Test results for the flexural modulus and the tensile modulus show an almost exact correlation (despite the fact that the SACTAC tensile modulus is closer in value to the compressive modulus from test results). During flexure, the specimens began to decrease in stiffness at around 120 MPa, which is approximately the value of the compressive strength.

It is not known which method was used to determine the SACTAC shear strength but, given its magnitude, it is assumed to be the stress at 5 %. This is an argument for using the 5 % strain value though it is possible that a manufacturer would favour quoting the higher value.

Both sets of results indicate that the compressive modulus and strength are considerably lower than tensile values. This confirms that the material is considerably weaker in compression. There is good agreement for shear properties: values are in the order of 10 % of other properties. This confirms that the material is indeed weak in shear.

SUMMARY OF CHAPTER

A series of coupon testing has been performed to determine the mechanical properties of the composite material.

Tensile properties have been ascertained and an important part of the beam has been investigated when in tension. It is believed that reasonable measurements of the compressive properties of the material have been obtained despite the fact that the test set-up is not yet satisfactory. Two forms of shear testing have been performed but the shear strength of the material remains difficult to quantify. Flexure testing provided a comparison of certain properties obtained from other coupon tests as well as information on the material's failure in bending.

Comparisons of test results with SACTAC values give greater confidence in the results given their close agreement. The composite material has been found to be particularly weak when loaded in compression or shear.

CHAPTER SIX

EXPERIMENTAL TESTING OF COMPOSITE BEAMS

Experimental testing of the thermoplastic composite beams has been carried out to understand their behaviour under static and impact loading. Test results provide a means to validate the predictions of beam models. Both static and impact tests have been carried out and these tests are presented in this chapter. Figure 6.1 is a block diagram of the structure of the chapter and includes the section numbers used in this thesis.

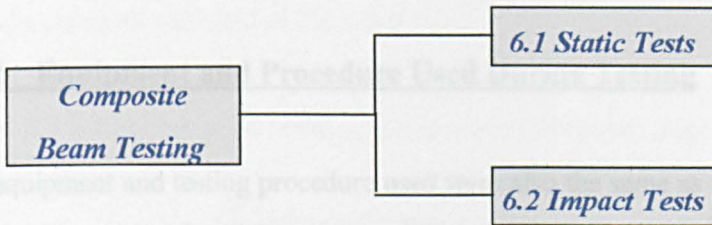


Fig 6.1: Block Diagram of Structure of Chapter

Static testing of beams has determined their behaviour in terms of load, deflection and energy absorption. Failure modes are identified, including delamination between the two layers of the top flange with different material orientation. Collapse values are well defined although there is significant variation between beams. The beams can carry substantial loading after collapse and their energy absorption is relatively unaffected by the collapse of the beams.

During impact testing, all of the beams behave in a similar manner up until collapse, after which there is considerable variation in their response. There are strong load fluctuations in the test results, which obscure the exact values at collapse. Because of the limited impact energy to be absorbed, the beam behaves in a predominately elastic manner. There is significant delamination at the top flange as well as some compressive and shear failure.

(A) Failure Modes
Comparison of static and impact behaviour suggests that there are important differences. The impacted beam appears to behave elastically for longer before failure. Failure modes seen in static tests are less dominant during impact conditions.

6.1 STATIC TESTING OF BEAMS

6.1.1 Introduction to Static Testing of Beams

The composite side impact beams were statically tested using the same three point bending test that was used for the steel beams and was presented in chapter three. All dimensions for the striker and supports and the distance between the supports were as before.

6.1.2 Equipment and Procedure Used During Testing

The equipment and testing procedure used were also the same as those used for the steel beam and details can be found in sections 3.7 and 3.8. Three composite beams were tested and figure 6.2 is a photograph of a beam prior to the testing.



Fig 6.2: Composite Beam Prior to Static Testing

6.1.3 Results of Static Testing

(A) Failure Modes

As the loading increased, each beam appeared to behave elastically. At an intermediate stage of the testing, a change was apparent as the beam became more v-shaped. The trace of load against deflection from the plotter also displayed a sharp fall in the load. The impactor

obscured the top flange of the beam and it wasn't until cracks formed in the side wall of the beam that damage was visible. These cracks were angled at approximately $\pm 45^\circ$ in the vertical plane.

Visible inspection of the beams after each test confirmed the side wall cracks and also revealed two other forms of damage. There was compressive failure of the top flange of the beam at mid-span extending across the whole width, into the corner fillets and meeting the side wall cracks. There was also delamination failure between the two layers of the top flange that have different material lay-ups. This delamination typically extended about 50 mm from the mid-span towards each end of the beam.

Figure 6.3 below shows the composite beam at an advanced stage of the static testing.

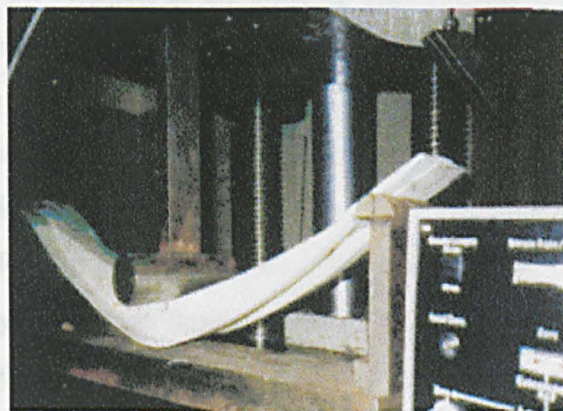


Fig 6.3: Composite Beam at Advanced Stage of Static Testing

(B) Loading Behaviour

Figure 6.4 below shows the results of the tests on the beams in terms of load against the deflection at mid-span. It can be seen that for each of the beams the load rises to some peak value at which point the load suddenly drops and continues to fall (at a more gradual rate) throughout the remainder of the test. This peak value is taken to be the initial failure, or collapse load, of the beam.

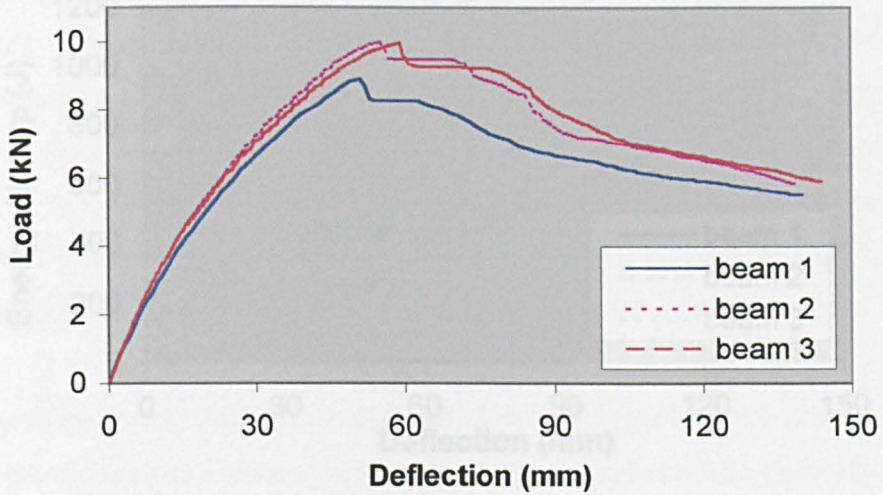


Fig 6.4: Load v Deflection for Beams During Static Testing

Figure 6.4 shows that the response of the beam up until collapse is not entirely elastic. The response is non-linear which may be accounted for by a number of factors. The beam's cross-section varies along its length, which may affect its elastic bending response. It is also possible that, given that the testing is static, viscoelastic effects are present. The beam is undergoing large deflections, which may contribute to this early non-linearity. Also, it cannot be discounted that some form of gradual failure is taking place. Much of the beam, particularly the side walls and a layer of the top flange, have a $\pm 45^\circ$ fibre orientation and so these parts of the beam are effectively loaded in shear, which, as has been seen, produces a gradual non-linear response in the material.

Although the load decreased after failure, the beam could still carry significant load for a considerably greater deflection.

(C) Energy Absorption

The energy absorbed by the beam has been calculated (using equation 3.8). A plot of this as a function of deflection is shown below in figure 6.5. Also noted is the point at which collapse occurs.

Table 6.1: Values at Collapse for Beams During Static Testing

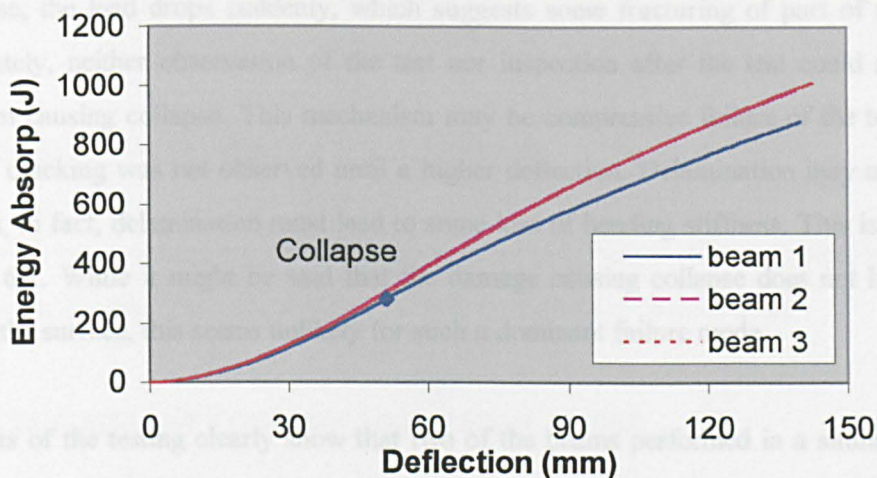


Fig 6.5: Energy Absorption v Deflection During Static Testing

The post-failure load carrying capacity is implicit in the plot of energy absorption against deflection. The curve of the energy absorption remains fairly linear and is relatively unaffected by the collapse of the beam.

(D) Collapse Behaviour

A number of values of interest relating to collapse can be derived from the tests and these are given below in table 6.1. The first is the collapse load for each beam, which has been previously defined. Then there are the collapse deflection and the collapse energy, which are the values of deflection and energy at which the collapse load occurs respectively. Also included in the table are the mean, standard deviation and coefficient of variation for these values.

Specimen	Collapse Load (kN)	Collapse Deflection (mm)	Collapse Energy (J)
1	8.90	51	281
2	9.96	55	345
3	9.96	59	377
Mean	9.61	55.0	334
Stan Dev	0.6	4.0	48.9
CV (%)	6.4	7.3	14.6

Table 6.1: Values at Collapse for Beams During Static Testing

At collapse, the load drops suddenly, which suggests some fracturing of part of the beam. Unfortunately, neither observation of the test nor inspection after the test could reveal the mechanism causing collapse. This mechanism may be compressive failure of the top flange. Side wall cracking was not observed until a higher deflection. Delamination may also be the cause and, in fact, delamination must lead to some loss of bending stiffness. This is shown in appendix 6.1. While it might be said that the damage causing collapse does not have to be visible at the surface, this seems unlikely for such a dominant failure mode.

The results of the testing clearly show that two of the beams performed in a similar manner while the other displayed a poorer performance. This latter beam was elastically less stiff before eventually failing at a lower load. This implies that the reason lies in variation during the manufacturing process, which may have led to voids or poor consolidation of the material. The results for this beam increase the statistical variation in collapse values for all the beams. The highest variation in these values is seen in the energy absorbed at collapse. This is not desirable from a crashworthiness point of view. It should be noted that the sample size is small and discussions of variation are thus limited.

6.2 IMPACT TESTING OF BEAMS

6.2.1 Introduction to Impact Testing of Beams

A series of dynamic tests were performed on the composite beams. This was done in the same manner as for the steel beam, the details of which were given in chapter three.

6.2.2 Equipment and Procedure Used During Testing

The dynamic tests were performed using the Drop Weight Facility (DWF) and a description of the equipment used was given in section 3.12. The equipment settings, initial conditions (in terms of impact velocities and mass) and the procedure used were all the same as for the steel beam and details can be found in sections 3.18 to 3.20.

A total of ten composite beams were tested. Table 6.2 below lists these beams and includes a brief description and the impact velocity used for each specimen. Note that one of the older type composite beams was included in the testing for comparison (specimen four). Also, two of the standard beams had a steel plate of 2 mm thickness placed on top of its top flange. The striker would therefore impact the plate rather than beam. This thin plate would add little to the stiffness of the beam but would prevent any local crushing to the beam at mid-span. This was to simulate the protection that the door skin may offer the beam when it is fitted in a vehicle.

Specimen	Description	Impact Velocity (m/s)
1	Standard beam	8.0
2	Standard beam	8.0
3	Standard beam	8.0
4	Older type beam	8.0
5	Standard beam	9.75
6	Standard beam	9.75
7	Standard beam	9.75
8	Standard beam	9.75
9	Standard beam & steel plate	9.75
10	Standard beam & steel plate	9.75

Table 6.2: Description of Test Specimens & Impact Velocity Used

6.2.3 Results of Impact Tests

(A) Video Playback

Playback of the HSVC recording allowed some features of the testing to be ascertained though, given the picture quality, assessments of damage were more difficult. All of the beams seemed to bend elastically. At times, particularly at the higher impact velocity, changes in the light reflected off the side wall suggested 45° cracking. On occasions, the top flange of the beam would tilt towards the camera during rebound and changes in the lighting suggested a line of damage at mid-span. There was no appreciable difference in the playback of the beams with the steel plate on their top flange. The plate was seen to be locally deformed when it separated from the beam during rebound. Failure of the older type beam was more apparent as it could be seen to crumple in on itself.

(B) Load Results for the Beams

It was found that test results did not show the same consistency as for the steel beam and so selecting a typical plot is not as straightforward. Instead, the results of a number of tests must be shown. The data was filtered (as discussed in appendix A3.16) and figure 6.5 below is a

plot displaying only the filtered load against time for all the beams at the lower impact velocity of 8 m/s.

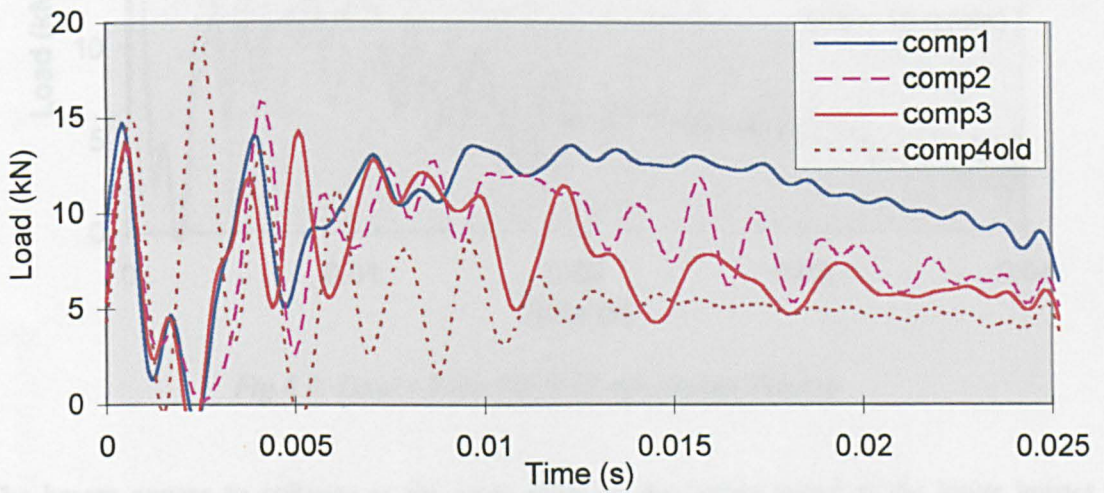


Fig 6.5: Load v Time For 8 m/s Impact Velocity

It can be seen in the above figure that, with the exception of the older type beam, the beams performed in a similar manner up until a load of around 11 kN after 8 ms. This point is very similar for all the standard beams and is taken to be the point of collapse. However, there is a wide diversity in the beams' post-collapse behaviour.

The older type beam failed at a lower load and its post-collapse performance is also poorer than for the standard beam. It is likely that this beam would be unable to absorb all the energy if a considerably higher impact energy was used in the test. It is thought probable that this beam failed in compression due to its 0/90° fibre orientation.

The results for the beams impacted at the higher velocity of 9.75 m/s were a little more consistent. Figure 6.6 below shows the filtered load against time for a selected set of these beams.

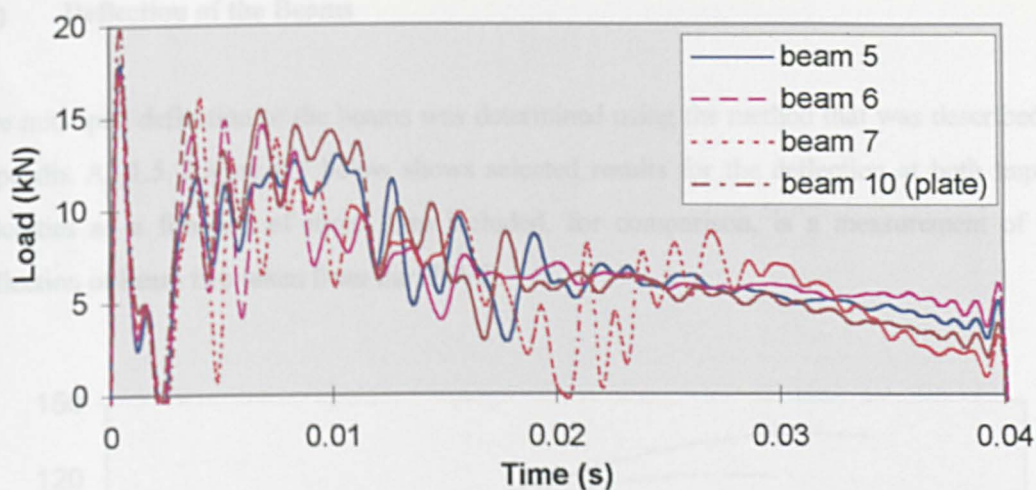


Fig 6.6: Load v Time For 9.75 m/s Impact Velocity

The beams appear to collapse at the same point as the beams tested at the lower impact velocity though there is a clear drop in load after collapse that was not present for the other beams. The whole event also takes longer as there is more impact energy to be dissipated. The results shown in figure 6.6 were chosen to show that, although they are fairly consistent, one or two of the beams (such as beam seven) can show significant variation. Also, the inclusion of a steel plate during the testing does not cause a great difference in the results although the failure load seems a little higher.

The variation seen in test results is not desirable in a practical side impact beam. It is assumed that this variation arises mainly from the manufacturing process used (wooden press) and would be much improved in a commercial product made in a metal press.

For both velocities, the same sort of load fluctuations, as seen for the steel beam, is present. These fluctuations decay over the duration of the impact event though they remain fairly strong throughout the test. There appears to be no sudden reduction in their magnitude at the point of collapse. This may be because the beam is not plastically deforming into a v-shape, which can decrease the magnitude of beam vibrations. Filtering does not remove the load fluctuations.

(C) Deflection of the Beams

The mid-span deflection of the beams was determined using the method that was described in appendix A3.1.5. Figure 6.7 below shows selected results for the deflection at both impact velocities as a function of time. Also included, for comparison, is a measurement of the deflection of beam two taken from the HSVC.

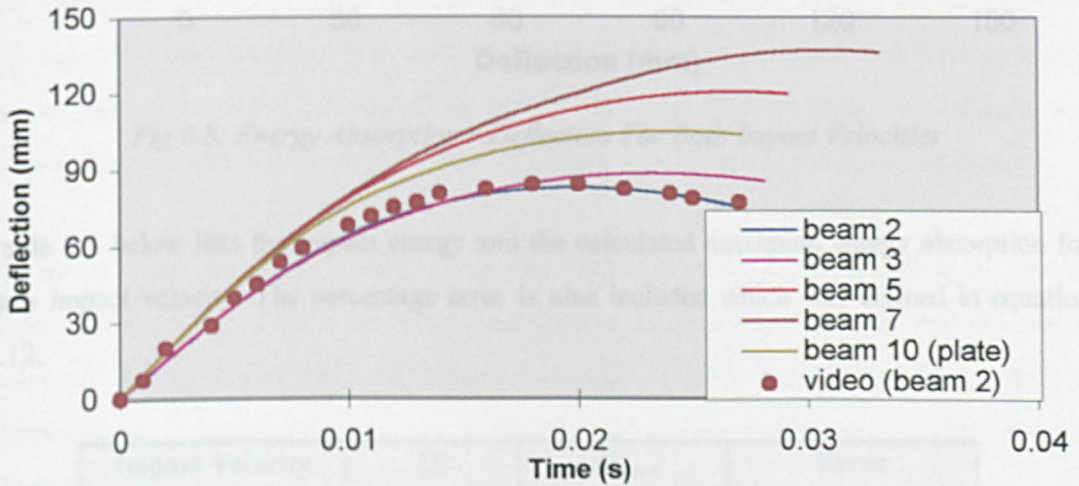


Fig 6.7: Deflection v Time For Both Impact Velocities

It can be seen in the above figure that there is a wide range in the results for the value of, and the time to reach, the maximum deflection. The effect of the steel plate is to reduce the deflection of the beam. Measurements of deflection from video agree fairly well with load cell based values although the former is generally a little higher. This is assumed to be due to the limited accuracy of video measurement as discussed in section 3.22.

(D) Energy Absorbed by the Beams

Figure 6.8 below shows the energy absorption as a function of the deflection. Also shown are the final values of absorbed energy for each impact velocity and the approximate point at which beam collapse occurs.

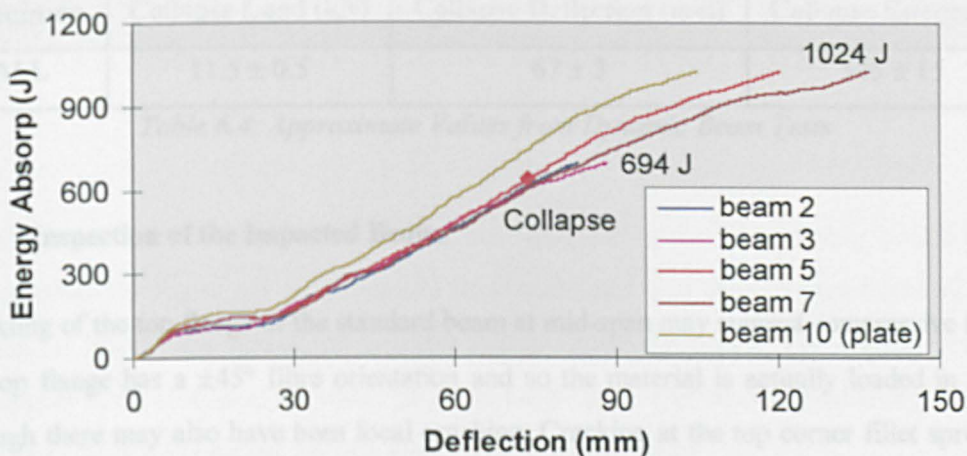


Fig 6.8: Energy Absorption v Deflection For Both Impact Velocities

Table 6.3 below lists the impact energy and the calculated maximum energy absorption for each impact velocity. The percentage error is also included which was defined in equation 3.12.

Impact Velocity (m/s)	IE (J)	$E_{a_{max}}$ (J)	Error (%)
8	695	694	0.1
9.75	1035	1025	1.1

Table 6.3: Impact and Absorbed Energy in Beam Tests

The impact and absorbed energy still agree with each other within around one percent. This is an indication of the suitability of the test rig (see section 2.4). Nevertheless, the difference at the higher impact velocity is considerably higher than for the lower velocity. No reason for this can be given.

(E) Collapse Behaviour and Other Values

The beams at both impact velocities exhibited more or less the same collapse behaviour. Approximate values for the load, deflection and energy absorption at the point of collapse are shown below in table 6.4. Also included is an estimation of the error that may arise due to the dynamic effects.

Specimen	Collapse Load (kN)	Collapse Deflection (mm)	Collapse Energy (J)
ALL	11.5 ± 0.5	67 ± 3	545 ± 15

Table 6.4: Approximate Values from Dynamic Beam Tests

(F) Inspection of the Impacted Beams

Wrinkling of the top flange of the standard beam at mid-span may suggest compressive failure (the top flange has a $\pm 45^\circ$ fibre orientation and so the material is actually loaded in shear) although there may also have been local crushing. Cracking at the top corner fillet spreading to the side walls may indicate shear failure. Another obvious form of damage was delamination between the two layers of the top flange with different material orientations.

The newer composite beams appear to have absorbed most of the impact energy in the form of elastic strain energy. This is the case even though the load plots showed that the beams collapsed during testing at both impact velocities. Higher impact energies would be informative as to further failure modes. Different failure modes were present in the older type of beam: shear failure and crushing of the web.

Fig 6.2: Load vs Deflection for all Test Results

Table 6.5 below compares the values at collapse during both static and impact testing. It can be seen that the impacted beam appears to deflect further, reaching a higher load and absorbing more elastic energy before collapse occurs.

Test	Collapse Load (kN)	Collapse Deflection (mm)	Collapse Energy (J)
Static	9.6	55	114
Impact	11.5 ± 0.5	67 ± 3	545 ± 15

Table 6.5: Comparison of Static and Impact Collapse Values

There are similarities in the types of damage of the post-impact beams but the damage in static conditions is more severe. This is partly because of the greater amount of energy being absorbed but tests at both impact velocities exceeded the static collapse load. It is surprising that

6.3 COMPARISON OF STATIC AND IMPACT BEHAVIOUR

Figure 6.9 is a comparison of static and impact beam test results. Reasonably typical results were selected for figure 6.9 but it should be remembered that there is significant variation between the beams' test results, particularly during impact conditions. The impact behaviour does appear to be similar to the static response but with a superimposed oscillating response. It is noticeable that the beams fail at a higher load when impacted.

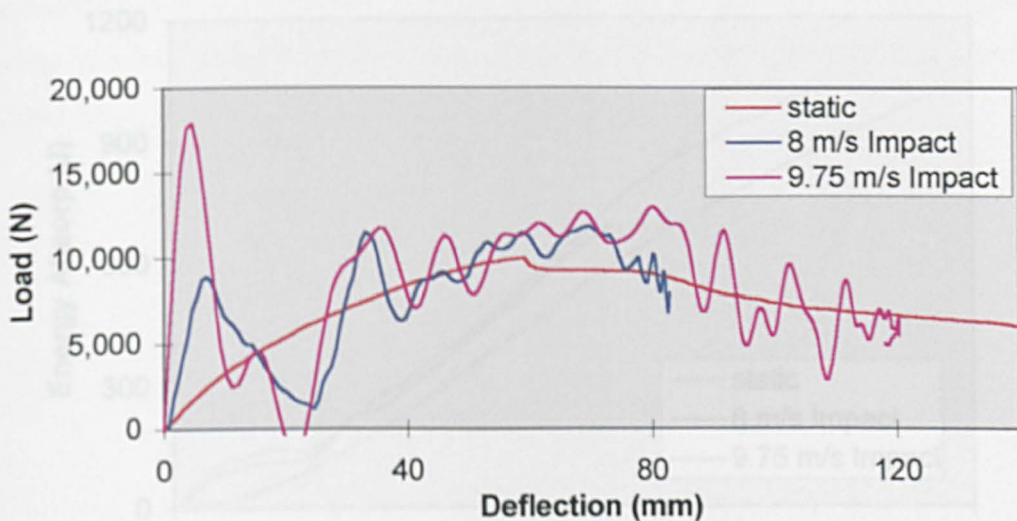


Fig 6.9: Load v Deflection for all Test Results

Table 6.5 below compares the values at collapse during both static and impact testing. It can be seen that the impacted beam appears to deflect further, reaching a higher load and absorbing more elastic energy before collapse occurs.

Test	Collapse Load (kN)	Collapse Deflection (mm)	Collapse Energy (J)
Static	9.6	55	334
Impact	11.5 ± 0.5	67 ± 3	545 ± 15

Table 6.5: Comparison of Static and Impact Collapse Values

There are similarities in the types of damage of the post-tested beams but the damage in static conditions is more severe. This is partly because of the greater amount of energy being absorbed but tests at both impact velocities exceed the static collapse load. It is surprising that

the impacted beams do not show more of the types of damage seen in static tests, namely, compressive and shear failure.

A plot of energy absorption against displacement is shown in figure 6.10 below. The difference between static and impact behaviour is much more apparent with statically tested beams deflecting considerably further for a given level of energy absorption. As figure 6.10 shows, beams tested at the lower impact rate even deflect slightly more than those tested at the higher rate.

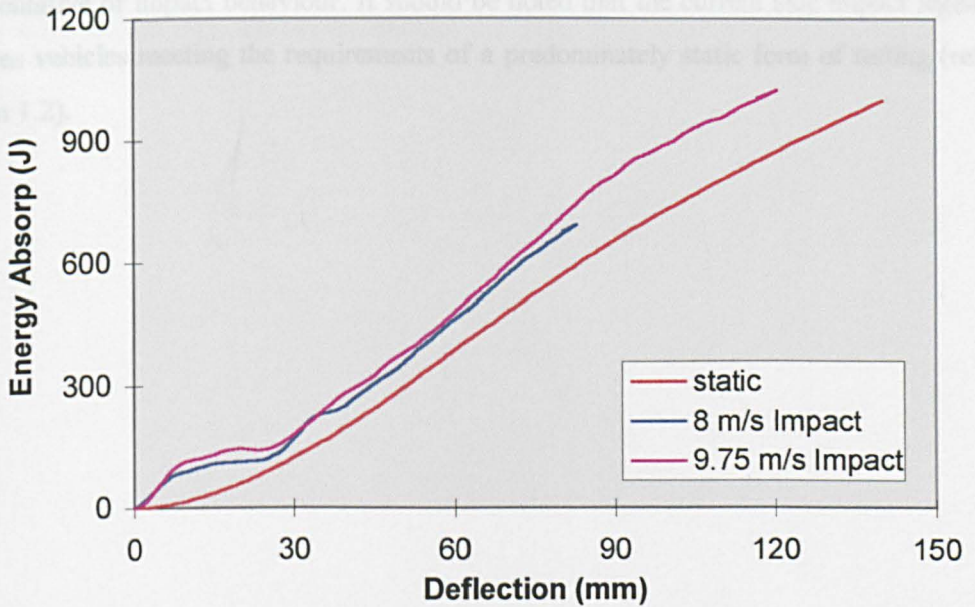


Fig 6.10: Energy v Deflection for all Test Results

It is believed that there are important differences between the static and impact behaviour of the composite side impact beam.

Static beam behaviour is characterised by viscoelastic deformation as the beam is loaded. There is a viscous component of the behaviour, which is loading rate (and so time) dependent and there is an elastic component, which is dependent on the loading. Viscoelastic deformation leads to a higher deflection for a given level of input energy. Static failure modes such as shear and compressive failure may even be (at least partly) dependent on the loading rate. This could be because such failure modes are predominantly matrix failures influenced by viscoelastic yielding. The time dependency of the material's strain has been seen in a number of composite coupon tests.

During impact conditions, viscoelastic deformation does not have the time to occur. Consequently, the beam seems to be able to behave elastically for longer. Yet some form of failure does soon occur and the post-collapse response of the beam is not so different to the response seen during static tests.

A practical side impact beam will always be functioning in (low or high) impact conditions and so static behaviour or failure modes are unimportant. However, if static testing is used to evaluate the beam or even the complete vehicle, it is possible that the results would not be representative of impact behaviour. It should be noted that the current side impact legislation involves vehicles meeting the requirements of a predominately static form of testing (refer to section 1.2).

SUMMARY OF CHAPTER

Static testing of beams has allowed the behaviour of composite beams to be determined in terms of load, deflection and energy absorption. Failure modes and collapse values have been identified. Tests have also been performed for impact conditions, although collapse values are not as well defined due to load fluctuations in the test results. In both forms of testing, there has been significant variation between beams. Comparisons of static and impact results suggest that there is a difference in behaviour, and possibly the failure modes, for beams tested at the impact rates used in this thesis.

CHAPTER SEVEN

QUANTITATIVE METHODS FOR PREDICTING COMPOSITE COUPON AND BEAM BEHAVIOUR

OVERVIEW OF CHAPTER

Chapter six presented the details of a series of static coupon tests that were carried out to define the mechanical properties of the composite material. Chapter seven presented the static and dynamic testing of the composite beams. This chapter presents the quantitative methods that have been used to predict the properties of the material and the behaviour of composite beams and coupons. Figure 7.1 is a block diagram of the structure of the chapter and includes the section numbers used in this thesis.

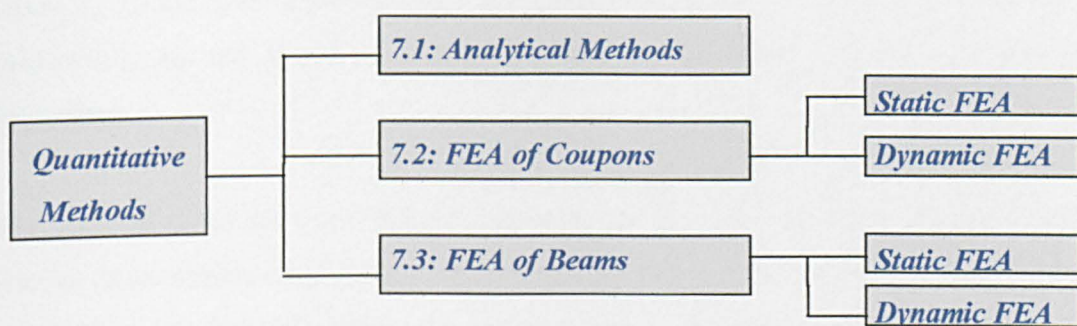


Fig 7.1: Block Diagram of Structure of Chapter

Analytical methods can be used for two purposes. The first is an approximate evaluation of the composite material's mechanical properties using the rule of mixtures. The second is to determine bending stresses during the flexural coupon testing using simple bending theory, which can be used to validate the static FEA.

Static coupon tests were modelled using both static and dynamic FEA. This determined whether the general approach to the FEA, in terms of the failure criteria used and how the response to failure was controlled, was suitable and gave a realistic failure mode. The approach for each loading condition could then be used with greater confidence in the static and dynamic modelling of the side impact beam. Therefore, coupon modelling provided some verification of the FEA approach and assumptions used for modelling the beam.

The modelling of the coupon tests also allowed an assessment of the capabilities of the static and dynamic FEA codes. In particular, their ability to represent composite failure could be

assessed. It was found that both the static and dynamic FEA models offer reasonable predictions of the beam's response though they have their limitations.

7.1 ANALYTICAL METHODS

7.1.1 Material Properties from Rule of Mixtures

Approximate values for the properties of composite materials can be obtained using the *rule of mixtures*. A general form of the rule is:

$$X_c = X_m V_m + X_f V_f \quad \text{Eq (7.1)}$$

where X_c , X_m and X_f are a particular property of the composite, matrix and fibre reinforcement respectively. V_m and V_f are the volume fractions of the matrix and fibre reinforcement respectively.

The accuracy of the rule of mixtures is limited as most properties are a complex function of a number of parameters which interact in a synergistic manner. Relevant parameters include the matrix/fibre interface, the shape, size and orientation of the fibres and the grain size for polycrystalline matrices. However, the volume fraction is generally regarded as the single most important parameter influencing the composite's properties [2.39].

A number of values for the matrix properties of the Twintex PP60 material are given by SACTAC which were presented in appendix 1.4 (the accuracy of the values is unknown). No values for the fibre properties are presented and therefore general values have had to be used, as quoted in standard materials textbooks. In all cases, the properties are assumed to be the longitudinal properties. The percentage volume for the fibre in the composite is listed by SACTAC as being 35 %. This figure includes longitudinal and transverse fibres and so it has been assumed that the volume fraction of the fibres in the longitudinal direction, V_f , is equal to 0.175 (and so the volume fraction of the matrix is 0.65).

The tensile longitudinal elastic modulus, E_c , is given by:

$$E_c = V_m E_m + V_f E_f$$

where the subscripts correspond to those used in equation 7.1 above.

The rule of mixtures for the longitudinal modulus is said to agree within 5 % of experimental data [2.39] but this is when exact values for each phase are known. It is not regarded as accurate in the case of compressive loading. An elastic modulus for an E-Glass fibre is widely quoted to be 72 GPa (for example, refer to Callister [7.1]). All other parameters are known from SACTAC. There is an expression from the rule of mixtures for the transverse elastic modulus but is only applicable for unidirectional materials.

The shear modulus of the composite material, G_c , is given by:

$$\frac{1}{G_c} = \frac{V_m}{G_m} + \frac{V_f}{G_f}$$

Although a value for the elastic modulus of E-Glass fibres is common, this author has not found a value for the shear modulus of such fibres. Therefore a value for the shear modulus cannot be determined.

For failure of the composite material, values for the tensile failure stress and strain, σ_c^{fail} and ϵ_c^{fail} , can be determined if it is assumed that the failure is dominated by the tensile failure of the fibres. The tensile fibre strength of E-Glass fibres is quoted to be 38 MPa [7.1].

$$\epsilon_c^{fail} = \frac{\sigma_f^{fail}}{E_f}$$

$$\sigma_c^{fail} = V_m \sigma_m^{fail} + V_f \sigma_f^{fail}$$

Table 7.1 below lists the values of the material properties determined using the rule of mixtures as well as empirically derived values. The percentage difference between the two sets of values is also included.

Property	Rule of Mixtures	Test Results	% Difference
Tensile Elast Mod (GPa)	13.6	14.8	8.1
Tensile Failure Stress (MPa)	327	318	2.8
Tensile Failure Strain (%)	2.40	2.66	10.8

Table 7.1: Material Properties Determined from Analytical and Test Results

It is clear that the rule of mixtures provides reasonable approximations of the properties of the composite material. The approximations may even have been in closer agreement to test results if more data was available for the properties of the fibres.

7.1.2 Flexural Stresses

Due to the varying cross-section of the composite beam, there are no simple closed-form analyses available to determine the beam's various stresses as it is loaded in bending.

Section 7.2.6 will present the static FEA of the flexural coupon tests. Given the simple geometry of the specimen, the flexural stresses can be readily obtained using simple bending theory. A representation of the four-point bending test is given below in figure 7.2.

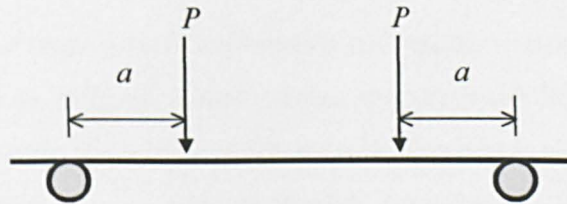


Fig 7.2: Representation of the Four-point Bending Test

The applied load, P_{appt} , is equal to $2P$. It can be shown, from simple bending theory, that the maximum bending moment, M_{max} , is equal to Pa . The flexural stress experienced by the coupon, σ , is given by:

$$\sigma = \frac{My}{I}$$

The maximum flexural stress will occur at the maximum bending moment and at the outer fibres (the distance from the neutral axis, y , is equal to half the coupon's thickness). The second moment of area, I , is determined by:

$$I = \frac{bd^3}{12}$$

7.2 STATIC FEA OF COMPOSITE COUPONS

7.2.1 Introduction to Static FEA of Composite Coupons

The static coupon tests have been modelled using both static and dynamic FEA. This has allowed an assessment of the FEA software, the failure criteria that the software uses and the development of appropriate modelling techniques. The techniques involve the control of failure under a particular loading condition in such a manner that the FEA predictions correlate with the relevant coupon test results. It is believed that this approach compensates for the limitations of any failure criterion, and of the FEA software, and has a valid basis to how failure is treated.

The coupon testing measured only in-plane properties. Both coupons and beams were modelled using shell elements which efficiently represent thin-walled sections and because only in-plane properties are required for such FEA models (even the beam models which experience out-of-plane bending).

7.2.2 Failure Criteria Within Static FEA

It is common within FEA of composites to implement some type of composite failure criterion. ANSYS can implement three different failure criteria: the Maximum Strain, the Maximum Stress and the Tsai-Wu criteria. Each of these criteria were reviewed in section 2.3. The Tsai-Wu criterion can either be in the conventional strength index form or in the strength ratio form.

The general approach used by ANSYS is limited to performing a purely elastic analysis; no change is made (such as to the material's properties or element deletion) when failure is reached. ANSYS only reports, for each element, a ratio of the element's stress or strain to the value calculated from the specified failure criterion. This ratio is termed the failure ratio. When (at which nominal stress or strain) and where (the element location) failure occurs is therefore known if a particular ratio becomes equal to unity. The onus is then on the user to make appropriate changes that simulate the failure and proceed with the analysis.

For the Maximum Stress and Strain criteria, the value calculated from the criterion is produced by whichever type of stress or strain (tensile, compressive or shear) is the greatest but the type cannot be directly ascertained from the ANSYS output. However, this information can be deduced by comparison of each element's stresses or strains with the specified failure values. This is important if the user wishes to simulate different types of failure for different loading conditions.

For the Tsai-Wu criterion, the value calculated from the criterion is based on the interaction of all three types of stress and a particularly dominant stress cannot be identified unless the user calculates by hand the criterion for every element. The user has some control over the degree of stress interaction by specifying the value of the F_{12} term discussed in section 2.3.6. In ANSYS, this is done by assigning a value to the stress interaction coefficient, C , which is simply twice the value of F_{12} . The value of C must lie between -2 and 2 and a value between -1 and 0 is recommended. Since the Tsai-Wu criterion is essentially a mathematical 'best fit' approach, the stress interaction coefficient can be looked upon as a tuning parameter to correlate criterion predictions with experimental data.

7.2.3 Static Modelling of Tensile and Compressive Coupons

(A) Modelling Procedure

Static modelling of the coupons was performed using ANSYS. Although quarter symmetry could have been employed in the FEA model, this was not done. Given the simplicity of the model (of flat rectangular coupons), a relatively small number of elements was involved and so the duration of analysis runs were short. Therefore, to aid in visualising the results, the complete coupon was modelled. The model consisted of 680 elements and 2197 nodes.

The geometry of the model was matched to the nominal dimensions of the standard tensile test coupon. The length of the model (170 mm) was equal to the coupon length (250 mm) minus the length of the tab (40 mm) at each end of the coupon. The width (25 mm) and the thickness (3.5 mm) were the same as the test coupon.

Note that the model geometry did not correspond to the dimensions of compressive specimens, which involved considerably smaller coupons. Since the FEA model assumes perfect boundary

conditions and material behaviour, it is unaffected by the scale used (the resulting stresses and strains will be the same).

ANSYS offers two types of shell elements for composite materials: 'shell91' and 'shell99'. Both elements were suitable but the latter type was selected as it offers the greatest flexibility. It is an eight noded element with orthotropic material properties. Up to one hundred layers can be defined for the element; each layer can have its own material properties and material orientation angle. For the weave material, only one layer had to be defined and the orientation angle was set to zero.

In-plane material properties were assigned the values determined from coupon tests and a summary of these values was given in table 5.11. Out-of-plane properties were given the values specified by SACTAC (see appendix 1.4).

Failure stresses and strains were also set to experimentally determined values, which were also listed in table 5.11. These were specified in an ANSYS data table provided for the purpose. The shear strength was set to the value using the proof stress method (refer to section 5.3.3) and the rationale for this is discussed in section 8.2.5 . Therefore, the shear strain at failure was assigned the strain value at which this offset stress occurs (1.5 %). The Ansys manual [7.2] recommends for a two dimensional analysis that the out-of-plane failure stresses and strains be set to values that are several orders of magnitude higher than in-plane properties. This recommendation was followed.

All three failure criteria were implemented. For the Tsai-Wu criterion, analyses using both the strength index and the strength ratio were carried out. The appropriate value of the stress interaction coefficient was unknown. Therefore, each of the analyses were repeated a number of times using different values of the stress interaction coefficient, C . Values of -2, -1, -0.5, 0, 1 and 2 were specified.

The nodes at one end of the model were fully constrained. At the other end, a force was applied as a line pressure. For the tensile modelling, the applied force had a final magnitude of 35 kN applied in seven sub-steps of 5 kN step. Failure could occur between these load steps but, because Ansys performs an elastic analysis, the exact failure load can be derived using interpolation. A plot of the boundary conditions used for the model is shown below in

figure 7.3 (the nodal constraints on the left-hand side edge of the model may be unclear as they show constraints on all degrees of freedom).



Fig 7.3: Plot of Boundary Conditions Used During Static Tensile Coupon FEA

The modelling of the compressive testing was the same as for the tensile testing except for the direction and magnitude of the loading. The force was reversed and, because failure was known to occur much earlier in compression, the magnitude of the maximum applied load was reduced to 15 kN, applied in three steps of 5 kN. Three steps were considered sufficient given the linear nature of the results.

(B) Results of Tensile FEA

Results of the analyses showed that, at every load step, the stress within each element were virtually the same and equal to the nominal stress (the applied force divided by the cross-sectional area of the model). The strain within each element was equal to its displacement divided by its distance from the fixed edge. The facts that the predicted stress and strain were equal to nominal values, and that the stress and strain distributions were uniform, are seen to validate the model in terms of the mesh density and accuracy of the elements.

The uniform stress or strain distribution was reflected in the failure ratio reported by Ansys, which were virtually the same for each element. For the Maximum Stress criterion, the ratio was equal to the longitudinal stress divided by the tensile failure stress. For the Maximum Strain criterion, the ratio was equal to the longitudinal strain divided by the tensile failure strain. Thus it could be deduced that failure occurred, as expected, due to tensile stresses or strains reaching the value at failure. For the Tsai-Wu criterion, no easy comparison could be made.

Table 7.2 below lists the failure ratio reported for each criterion. For the Tsai-Wu criterion, both the strength index and the strength ratio results are provided. Also shown are the values of nominal stress and strain for each load step.

Load (kN)	Stress (MPa)	Strain (%)	Max Strain ratio	Max Stress ratio	Tsai-Wu	
					Str Index	Str Ratio
5	57.1	0.39	0.15	0.18	-0.20	0.18
10	114.3	0.78	0.29	0.36	-0.23	0.36
15	171.4	1.17	0.44	0.54	-0.10	0.54
20	228.6	1.56	0.58	0.72	0.20	0.72
25	285.7	1.95	0.73	0.90	0.66	0.90
30	342.9	2.33	0.87	1.08	1.29	1.08
35	400.0	2.76	1.02			

Table 7.2: Failure Ratios Determined During Static Tensile Coupon FEA

The above table shows that failure occurs earlier if based on stress rather than strain. This is because the behaviour of the tensile specimens during testing was not entirely elastic (thought mainly to be due to viscoelastic effects). An elastic analysis does not account for this and will predict a linearly increasing stress, the gradient of which is determined by the elastic modulus. This modulus was derived from an early stage of coupon testing where the stiffness of the material was at its highest. Therefore, the FEA will predict a stress that reaches the failure stress at a strain that is less than the failure strain. This is shown (in an exaggerated form) in figure 7.4 below.

$$v_f = v_{f-1} + \left[\frac{v_f - v_{f-1}}{v_{f-1} - v_{f-2}} \right] (v_{f-1} - v_{f-2}) \quad (7.1)$$

where v_f is the value at failure, v_{f-1} and v_{f-2} are the values immediately before and after failure respectively and v_{f-1} and v_{f-2} are the values immediately before and after failure respectively.

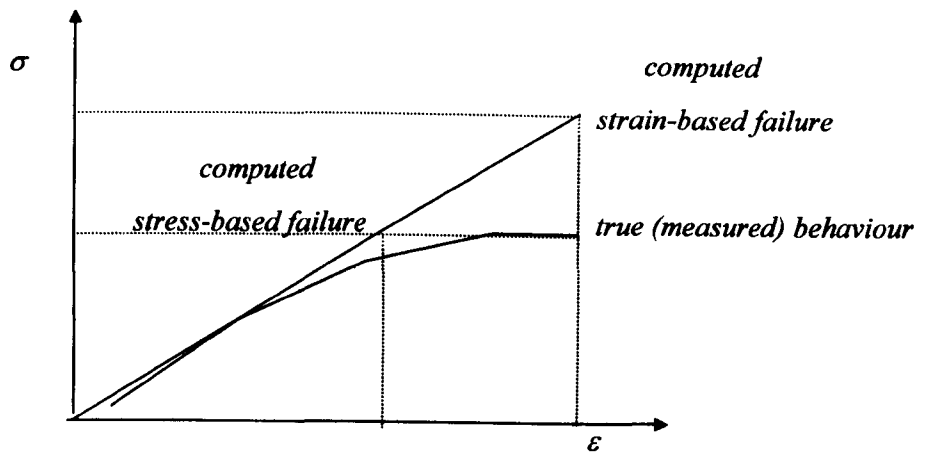


Fig 7.4: Idealisation of Tensile Coupon FEA and Test Results

Tsai-Wu results using the strength index produced surprising results. Negative values should not arise and seem to indicate a flaw in the software's implementation of the theory. Results using the strength ratio are exactly the same as those obtained from the Maximum Stress criterion. This is realistic as the Tsai-Wu theory is based on stresses and there should be little influence of any stress except the tensile stress for the boundary conditions being considered. This is also why, for both forms of the Tsai-Wu criterion, the value of the stress interaction coefficient was found to have no effect whatsoever on the results. There should be no stress interaction since there is virtually only one stress present during a uniaxial test.

All of the values (in terms of load, stress or strain) and failure ratios in table 7.2 are linearly increasing for the Maximum Stress and Strain criteria. Therefore, the exact value at failure (when the relevant ratio is equal to unity) can easily be determined by dividing any of the values at any load step by the appropriate failure ratio. Because the results of the Tsai-Wu criterion are not linear, some form of interpolation must be used. This has been done using equation 7.1 below.

$$v_f = v_{(i-1)} + \left[\frac{1 - r_{(i-1)}}{r_{(i)} - r_{(i-1)}} \times (v_{(i)} - v_{(i-1)}) \right] \quad \text{Eq (8.1)}$$

where v_f is the value at failure, $v_{(i-1)}$ and $v_{(i)}$ are the values immediately before and after failure respectively and $r_{(i-1)}$ and $r_{(i)}$ are the ratios immediately before and after failure respectively.

Equation 7.1 represents a linear form of interpolation but the results for failure values indicate that it is adequate. Table 7.3 below presents these results for each of the criteria.

Value at Failure	Max Strain ratio	Max Stress ratio	Tsai-Wu	
			Str Index	Str Ratio
Load (kN)	34.3	27.8	27.7	27.8
Stress (MPa)	392	317	317	317
Strain (%)	2.70	2.16	2.16	2.16

Table 7.3: Failure Values Determined During Static Tensile Coupon FEA

Table 7.3 emphasises a number of the points made above. The Maximum Strain criterion predicts failure at a strain equal to the specified failure strain but at a stress considerably higher than the specified failure stress (24 % higher). The Maximum Stress criterion predicts failure at a stress equal to the specified failure stress but at a strain considerably lower than the specified failure strain (19 % lower). This is solely the effect of using experimental results where the material behaviour was not entirely elastic. Figure 7.5 is a plot of the stress against strain predicted by the tensile FEA, which also includes a typical test result. The pertinent question is whether it is a particular value of stress or strain that causes failure. No answer is known at this point.

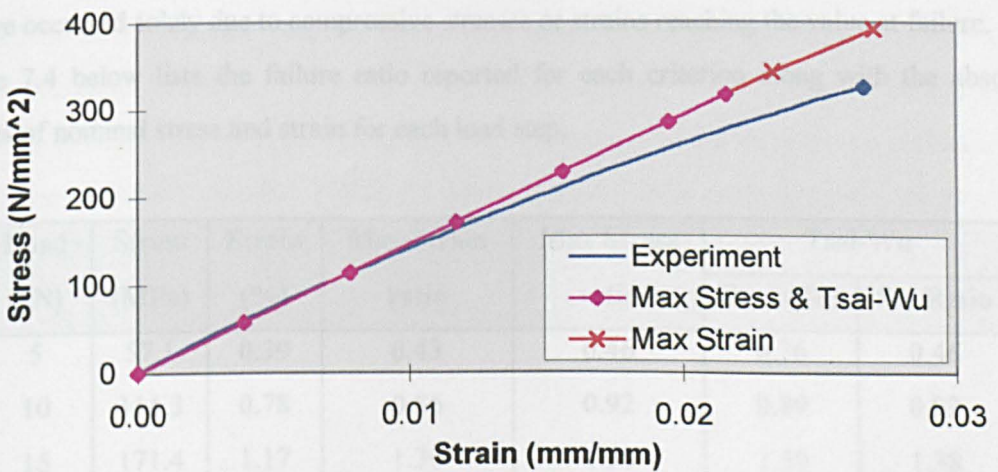


Fig 7.5: Plot of Stress v Strain for Static Tensile FEA & Test Results

Table 7.3 above shows that both forms of the Tsai-Wu criterion generate predictions that are more or less equal to those of the Maximum Stress criterion. It seems that the strength index

form of the Tsai-Wu criterion, despite producing apparently erroneous results initially, gives realistic results for the ratio for the final two values at least. Also, the interpolation method used appears to be adequate given that it produces realistic results.

It would have been possible to re-run each of the analyses to the relevant failure load for each failure criterion and then modify the material's properties in some manner so that, when the analyses were continued up to a higher load, the elements behaved in an appropriate manner. However, tensile failure is catastrophic and the modification would need to simulate this. Element deletion was considered simpler and more representative of a fracture process. However, deletion would have had to be applied to every element as they all failed at the same point. Therefore, the analyses were not continued to a higher load although it was recognised that the technique of element deletion could be used in any other types of analyses where only a particular set of elements (local failure) reach failure in tension.

(C) Results of Compressive FEA

Once again, stress and strain results for all the elements were virtually the same and equal to the nominal stress and strain. The model remains valid with the loading reversed. This time, for the Maximum Stress and Strain criteria, the failure ratio was found to be equal to the longitudinal stress or strain divided by the *compressive* failure stress or strain. Therefore, failure occurred solely due to compressive stresses or strains reaching the value at failure.

Table 7.4 below lists the failure ratio reported for each criterion along with the absolute values of nominal stress and strain for each load step.

Load (kN)	Stress (MPa)	Strain (%)	Max Strain ratio	Max Stress ratio	Tsai-Wu	
					Str Index	Str Ratio
5	57.1	0.39	0.43	0.46	0.36	0.46
10	114.3	0.78	0.86	0.92	0.89	0.92
15	171.4	1.17	1.30	1.38	1.59	1.38

Table 7.4: Failure Ratios Determined During Static Compressive Coupon FEA

As before, failure occurs earlier if the analysis is based on stress rather than strain although the difference is not so pronounced. This is because the behaviour of the material in

compression has been seen to be more linear than in tension (see section 5.2). This is believed to be because the viscoelastic yielding increases with time and thus increases at higher values of strain. Therefore, the yielding will be greater in a tensile test which involves a strain range about three times the range seen in compression tests.

The value of the stress interaction coefficient had no effect on the results of either form of the Tsai-Wu criterion. Tsai-Wu results using the strength index differ significantly from the other results though they appear less erroneous than before. Results for the strength ratio are once again equal to the results using the Maximum Stress criterion.

The values at failure were determined and are presented below in table 7.5.

Value at Failure	Max Strain ratio	Max Stress ratio	Tsai-Wu	
			Str Index	Str Ratio
Load (kN)	11.6	10.9	10.8	10.9
Stress (MPa)	132	124	123.3	124.2
Strain (%)	0.90	0.85	0.84	0.85

Table 7.5: Failure Values Determined During Static Compressive Coupon FEA

As with the tensile FEA, the Maximum Strain criterion predicts failure at a strain equal to the specified failure strain but at a stress higher than the specified failure stress (6 % higher). The Maximum Stress criterion predicts failure at a stress approximately equal to the specified failure stress but at a strain lower than the specified failure strain (6 % lower). Both forms of the Tsai-Wu criterion give predictions that are approximately the same as the predictions of the Maximum Stress criterion. Figure 7.6 below is a plot of the stress against strain predicted by the compressive FEA and also includes a typical test result.

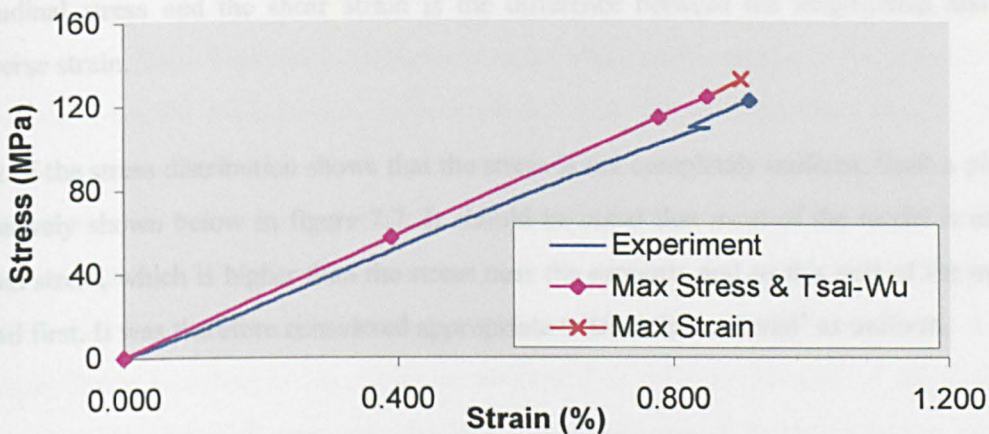


Fig 7.6: Plot of Stress v Strain for Static Compressive FEA & Test Results

Compressive failure, like tensile failure, has also been seen, in coupon tests, to be catastrophic. The procedure of deleting failed elements at the failure load and continuing the analyses could have been performed but was deemed unnecessary since all elements failed at the same point. It should be noted that it is compressive failure of a whole cross-section that is being considered.

7.2.4 Static Modelling of Shear Coupons

(A) Modelling Procedure

FEA modelling of the shear testing was the same as for the tensile testing with two exceptions. Firstly, the loading was applied as a 3 kN tensile force in three 1 kN steps. Secondly, the material orientation angle was set to 45°. Therefore, the shear test being modelled was the $\pm 45^\circ$ tensile test. It was not thought necessary to model the Iosipescu shear test.

(B) Results of Analyses

ANSYS reports the results of the analyses, in terms of the shear stress or shear strain, to be virtually zero. It is not known why this is the case. However, shear stresses and strains could be determined using direct stresses and strains in exactly the same manner as was done during the coupon testing (refer to equations 5.1 and 5.2). The shear stress is simply half of the

longitudinal stress and the shear strain is the difference between the longitudinal and the transverse strain.

A plot of the stress distribution shows that the stress is not completely uniform. Such a plot is qualitatively shown below in figure 7.7. It should be noted that most of the model is at the nominal stress, which is higher than the stress near the supports and so this part of the model will fail first. It was therefore considered appropriate to treat the ‘material’ as uniform.

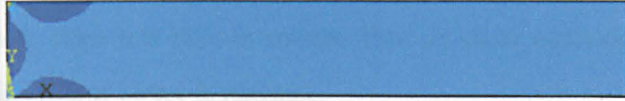


Fig 7.7: Plot of Stress Distribution During Static Shear Coupon FEA

Despite reporting shear stresses and strains to be zero during post-processing, the software uses the correct values within the failure criteria to calculate the failure ratios. For the Maximum Stress and Strain criteria, the failure ratio was found to be equal to the shear stress or strain divided by the specified shear stress or strain at failure. Therefore, failure occurred solely due to *shear* stresses or strains reaching the value at failure.

Table 7.6 below lists the failure ratio for each criterion along with the values of nominal stress and strain for each load step.

Load (kN)	Stress (MPa)	Strain (%)	Max Strain ratio	Max Stress ratio	Tsai-Wu	
					Str Index	Str Ratio
1	5.7	0.55	0.42	0.49	0.18 ± 0.01	0.46
2	11.5	1.09	0.83	0.98	0.85 ± 0.01	0.92
3	17.2	1.64	1.25	1.47	1.99 ± 0.01	1.39

Table 7.6: Failure Ratios Determined During Static Compressive Coupon FEA

Once again, failure occurs earlier if based on stress rather than strain, however, the reason for this is different. The offset strength is based on a perfectly linear stress line but the line has been offset by 0.2 % strain. Therefore, the failure strain is 0.2 % strain greater than the strain at which the failure stress occurs.

The value of the stress interaction coefficient had no effect on the results of the strength ratio form of the Tsai-Wu criterion but had a small effect on the strength index results. While analysis using a coefficient of -1 to 0 produced the same results, coefficients of 2 and -2 gave variations of +0.01 and -0.01 respectively. This small difference is assumed to be negligible and not considered further. Tsai-Wu results using the strength index still differ significantly from the other results. This time, results for the strength ratio lie between the results for the Maximum Stress and the Maximum Strain criterion. It is not that this form of the Tsai-Wu criterion considers strain. Rather, the ratio of the tensile stresses to the tensile failure stress is also considered which, since this ratio is smaller than its shear equivalent, has the effect of delaying failure until a higher stress is reached.

The values at failure were determined and are presented below in table 7.7.

Value at Failure	Max Strain ratio	Max Stress ratio	Tsai-Wu	
			Str Index	Str Ratio
Load (kN)	2.4	2.0	2.1	2.2
Stress (MPa)	13.6	11.7	12.3	12.5
Strain (%)	1.31	1.11	1.16	1.18

Table 7.7: Failure Values Determined During Static Compressive Coupon FEA

As before, the Maximum Strain criterion predicts failure at a strain equal to the specified failure strain. The Maximum Stress criterion predicts failure at a stress equal to the specified failure stress. The results of both forms of the Tsai-Wu criterion are similar and lie between the results for the Maximum Stress and the Maximum Strain criterion.

Shear failure has been experimentally seen to be a non-linear and non-catastrophic event. It would not have been appropriate to terminate the analyses at this stage, nor to use element deletion for failed elements (which would have been all elements). An alternative method is to reduce material properties to some degree and this method was chosen.

The degree by which properties are reduced required some justification. The approach taken was to redefine the shear failure values as those of the second form of shear strength (23.3

MPa and 5 % strain). The shear modulus was reduced in such a way that the coupon's elastic behaviour, in subsequent analyses, would pass through these values.

This approach meant that the degree of reduction of the shear modulus differed slightly depending on the failure criteria. The new modulus, G^* was taken to be the ratio of the difference in shear stress, τ_f , and shear strain, γ_f , values at the original point of failure and the new point of failure. This is expressed below as equation 7.2.

$$G^* = \frac{\Delta\tau}{\Delta\gamma} = \frac{\tau_f^{new} - \tau_f^{original}}{\gamma_f^{new} - \gamma_f^{original}} \quad Eq (7.2)$$

Equation 7.2 gives the values for each failure criterion shown in table 7.8 below. For the Tsai-Wu criterion, since the difference was small, an average of the results of the two forms was taken.

Failure Criterion	Reduced Shear Modulus (MPa)	Percentage of Original
Maximum Strain	510.5	49
Maximum Stress	297.4	28
Tsai-Wu (Average)	320.6	31

Table 7.8: Values of the Reduced Shear Modulus for each Failure Criterion

For each failure criterion, the subsequent analyses were continued from the original point of failure. The new failure values were determined which were virtually the same in all cases (a load of 3.2 kN, a stress of 23.3 MPa and a strain of 5 %). The results of the Tsai-Wu criterion were slightly different, again due to the interaction of the tensile stresses.

Figure 7.8 below shows the results of all of the analyses for each failure criterion in terms of stress against strain (the average of the Tsai-Wu results was again used). A typical experimental curve from both forms of shear testing is included for comparison. Section 5.3.8 explained how the difference between the two experimental curves could be caused by the strain rate being higher, and so the viscoelastic yielding less, during the Iosipescu testing

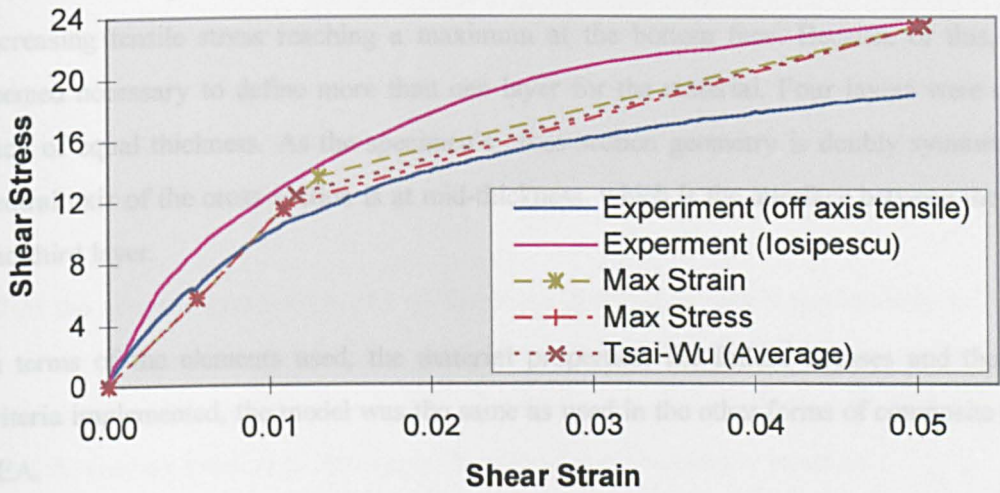


Fig 7.8: Plot of Stress v Strain for Static Shear FEA & Test Results

All of the FEA predictions, on the whole, lie between the results of the two forms of shear testing. This is due to the use of two shear strengths, derived from each form of testing. It is considered to be desirable given the uncertainty over the material's shear behaviour. Because of this uncertainty, or experimental scatter in results, it seems futile to use more complex analyses that would track one of the test curves with greater accuracy. It can at least be said that the FEA approach accounts for the non-linear shear stiffness of the material. This approach could be used in the FEA of beams when shear failure is detected.

7.2.5 Static Modelling of Flexural Coupons

(A) Modelling Procedure

In this case, the geometry of the model was matched to the nominal dimensions of the flexural test coupon. Also, one plane of symmetry, about the mid-span of the coupon, was utilised. The length of the model (63.5 mm) was therefore equal to half the coupon length (127 mm) while the width (25 mm) and the thickness (3.5 mm) of the model were the same as for the test coupon. A total of 1550 elements and 4825 nodes were used.

A specimen in bending will experience a range of stresses through its thickness: compressive stress on the top face linearly decreasing to zero stress at the neutral axis then a linearly increasing tensile stress reaching a maximum at the bottom face. Because of this, it was deemed necessary to define more than one layer for the material. Four layers were defined, each of equal thickness. As the specimen's cross-section geometry is doubly symmetric, the neutral axis of the cross-section is at mid-thickness, which is the interface between the second and third layer.

In terms of the elements used, the material properties, the failure stresses and the failure criteria implemented, the model was the same as used in the other forms of composite coupon FEA.

The nodes at one edge of the model were assigned the appropriate symmetry conditions. At a distance of 51 mm from this edge, the nodes were constrained but only in the z axis (out-of-plane axis). Thus, the model simulated the simply supported condition (of 102 mm span), with the supports equidistant from the mid-span, and the overhang of the coupon on the supports.

The various loads of the analyses were applied as nodal forces in the z direction to all the nodes at a distance of 25.5 mm from the edge with symmetry conditions. The magnitude of each nodal force was equal to half the desired applied load, to allow for symmetry, and then divided by the number of nodes across the width (51). Initially, a total load of 0.82 kN was applied in two steps of 0.41 kN. Figure 7.9 below is a plot of all the boundary conditions used for the flexural coupon FEA.

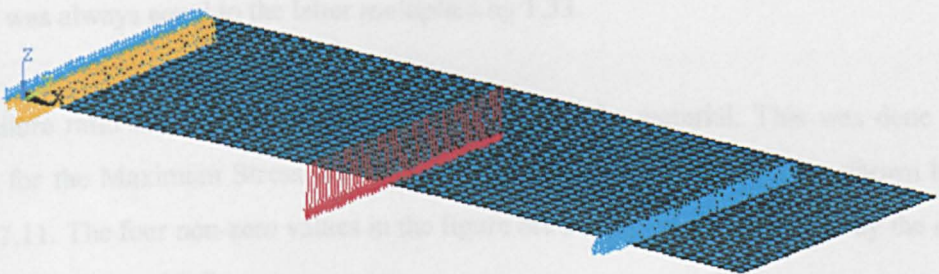


Fig 7.9: Plot of Boundary Conditions Used for Static Flexural Coupon FEA.

(B) Results of Analyses

For the flexural testing, the flexural stress and strain had to be calculated from the loading and the (cross-head) displacement respectively. This was not necessary in the FEA; the longitudinal stress and strain, at the outer layers, predicted by Ansys correspond to the flexural stress and strain.

All of the analyses produced a plot of the stress distribution that is qualitatively as expected for a four-point bending test. Such a plot is shown below in figure 7.10. It can be seen that the region between the loading is in a state of uniform stress (in each through-thickness plane). From the loading location to the support location the stress linearly increases.

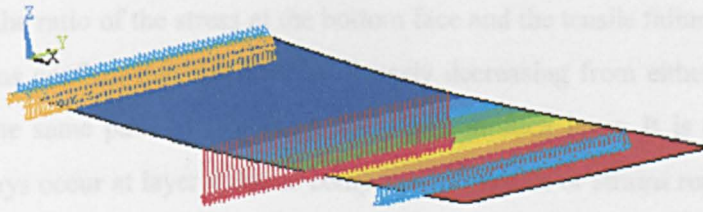


Fig 7.10: Plot of Stress Distribution During Static Flexural Coupon FEA

At both load steps, the longitudinal stresses at the top and bottom planes of the elements were compared to the predictions from bending theory as discussed in section 7.1.3. Both sets of results were virtually the same and this is considered to be a validation of the FEA model.

At both load steps, the deflection at mid-span was compared to the deflection at the loading location (the cross-head displacement in the flexure tests). As was shown in appendix 5.3, the former was always equal to the latter multiplied by 1.33.

The failure ratio can be investigated for each layer of the material. This was done and the results for the Maximum Stress criterion, at an applied load of 0.5 kN, are shown below in figure 7.11. The four non-zero values in the figure are actual values calculated by the software (the zero has been added).

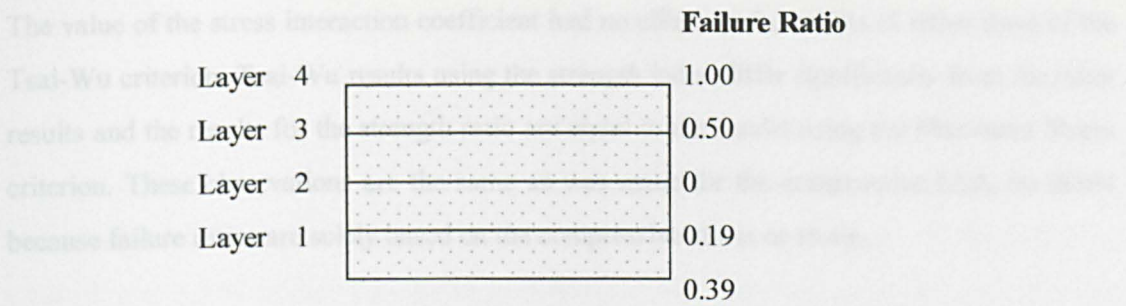


Fig 7.11: Layers of the Static Flexural FEA Model

ANSYS reports the maximum failure ratio seen within each layer. This is convenient as the maximum value at both extreme faces can be easily seen. A load of 0.5 kN produces a maximum stress at the top and bottom face of 124 MPa. The ratio of 1.00 in figure 8.8 denotes that compressive failure stress has been reached. The ratio of 0.39 for layer 1 corresponds to the ratio of the stress at the bottom face and the tensile failure stress. The other two failure ratios confirm that the stress is linearly decreasing from either face towards the neutral axis. The same pattern is seen for the strain at each layer. It is evident that initial failure will always occur at layer 4 due to compressive stresses or strains reaching their failure values.

For the Maximum Stress and Strain criteria, the failure ratio was found to be equal to the compressive stress or strain divided by the specified compressive stress or strain at failure. This confirms the hypothesis given in section 5.4 that initial failure occurred solely due to compressive stresses or strains reaching the value at failure.

Table 7.9 below lists the failure ratio, for layer 4, for each criterion along with the values of nominal stress and strain for each load step.

Load (kN)	Stress (MPa)	Strain (%)	Max Strain ratio	Max Stress ratio	Tsai-Wu	
					Str Index	Str Ratio
0.41	102	0.7	0.77	0.82	0.65	0.82
0.82	204	1.4	1.54	1.64	1.83	1.64

Table 7.9: Layer 4 Failure Ratios Determined During Static Flexural Coupon FEA

The value of the stress interaction coefficient had no effect on the results of either form of the Tsai-Wu criterion. Tsai-Wu results using the strength index differ significantly from the other results and the results for the strength ratio are equal to the results using the Maximum Stress criterion. These observations are the same as was made for the compressive FEA, no doubt because failure ratios are solely based on the compressive stress or strain.

The values at failure were determined and are presented below in table 7.10.

Value at Failure	Max Strain ratio	Max Stress ratio	Tsai-Wu	
			Str Index	Str Ratio
Load (kN)	0.53	0.50	0.50	0.50
Stress (MPa)	133	124	124	124
Strain (%)	0.90	0.85	0.85	0.85

Table 7.10: Failure Values Determined During Static Flexural Coupon FEA

As before, the Maximum Strain criterion predicts failure at a strain equal to the specified failure strain. The Maximum Stress criterion predicts earlier failure at a lower strain and at a stress equal to the specified failure stress. The Tsai-Wu criterion gives the same results as obtained from the Maximum Stress criterion.

In the compressive coupon testing, compressive failure of the specimen was catastrophic because it was the whole cross-section that failed. Initial failure in flexure tests was not catastrophic because it is only the top face in compression that fails; the stiffness of the material is reduced but the coupon can go on to sustain significantly higher loads. This should be represented in the FEA model.

It would have been desirable to simulate the compressive failure of the top face by, for instance, deleting one layer of the failed elements. However, this is not possible in ANSYS. Redefining the failed elements as having only three layers after initial failure was attempted but this produced erroneous results (a small change in the applied load produced an excessively large change in the elements' stress and strain and with no reduction in the original stiffness). Also attempted was redefining the failed elements so that layer four had a different set of material properties where the longitudinal elastic modulus was either reduced or zero.

However, this produced the same sort of erroneous results as when failed elements were modified to have only three layers.

The approach that was used was similar to that used for the shear FEA. Compressive failure values were redefined to be the stress and strain at which the ultimate flexural strength occurs (204 MPa at 1.9 % strain). The elastic modulus (for every layer) was reduced in such a way that the coupon's elastic behaviour, in subsequent analyses, would pass through these values of stress and strain. As with the shear FEA, this approach entailed that the degree of reduction of the elastic modulus differed slightly depending on the failure criteria.

Table 7.11 below lists the reduced elastic modulus used within each criterion.

Failure Criterion	Reduced Elastic Modulus	Percentage of Original
Maximum Strain	7200	49
Maximum Stress	7620	52
Tsai-Wu	7620	52

Table 7.11: Values of the Reduced Elastic Modulus for each Failure Criterion

Looking at flexural test results, after the ultimate flexural stress is reached, the stress remains fairly constant before gradually decreasing. It was considered necessary to represent this behaviour in the FEA model and so another modification was carried out. The simplest approach was to again reduce the elastic modulus, this time to zero which entailed a state of constant stress for any increase in strain.

Figure 7.12 below shows the results of all of the analyses for each failure criterion in terms of stress against strain. A typical curve from the flexural testing is included for comparison.

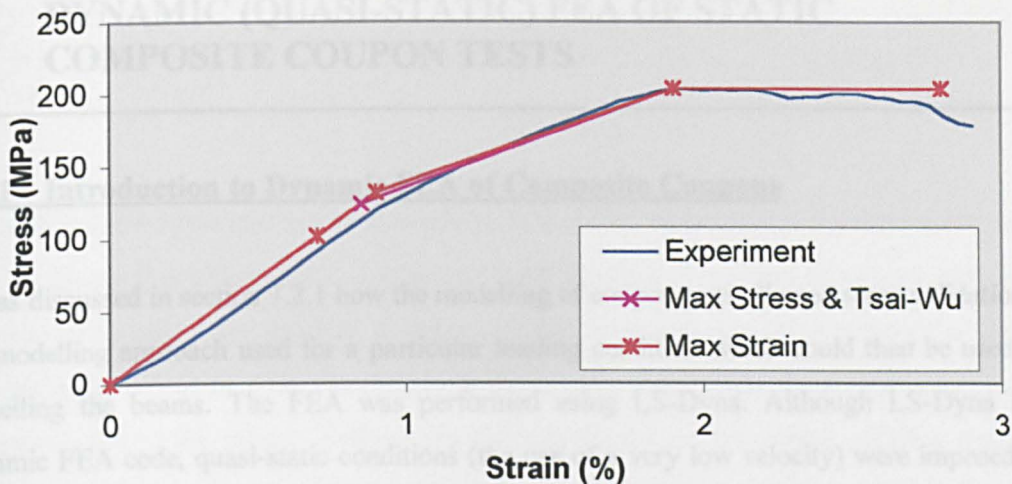


Fig 7.12: Plot of Stress v Strain for Static Flexural FEA & Test Results

All of the criteria can be said to represent the experimental behaviour fairly well. For flexural strains above about three percent, a further modification may be required. It is expected that this approach will transfer well to the FEA of beams however it is unfortunate that a method that simulated compressive failure more closely has not been established in this study.

7.3 DYNAMIC (QUASI-STATIC) FEA OF STATIC COMPOSITE COUPON TESTS

7.3.1 Introduction to Dynamic FEA of Composite Coupons

It was discussed in section 7.2.1 how the modelling of coupon tests allowed some validation of the modelling approach used for a particular loading condition which could then be used for modelling the beams. The FEA was performed using LS-Dyna. Although LS-Dyna is a dynamic FEA code, quasi-static conditions (the use of a very low velocity) were imposed for the modelling of static coupon tests. It was shown in section 4.2.4 how using a low velocity (such as 1 m/s) in the modelling of the steel beams could be used to correctly predict their quasi-static response. The same approach is used here in an attempt to model the static response of the composite coupons. In order to distinguish this FEA work from the static FEA using ANSYS, it shall be referred to as the Dynamic FEA.

7.3.2 Failure Criteria Within Dynamic FEA

LS-Dyna has only two composite failure criteria of any complexity or usefulness. These are implemented when the material models 'mat54' and 'mat55' are used. Other material models are available for composite materials but they all have more limited, or no, capabilities to represent material failure.

The first, more practical, criterion is the Chang-Chang criterion. It should be stated that the author is not aware of this criterion in the literature and the reference that the LS-Dyna manual [7.3] quotes is incorrect (this is why the criterion was not reviewed in section 2.3.6).

Four modes are defined within the criterion: two fibre modes and two matrix modes. Each mode relates to a principal plane of stress and its direction (tensile or compressive) and has a governing equation for when failure will occur. These are given below in equations 7.3 to 7.6. In these equations, longitudinal and transverse stresses refer to stresses in the direction of, and normal to, the loading respectively.

For a tensile longitudinal stress, $\sigma_x > 0$, Tensile Fibre failure occurs when:

$$\left(\frac{\sigma_x}{X_t}\right)^2 + \beta\left(\frac{\sigma_{xy}}{S_c}\right)^2 = 1 \quad \text{Eq(7.3)}$$

where X_t is the longitudinal tensile strength, S_c is the shear strength and σ_{xy} is the shear stress. The parameter β is a shear stress coefficient, specific to LS-Dyna, and its value is defined by the user. The parameter is given a value between zero and one. This allows the user to determine the degree of shear interaction in the Tensile Fibre mode. When the above failure criterion is met in this mode, LS-Dyna sets the longitudinal and transverse modulus, the shear modulus and Poisson's ratio to zero. The software evaluates whether the criterion has been met at each layer (integration point) defined for the material (elements).

For a compressive longitudinal stress, $\sigma_x < 0$, Compressive Fibre failure occurs when:

$$\left(\frac{\sigma_x}{X_c}\right)^2 = 1 \quad \text{Eq(7.4)}$$

where X_c is the longitudinal compressive strength. When failure in this mode occurs, the longitudinal modulus and Poisson's ratio are set to zero.

For a tensile transverse stress, $\sigma_y > 0$, Tensile Matrix failure occurs when:

$$\left(\frac{\sigma_y}{Y_t}\right)^2 + \left(\frac{\sigma_{xy}}{S_c}\right)^2 = 1 \quad \text{Eq(7.5)}$$

where Y_t is the transverse tensile strength.

For a compressive transverse stress, $\sigma_y < 0$, Compressive Matrix failure occurs when:

$$\left(\frac{\sigma_y}{2S_c}\right)^2 + \left[\left(\frac{Y_c}{2S_c}\right)^2 - 1\right]\frac{\sigma_y}{Y_c} + \left(\frac{\sigma_{xy}}{S_c}\right)^2 = 1 \quad \text{Eq(7.6)}$$

where Y_c is the transverse compressive strength. When failure in either the Tensile or Compressive Matrix mode is detected, the transverse modulus, the shear modulus and Poisson's ratio are all set to zero.

Examination of these different modes reveals that, if the β parameter is equal to unity, the criterion is exactly the same as the Hashin criterion that was presented in section 2.3.6. Nevertheless, the criterion shall be referred to as the Chang-Chang criterion within this thesis.

In general, failure occurs when the relevant failure stress is reached although, in most of the modes, there is an allowance for the interaction of different types of stress, particularly the shear stress. Failure modes termed 'fibre' and 'matrix' modes may not appear to apply to non-unidirectional materials (such as weaves with fibres running in perpendicular directions), however the fibre mode can be considered to be in the direction of the loading and the matrix mode to be in the direction normal to the loading. When it is not parallel to the loading direction, the material's fibre direction can be specified using a material angle, α . This is illustrated in figure 7.13 below for a weave material.

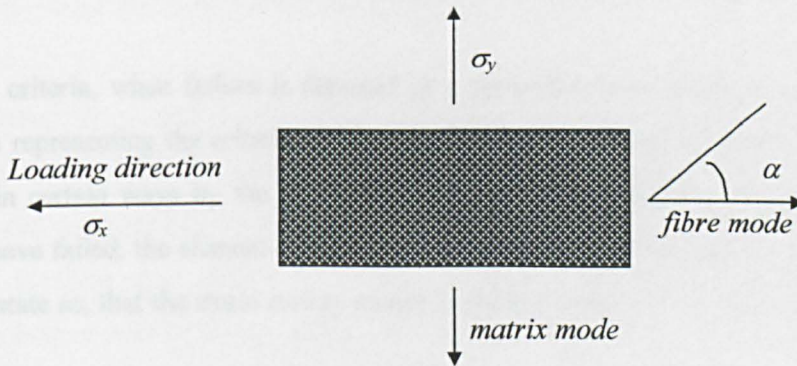


Fig 7.13: Failure Modes for a Weave Material

The second failure criterion, which is referred to as the Tsai-Wu criterion, has the same governing equations for each of the fibre modes as the Chang-Chang criterion. One equation governs both of the matrix modes and this is given below in equation 7.7. There is a greater degree of stress interaction within this relationship than found in the matrix modes of the Chang-Chang criterion. Failure is treated in the same manner as with the Matrix modes of the Chang-Chang criterion.

$$\left(\frac{\sigma_y^2}{Y_c Y_t}\right) + \left(\frac{\sigma_{xy}}{S_c}\right)^2 + \frac{(Y_c - Y_t)\sigma_y}{Y_c Y_t} = 1 \quad \text{Eq (7.7)}$$

It should be noted that LS-Dyna's version of the Tsai-Wu criterion is neither the conventional Tsai-Wu criterion, the strength index, nor the lesser-known strength ratio. The nature of the two fibre modes, and the fact that there are a number of different failure modes, mean that important differences exist. However, LS-Dyna's version shall still be referred to as the Tsai-Wu criterion.

The LS-Dyna manual [7.3] makes the statement that setting the value of β to zero gives a Maximum Stress criterion. This is true only for the failure conditions of the tensile fibre mode (by using β to prevent any shear interaction) and for the compressive fibre mode (where there is never any interaction from stresses other than the maximum compressive stress). Given that both of the matrix modes still involve some form of stress interaction, and the fact that there are still four separate failure modes, setting β to zero does not entail that the user is implementing the Maximum Stress criterion (the four equations of the Chang-Chang or the Tsai-Wu criteria do not reduce to the one equation of the Maximum Stress criterion).

For both criteria, when failure is detected at a particular layer (when any of the governing equations representing the criteria are satisfied) then the material properties of that layer are reduced in certain ways by the software and the analysis continues. When all layers of an element have failed, the element is deleted. It is assumed, although the LS-Dyna manual [7.3] does not state so, that the strain energy stored in deleted elements is simply dissipated.

The user cannot vary which of the material properties are modified or the degree by which they are reduced. The user cannot prevent element deletion when all layers have failed. Unlike the static FEA, it is not possible to run an analysis up until a certain point (such as initial failure), modify a material's properties or layer configuration and then restart the analysis.

Although both of the failure criteria available are stress-based (the user specifies failure stresses and the software compares the calculated stresses at each element with the failure stresses), the user can also specify failure strains (tensile, compressive and shear). When any

type of strain exceeds the specified failure strains then element deletion will occur although the user has the option to suppress this.

7.3.3 Dynamic Modelling of Tensile Coupons

(A) Modelling Procedure

The same geometry was used for the model as used during the static FEA. The number of elements was the same but LS-Dyna only allows the use of four-noded shell elements. Being a dynamic FEA code, the loading had to be applied in a different manner. The elements at one edge of the model were fixed to a separate part consisting of rigid elements. These rigid elements were given a high mass (1700 kg) and a low initial velocity (1 m/s). The software can report the nodal forces at the boundary. This allowed an assessment of the nominal longitudinal stress in the model (the ratio of the summation of the nodal forces and the area of the model's cross-section). A suitably high mass of the separate part was selected so that its displacement would be virtually unaffected by the elastic restraint of the coupon model. This was verified to be true in each of the analyses. The ratio of the part's displacement to the length of the coupon model gave the nominal strain.

Six analyses were performed: three involving the Chang-Chang criterion and three implementing the Tsai-Wu criterion. For each criterion, two of the analyses were standard analyses and only differed in the value of the β parameter (set to zero and one). It shall be seen that, for these analyses, the stresses always reached the failure stresses before the strains reach the failure strains. These analyses are therefore termed the stress-based analyses. The third analysis for each criterion used a β value of zero however all of the failure stresses were set artificially high so that failure would only occur through element deletion when the failure strains were reached. This is termed the strain-based analysis.

In all of the analyses, element deletion was activated when the failure strains were reached. It was considered that this would simulate the fracturing phenomenon seen during testing. Failure and deletion of an element at a particular cross-section would cause the rest of the elements at that cross-section to sustain a greater stress and these elements would also soon

fail if they had not done so already. Thus, a crude representation of crack propagation is implemented though there is no detailed simulation of the fracture process.

(B) Results of Analyses

Post-processing revealed that the various stress and strain distributions of the elements representing the coupon in all cases remained highly uniform, and at approximately nominal values, up until failure occurred. It was therefore assumed that the model, in terms of the elements and mesh density used, was sufficiently accurate.

LS-Dyna allows identification of the relevant failure mode. For the stress-based analyses, it was, as expected, always failure in the tensile fibre mode that occurred which soon led to the tensile failure strain being reached which would cause element deletion. In the strain-based analyses, failure only involved element deletion when the tensile failure strain was reached. In both cases, the failure was highly catastrophic and tended to occur at various locations within the specimen. This is no doubt because the model does not account for imperfections. During an actual test, fibre breakage would occur at an imperfection and spread in the form of a crack leading to failure within the specimen at one cross-section. In the FEA model the 'material' is virtually uniform and reaches the failure stress at much the same time. The longitudinal stress distributions (in the direction of the loading) within the elements before and after failure are shown below in figure 7.14.

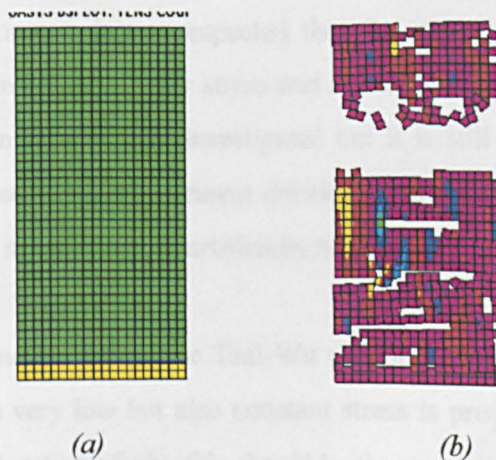


Fig 7.14: Longitudinal Stress Distribution in Tensile Coupon FEA (a) Before Failure and (b) After Failure

7.3.4 Dynamic Modelling of Compressive Coupons

A graph of the FEA predictions of stress against strain is shown below in figure 7.15, which also includes a typical tensile test result for comparison. It can be seen that the FEA always predicts a stiffer response than is seen in the experiments. As with the static FEA, viscoelastic effects were not represented in the FEA model.

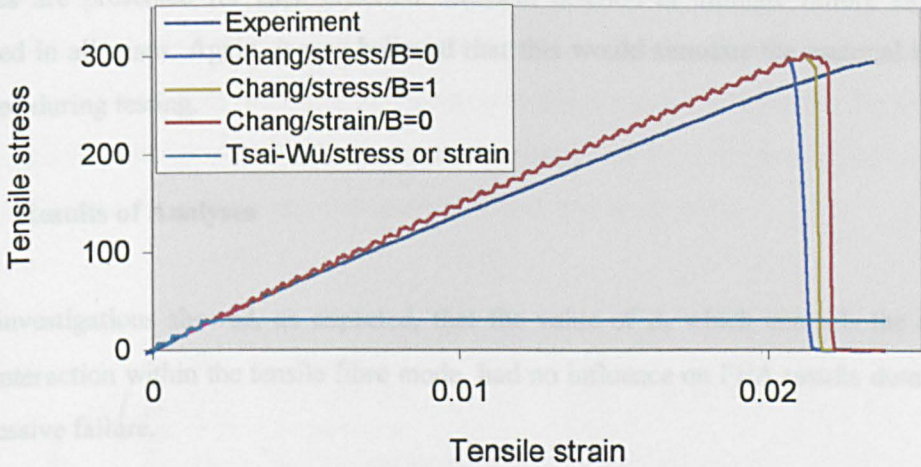


Fig 7.15: Dynamic FEA predictions & Test Results for Stress v Strain in Tensile Coupons

Figure 7.15 shows that, for the stress-based Chang-Chang analyses, setting β to one caused failure at a slightly higher stress and strain than for a β value of zero. Investigations not presented here showed that setting β to a value between zero and one gave predictions lying between these two extremes. Using a strain-based analysis gave slightly higher values again. However, there is little difference between these three sets of results and, in general, failure is at the specified failure stress. It was expected that the strain-based analyses would have predicted failure at a significantly higher stress and at the specified failure strain but this was not the case. The reason for this was investigated but it is still not clear. It appears to be because, for a strain-based analysis, element deletion involves elements that have not failed any criterion (the failure stresses are set artificially high).

It is clear that all the analyses using the Tsai-Wu criterion produced erroneous results. Not only is the failure stress very low but also constant stress is predicted after failure, which is very unrealistic. No explanation of why this should be the case can be offered.

7.3.4 Dynamic Modelling of Compressive Coupons

(A) Modelling Procedure

The FEA of compressive coupon testing involved the same model and restraints as used for the tensile FEA but with the load direction reversed. Results of both stress- and a strain-based analyses are presented for each criterion. Element deletion at ultimate failure strains was activated in all cases. Again, it was believed that this would simulate the material behaviour observed during testing.

(B) Results of Analyses

Early investigations showed, as expected, that the value of β , which controls the degree of shear interaction within the tensile fibre mode, had no influence on FEA results dominated by compressive failure.

For all of the analyses, LS-Dyna predicted that the stress and strain distributions remained uniform up until failure. When failure did occur, it was again catastrophic though more localised at one cross-section (at the coupon's mid-length) than was found for the FEA of tensile coupons. There was also evidence of the influence of in-plane shear with 45° crack formations. These longitudinal stress distributions are shown below in figure 7.16.

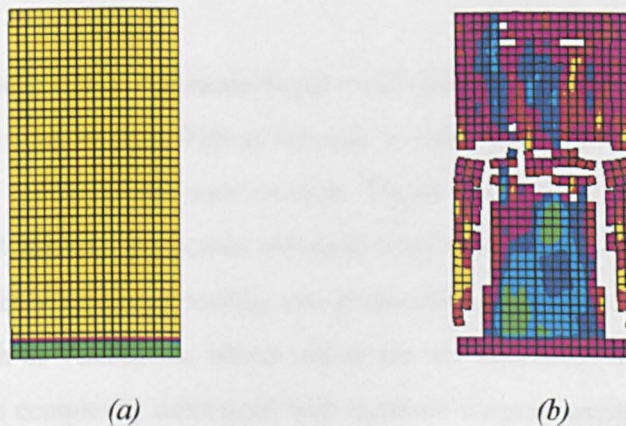


Fig 7.16: Longitudinal Stress Distribution in Compressive Coupon FEA (a) Before Failure and (b) After Failure

A graph of the FEA predictions of stress against strain is shown below in figure 7.17 which again includes a typical test result for comparison. It can be seen that all FEA analyses predict the same stiffness but differ on the point of failure or what happens following failure. The predicted stiffness is again higher than seen in experimental testing and this is due, apart from the viscoelastic effects described above, to another reason. Only one elastic modulus can be defined for each material direction and this was chosen to be the tensile modulus. However, experiments gave a higher average tensile value (14.8 GPa) than the compressive value (13.4 GPa) and so FEA predictions based on a tensile modulus will be over-stiff. The compressive modulus could have been used but, as only one modulus can be selected for the whole beam and the tensile modulus is generally favoured at a component level, it was deemed important to evaluate FEA results using properties associated with the whole beam.

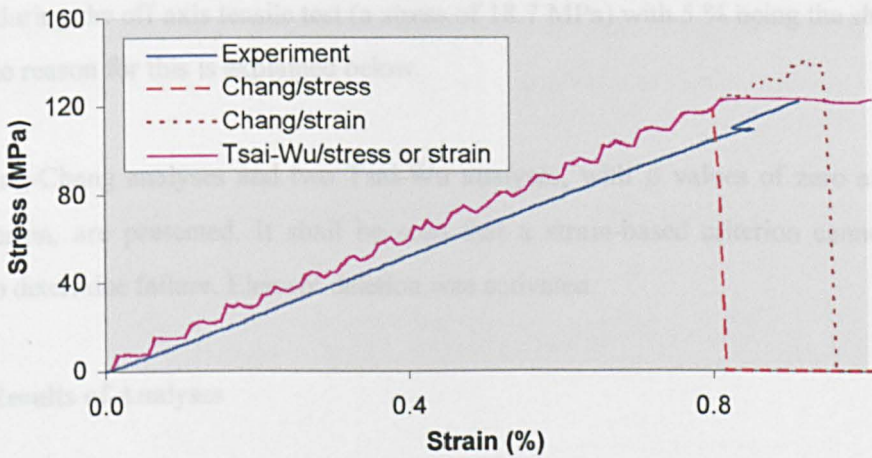


Fig 7.17: FEA predictions & Test Results for Stress v Strain in Compressive Coupons

The difference between stress- and strain-based predictions is even more pronounced than was found in the tensile coupon FEA. This is because, in this case, the strain-based analyses did continue until the failure strain was reached. Figure 7.17 illustrates that any dynamic modelling that uses material properties obtained from static coupon tests will be to some extent flawed. Not only are higher loading rate properties neglected but static test results may contain effects such as viscoelastic effects which are not significant in dynamic conditions. However, given the complexity associated with dynamic coupon testing, this problem is not easy to rectify.

The Chang-Chang analyses offer realistic predictions of coupon behaviour. Both the Tsai-Wu analyses predicted failure at the maximum stress but then a state of constant stress occurred. This is not realistic and could introduce large errors into the FEA of whole beams.

7.3.5 Dynamic Modelling of Shear Coupons

(A) Modelling Procedure

Shear coupon testing was, in essence, a tensile coupon test but with the composite fibres at 45° to the direction of the loading. Therefore, the FEA of this test used the same geometry and loading conditions as the tensile test FEA with the only difference being the inclusion of the material angle, α , which was set to 45° . The shear failure stress was set to the value at 5 % strain during the off axis tensile test (a stress of 18.7 MPa) with 5 % being the shear failure strain. The reason for this is explained below.

Two Chang-Chang analyses and two Tsai-Wu analyses, with β values of zero and one for each criterion, are presented. It shall be seen that a strain-based criterion cannot be used directly to determine failure. Element deletion was activated.

(B) Results of Analyses

While the software could report the correct shear stress, the shear strain reported was not equal (rather it was significantly less) to the difference between the longitudinal and transverse strain. This had the implication that all strain-based analyses predicted an elastic response without the shear failure strain being reached. Element deletion would have occurred when the tensile failure strain was reached (compressive strains were very small due to the loading condition). However, this would occur at an excessively high shear stress. These unrealistic results shall not be considered further.

Review of the other analyses indicated that, from the outset, complex stress patterns would develop. Refining the element mesh did not affect this stress pattern. A typical pattern for the shear stress is shown below in figure 7.18.

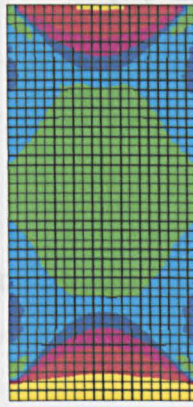


Fig 7.18: Longitudinal Stress Distribution in Shear Coupon FEA

Because of this stress pattern, determining the results in terms of the shear stress against the shear strain was no longer straightforward. Since the central region of the model in figure 7.18 is both the largest region and the region of highest stress, values from this location were noted at regular intervals. A graph of shear stress against shear strain is shown below in figure 7.19.

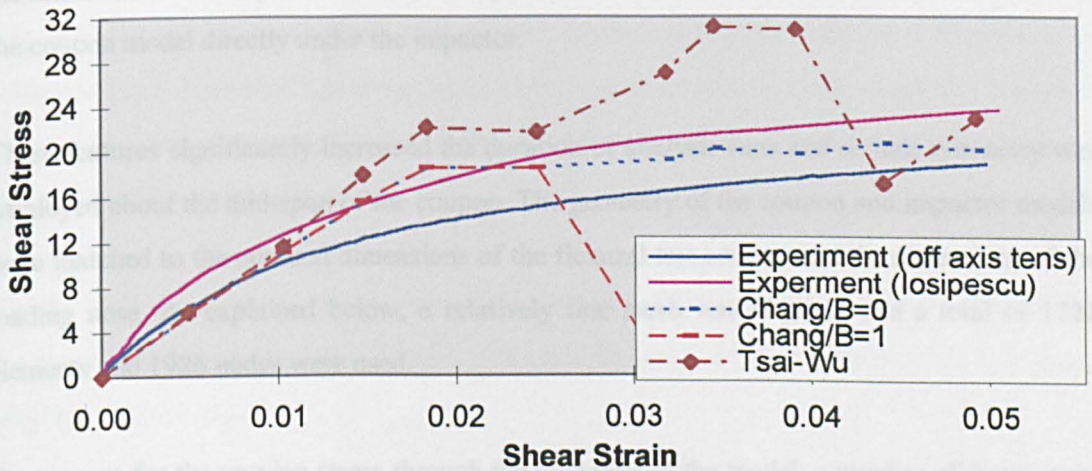


Fig 7.19: FEA predictions & Test Results for Stress v Strain in Shear Coupons

For the Chang-Chang criteria, the analysis using a β value of zero predicted initial failure at the shear failure stress and then the stress was more or less constant for any increase in strain. It is for this reason that the failure stress was taken to be the stress at 5 % during the off axis tensile test (18.7 MPa). Using the offset strength from either shear test (about 11.7 MPa) or the stress at 5 % from the Iosipescu shear test (23.3 MPa) would have produced results that were too high or too low respectively. For the analysis that used a β value of one, the greater influence of the shear behaviour in the criterion caused failure in both the Tensile Fibre and

Matrix modes when the failure stress was reached. The reduction in material properties this entailed soon led to the tensile failure strain being reached which in turn caused element deletion and a sudden drop in the shear stress to zero.

The value of β had no influence of the results of the Tsai-Wu criterion. The results from both analyses were the same and somewhat unusual in that the shear stress significantly exceeded the failure stress and also fluctuated over the strain range.

7.3.6 Dynamic Modelling of Flexure Coupons

(A) Modelling Procedure

Dynamic modelling of the flexure test involved modelling of the impactor and the use of contact elements. The impactor was modelled using solid elements and assigned the properties of a typical steel material. It was given an initial velocity of 1 m/s. A number of elements on the underside of the impactor model were specified to be contact elements, as were elements of the coupon model directly under the impactor.

These features significantly increased the duration of analysis runs and so half symmetry was employed about the mid-span of the coupon. The geometry of the coupon and impactor models were matched to the nominal dimensions of the flexural test coupon and the dimensions of the loading nose. As explained below, a relatively fine mesh was required and a total of 1728 elements and 1926 nodes were used.

To account for the varying stress through the thickness of the model, a number of layers were defined. In LS-Dyna, this is done by specifying the number of integration points. Six integration points, and thus six layers, were defined.

Both Chang-Chang and Tsai-Wu analyses were performed, each with a β value of zero and one. No strain-based analyses were even attempted. It was desirable that a gradual, progressive type of failure, involving failure of successive layers, be represented but strains reaching failure values would only cause element deletion which is a catastrophic form of failure.

(B) Results of Analyses

Examination of the longitudinal stress in the model before failure showed the expected distribution for a coupon in bending. In all of the layers (an even number of layers entailed that no layer represented the neutral axis) the stress was constant between the impactor and the plane of symmetry and linearly decreased to zero from the impactor to the support location. Through the thickness, the longitudinal stress varied in a linear manner.

For the Chang-Chang analyses, the first layer failed in the Compressive Fibre mode at a mid-span deflection of about 5 mm. This was for all the elements between the impactor and the plane of symmetry. Failure did not occur in the second layer until a deflection of around 7 mm. Immediately following this, there was total failure of the model. In the first two or three layers, the elements directly under the impactor had failed in many of the different failure modes and a small number of elements had been deleted. The model could be seen to have virtually split in two. Yet, surprisingly, none of the elements in the tensile layers had failed in any failure mode. It is not clear why element deletion occurred though it is thought to be related to local regions of high stress caused by contact with the impactor. Early investigations had revealed this phenomenon and although the element mesh was significantly refined this did not prevent the catastrophic failure.

For the Tsai-Wu analyses, the mode and time of failure were as before but it was noticed that the longitudinal stress was low from a mid-span deflection of about 3 mm. It is not known why this was the case.

The software can report the total contact force as a function of time. This force, in the out-of-plane direction, corresponds to the applied force and can be used to derive the flexural stress in the same manner as done for test data using equation 5.6. The flexural strain is simply the longitudinal strain and is determined from the time data: the displacement of the impactor is equal to the product of the impactor's velocity and the time from impact and the strain is related to the impactor's displacement using equation 5.5. Using this method gives a more continuous plot of stress against strain. A graph of the flexural stress against the flexural strain is shown below in figure 7.20 for each of the analyses.

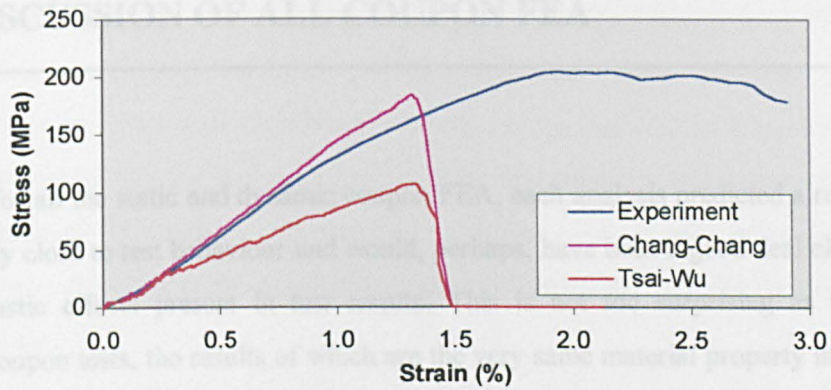


Fig 7.20: FEA predictions & Test Results for Stress v Strain in Flexural Coupons

The value of β had no effect on either of the criteria. This is no doubt because failure is dominated by the Compressive Fibre mode which does not include this parameter. For the Chang-Chang analyses, initial failure caused a small change to the material's stiffness but not to the degree seen in test results. Nevertheless, the Chang-Chang analyses can be said to provide realistic predictions up until a flexural strain of about 1.3 %. After that point the catastrophic failure is unrealistic. The Tsai-Wu analyses do not provide realistic predictions of the material's behaviour even before the point of initial failure.

7.4 DISCUSSION OF ALL COUPON FEA

Generally, for all the static and dynamic coupon FEA, each analysis predicted a response that is reasonably close to test behaviour and would, perhaps, have been a good deal closer but for the viscoelastic effects present in test results. This is not too surprising as the FEA is modelling coupon tests, the results of which are the very same material property inputs for the FEA. However, the coupon modelling has served three important functions. Firstly, the strengths and limitations of the static and dynamic FEA software have become evident. Secondly, the suitability (or lack of suitability) of particular failure criteria, or at least how they are implemented within the FEA, has been assessed. Thirdly, FEA techniques for particular loading conditions have been developed. It is expected that these techniques can transfer to the modelling of more complex structures such as the side impact beam. These three functions are discussed in more depth below.

Ansys is fairly simplistic in the manner that it treats composite failure. The analyses are entirely elastic with the failure calculations being somewhat marginal or additional to the solution; even obtaining the output of the failure ratios requires some effort. This does at least allow the user more control on how material failure is simulated. Yet, this control is essentially limited to the modification of material properties or failure values for selected elements. Making changes to the model's geometry or layer configuration invariably leads to erroneous results.

LS-Dyna is perhaps more sophisticated in its solution in that modifications to specific elements to represent failure are automatically carried out. But this is at the expense of user control. In fact, in certain conditions, it may not be possible to realistically simulate the measured behaviour of the material (at least beyond a certain value of deflection or strain).

It is clear from the static and dynamic coupon modelling that certain failure criteria, in particular loading conditions, are more suitable while other criteria are clearly inappropriate. There is no requirement to choose the best criterion at this stage: a number of different criteria can be implemented in the FEA of the composite beam. However, a number of points are worth noting.

In all of the different types of static coupon FEA, any one of the three criteria implemented in ANSYS gave results that correlated well with test data. There was often a noticeable difference between stress- and strain based analysis results, but it is not known which type of analysis best represents the material. For the Tsai-Wu criterion, there was no appreciable difference between the results of the analyses using either the strength index or the strength ratio. Similarly, the value of the stress interaction coefficient had virtually no influence on the analyses results.

In all of the dynamic modelling, only the Chang-Chang analyses provided a realistic simulation of test behaviour. The Tsai-Wu analyses often produce erroneous results. This is either because the criterion is not applicable or because it is not correctly implemented within the FEA software. The value of β was often unimportant but, for shear loading conditions, only a value of zero (therefore no shear interaction in the Tensile Fibre mode) produced realistic results. In some loading conditions, the difference between stress- and strain-based analyses was comparable to that seen for the static FEA but, in other conditions, a strain-based analysis was not appropriate as it would have led to catastrophic failure.

In general, the priority in the modelling approach has been to produce analyses results that correlate with test data for different loading conditions. Such an approach has entailed treating the failure in some loading conditions differently to the failure in others. This priority was deemed more important than, for instance, modelling the mechanics of the failure mode. This is partly because of the limitations of failure criteria which assume an elastic response up until failure and there is little consensus on how a failed material should be treated. The criteria themselves do not particularly represent the mechanics of failure. It is also because FEA models tend to treat the advent of failure with some severity. In the dynamic FEA, elastic properties of a failed layer are reduced to zero. In the static FEA, for failure of only one layer, the user cannot reduce the properties of only that layer (or remove the layer).

The approach of correlating coupon FEA predictions with coupon test data, to define the degree of reduction of material properties in the analysis of more complex structures, may prove to be a powerful modelling technique. The coupon testing usually has to be carried out for any FEA modelling to determine the material properties. Taking the effort to model the coupon tests provides a validation of the way that material failure is treated, both qualitatively and quantitatively.

7.5 STATIC FEA OF COMPOSITE BEAM

7.5.1 Introduction to Static FEA of Composite Beam

Chapter six presented the static and impact testing of the composite beams. In this section, the static modelling of the composite beam is presented and the predictions of the modelling compared with static test results. The general method used was to apply the techniques developed in the coupon modelling. The analyses, using ANSYS, were elastic until failure and then failure would be represented in a manner specific to the loading condition (tension, compression or shear) in which any particular elements reached the failure values.

7.5.2 Static Modelling of Beam

(A) Modelling Procedure

The static modelling of the composite beam was performed using Ansys 5.4. A quarter model of the beam with symmetrical boundary conditions was used. Symmetry was applied about vertical planes at both the mid-span and the mid-width of the beam.

The top flange of the beam consists of a six millimetre layer of the Twintex material with a fibre orientation of $\pm 45^\circ$, the same configuration as the rest of the beam, bonded to a four millimetre layer of unidirectional Twintex. This part of the beam was modelled using two different approaches.

The first approach was to represent the full flange using one plane of shell elements. Eight layers were specified for these elements: four layers (each 1.5 mm thick) with a material orientation angle of 45° and four layers (each 1 mm thick) with an angle of 0° . The model using this approach is referred to as the standard model.

The second approach was to model each of the two layers of the top flange with a separate plane of shell elements. This presented a common problem encountered in any FEA modelling, using shell elements, of two adjacent components. The use of shell elements will entail

representing a three-dimensional layer with a two-dimensional reference plane. Two layers of a structure that are physically in contact (whether connected in some manner or not) must be modelled using two planes of elements that are separated by some distance. This distance will be the summation of half the thickness of each layer. This is illustrated, for the two layers of the top flange of the composite beam, in figure 7.21 below.

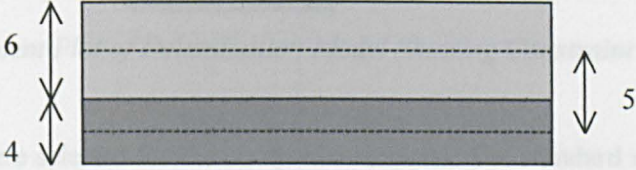


Fig 7.21: Illustration of Modelling of Adjacent Layers

As the nodes of each layer of elements are at a distance from each other, they are not connected and a method is required to specify their relationship with each other. However, this can be done using *constraint equations*. These equations can be assigned to a set of nodes and will ensure that the displacement of one node in any degree of freedom specified by the user corresponds to the displacement of all other nodes in the same set for the same degrees of freedom.

In the model of the composite beam, constraint equations, for all degrees of freedom, were applied to a number of pairs of nodes. Each pair consisted of one node from the elements of the first layer and the other node, belonging to the second layer, which had the same spatial co-ordinates except for in the out-of-plane axis. It was not practical to apply constraint equations to every node of the top flange. Rather, the equations were applied to every fourth node across the width of the flange, generally at 100 mm intervals along the beam's length though at 50 mm intervals near the mid-span. This is shown below in figure 7.22. The advantage using this approach, unlike the first approach, is that delamination of the two layers can be simulated by deleting the constraint equations at the appropriate location. The model using this second approach is referred to as the delamination model.

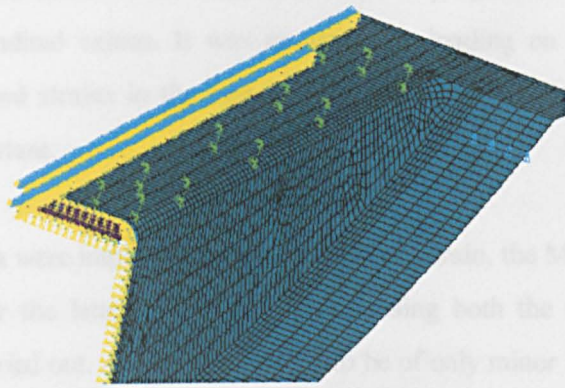


Fig 7.22: Element Plot of Delamination Model Showing Constraint Equations

'Shell99' elements were selected for the composite material. The standard model consisted of 2750 elements and 8662 nodes while the delamination model consisted of 3250 elements and 9132 nodes.

For both models, to represent the simply supported condition, the nodes at a distance of 375 mm from the mid-span, the support location, were constrained only in the vertical axis with rotation still permitted. Ansys has the feature that it can plot the two-dimensional elements in a three-dimensional form (the elements have the specified thickness). All of the boundary conditions are shown below for the standard model, in a three-dimensional form, in figure 7.23.

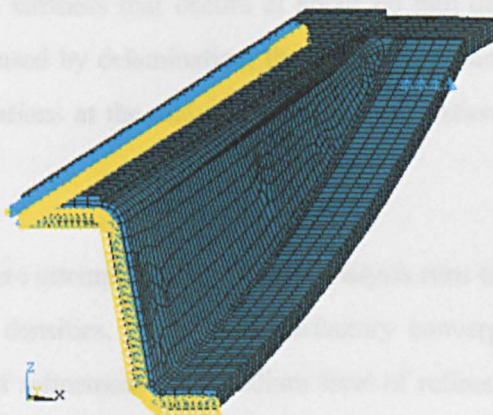


Fig 7.23: Element plot of Standard Model Showing Boundary Conditions

The material's properties and the failure stresses and strains were assigned in the same manner as for the composite coupon FEA. For the unidirectional layer of the standard and

delamination models, the values of the transverse material properties are not known but they were set to the longitudinal values. It was assumed the loading on the beam would have entailed low stresses and strains in the transverse direction and so the transverse properties were relatively unimportant.

All three failure criteria were implemented: the Maximum Strain, the Maximum Stress and the Tsai-Wu criterion. For the latter criterion, analyses using both the strength index and the strength ratio were carried out. As it has been seen to be of only minor importance (see section 7.2), only one value of the stress interaction coefficient (-1) was used.

One node on the top flange at mid-span was assigned a value of deflection (the node at mid-width). The analysis was run with the user-defined value of deflection and the magnitude of force, determined by the software, was noted. The analysis was then re-run using a higher value of deflection. Early investigations revealed at what deflection first failure would occur in any of the elements for a particular failure criterion. The analysis was run to this value of displacement and then the properties of the failed elements were modified in a manner dependent on the type of failure.

Section 6.1.3 explained how it could not be determined, during static beam tests, at what point delamination occurred. However, it shall be seen that the other forms of failure observed during the tests can be predicted by the FEA at certain levels of deflection which do not include the sudden drop in stiffness that occurs at about 60 mm deflection. If it is assumed that this sudden drop is caused by delamination, then this failure mode can be represented by deleting the constraint equations at the mid-span of the delamination model at a deflection of 60 mm.

Different mesh densities were attempted during initial analysis runs to justify the element mesh used. For practical mesh densities, there was satisfactory convergence in the results of a medium and a high level of refinement. The medium level of refinement was selected to keep analysis times as short as possible. It was assumed that the coupon modelling verified the accuracy of the elements used.

(B) Results of Analyses

Results of the analyses, for both beam models and for each failure criterion, showed that the first elements failed at a deflection of about 20 mm. These elements were all located at the top flange of the model at mid-span and this is shown qualitatively in figure 7.24.

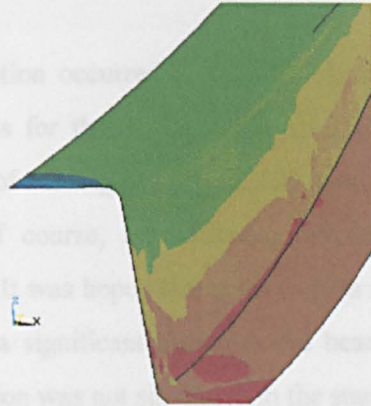


Fig 7.24: FEA Plot of Failure Ratio in Standard Beam Model At Deflection of 20 mm

It was found, for the Maximum Stress and the Tsai-Wu criteria, that the failure ratio was equal to half the element's longitudinal stress, divided by the shear failure stress. Given these elements' material orientation angle of 45° , half of the longitudinal stress (whether tensile or compressive) corresponds to the shear stress. Therefore, failure occurred when the failure shear stress was reached. For the Maximum Strain criterion, failure occurred when the failure shear strain was reached.

This form of failure was treated in the same manner as for shear failure of the composite coupon model. The shear modulus of the failed elements was reduced to the values that were given in table 7.8 for each failure criterion. Each analysis was then restarted.

By a deflection of 50 mm, a number of other elements had failed, also in shear. These elements were in the beam's top corner fillet and spreading to the side walls. The shear modulus of these elements was also reduced and the analyses continued.

It should be noted that, by a deflection of 50 mm, two of the three obvious forms of damage to the beam, observed during beam tests, have already occurred: failure at the top flange and at

the top corner fillet (spreading to the side walls). Beam test results for this stage of deflection show only a gradually decreasing stiffness and it is not until a deflection of 60 mm that there is a sudden drop in stiffness. The two possible reasons for this are that the FEA model is not representing the failure adequately or that the stiffness drop is caused by the third observed form of damage: delamination of the two layers of the top flange. The former reason seems less likely since, as shall be seen, the FEA predictions of the load sustained by the beam correlate well with experimental results.

It was assumed that delamination occurred at 60 mm. At this point, for the delamination model, the constraint equations for the nodes at mid-span of the model were deleted. This simulated a delaminated area of rectangular shape, 100 mm in length and 52 mm wide (the width of the top flange). Of course, any distance between the constraint equations is effectively a delaminated area. It was hoped that such an area at the most critical region of the beam, mid-span, would have a significant effect on the beam's performance. The analyses were then restarted. Delamination was not simulated in the standard model.

For both models, most of the cross-section of the beam had failed by a deflection of 80 mm. The shear modulus of these elements was reduced. It was also noticed that the elements of the unidirectional layer at mid-span had recently failed. This failure was direct compressive failure and it was treated in the same manner as used for the flexural coupon FEA. The elastic modulus was reduced, for each criterion, to the values given in table 7.11. The analyses were then restarted.

There was no significant change in the elements' failure ratio distribution for higher levels of deflection. Therefore, no further modifications were required. Figure 7.25 below is a plot of all the analyses results in terms of load against mid-span deflection for both of the FEA models. The results of a typical static beam test are included for comparison.

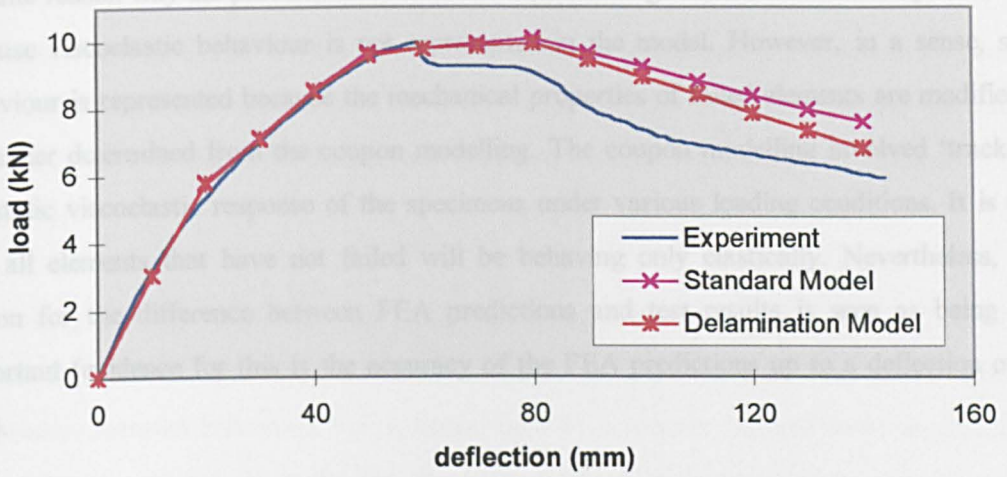


Fig 7.25: Plot of Load v Deflection for Static Beam FEA & Test Results

For both models, the results for each criterion were virtually the same. Therefore, the results for only one of the criteria (the Maximum Stress Criterion) are shown in the above figure. This is because it was not practically possible to modify each element at the exact point of failure. Rather, judgement was used to choose deflection values where a significant change in the number of failed elements had taken place. Since the difference in the results of each criterion was small (refer to section 7.2), there was no difference in the deflection value where a change had occurred.

The predictions of both models for the initial stiffness of the beam correlate very well with experimental results. Even before any modifications are made (and even though the analyses are elastic) there is a slight decrease in the beam's stiffness as the deflection increases. This is probably due to the effect of large deflections; as was originally intended, the beam is opening up a little which causes its stiffness to decrease.

Both models are in good agreement up until a deflection of 60 mm. At this point, delamination is simulated in the delamination model which causes a decrease in the predicted stiffness. However, the decrease is not particularly large and there is certainly not the sudden drop in load seen in the experimental results. The load sustained by the beam only begins to decrease from a deflection of 80 mm. This is thought to be mainly due to failure of the beam's side wall, which is the stiffest part of the beam in bending, and also because of compressive failure of the unidirectional layer.

Another reason why the predictions of the FEA model diverge from test results may have been because viscoelastic behaviour is not represented in the model. However, in a sense, such behaviour is represented because the mechanical properties of failed elements are modified in a manner determined from the coupon modelling. The coupon modelling involved ‘tracking’ the static viscoelastic response of the specimens under various loading conditions. It is true that all elements that have not failed will be behaving only elastically. Nevertheless, this reason for the difference between FEA predictions and test results is seen as being less important (evidence for this is the accuracy of the FEA predictions up to a deflection of 60 mm).

Figure 7.26 below is a plot of both models’ predicted energy absorbed by the beam as a function of deflection. Typical static beam test results are included for comparison. The figure shows, once again, that FEA predictions correlate fairly well with, but overestimate, experimental behaviour.

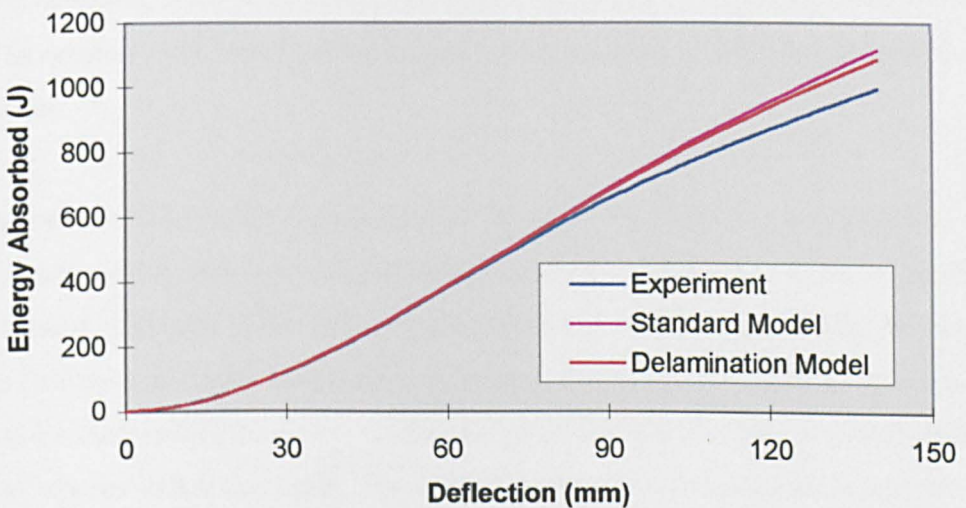


Fig 7.26: Plot of Energy Absorbed v Deflection

In general, it is believed that both FEA models offer reasonable predictions of the composite beam’s load response. This is particularly true up until first failure and even beyond until delamination occurs (if this assumption is correct). The modelling of the delamination failure produced more limited success. Nevertheless, the predictions remain reasonable. However, it should be noted that the FEA predictions overestimate the load carrying and energy absorbing capabilities of the beam and so they are not conservative.

It is believed that better models could be developed which would include more detailed modelling of the delaminated area. This would require further investigations into the damage within the beam to determine the size and shape of the delaminated area as a function of the deflection.

It is recognised that there may be other reasons why the FEA predictions differed from experimental results, apart from the limited simulation of delamination and not representing viscoelastic material behaviour. For instance, both FEA models required some simplification of the beam's geometry. In particular, the gradual change in thickness of the top corner fillet (from 6 mm to 10 mm) was not represented.

7.6 DYNAMIC FEA OF COMPOSITE BEAM

7.6.1 Introduction to Dynamic FEA of Composite Beam

This section presents the dynamic modelling of the composite beam and the predictions from the modelling are compared with impact test results. Once again, the general approach used was to apply the techniques developed in the coupon modelling. LS-Dyna was used for the analyses.

7.6.2 Dynamic Modelling of Beam

(A) Modelling Procedure

The dynamic modelling of the composite beam was performed using LS-Dyna v940. As for the static modelling, a quarter model of the beam with symmetrical boundary conditions was used. The symmetry was applied about vertical planes at both the mid-span and the mid-width of the beam.

The beam was modelled using four-noded shell elements. The striker was also modelled, using solid elements, which were assigned the material properties of nylon 66 except for the density of the material. The value of the density was set so as to produce a total mass for the striker of 21.7 kg (the same as during impact tests on beams). Initial velocities of 8 or 9.75 m/s were specified for each node of the striker. Surface-to-surface contact elements were defined for the interface between striker and beam. The applied load against time was determined using the total contact force between these contact elements.

As for the static modelling of the composite beam, two models were employed: the standard model and the delamination model. In the standard model, the top flange of the beam was modelled using one plane of elements, which were assigned eight layers (eight integration points were specified). The upper four layers were given a thickness of 1.5 mm and a material orientation angle of 0°. The lower four layers were assigned a thickness of 1 mm and an angle of 45°. The standard model consisted of 2447 nodes and 2239 elements.

The delamination model represented the beam's top flange using two planes of elements. These elements were connected by nodal constraints. A number of different types of constraints are available within LS-Dyna but the only type suitable (for the nodes of shell elements that are not coincident) is termed a spot weld constraint. It is possible for the user to specify failure of the nodal constraint at a particular value of either strain or the nodal force. It is intended, according to the LS-Dyna manual [7.3], that using strain to specify failure provides a ductile mode of failure while using force provides a brittle mode. A value of force was used, to represent the more brittle thermoplastic material, which was set to the dynamic collapse load of 11.5 kN. The delamination model consisted of 3028 nodes and 2731 elements. Figure 7.27 below shows the delamination model of the beam and striker.

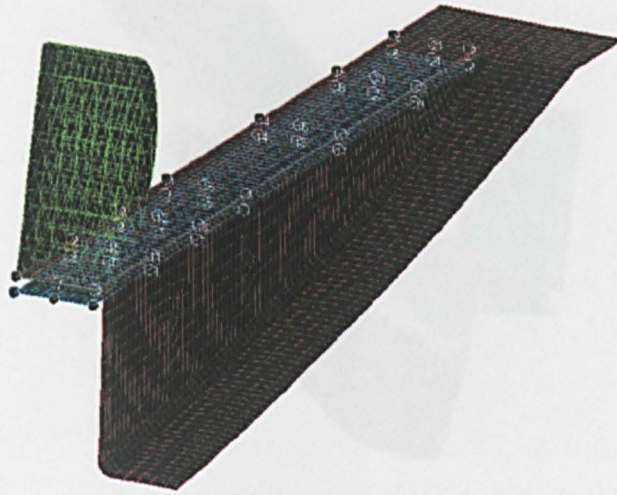


Fig 7.27: Delamination Model Including Nodal Constraints

Four analyses were performed for each FEA model at each of the two impact velocities: two involving the Chang-Chang criterion and two implementing the Tsai-Wu criterion. There were therefore a total of sixteen analyses. For each criterion, the two analyses differed only in the value of the β parameter (set to zero and one). In addition, an analysis was run where the elements had only orthotropic properties (using the 'mat2' material model) where no failure was implemented. It was considered informative to investigate the purely elastic response of the beam for a given level of impact energy.

No strain-based analyses were attempted (where the failure stresses are set artificially high). It was considered that failure control using only element deletion was not appropriate for the beam model. Element deletion, when any failure strains were reached, was activated in initial

analysis runs. However, it was found that this caused an unrealistic catastrophic failure of the beam and so it was not activated in subsequent analyses.

(B) Results of the Analysis

Post-processing revealed the various stress distributions for each analysis. In each case, the results were qualitatively similar and showed a number of similarities to the static analysis. Before collapse, they were within elastic limits and were as expected for a simply supported beam in bending. The stresses varied from the beam end to mid-span and from the neutral axis to the top and bottom flanges. This is qualitatively shown below in figure 7.28.

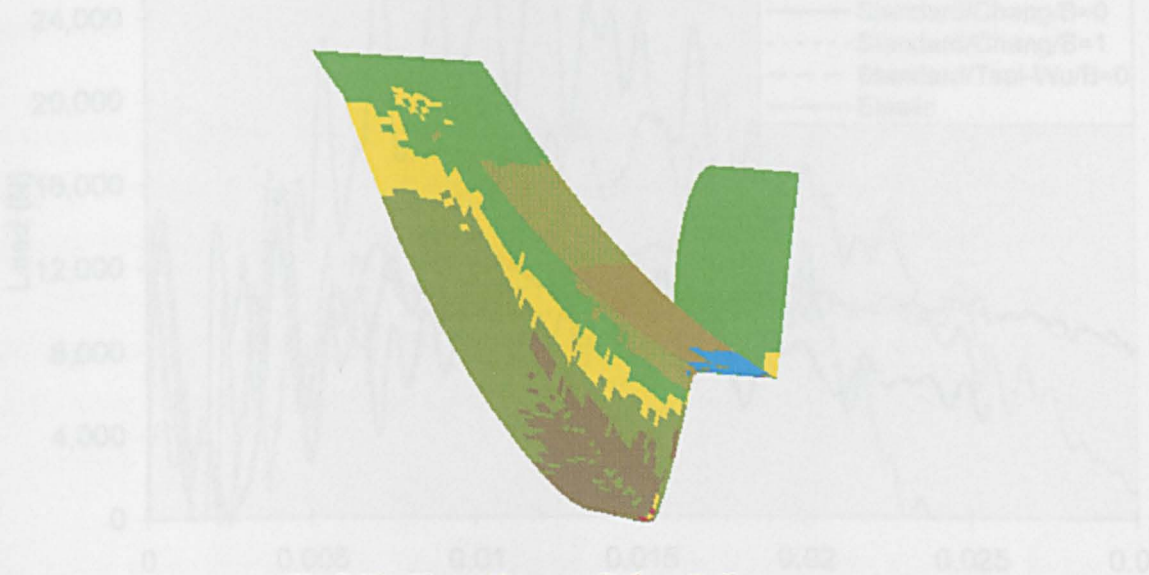


Fig 7.28: Plot of Stresses Before Collapse

The first elements failed early in the analyses (from 3 ms) and were located on the top flange of the beam. Failure soon spread to the corner fillet. At about 12 ms, elements of the side wall began to fail. It is at this point that the beam collapsed (which can be seen in the graph of load against deflection). From a time of about 18 ms, virtually the whole cross-section at mid-span has failed. Throughout the rest of the impact event the stresses at all other cross-sections, even at the support location, remained within elastic limits.

LS-Dyna allows identification of the relevant failure mode. These were, as expected, the compressive fibre mode and, to a lesser extent, the compressive matrix mode. More unexpectedly, some elements of the bottom flange failed in the tensile fibre mode (the impacted beam shows no visible damage in this region).

Figure 7.29 below is a graph of selected (to maintain clarity) FEA predictions for the standard model, all at an impact velocity of 8 m/s. It was discussed in section 6.2.3 that there was substantial variation in the results of the impact tests on composite beams. Therefore, it was not straightforward to select typical results with which to compare the FEA predictions. Two sets of beam test results are included in figure 7.29 (the ‘bold’ lines) to show this variation but they do not represent the extremes of the beam’s performance (refer to figure 6.5).

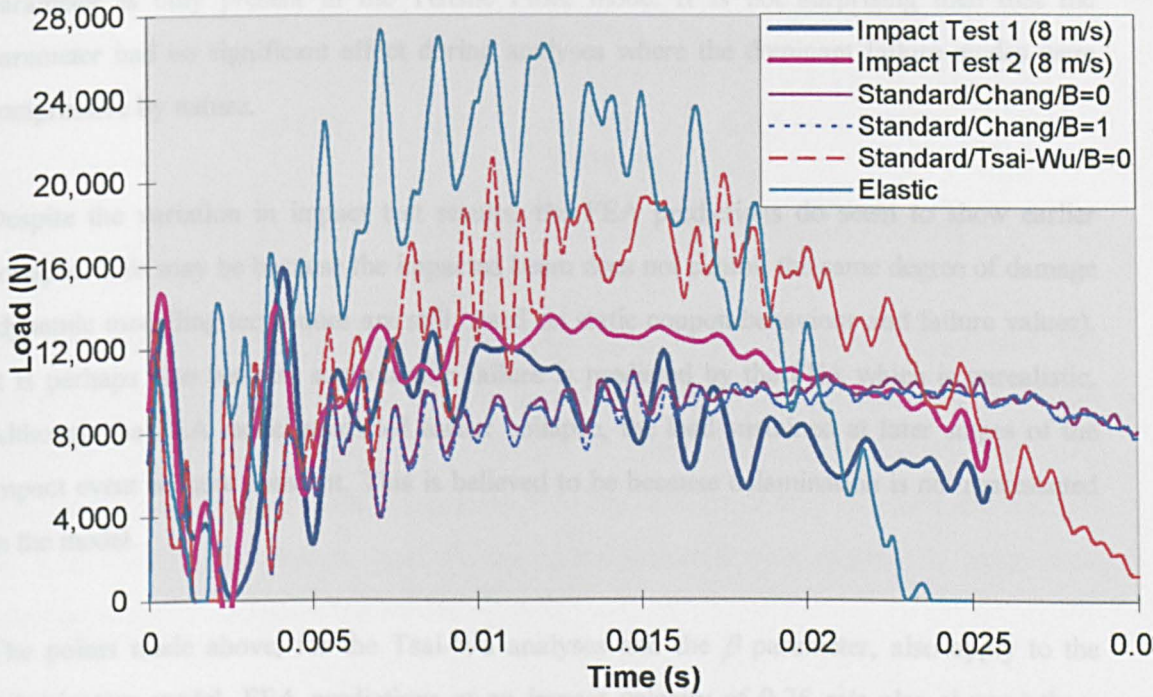


Fig 7.29: Selected Dynamic FEA predictions for Standard Model

The prediction for the elastic analysis shows, as expected, that the beam could sustain a significantly higher load if no type of failure occurred. Also, whether failure is included or not produces a difference in the analyses results even in the initial response of the beam when a statically tested beam (or the static FEA model of the beam) would be behaving only elastically. This is no doubt due to the peak loads under impact conditions that exceed the static collapse load (of about 10 kN). It is perhaps surprising then that the performance of the impacted beam is better than that of the statically tested beam (refer to section 6.3).

The prediction using the Tsai-Wu criterion always overestimates the load carrying capacity of the beam. This is not too surprising considering the results of the dynamic shear coupon

modelling (section 7.3.5), in which the predicted shear stress significantly exceeded the failure stress, and since shear is such a dominant form of loading for the impacted beam. Such non-conservative predictions are surely unacceptable and the Tsai-Wu criterion shall not be considered further.

The value of β had little effect on the results of the Chang-Chang analyses. This is unlike the shear coupon modelling where a non-zero value of β tended to cause catastrophic failure. However, this was because the shear test (and modelling) involved tensile loading and the β parameter is only present in the Tensile Fibre mode. It is not surprising then that the parameter had no significant effect during analyses where the dominant failure modes were compressive by nature.

Despite the variation in impact test results, the FEA predictions do seem to show earlier collapse. This may be because the impacted beam does not exhibit the same degree of damage (dynamic modelling techniques are still based on static coupon behaviour and failure values). It is perhaps also because some tensile failure is predicted by the FEA which is unrealistic. Although the FEA model predicted earlier collapse, the load sustained at later stages of the impact event is more constant. This is believed to be because delamination is not represented in the model.

The points made above, for the Tsai-Wu analyses and the β parameter, also apply to the delamination model. FEA predictions at an impact velocity of 9.75 m/s also showed these features. Therefore, figure 7.30 below shows two predictions for the delamination model at an impact velocity of 8 m/s, using only the Chang-Chang criterion with a β value of zero. The difference between the two predictions is whether delamination failure has been activated (deletion of nodal constraints) or not. Included in the figure are the two sets of impact test results and the predictions of the standard model (using the same criterion and β value) for comparison.

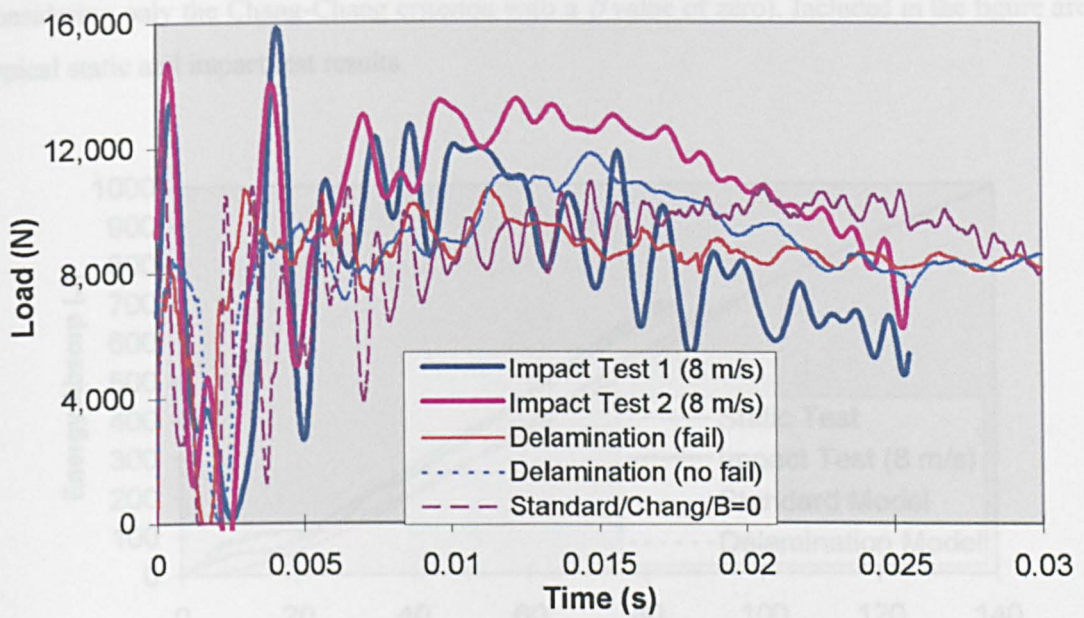


Fig 7.30: Selected Dynamic FEA predictions for Delamination Model

Fig 7.31: Plot of Energy Absorbed vs Deflection, for FEA & Test Results

The delamination model appears to be fairly accurate and represents a small improvement on the standard model. The predicted collapse is still earlier than occurs in impact tests and this supports the view that this is due to the use of static modelling techniques. Activating delamination failure does produce some success. The stiffness of the beam does decrease and at approximately the correct time. However, the load following collapse is again more constant than seen in impact test results.

Both FEA models offer reasonable predictions of the beam's impact performance. It is not easy to suggest how the models could be improved since their predictions, at times, fall within the variation seen in test behaviour. Perhaps collapse could be better predicted if failure values, and how failure is treated, was determined using dynamic coupon testing. And no doubt the delamination failure of the beam could be better represented. However, the models' predictions will probably be sufficiently accurate for most purposes though it should be remembered that they tend to overestimate the beam's performance and so are not conservative.

Figure 7.31 below is a plot of the predicted energy absorbed against deflection for the standard and the delamination (with failure) models using an impact velocity of 8 m/s (and

considering only the Chang-Chang criterion with a β value of zero). Included in the figure are typical static and impact test results.

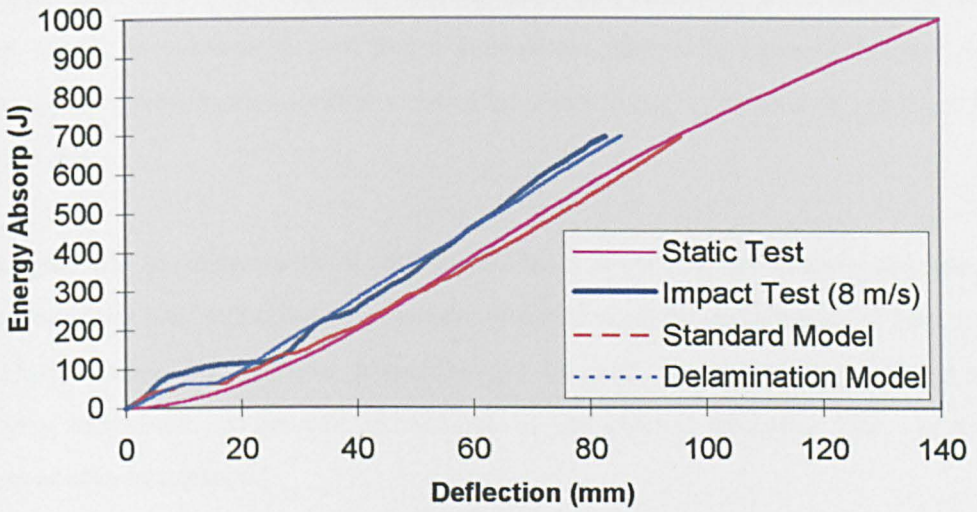


Fig 7.31: Plot of Energy Absorbed v Deflection. for FEA & Test Results

The predictions of the standard model are in good agreement with static test results. Surprisingly, and encouragingly, the predictions of the delamination model are also in good agreement with impact test results. This suggests that delamination is an important factor in the beam's ability to absorb impact energy and that the delamination model adequately accounts for this factor.

CHAPTER EIGHT

DISCUSSION AND CONCLUSIONS FOR ALL RESULTS

8.1 DISCUSSION OF ALL RESULTS

The main objective of this thesis has been to assess and model the performance of two side impact beams: a commercial steel and a prospective composite beam. This chapter shall discuss all the investigations carried out with the focus being on whether or not the objective has been met.

It is argued that the experimental investigations have, in general, successfully determined the properties of the steel and composite material and evaluated the performance of both types of side impact beam. The material properties can be used, in conjunction with appropriate modelling techniques, to produce predictions of the beams' behaviour that are in good agreement with test results.

The results for the steel and the composite beam are discussed in detail. It is also considered interesting to compare the performance of both types of beam. The overall conclusions of this thesis are then presented. Finally, a number of suggestions are made for further study that could enhance and develop the work that has been carried out.

8.1.1 Discussion of All Steel Results

Tensile tests on steel coupons have been used to determine the properties of the material, namely, the elastic modulus, the yield stress and the strength (in terms of stress and strain) of the material. The yield stress was obtained using the concept of a proof stress as there was no well-defined yield point in the test results. The variation between the coupons' results was low although only a small number of specimens were tested.

Static testing of the steel beam has ascertained its static bending crashworthiness. The loaded beam behaves elastically up until a well-defined collapse load and then sheds load. The beam's ability to absorb the impact energy is relatively unaffected by the collapse. The impact behaviour of the beam appears to be similar to its static response except for load fluctuations caused by the dynamic interaction between the beam and striker. Modal testing shows that these load fluctuations are not simply vibrational modes of the beam.

Theoretical predictions using elastic bending theory and plastic analysis can provide a first approximation of static elastic behaviour and the plastic collapse load. However, as it assumes that the strain in the material is constant following plastic collapse, it does not accurately predict the post-collapse behaviour.

Non-linear static FEA provides a much better prediction of the beam's static behaviour. The predicted stresses in the beam can be used to understand its behaviour throughout the loading history.

Dynamic FEA has successfully predicted the impact behaviour of the beam. The large load fluctuations, seen in impact test results, are predicted by the FEA and this confirms that they are not some function of the test rig instrumentation. The dynamic FEA can be used to help understand the effect of a number of parameters within an impact test. In particular, beam collapse is not dependent on the mass of the striker and increasing the impact velocity from a quasi-static loading condition to the conditions of the impact tests can show the development of the load fluctuations.

It has been found that a particular form of buckling analysis, the Finite Width method, is unsuitable for the steel beam due to the dominance of plastic behaviour. Static buckling FEA predicts high buckling loads and this confirms that the beam fails by plastic collapse with little or no influence of elastic buckling.

The modal FEA, using the shell element model of the beam, predicted vibrational modes that are in good agreement with the modal test results. This offers a validation of the FEA model. Modal FEA using beam elements gives predictions that correlate with theoretical modes of vibration but neither approach gives an accurate prediction of the modal behaviour of the beam. This is because of the simplifications in geometry that they both involve.

8.1.2 Discussion of All Composite Results

A series of static coupon tests were carried out to determine the elastic properties and failure stresses and strains of the composite material under a range of loading conditions. The results of the various tests were not always completely satisfactory (in particular the compressive testing which is widely known to be problematic) but, in general, it is believed that reasonable

measurements of the material properties have been achieved. This is supported by the good agreement with the values presented by the SACTAC programme and also with the approximate predictions using the rule of mixtures. The material has been found to be particularly weak in compression and shear.

Static and impact testing have determined the composite beam's bending crashworthiness characteristics. Failure modes have been identified, such as delamination, compressive and shear failure, though it is not always apparent when these types of damage occur. There is a greater variation in the composite beam's behaviour, particularly in its impact response, probably due to limitations in the manufacturing process. There appear to be significant differences between the beam's static and impact performance. The impacted beam behaves in an elastic manner up until a higher load and deflection and consequently, can absorb more energy for a given value of deflection.

The static coupon tests have been modelled using both static and dynamic FEA operating in a quasi-static manner. This has allowed an assessment of the FEA software, the failure criteria that the software uses and the development of appropriate modelling techniques. The techniques all involve controlling failure under a particular loading condition in such a manner that the FEA predictions correlate with the relevant coupon test results. It is believed that this approach compensates for the limitations of any failure criterion and has a valid basis to how failure is treated.

These techniques have been successfully transferred to the modelling of the composite beam. Static FEA models offer reasonable predictions of the beam's response whether delamination is included or not. It is believed that the models could be improved by more detailed modelling of the delaminated area. The predictions of the dynamic beam FEA are limited to a degree by their reliance on static modelling techniques and, as with the static FEA, their crude representation of delamination. Nevertheless, the models do offer reasonable predictions of the beam's impact behaviour. It should be remembered, however, that the results of both the static and the dynamic FEA tend to overestimate the performance of the beam.

8.1.3 Comparison of Steel and Composite Test Results

The load histories of impact beam tests involving steel and composite specimens can be compared with each other and this is done, for selected beams, in figure 8.1 below.

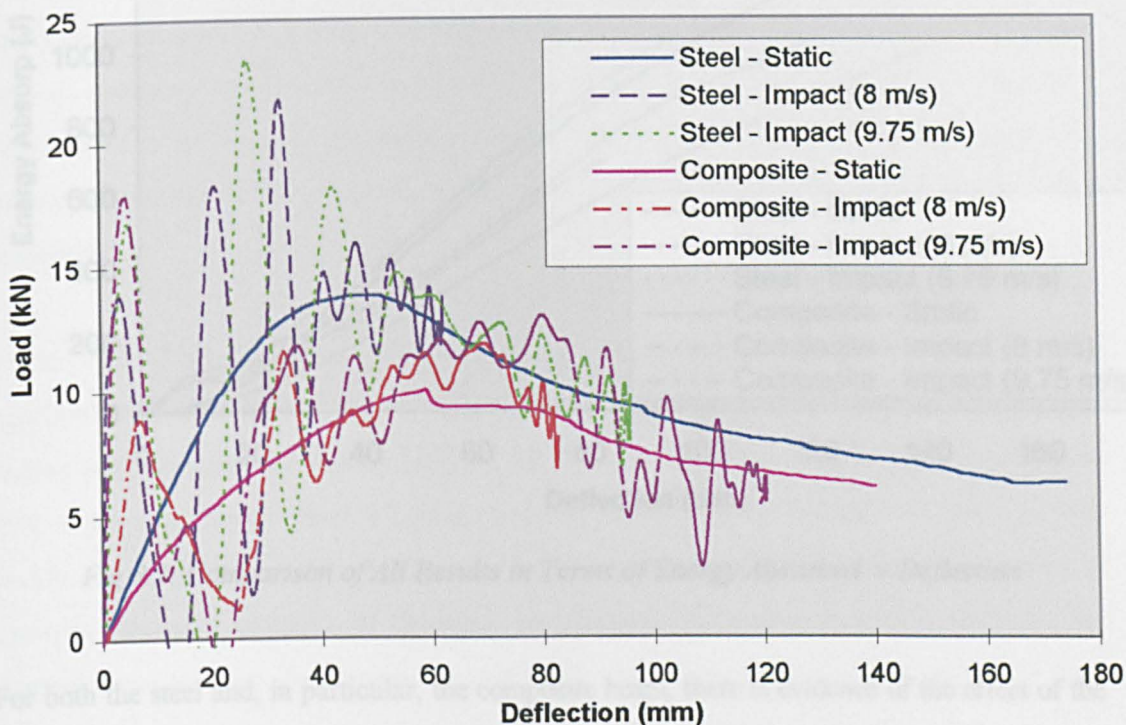


Fig 8.1: Comparison of All Results in Terms of Load v Deflection

Clearly, the performance of the steel beam is significantly better than that of the composite beam. The steel beam is initially more stiff, has a higher collapse load and there is no sudden drop in load at collapse. It should be borne in mind that the steel beam is physically smaller and thinner than the composite beam and is even 5% lighter. The composite beam does at least have a more constant load carrying capacity following collapse though it cannot, at any point, sustain the load carried by the steel beam.

The load fluctuations in the impact test results are similar although their magnitude is greater for the steel beam. Given the two material types' considerably different properties (composites known to have good damping characteristics [2.39]), and the two beams' different modal

fluctuations.

Figure 8.2 below is a plot of the energy absorbed by selected steel and composite beams as a function of deflection.

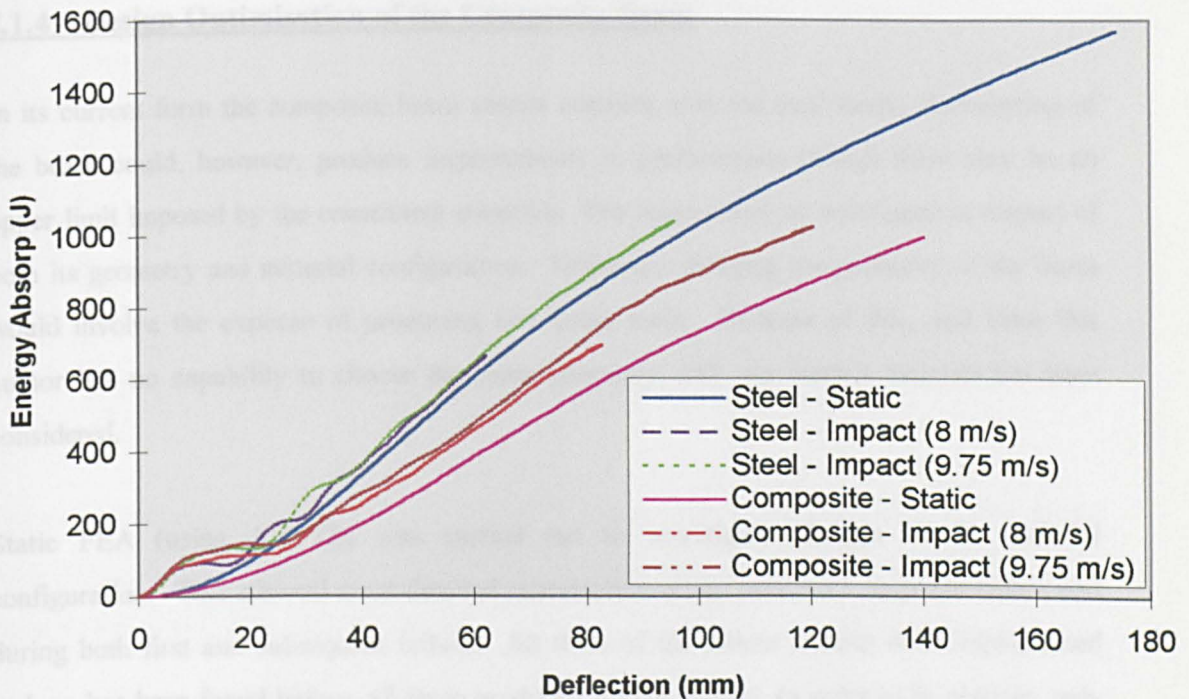


Fig 8.2: Comparison of All Results in Terms of Energy Absorbed v Deflection

For both the steel and, in particular, the composite beam, there is evidence of the effect of the loading rate: the beams' performance increases as the loading rate increases. In fact, the dynamic crashworthiness, or the dynamic energy absorbing capacity, of the composite beam is approaching the crashworthiness of the steel beam. It would be interesting to investigate the composite beam's behaviour at substantially higher load rates than those considered in this thesis.

The repeatability of the steel beams is greater than the composite beams, a view supported by deflection and energy absorption against time plots and the statistical analysis of results. It should be noted that the smaller number of steel samples will have an influence on the plots and associated statistical values. Although the composite beams show a greater variation in

their performance, it is reasonable to assume that improved manufacturing processes can significantly reduce the variation (such as the use of a metal press to produce the beams).

8.1.4 Design Optimisation of the Composite Beam

In its current form the composite beam cannot compete with the steel beam. Redesigning of the beam could, however, produce improvements in performance though there may be an upper limit imposed by the constituent materials. The beam could be redesigned in respect of both its geometry and material configuration. However, changing the geometry of the beam would involve the expense of producing new press tools. Because of this, and since this author has no capability to choose the beam geometry, only the beam's material has been considered.

Static FEA (using ANSYS) was carried out to investigate changes in the material configuration. This allowed more detailed examination of the material's response before and during both first and subsequent failure. All three of the failure criteria were implemented and, as has been found before, all three produced similar results. In order to be concise, only results for the Maximum Stress criterion shall be presented. It was considered convenient to examine structural members of the beam in isolation. The two most critical members are deemed to be the top flange and the side walls, as failure predominantly occurs in these members.

(A) Top Flange

The modelling of the top flange was identical to the static modelling of the flexural testing in terms of the loading and support conditions and the dimensions of the plate except that the thickness of the shell elements was set to 10 mm (the thickness of the beam's top flange).

Three models were used for the analyses. In the first model, all four of the layers were set to a thickness of 2.5 mm and with a material angle of 0° . This represented a $0/90^\circ$ weave orientation. The second model had two top layers (relative to the loading) each of 3 mm thickness and 45° material angle and two bottom layers of 2 mm thickness and 0° material angle. This represented the material configuration, in terms of weave orientation and laminate lay-up, of the top flange of the composite beam that was tested. In the third model, all four of

the layers were set to a thickness of 2.5 mm and with a material angle of 45°. This represented a $\pm 45^\circ$ weave orientation. All three models were ran until first failure. Table 8.1 presents the results of the analyses for the three models.

Value at Failure	Model 1 0/90°	Model 2 mixed	Model 3 $\pm 45^\circ$
Load (kN)	4.05	1.13	0.78
Stress (MPa)	125	11.7	11.7
Strain (%)	0.85	1.09	1.09
Deflection (mm)	2.16	1.26	1.55

Table 8.1: Failure Values Determined During Static Tensile Coupon FEA

The above table shows that the first model could sustain a far higher load (and stress) before the top layer failed in compression. The other two models failed in shear at the top layer at far more modest loads (and stresses).

For each model, the properties of the material were then reduced in accordance with the relevant type of coupon testing. In the first model, the elastic modulus was reduced while, in the second and third models, the shear modulus was reduced. The analyses for each model were then continued until second failure was detected. Figure 8.3 below shows the results of the analyses for the three models.

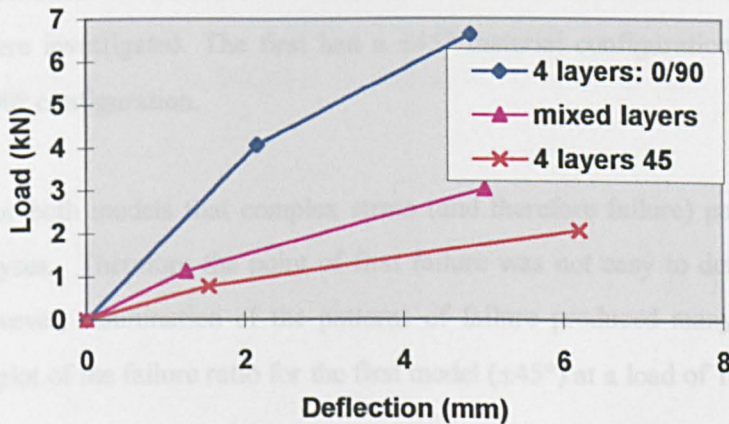
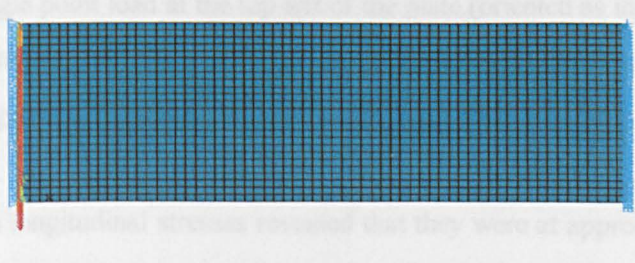


Fig 8.3: Results of Analyses for the Three Models

The above figure shows that the first model is also considerably stiffer. A 0/90° configuration appears to be the optimum choice for the top flange. A laminate lay-up offers no advantage for this part of the beam. It was not deemed necessary to continue the analyses for any subsequent failures.

(B) Side Wall

The dimensions of the plate used in the analyses of the side wall were the same as for the top flange but the loading and support conditions were different. On one side of the plate, each node was fully restrained. At the other side, symmetry conditions were applied to each node and, also, a shearing force was applied to each node in the direction of the plate's width. These conditions are shown below in figure 8.4.



*Fig 8.4: Loading and Support Conditions during Side Wall Analyses
(fully fixed at right end and loaded at left end)*

The above conditions do not represent pure shear conditions (normal stresses are still present). However, the conditions enhance the effects of shear so that these effects can be appreciated. Two models were investigated. The first had a $\pm 45^\circ$ material configuration and the second model had a 0/90° configuration.

It was found for both models that complex stress (and therefore failure) patterns developed during the analyses. Therefore the point of first failure was not easy to determine with any accuracy. However, examination of the patterns of failure produced many useful insights. Figure 8.5 is a plot of the failure ratio for the first model ($\pm 45^\circ$) at a load of 1 kN.

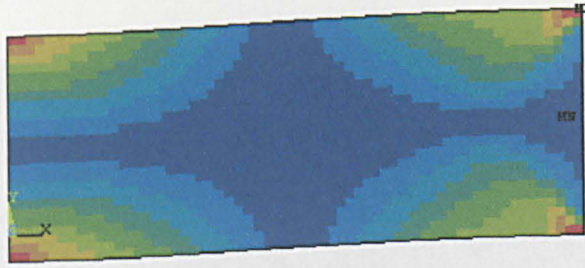


Fig 8.5: Plot of Failure Ratio for First Model ($\pm 45^\circ$)
 (red = high failure ratios, blue = low failure ratios)

High values of failure ratios were restricted to the four corners of the plate and corresponded to shear stress values at about 60 % of the shear strength of the material. These results are for the conditions applied. An additional analysis involving a simple support at the bottom right of the plate, and a single point load at the top left of the plate (oriented as in figure 8.5) produced high values of failure ratios only in the top left corner. The contours of failure ratios in the above figure do suggest a 45° orientation.

Examination of the longitudinal stresses revealed that they were at approximately 50 % of the compressive failure stress in a number of locations in the plate. At a higher load of 2 kN, failure was seen to be a mixed mode of both compressive and shear failure.

The FEA model did not directly simulate any fracturing of the material. It can be hypothesised that any cracks would develop at the top left corner of the plate and would be likely to propagate at 45° in the direction of the fibres. Bearing in mind the symmetry conditions, half of the fracture energy would be available to propagate the crack at each side of mid-span cross section.

(C) Optimum Material Configuration

Figure 8.6 is a plot of the failure ratio for the second model ($0/90^\circ$) at a load of 1 kN.

The optimum material configuration for the beam would appear to be a $0/90^\circ$ lay-up in the top flange and a $\pm 45^\circ$ lay-up in the side walls of the beam. This configuration was used in an analysis of the complete beam. The modelling procedure used was the same as detailed in section 7.1.2. Only the standard model (no representation of delamination) was used, since some of the layers of the top flange were at a different orientation, delamination was not expected to occur.

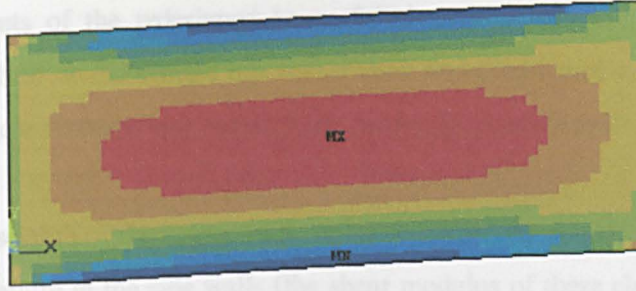


Fig 8.6: Plot of Failure Ratio for Second Model (0/90°)
(red = high failure ratios, blue = low failure ratios)

Much of the core of the material is now exhibiting high failure ratios which correspond to shear stress values at about 90 % of the shear strength of the material. Examination of the longitudinal stresses revealed that the plate has already failed in compression at the top left corner. At only a slightly higher load, a mixed mode of compressive and shear failure was again seen.

Any cracks that developed at the top left corner of the plate would be likely to propagate downwards in the direction of the fibres. All of the fracture energy would be available to propagate the crack until the whole section at mid-span had fractured. This hypothesis appears to correspond with the test behaviour of the older type of composite beam which had a 0/90° material configuration in the side walls. During playback of the high speed video recording, the side walls seemed to crumple and fold in on themselves at mid-span. The load that the beam could sustain (and the energy absorption characteristics) were significantly lower than the newer type of beam.

(C) Optimum Material Configuration

The optimum material configuration for the beam would appear to be a 0/90° lay-up in the top flange and a $\pm 45^\circ$ lay-up in the side walls of the beam. This configuration was used in an analysis of the complete beam. The modelling procedure used was the same as detailed in section 7.5.2. Only the standard model (no representation of delamination) was used; since none of the layers of the top flange were at a different orientation, delamination was not expected to occur.

None of the elements of the redesigned beam failed until a deflection of 50 mm. These elements failed in shear at the beam's top corner fillet and propagated to the side walls. The shear modulus of these elements was reduced and the analysis continued.

Much of the cross-section of the beam at mid-span had failed by a deflection of 80 mm. This was mainly shear failure in the side walls (the shear modulus of these elements was reduced) and compressive failure in the top flange and some elements of the side walls (the elastic modulus of these elements was reduced). The analysis was then restarted. There was no significant change in the elements' failure ratio distribution for higher levels of deflection.

Figure 8.7 below is a plot of the load against mid-span deflection predicted by the analysis. The results of a standard static beam test and predictions for a standard beam ('standard' meaning a beam with the laminate lay-up in the top flange) are included for comparison.

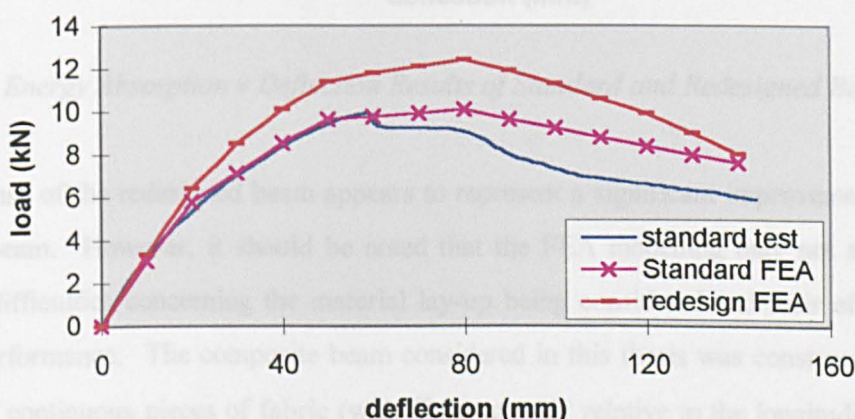


Fig 8.7: Load v Deflection Results of Standard and Redesigned Beam FEA

The above figure shows that the redesigned beam is only a little stiffer than the standard beam at low levels of deflection. This is presumably because the top flange is less important as a load carrying member than the side walls. Significantly, however, the material of the top flange does not fail until 50 mm and so the decrease in stiffness is less than for the standard beam and a higher load can be sustained.

Following failure of the side walls, the stiffness of the beam decreases, only a little less rapidly than for the standard beam. Compressive failure of the top flange occurs at 80 mm. Because

the reduction in properties due to compressive failure is a little greater than for shear failure, the load then falls more rapidly than for the standard beam.

Figure 8.8 below is a plot of the energy absorption against mid-span deflection predicted by the analysis. The results of a standard static beam test and predictions for a standard beam are also included.

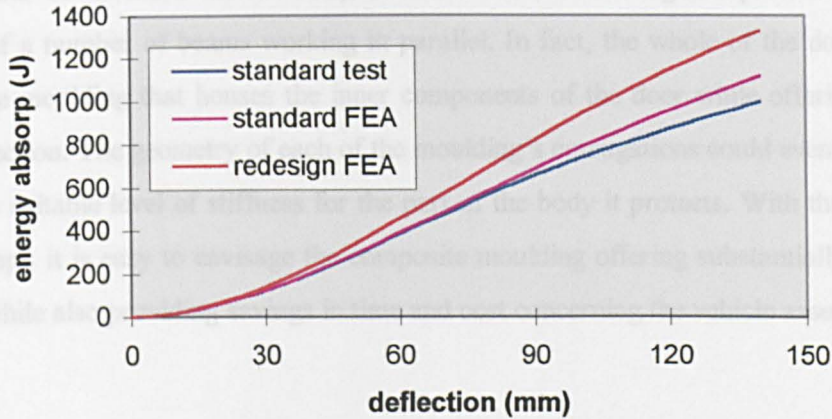


Fig 8.8: Energy Absorption v Deflection Results of Standard and Redesigned Beam FEA

The response of the redesigned beam appears to represent a significant improvement over the standard beam. However, it should be noted that the FEA modelling may not account for practical difficulties concerning the material lay-up being considered and their effect on the beam's performance. The composite beam considered in this thesis was constructed using a number of continuous pieces of fabric (with fibres at $\pm 45^\circ$ relative to the longitudinal axis of the beam) for a single layer of the complete beam, along with other pieces of fabric (with fibres at $0/90^\circ$ relative to the longitudinal axis of the beam) that formed a layer at the top flange. It has been seen that delamination between the two layers has limited the performance of the beam. The material lay-up for the optimised beam would entail that the fibres of the weave are not continuous and that single pieces of fabric could not be used. There would then be discontinuity and a lack of structural connectivity at the top corners of the beam (the intersections between the top flange and the side walls). Such a beam may prove to have a lesser performance for this reason.

It should also be noted that the response of the beam, as predicted by the FEA, still falls short of the performance of the steel beam. It seems probable that the performance of the composite beam will always be limited while the combination of glass fibres and, in particular, a polypropylene matrix is used.

The composite beam does, however, offer a potential flexibility that the steel beam cannot if changes to geometry were made. Rather than being one open-section beam, the composite material could be moulded into a complex section with a corrugated profile that is the equivalent of a number of beams working in parallel. In fact, the whole of the door cassette could be one moulding that houses the inner components of the door while offering the side impact protection. The geometry of each of the moulding's corrugations could even be tailored to provide a suitable level of stiffness for the part of the body it protects. With this 'multiple beam' concept, it is easy to envisage the composite moulding offering substantially increased protection while also providing savings in time and cost concerning the vehicle assembly.

8.2 CONCLUSIONS FROM ALL RESULTS

The main conclusions of this thesis are itemised below.

- *The steel beam collapses due to plastic material behaviour rather than by elastic buckling.*
- *Dynamic effects in the impact test results appear to be caused by the interaction of the contact stiffness of the beam and striker. They are not simply functions of the beam's modal properties.*
- *A relatively simple elastic-plastic analysis can provide a first approximation of the beam's static behaviour.*
- *Successful modelling of the beam's static and impact beam behaviour has been achieved using FEA.*

- *The composite beam is weak in compression and shear, which unfortunately are dominant loading conditions for the beam and so the beam fails in these modes.*
- *The impacted composite beam shows a significant improvement in its crashworthiness characteristics, at the loading rates considered in this thesis, over its static performance.*
- *Successful static and dynamic FEA modelling of the composite beam is possible although, in both cases, the results are limited by how they represent delamination. For the dynamic FEA, the use of static modelling techniques further limits the accuracy of the FEA predictions.*
- *The material configuration of the beam has been optimised to provide the best possible performance.*

- *Both the steel and composite beam can sustain substantial loading after collapse and the impact energy absorbed by the beam is relatively unaffected.*
- *The performance of the steel beam is significantly better than that of the composite beam and there is less variation in test results. The composite material is limited by its poor properties in certain loading conditions but does offer flexibility in the moulding profile which could be used to some advantage.*

8.3 FUTURE WORK

A number of areas have been identified where further study would develop the points made in this thesis. These areas are discussed below.

Generally, the work on the steel material and beam is seen as adequate since it is primarily being used as a standard with which to compare alternative materials and designs. If improvements to the modelling of the steel beam were required, there are two main ways of doing this. A more complex plastic analysis could be derived which accounts for, for instance, the effect of finite displacements. For the dynamic FEA modelling, the effect of the strain rate could be represented. This would typically be achieved using the Cowper-Symonds constitutive equations (refer to section 2.1) and would require testing of the material at different strain rates to determine the values of the constants used in these equations.

For the composite material, further work could be carried out to improve the various coupon tests. In particular, a more reliable form of compressive testing could be developed. As with the steel material, the effect of the strain rate is again of interest and perhaps the concept of constitutive equations that incorporate strain rate behaviour could be extended to apply to the composite material. Certainly, tests to measure the viscoelastic properties of the composite material would be informative. Also, dynamic coupon testing could be used to develop modelling techniques for the dynamic FEA.

More extensive investigation of the damage within the loaded composite beam would be useful. This may require the use of advanced procedures such as ultrasonic or acoustic emission measurements. Ideally, if practically possible, it would be desirable to identify when each type of damage occurs and how it increases as the loading or beam deflection is increased. It is unlikely that accurate measurements of damage can be made in real time during the impact event without sophisticated instrumentation. However, if a large number of beams were available, impact tests at a range of different impact energies could be carried out so that the types and the extent of damage could be related to a particular degree of energy absorbed. In particular, the shape and extent of delamination, as a function of beam deflection, would be of some interest.

With greater knowledge of the damage to the composite beam, FEA models could be improved, particularly by better representation of the delaminated area. Composite failure criteria have their own limitations but, at present, there is no alternative. However, the software's implementation of the criteria could be significantly improved. ANSYS has the facility for the user to define other types of failure criteria though this does not seem necessary as there was little difference in the criteria's results for the work in this thesis. LS-Dyna allows the use of user-defined material models. More conventional criteria could be defined (such as the Maximum Stress or Strain criteria) and, perhaps more importantly, this would allow greater control over how failure is treated. However, it is known that defining these material models is complex, requiring substantial knowledge of a programming language specific to LS-Dyna.

The FEA techniques developed within this thesis could be used to enhance or optimise the geometry of the composite beam. This has not been done because the manufacturing capabilities (the press tooling) are not available to this author to produce, and subsequently test, any newly designed beams. Therefore this work has been considered to be outside of the scope of the present project.

Appendix 1.2: Composite Material Properties Compiled by SACTAC

Referred to in Section 1.4

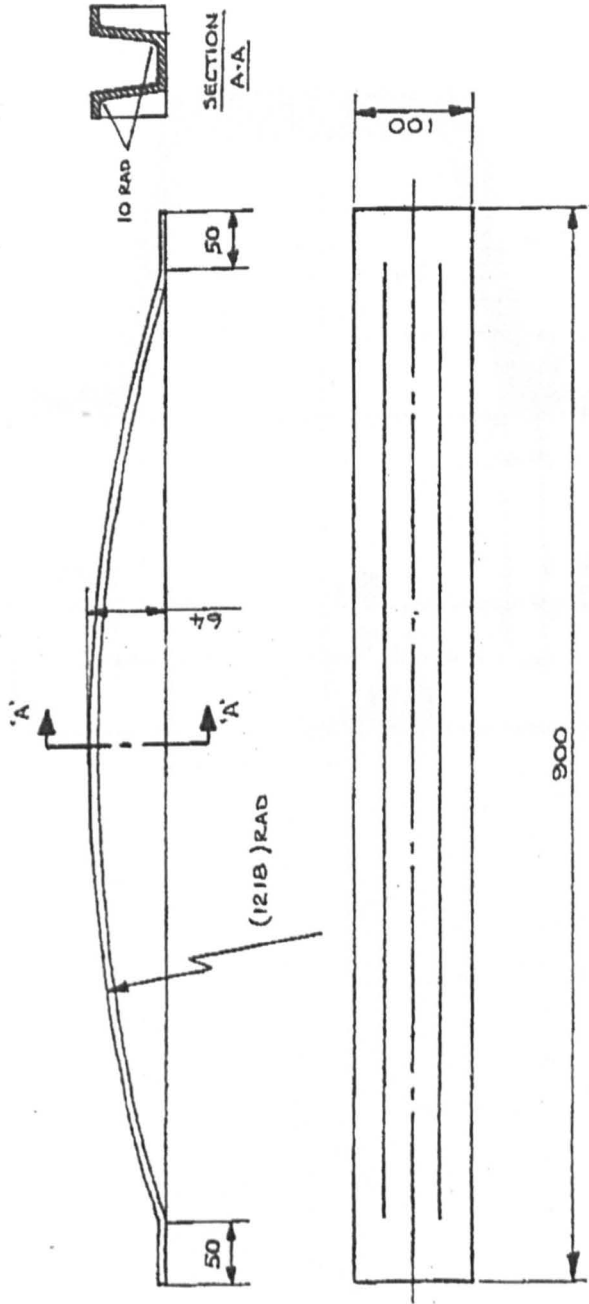
	Symbol	Unit	Test Type	Test Standard	Twintex
Material Information					PP Twintex 1:1
WF		%			60
VF		%			35
Density	ρ	g/cm ³			1.5
Matrix					PP
Fibre					Glass
Reinforcement Type					Balanced Weave
Supplier					Vetrotex
Matrix Properties					
Melt Temperature	Tm	oC			160
Density	ρ	Kg/m ³			910
Tensile Modulus (Long)	E11T	GPa			1.6
Tensile Modulus (Trans)	E22T	GPa			1.6
Ultimate Tensile Strength (Long)	ST11	MPa			38
Ultimate Tensile Strength (Trans)	ST22	MPa			38
Poissons Ratio	v12	-			0.35
Poissons Ratio	v21	-			0.35
Ultimate Compressive Strength (Long)	SC11	MPa			38
Ultimate Compressive Strength (Trans)	SC22	MPa			38
Shear Modulus	G12	GPa			0.94
Fibre Properties					
Density	ρ	Kg/m ³			
Tensile Modulus (Long)	E11T	GPa			
Ultimate Tensile Strength (Long)	ST11	MPa			
Composite Properties					
Tensile Modulus (Long)	E11T	GPa	Tensile	BS ISO 527-4	13.6
Tensile Modulus (Trans)	E22T	GPa	Tensile	BS ISO 527-4	13.6
Tensile Modulus (TT)	E33T	GPa	TT Tensile		5.3
Ultimate Tensile Strength (Long)	ST11	MPa	Tensile	BS ISO 527-4	315
Ultimate Tensile Strength (Trans)	ST22	MPa	Tensile	BS ISO 527-4	315
Ultimate Tensile Strength (TT)	ST33	MPa	TT Tensile		7.6
Compressive Modulus (Long)	E11C	GPa	Compressive	ASTM D3410	
Compressive Modulus (Trans)	E22C	GPa	Compressive	ASTM D3410	
Compressive Modulus (TT)	E33C	GPa	TT Compressive		
Ultimate Compressive Strength (Long)	SC11	MPa	Compressive	ASTM D3410	125
Ultimate Compressive Strength (Trans)	SC22	MPa	Compressive	ASTM D3410	125
Ultimate Compressive Strength (TT)	SC33	MPa	TT Compressive		424
Flexural Strength	SF11	MPa	3PB	BS ISO 14125	280
Flexural Modulus	EF11	GPa	3PB	BS ISO 14125	13
Poissons Ratio	v12	-	Tensile	BS ISO 527-4	0.08
Poissons Ratio	v13	-	Tensile	BS ISO 527-4	0.36
Poissons Ratio	v21	-	Tensile	BS ISO 527-4	0.08
Poissons Ratio	v23	-	Tensile	BS ISO 527-4	0.38
Poissons Ratio	v31	-	TT Tensile		0.14
Poissons Ratio	v32	-	TT Tensile		0.15
Damage Modulus Function	d1	-	Tensile	BS ISO 527-4	
Damage Modulus Function	du	-	Tensile	BS ISO 527-4	
Shear Modulus	G12	GPa	Iosipescu		1.2
Shear Modulus	G13	GPa	Iosipescu		1.52
Shear Modulus	G23	GPa	Iosipescu		1.52
Shear Strength A30	SS11	MPa	Iosipescu		22.5

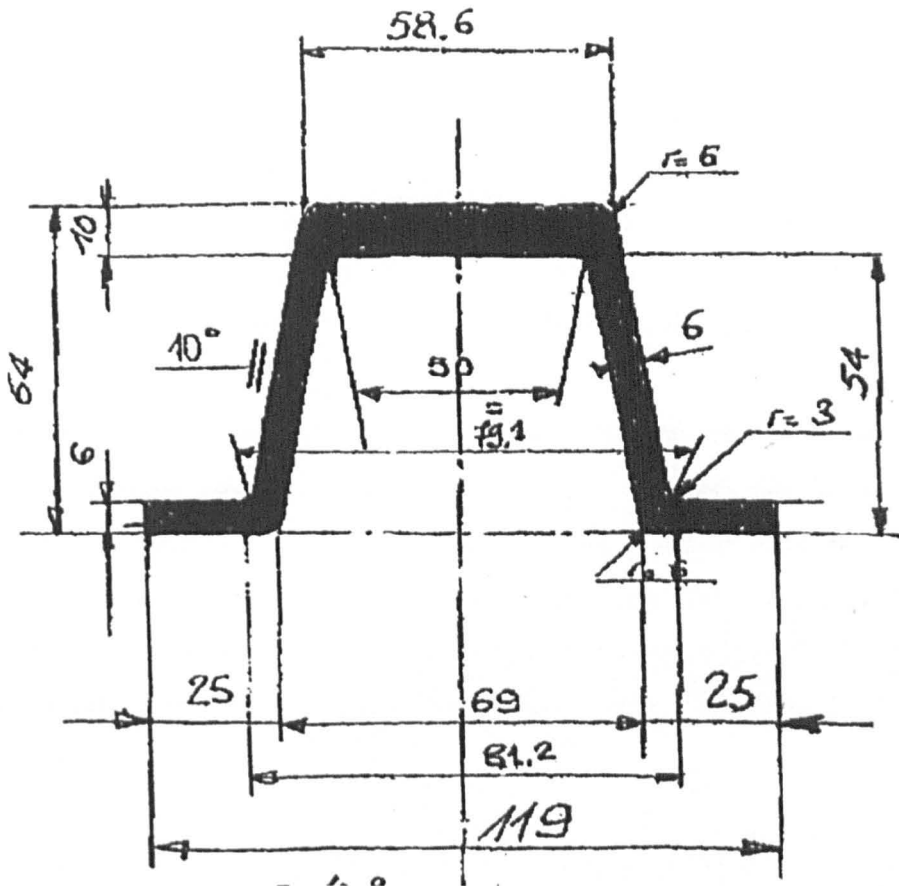
Appendix 1.3: Photograph of Tooling Used to Produce Composite Beams
Referred to in Section 1.4



Appendix 1.4: Nominal Dimensions of Composite Beams

Referred to in Section 1.4





A2.1: Review of Literature on Structural Crashworthiness

Referred to in section 2.2.1

Introduction

Structural crashworthiness is concerned with improving vehicle safety through structural design. This is achieved by designing components such as the vehicle frame to progressively deform on impact at suitable load levels, thereby absorbing the energy imparted by the collision of the vehicle and some other object. Therefore, the field of Structural Crashworthiness is usually concerned with evaluating the energy absorption and stability of structures during loading (quasi-static and dynamic) although other factors can be important such as space effectiveness and non-interference with other vehicle functions.

The study of structural crashworthiness began around 1960 with Minorsky's [A2.1] investigation of major collisions of ships in 1959 and Pugsley's [A2.2] study of the crashworthiness of trains in 1960. Several groups looked at oil tankers in the early 70s, in the mid 70s the focus was on aircraft and, as late as the 80s, the automotive industry began their research programs in earnest. However, considerable knowledge has been acquired on the behaviour of metal structures and in the past decade the emphasis has been on the behaviour of composites.

The term 'metal' beams refers mainly to steel primarily and aluminium occasionally. Other metals are seldom considered and this is for two reasons. Firstly, steel and aluminium are by far the two most widely used metals within structural engineering in general and automotive construction in particular. Secondly, and no doubt due to the first fact, the vast bulk of existing research has been restricted to these metals.

Energy absorption (EA) devices can be classified into two groups: axial tubes and any other form of device. Again, these devices are primarily for use in axial impacts. Lin and Mase [A2.3] gave values of specific energy absorption for each device and this is represented below in table A2.1. The specific energy is the energy absorbed divided by the mass of the crushed portion of the tube. Values for composite tubes show a wide range, as they are highly dependent on the material composition and geometry.

Device	Specific Energy Absorption (kJ/kg)
Tubes:	
Mild 1024 Steel	15
HS 4340 Steel	20
Aluminium 6009-T6	30
Foam filled 1010 Steel	20
Foam filled YST 100 Steel	20
Glass/Epoxy	20-60
Kevlar/Epoxy	20-75
Graphite/Epoxy	30-80
Other:	
Strap/wire over roller	4
Inversion tube	4
Rolling torus	4
Metal tube extrusion	13
Cable extension	13
Rod pulling through tube	2
Tube flaring	2
Tube fragmentation	45
Honeycomb compression	40

Table A2.1: Specific Energy Absorption of Various Devices [A2.3]

The table shows that other EA devices offer no real advantage over axial tubes except for tube fragmentation and honeycomb compression.

Metallic Structures – Axial Crushing

(A) Progressive Buckling of Metallic Structures

There are three factors involved in the energy absorption of metallic structures: material properties, structural geometry and the collapse mode [A2.4]. The collapse mode that is sought is the progressive buckling mode for metals, which gives the highest energy absorption. This mode involves the formation of multiple plastic hinges and the column exhibits an accordion-like deformation pattern that is shown below in figure A2.1 (a). If the load on the column is plotted against its displacement the curve would exhibit some typical features. Such a plot is given below in figure A2.1 (b).

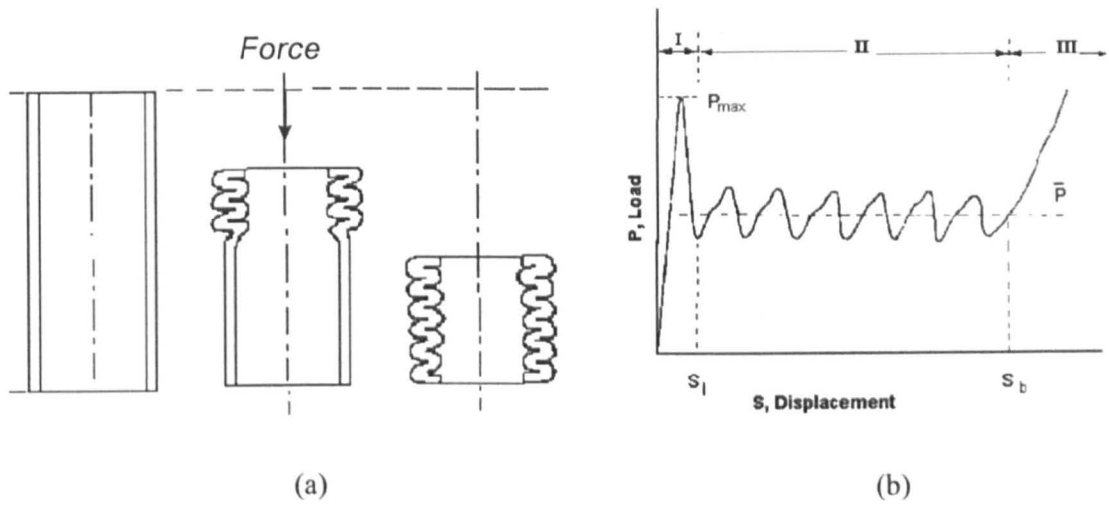


Fig A2.1: (a) Plastic Hinge Formation and (b) Load v Displacement Curve [A2.5]

Referring to figure A2.1 (b), in region I the load rises rapidly until a peak load (P_{max}) is achieved at which point the first fold is initiated. The load drops as the fold (a structural element in bending) cannot support the load carried by the non-deformed column until the fold is completely formed at displacement S_1 . In region II the load oscillates as more folds form successively, always about a mean load (P_{mean}). At displacement S_b the tube is fully folded. The load will rise again after this point but, from an energy absorption point of view, region III is of little interest. The value of energy absorption is given by the work done, W :

$$W = \int_0^{S_b} P \cdot dS$$

Thus, metals achieve energy absorption through plastic deformation involving very high strains in bending and stretching. It has been found that the strain energy is concentrated over narrow zones [A2.6].

According to Thornton and Magee [A2.7], for a given collapse mode, the specific energy absorption, E_s , of a metal tube is linearly dependant on the specific ultimate tensile strength, $Sp \cdot \sigma_{ult}$, of the material and this relationship is a function of the geometry of the structure alone [A2.8]. Figure A2.2 below shows this relationship for a number of circular tubes with two different thickness-to-diameter (t/D) ratios.

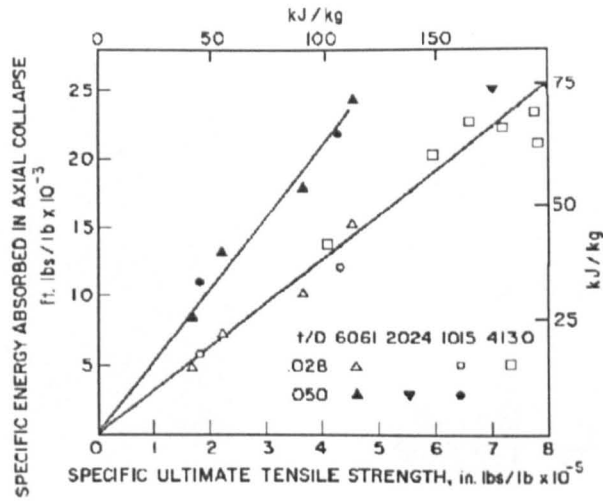


Fig A2.2: Relationship for Specific Energy Absorption to Specific Ultimate Tensile Strength in Circular Tubes [A2.8]

As it can be seen, the gradient of the lines depends on the structural geometry and this parameter has been defined as the structural effectiveness, η (therefore $\eta = E_s / Sp \cdot \sigma_{ult}$). Empirically, a common relationship between η and the relative density, ϕ , of the tube has been found (the relative density is the ratio of the volume of material to the volume enclosed by the outer perimeter of the section). For circular tubes $\eta = 2 \cdot \phi^{0.7}$ whereas for square tubes $\eta = 1.4 \cdot \phi^{0.8}$. At higher values of $Sp \cdot \sigma_{ult}$, however, the collapse mode may change from progressive folding to fracture with less energy absorption.

Thus it has been suggested that the specific ultimate tensile strength is the relevant material property. However, Mahmood and Paluszny [A2.9] disagreed with that conclusion, at least in the case of box columns. They went on to derive, from buckling theory of flat plates, expressions which included, instead, the yield strength of the material (the two theories are said to be in close agreement until the thickness-to-width ratio of a structure becomes quite large [A2.10]).

As stated previously, progressive buckling is the desired collapse mode. However, while Euler type buckling is not usually a concern in automotive size columns [A2.4], for excessively thin-walled columns a different mode is possible, which is known as irregular crumpling or non-compact compression. This mode is characterised by the formation of folds which are separated by curved panel sections. Figure A2.3 below shows the effect of progressive folding and irregular crumpling.

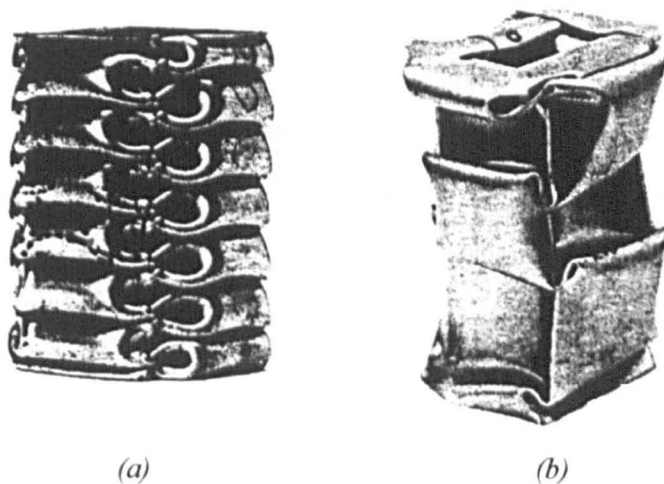


Fig A2.3: (a) progressive folding and (b) irregular crumpling [A2.11]

Mahmood and Paluszny [A2.10] described how the folding during irregular crumpling causes moments that can cause the column to fail in bending and so energy absorption capacity is greatly reduced. They gave relationships between the ratio of thickness-to-sectional width, t/b , and the collapse mode for mild and high strength steel. Both these researchers and Wierzbicki and Abramowicz [A2.6] discussed how the mean crushing load, P_{means} , is strongly dependent on wall thickness while having a much weaker dependence on column width.

Abramowicz and Jones [A2.12] performed a kinematic analysis of the crushing of square sections, which led to the development of two folding elements (type I and II). From these elements could be formed the collapse behaviour of tubes as observed experimentally. The observed behaviour was both symmetric and asymmetric collapse, which correspond to progressive folding and irregular crumpling. The effective crushing distance in tubes was also taken into account (as was material strain rate sensitivity) as not all of the tube's crushed length is ever fully collapsed. It is stated that the effective crushing distance is 70% of the initial length in box columns.

In another paper by the same authors [A2.13], the axial crushing of circular tubes is considered. Two modes are again identified: progressive folding and 'diamond' deformation. These are shown below in figure A2.4.

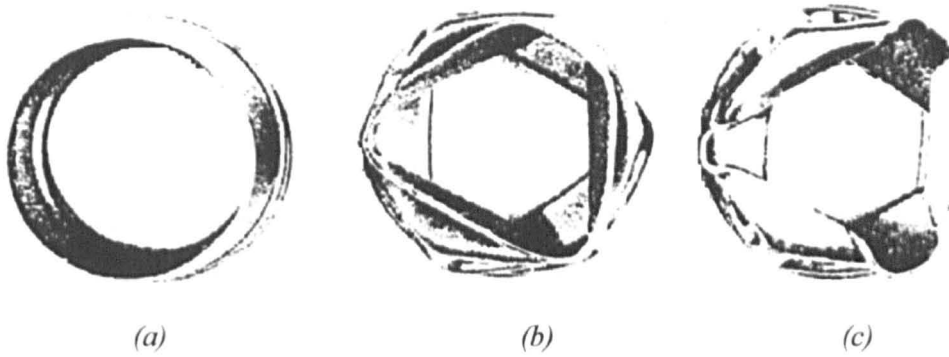


Fig A2.4: (a) progressive crushing, (b) and (c) diamond modes [A2.13]

Birch and Jones [A2.14] examined the effect of using stiffeners on circular tubes during crushing. It was found that the main influence of stiffeners, inside or outside the tube, was to alter the collapse mode, hindering global buckling and thus improving energy absorption. However, it was found that a thickness-to-diameter ratio seemed to exist beyond which there was no improvement in energy absorption. The static and dynamic collapse modes of stiffened tubes were noticed to be quite different with static collapse involving external stiffeners being less stable. For this reason, it was said that it is advantageous to place the stiffeners on the inside of the tube.

Jones and Birch [A2.15] considered the axial crushing of stiffened square tubes. Again, the stiffeners main effect was to alter the collapse mode and an aspect ratio value (thickness-to-side length) seemed to exist below which there was little improvement in energy absorption. However, unlike with circular tubes, there was less difference between static and dynamic collapse behaviour.

A number of researchers have looked at the effect of foam filling on the collapse behaviour of tubes. Reid *et al* [A2.11] described how its use improves energy absorption by increasing the mean crush load due to the crushing strength of the filler material and also by improving stability during collapse. The mean crush load increased with increasing foam density and the effect of foam filling was greater in square than in rectangular tubes.

Thornton [A2.16] examined the effect of foam filling on steel, aluminium alloy and glass fibre composite structures. It was concluded that, from a weight effectiveness point of view, foam filling is advantageous only in a limited number of cases: structures of low relative density made from a high density, low strength material such as mild steel. Thornton did note that

weight effectiveness is not the only concern and that there was evidence of an increase in stability with large sections. He also suggested that foam might be more effective in composites and for sections in bending.

Laterally compressed metal tubes have also been considered [A2.4]. Crushing of these rings produces the square wave load-deflection curve of the ideal absorber for diameter-to-thickness (d/t) ratios greater than 120. Though automotive applications often require a more triangular curve, strain hardening properties can be used to good effect which increase with decreasing d/t . Higher energy absorption can be achieved if higher buckling modes are induced by restraining deflection perpendicular to the applied load.

(B) Plastic Buckling of Metallic Structures

Progressive buckling is concerned with loading, even if it is dynamic, which is sufficiently slow so that axial or lateral inertia effects are not significant. Typically, the velocity of the impact load will be in tens of metres per second. These are the typical loads seen in automotive impacts. For this situation, static theoretical predictions (particularly if they account for the dynamic properties of the material) give reasonable agreement with dynamic tests.

However, if the velocity of the loading is sufficiently large, inertia effects become important. The deformed shape of the tube can be considerably different and an axially loaded tube will show a more wrinkled appearance with these wrinkles distributed over the whole length rather than at one end. This phenomenon is known as dynamic plastic buckling. Such loading velocities are more associated with aircraft and train impacts. This thesis is not concerned with such high velocities and dynamic plastic buckling will not be considered further.

Metallic Structures - Bending

The bending crashworthiness of beams is typically treated using plastic analysis methods as were reviewed in section 2.1. Such methods investigate, and attempt to predict, the beams' response to loading including the collapse and post-collapse behaviour. It should be noted, however, that the beams' capacity to absorb energy is often not considered.

Kecman [2.21] explained how the hinge behaviour of thin-walled beams may significantly differ from the predictions of plastic theory. Fully plastic moments may not develop, or the moment may decrease following collapse (rather than remain constant) due to the elastic buckling of beam section walls. The maximum bending strength of thin-walled beams of rectangular and square section were calculated [A2.16a] using the work of Rhodes and Harvey [A2.16b] and then the possibility of elastic buckling considered. Theoretical models of the hinge collapse mechanism were developed. It was determined that fully plastic moments could only develop if the critical buckling stress was greater than 1.5 to 3 times the yield stress of the material. the bending collapse behaviour. Experiments at impact rates of up to 10 m/s showed that the dynamic collapse modes observed were very similar to the static collapse modes.

Mamalis [A2.17] has investigated the energy absorption of steel tubes in bending. The study does offer some information on the load response and deformation modes of circular steel tubes. For instance, two distinct deformation modes were identified. However, rather than three or four point bending, a different experimental set up was used where the specimen was clamped at one end, supported at the other and torque was applied to the clamped end by an electric motor. The clamping arrangement was found to affect the type of deformation and the value of the maximum bending moment. Theoretical methods for the analysis of tube behaviour during both the elastic and plastic phases are also presented.

Composite Structures – Axial Crushing

(A) Introduction

The use of composites in primary structural areas is limited but growing. The industrial impetus for this thesis is an example of that fact. The benefits from their use are mainly weight reduction (a typical composite has a third the density of steel) and parts integration possible at the manufacturing stage. Limitations to their greater use are a lack of data on their behaviour and their processing time.

(B) Modes of Failure

Composite members have a number of modes of collapse often very different from metal sections. Unlike with metals, energy is absorbed through multiple microfracture processes. A number of collapse modes have been identified depending on such factors as material properties and wall thickness. Price and Hull [A2.18] observed that thin-walled tubes collapse by progressive folding, similar in manner to metal tubes, while thick-walled tubes fail by catastrophic fracture when the load equals the compressive strength of the material. Thick-walled tubes will fail by progressive crushing, however, when an appropriate trigger mechanism is employed.

A trigger mechanism creates a local region of high stress, which initiates the formation of a zone in which the material is highly fragmented. This crush zone propagates down the tube without any global fracturing. This process is much more efficient in absorbing energy than the progressive folding of metallic structures [A2.19].

The crushing process is described by Hull [A2.5] who notes that there are two extremes of the crushing modes, namely, splaying and fragmentation. The mode of crushing will affect the value of the crush load. Figure A2.5 below shows a diagram of the splaying mode.

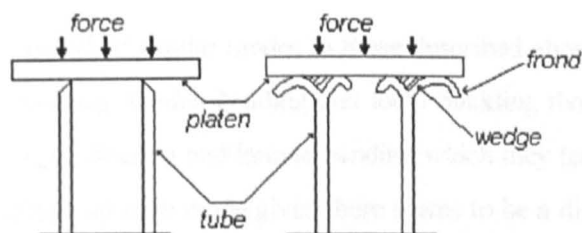


Fig A2.5: The Splaying Mode [A2.19]

As crushing takes place a wedge of debris forms at the surface of the platen and this wedge forces axial fibres to splay outwards and inwards. Hoop fibres are brought into tension until fracture occurs on the outer part of the tube and compression until buckling takes place on the inner part of the tube. The splaying fibres are often referred to as fronds.

In the fragmentation mode, high shear forces caused by the load result in lateral cracks forming at the centre of the thickness of the tube and spreading out to the tube wall, usually at about 30° to the axis of the tube. This is shown below in figure A2.6.

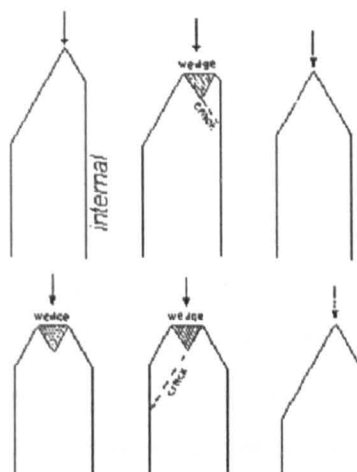


Fig A2.6: The Fragmentation Mode [A2.19]

Sigalis *et al* [A2.19] stated that the splaying mode is the most commonly encountered although crushing will often begin with the fragmentation mode before splaying takes over. Hull [A2.5] concluded that there is competition between the two different crushing modes and which mode dominates is dependant on a number of material properties.

Farley and Jones [A2.20] identified similar modes to those described above. Their three main categories are transverse shearing, lamina bending and local buckling though most tubes fail by a combination of transverse shearing and lamina bending which they term brittle fracturing crushing. From the descriptions of each mode given there seems to be a direct correspondence between transverse shearing and lamina bending to fragmentation and splaying respectively and the combination of the two would agree with the statements of Hull [A2.5] and Sigalis *et al* [A2.19]. The local buckling mode is restricted to composites of a certain class. This includes Kevlar composites (which are discussed below) and composites where the matrix has a higher failure strain than the fibres or the matrix plastically deforms under high stress.

(C) Factors in Energy Absorption

There are many more factors in a composite tube's degree of energy absorption than with metal tubes. These include the type, arrangement and nature of the fibre and resin, the manufacturing process used, the structural geometry, the method of triggering, material thickness, temperature and the rate of loading.

Thornton *et al* [A2.21] noted that the effect of fibre type in specific energy absorption is probably small compared to the effect of fibre form (chopped strand mat, woven roving etc.) and content. Graphite tubes often produce a specific energy more than twice that of their glass counterparts but much of the difference is due to the lower density of graphite. With Kevlar tubes, due to their greater toughness, energy absorption is by fibre buckling as well as by fracture processes giving them the buckled appearance of metal tubes. Including unidirectional fibres may sometimes increase the specific energy though the evidence is inconclusive. For the resin, an epoxy resin has greater energy absorption characteristics than a polyester matrix, which is superior to a phenolic resin.

Farley [A2.22] found considerable differences with tubes of varying lay-up angle, θ . For tubes of lay-up $(0 \pm \theta)$, there was little change in the energy absorption of glass fibre and Kevlar tubes but in carbon fibre tubes the energy absorption increased as θ decreased and (0 ± 15) lay-ups could absorb twice the energy of (0 ± 45) lay-ups.

With regard to the manufacturing process, the specific energies of hand-made Sheet Moulded Compounds (SMCs) were found to be higher than for machine made SMCs though the values were much more dependant on fibre type and content [A2.21].

In terms of geometry, a circular tube will absorb more energy than a square tube, which will outperform a rectangular tube. Most research has focused on these configurations though some work does exist on other geometries. For instance, Price and Hull [A2.18] showed that composite cones also fail by progressive crushing starting at the small end of the cone without the aid of triggering. Cones with a certain taper angle and wall thickness displayed greater energy absorption capabilities than axisymmetric cones made from the same material.

Mamalis *et al* [A2.23] investigated automotive frame rails of hourglass cross-section and again the same microfracture process was encountered with only slight differences.

The method of triggering the crushing process is important. The most common method is to bevel or chamfer the tube end and the trigger load is strongly dependant on the chamfer angle used [A2.19]. However, Czaplicki and Robertson [A2.24] reported that a tulip triggered tube (see figure A2.7) can absorb up to 100 % more energy per unit weight than the bevel triggered tube with the crushing being more controlled and predictable.

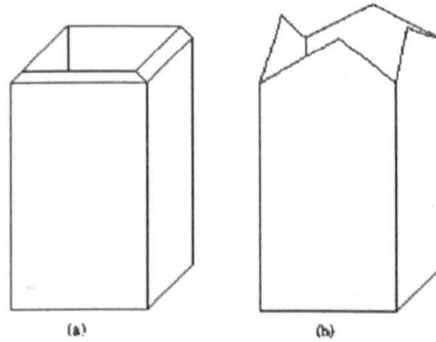


Fig A2.7: a) bevel triggered tube and b) tulip triggered tube [A2.24]

As noted above, the thickness of the tube wall also affects the tube's energy absorption capabilities. The thickness of the tube affects the collapse mode, which in turn affects the energy absorption.

The effect of temperature conditions during crushing is less significant though specific energy decreases with increasing temperature. Thornton [A2.25] found that glass fibre composites show this decrease beginning at more modest temperature values than graphite composites though in another paper, co-written by the same author, [A2.21] it is stated that the effect of temperature is primarily to cause a change in the resin properties.

The rate of loading a composite tube has a curious effect on the energy absorbed though the mode of collapse is unchanged [A2.25]. This effect seems to be dependent on the type of material though there is some disagreement to the nature of the effect. Thornton *et al* [A2.21] stated that the specific energy increases with loading rate in epoxy resins though more so when the reinforcement is carbon than when it is glass. However, when the matrix is polyester the

specific energy decreases with an increase in rate. On the other hand, Schmueser and Wickliffe [A2.26] found that the static test results of glass, graphite and Kevlar tubes (always in an epoxy matrix) exceeded the impact test results by up to 30%. Farley [A2.27] concluded that the effect of crushing speed on energy absorption was related to whether the dominant factor for a particular fibre-matrix system was a function of strain rate or not.

It can be seen that the energy absorption of composite tubes is a complex issue and further research is still required. Consequently, few theoretical analyses exist for the crushing of composite tubes.

Mamalis *et al* [A2.23] proposed a theory which calculated, then summated the energy dissipated during friction between the annular wedge and the fronds and also between the fronds and the press platen, fronds bending, crack propagation and axial splitting. Thornton *et al* [A2.21] offered an empirical estimate of the specific energy of different composites with multiplication factors for various shapes of tubes. Farley and Jones [A2.20] presented a simplified procedure for determining the qualitative effect of material property and geometry parameters on the crushing response of tubes. An analogy of the buckling load of a column on an elastic foundation was used.

A number of other points are worth mentioning on this subject. These are in terms of non-standard composites and load conditions.

Composites that contain a combination of fibres in a matrix are known as hybrid composites. Farley [A2.22] investigated a number of different combinations and concluded that the energy absorption of hybrid composites were only slightly better than that of single type fibre composites. Hamada *et al* [A2.28] claimed that problems facing the manufacturing of high quality thermoplastic matrix tubes using continuous fibres had been overcome. They went on to test composites with a polyetheretherketone (PEEK) matrix and achieved the highest values of energy absorption recorded to date.

As most real life collisions deviate from the pure axial loading condition, Czaplicki *et al* [A2.29] examined the effect of non-axial crushing of tubes. Angled loading (when the vehicle impacts an object which is at an angle rather than normal to its longitudinal axis) and off-axial loading (when the spinning vehicle impacts an object from a direction not along its

longitudinal axis) were both represented. It was found that energy absorption during angled loading (up to 30°) was roughly equivalent to the axial condition but, during off-axial loading, energy absorption decreased with increasing angle of inclination.

Composite Structures – Bending

To date, most of the investigative work on the crashworthiness of composite components in bending has been carried out by Mamalis and his co-workers. In a number of papers [A2.30-A2.33] the bending of glass reinforced vinylester and polyester tubes were considered. The tubes were circular [A2.30], rectangular [A2.31] and of hourglass geometry [A2.32]. The same experimental set up as used for the steel tubes in bending [A2.17] was utilised. For each type of tube a macroscopic and microscopic description of the collapse process were given.

For circular tubes, collapse was initiated due to local fibre buckling in compression on the upper part of the tube near the clamp and fibre debonding begins. In the lower part of the tube, which is under tension, high stress concentrations cause cracking of the matrix though fibre breakage only occurs when the fibre fracture strength is reached. There is also a narrow transition zone between the tensile and compressive regions which exhibits characteristics of both regions. The overall failure mechanism results in transverse cracking.

The tube initially deforms elastically until a maximum bending moment is reached at which point cracking begins. A plug was, at certain times, inserted into the tube as an additional clamping device. This was found to have a significant effect on the beams response, namely, a higher maximum moment followed by a shorter post-crushing stage. Also, a longer plug led to increased maximum moment and a plug with rounded edges would crack initiation and propagation.

Rectangular tubes of various dimensions were bent about both their major and minor axis. Three distinct regions were observed as with the circular tubes. In this case they were the top wall in compression, the bottom wall in tension and the side walls which showed features of compression and tension. Cracking again initiates on the top wall at the clamp edge and rapidly spreads to the corners where delamination cracking occurs. The tube can sustain higher loads as the corners crush and the top and side walls begin to buckle. Once the maximum moment is attained, buckling and splintering results in the separation of the tube in

its compressive regions. This separation occurs at 45° to the longitudinal axis following the direction of maximum shear stress.

It was found that the extent of tube separation was greater for thinner beams and the maximum bending moment being less than that for thicker sections. Energy absorption was greater when bent about their major axis and, in general, was higher than obtained for circular tubes. This latter point was explained by corner crushing and increased tube strength. Figure A2.8 below shows a typical plot of the bending moment achieved against angle of rotation for two of the specimens.

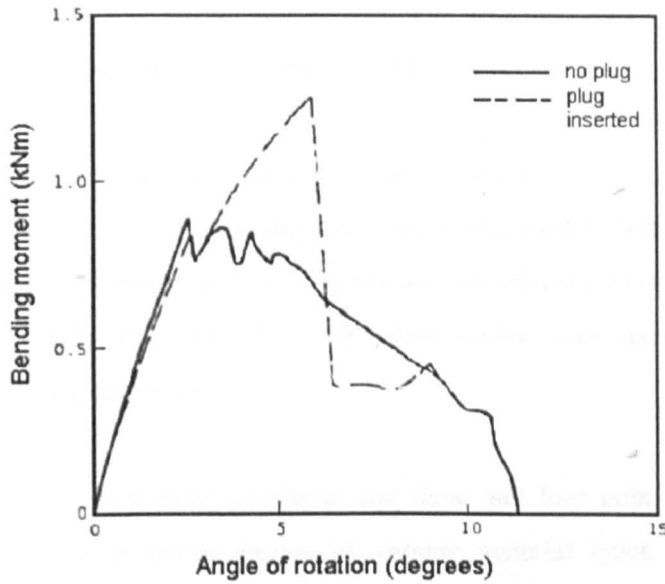


Fig A2.8: Bending Moment v Angular Rotation [A2.30]

In the case of hour glass frame rails, the beams showed very similar collapse behaviour to those described above. Collapse again initiated at the clamp edge in the compressive region leading to delamination and shear cracking. Bending about the major axis once again produced a greater energy absorption. However, unlike with circular tubes, plug inserts were found to be beneficial by lengthening the post-buckling stage without influencing the peak bending moment. The hour glass tubes' energy absorption is not compared with other tubes by the author. However, inspection of values for specimens of equal thickness bent over its weak axis (to give a similar depth to rectangular specimens) suggests an equal or better energy absorption capacity.

Mamalis [A2.33] also provides a theoretical analysis of the bending of various types of tubes, which will predict the ultimate bending strength and the bending response over the whole load range (including the elastic region). The theory is a modification of the classical lamination theory.

It should be noted that, for each type of tube, the collapse mode is similar to composites in axial compression and can be contrasted with metal beams. Collapse is due to microcracking without the presence of any plastic deformation. It is also interesting that rectangular beams outperformed circular beams in terms of energy absorption which has not been found in the case of axial loading. It should be stated, however, that the test conditions used by Mamalis may have had a large influence on the beams' behaviour (this seems to be confirmed by the presence and type of plug influencing the behavioural response).

Cheon *et al* [A2.34] tested glass fibre-epoxy side impact beams of various cross sections in both static and dynamic three point bending. Static tests were used to determine the optimum lay-up of the beams and numerical analysis was also performed using ABAQUS. It was found that circular beams performed relatively poorly while square cross sectional beams could perform as well as steel impact beams.

Broughton *et al* [A2.35] performed cantilever and three and four point static tests on U-channel and box section pultruded beams of various material types. Relatively simple theoretical analyses were presented for beam stiffness and failure loads, which provided reasonably accurate predictions.

Palmer *et al* [A2.36] looked at the progressive failure of pultruded rectangular composite beams during three point bending. However, a particular mode of failure specific to the beam type tested was investigated, namely tearing damage where the vertical and horizontal members of the beam are torn apart from one another due to out-of-plane shearing. This tearing failure was simulated using LS-Dyna Finite Element Analysis with simulated spotwelds used to connect the different members of the beam, which can be released at suitable load levels.

CERTIFICATE OF CONFORMANCE

MECHANICS OF MATERIALS DIVISION - MATERIALS TESTING LABORATORIES

200,000 lbf ELECTRO-MECHANICAL TEST MACHINE Serial No. 81000

MAKER - Tinius Olsen, USA

COST £12,000 Mod £2,000

LOCATION - Lab M7

INSTALLED 1964 Mod 1986

SPECIFICATION

Load Ranges (tension and compression) 0 to 200,000 lbf

Load Ranges 0 - 20,000 lbf, 0 - 50,000 lbf,
0 - 10,000 lbf and 0 - 2,000 lbf

Machine Compliance Not measured

Machine Calibration Tension BS EN10002:- 2 Class 0.5 or 1.0
Compression BS1610 : Grade 1.0 or 0.5

MACHINE PERFORMANCE & CAPABILITY

Displacement Rates 0.1 - 100 min/min

Daylight (Tension and Compression) 7 feet vertically
2 feet 6 ins sq horizontally

Recorder Mechanical System - A4 Plot ($\pm 2\%$ accuracy)
BNC Outputs - A3 Plot ($\pm 1\%$ accuracy)

Extensometer available - 2 in gauge length - not calibrated

Tension Grips Round Bar to 3 in diameter
Flats to 2.5 in thick x 80 mm wide

Daylight between columns 740/760 mm

Compression area 610 mm square

Bend Rig Centres 1448 to 4267 mm

The machine complies with the requirements for the following grading and ranges:

200,000lbf Range:	GRADE 0.5	40,000lbf
50,000lbf Range:	GRADE 0.5	10,000lbf
10,000lbf Range:	GRADE 0.5	2,000lbf
2,000lbf Range:	GRADE 0.5	400lbf

CERTIFICATE OF CALIBRATION

ISSUED BY THE TESTING MACHINE CALIBRATION SERVICES
OF
BAYLISS BROWN LIMITED

DATE OF ISSUE

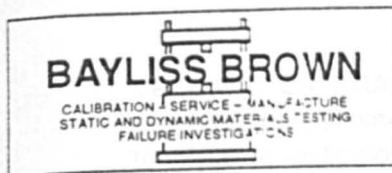
30th July 1998

CERTIFICATE NUMBER

O8357



CALIBRATION
No. 0090



THE BANKS
LONG BUCKBY
NORTHANTS, NN6 7QQ
Telephone: (01327) 843244
Fax: (01327) 843222

Page 1 of 2 Pages

Approved Signatory

D. A. ARNOLD

FOR: University of Strathclyde
James Weir Building
75 Montrose Street
Glasgow, G1 1XJ.

LOCATION: As above

DESCRIPTION: 200,000lbf Tinius Olsen testing machine
having 4 ranges in compression and tension.

0 to 200,000lbf with an analogue scale interval of 200lbf
0 to 50,000lbf with an analogue scale interval of 50lbf
0 to 10,000lbf with an analogue scale interval of 10lbf
0 to 2,000lbf with an analogue scale interval of 2.0lbf

MACHINE TYPE: TINIUS OLSEN SERIAL NUMBER: 81000

YEAR OF MANUFACTURE: Not Known

DATE OF VERIFICATION: 24th July 1998

GRADING:

The above testing machine has been verified, in compression only, to the BS 1610 : Part 1 : 1992 and to NAMAS Technical Policy Statement 10 Edition 2 dated May 1996, using verification equipment calibrated to BS 1610: Part 2 : 1985.

The machine complied with the requirements of the standard for the following grading and ranges:

200,000lbf Range:	GRADE 0.5	COMPRESSION only	200,000lbf down to 40,000lbf
50,000lbf Range:	GRADE 0.5	COMPRESSION only	50,000lbf down to 10,000lbf
10,000lbf Range:	GRADE 0.5	COMPRESSION only	10,000lbf down to 2,000lbf
2,000lbf Range:	GRADE 0.5	COMPRESSION only	2,000lbf down to 400lbf

xxvi

The reported expanded uncertainty is based on a standard uncertainty multiplied by a coverage factor $k=2$, providing a level of confidence of approximately 95%. The uncertainty evaluation has been carried out in accordance with UKAS requirements

This certificate is issued in accordance with the requirements of the United Kingdom Accreditation Services as specified in the NAMAS Accreditation Standard and NAMAS Regulations. It provides traceability of measurement to recognised national standards and to units of measurement realised at the National Physical Laboratory or other recognised national standards laboratories. This certificate may not be reproduced other than in full, except with prior written approval of the issuing laboratory.

CERTIFICATE OF CALIBRATION

UKAS ACCREDITED CALIBRATION LABORATORY No. 0290

Certificate
Number O8357

Page 2 of 2 Pages

VERIFICATION EQUIPMENT:

The following equipment,calibrated to BS 1610:Part 2:1985 was used to effect the verification.

1MN universal loadcell No 9497

Certificate No 08C011/96490/LL186/3 dated 16th December 1996

200kN universal loadcell, No B19869

Certificate No. 963010 dated 22nd October 1996

20kN universal loadcell, No B41248

Certificate No. 963009 dated 22nd October 1996

NOTE:

The expiry date of each of the above certificates of calibration is 24 months from the above given date.

METHOD:

The indicated force method was used to effect the verification.

Three verification tests were made on each range.

One series of tests were made on each range with the slave pointer connected.

The average temperature of the verification equipment at the time of the verification was 20.2 degrees C.

NOTE:

Clause 2.6 of BS 1610 : Part 1 : 1992 states that a materials testing machine shall be reverified annually or if it has been dismantled for moving or subjected to major repair or adjustment.

A3.3: Nominal and Measured Dimensions of Steel Coupons

Referred to in section 3.1.2

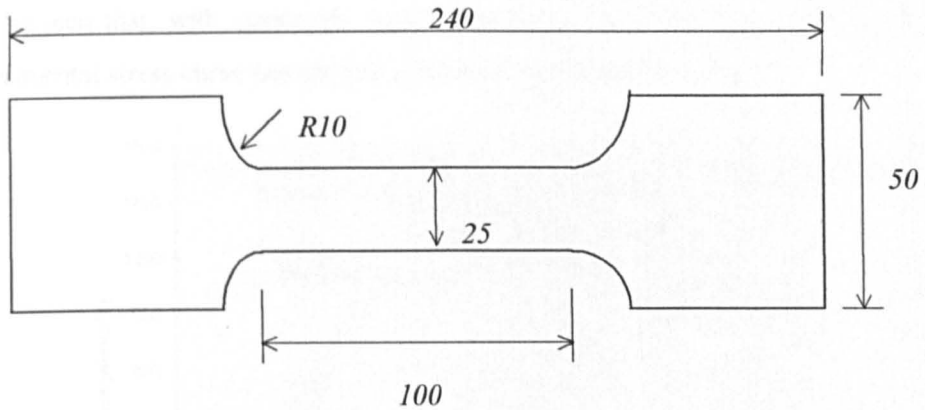


Fig A3.1: Illustration of Dog-bone Coupon Showing Nominal Dimensions (in mm)

Coupon	Thickness (mm)	Width (mm)	Cross-sectional Area (mm ²)
1	2.01	25.00	50.25
2	2.00	25.01	50.02
3	1.99	25.01	49.77
Average	2.00	25.01	50.02

Table A3.1: Measured Dimensions of Steel Coupons

A3.4: Justification For Selected Value of Proof Stress

Referred to in section 3.1.4

Figure A3.2 below shows a number of proof stress lines and the resulting proof stresses. It can be seen that, with commonly used values of offset strain such as 0.1% and 0.2%, the experimental stress curve has already reached a high degree of linearity.

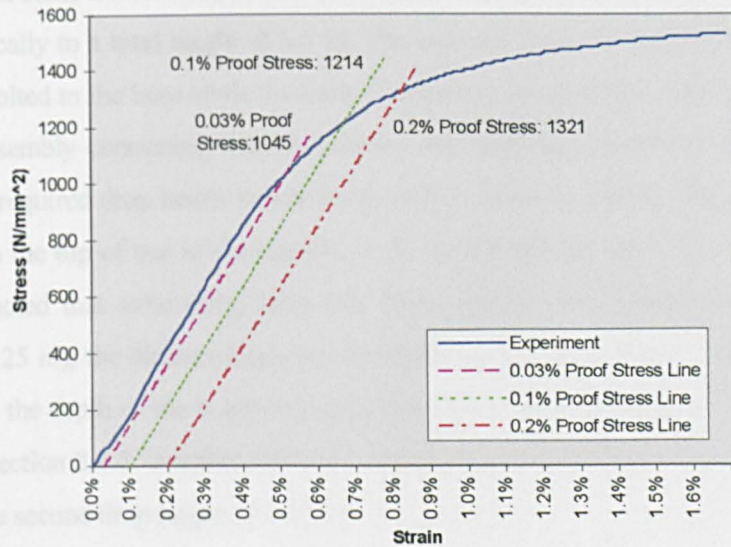


Fig A3.2: Stress v Strain with Various Proof Stress Lines

If a trend line is inserted in the data leading up to each proof stress then a measure of the linearity of the line can be made using the ' R^2 ' value. This has been done and table A3.2 below shows the results.

Offset Strain (%)	Proof Stress (MPa)	R^2 Value
0.03	1045	0.9972
0.05	1114	0.9947
0.1	1214	0.986
0.2	1321	0.961

Table A3.2: Linearity For Various Proof Stress Lines

It was arbitrarily decided to keep the linearity of the line to well within 0.5% and so a proof stress using an offset strain of 0.03% was selected.

A3.5: Details of Guide Rails, Base and Support Columns

Referred to in section 3.3.2

A thick metal base, on wooden plinths sits on the basement floor. Guide rails begin at the base and extend vertically to a total height of 5.5 m. The rails are bolted to thick C-columns with the front C-column bolted to the base while the back C-column is fixed to the wall and there is a rigid plate and tube assembly connecting both C-columns near their top. A mark on one of the guide rails denotes the required drop height to which the striker should be raised. The mark is intended to be aligned with the top of one of the runners of the striker and this mark is 4.3 m above the base. It should be noted that subtracting from this figure the distance from the base to the top of the supports (0.25 m), the distance from the top of the runner to the impact point of the striker (0.76 m) and also the depth of the beam (about 0.04 m) gives the required drop height of 3.25 m that is derived in section 8.3.3. Another mark at a height of 5.9 m from the base aids in positioning the striker at the second drop height of 4.85 m.

A3.6 : Diagrams of Striker Construction

Referred to in section 3.3.3

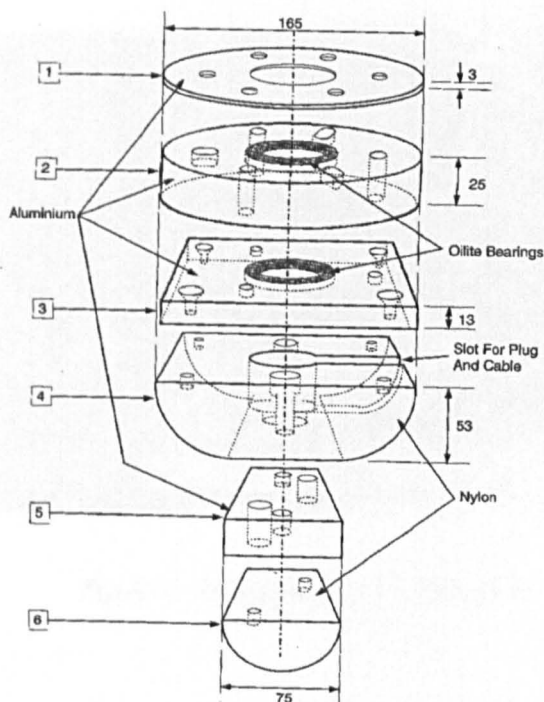


Fig A3.3: Exploded View of Striker Head

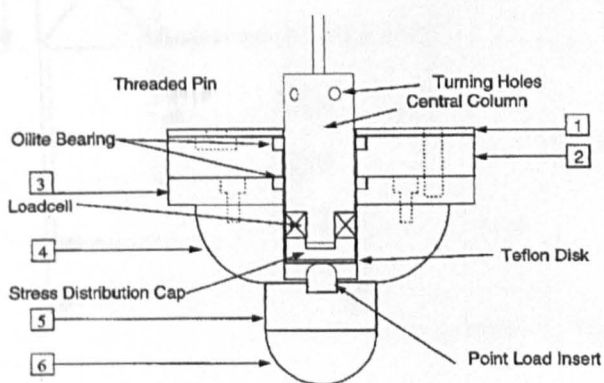


Fig A3.4: Internal View of Striker Head

A3.7: Illustrations and Technical Data of the Load Washer

Referred to in section 3.3.3

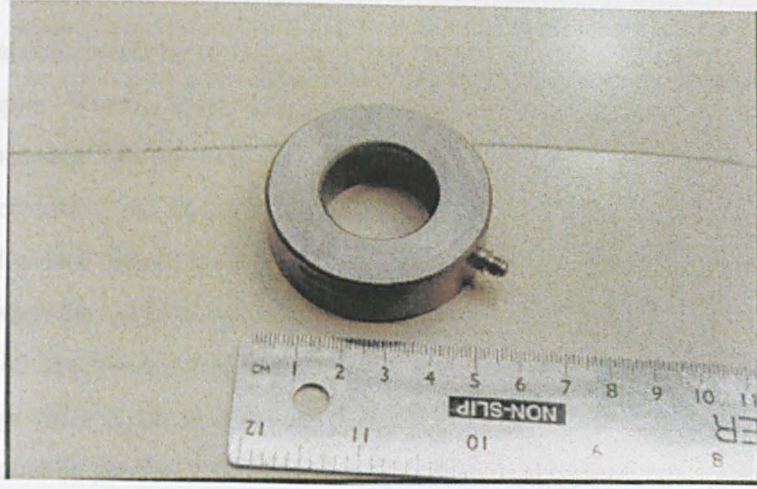


Fig A3.5: Photograph of Load Washer

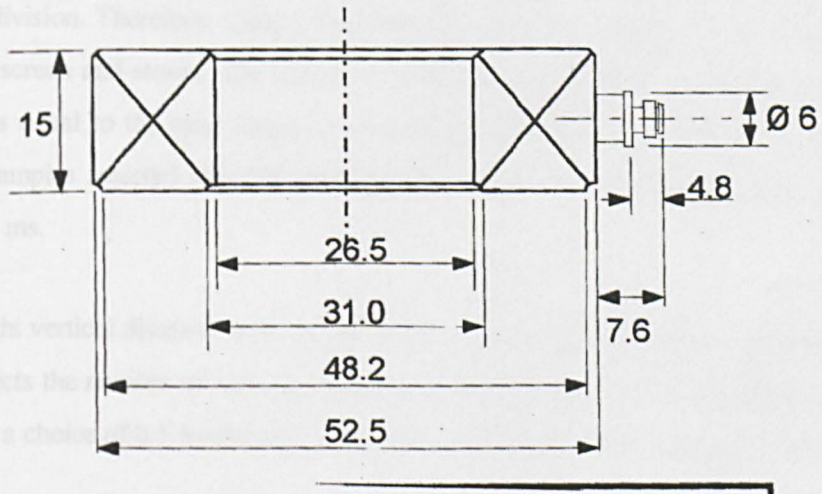


Fig A3.6: Dimensions of Load Washer

A3.8: Details of the Digital Storage Oscilloscope (DSO)

Referred to in section 3.3.5

The DSO can accommodate up to four inputs simultaneously and allows the storage of 500, 5 000 or 50 000 samples. When in RUN mode, no data is stored and a signal is displayed in real time however, by pressing NORM then ARMED, the oscilloscope will begin to store the data it collects. Trigger control can be used to initiate data storage so that the DSO does not begin to store data until a user defined input level is reached. This is beneficial in initiating data storage automatically when the test is performed and an appropriate trigger level eliminates noise initiated data storage. Both positive and negative signal triggering and pre- and post-triggering are possible and a percentage value is set. If, for example, 20% pre-triggering for 500 samples was selected, the first 100 would be prior to triggering. The data that is stored can be saved to a 3.5 in floppy disk via the disk drive incorporated into the DSO.

The DSO stores only the signal shown on its screen, which is divided by the number of samples specified. There are ten horizontal divisions and the user selects the time base, which is the length of time per division. Therefore, using a time base of 5 ms, for example, 50 ms of signal would be captured on screen and stored. The time size, which is the constant length of time between each data point, is equal to the total length of time stored divided by the number of samples. If the number of samples selected was 500 and 50 ms of signal was stored, as above, the time size would be 0.1 ms.

There are eight vertical divisions with 30 subdivisions per division available for representing data. The user selects the number of volts per division and also the gain of the amplifier. For a gain of 10 kN/V and a choice of 0.5 V/division, for instance, the signal would represent 5 kN/division.

A3.9: Calculation of the Force on the Load Cell

Referred to in section 3.3.6

The data values generated by the DSO can be converted into force data in the manner specified by the manufacturer. Values are in the units of vertical subdivisions and there are 30 of these subdivisions per division. The values represent the distance in subdivisions from an initial or, in practice no-signal, condition which would be at the very bottom of the screen and so, to center the no-signal position, a value of 127 should be subtracted from the data values. The result of this is divided by 30 to give the signal in units of the number of divisions. However, as the DSO user may position the no-signal trace anywhere on the screen, the difference between the central position and the user's selected position, termed the trace offset, is also subtracted. This is represented below in equation A3.1:

$$No. of Div = \frac{Data Value - 127}{30} - Trace Offset \quad Eq (A3.1)$$

The signal voltage, S , is simply the product of the number of divisions and the number of Volts per division, $No.V/D$, chosen by the user. The load cell force, F_{lc} , is the product of the signal voltage and the gain of the amplifier. These relationships are shown below in equations A3.2 and A3.3 respectively.

$$S = No. of Div \times No.V / D \quad Eq (A3.2)$$

$$F_{lc} = S \times Gain \quad Eq (A3.3)$$

A3.10: Details of the High Speed Video Camera (HSVC)

Referred to in section 3.3.7

The HSVC system used was a Kodak Ektrapro 1000, which allowed recording at up to 1000 frames per second (fps). Later viewing of the recording could be done frame by frame if desired. The HSV was used during the tests for two purposes. Firstly, viewing the recorded tests would provide a qualitative description and understanding of the beams' behaviour and lend confidence to any conclusions drawn from the results. Secondly, the HSV can be used as a measuring device. The displacement of the midpoint of the beam can be measured at each video frame and, adjusting for the camera's focal distance and angle, the actual displacement can be derived. As the length of time between each frame is known (from the frames-per-second setting) a relationship between displacement and time is obtained.

A3.11: Calibration of Charge Amplifier

Referred to in section 3.4.3

The charge amplifier was calibrated using an FFT analyzer and a multimeter and the testing work consisted of two particular stages. Stage One had the objective of assessing any possible error in the charge amplifier's functioning over a range of input voltages. The FFT analyser was used to generate inputs to the amplifier at a particular frequency, namely a sine wave, and the multimeter was used to measure the output of the amplifier, and also the input signal generated by the FFT analyser, because of its greater accuracy. Stage Two had the purpose of investigating the effect of the amplifier's filters on its output. The FFT analyser generated a random signal over a broad frequency range and then measured the amplifier's response. Figure A3.8 below is a block diagram of this system.

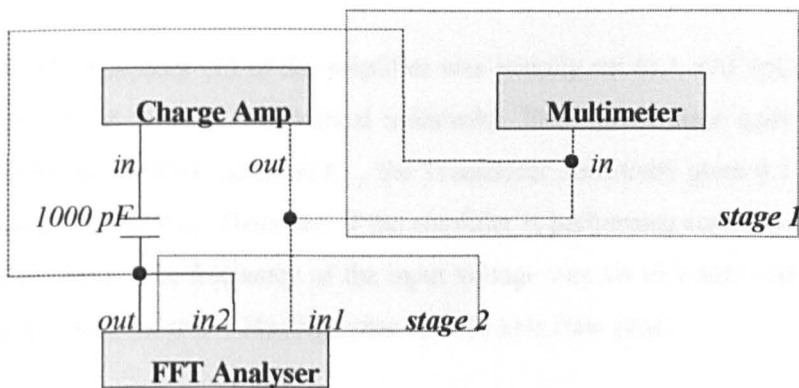


fig A3.8: Diagram for Calibration of Charge Amp

Equipment

The FFT analyzer used was a DataPhysics DP104 analyzer, which can be slotted into the port of a PC computer. The multimeter was a Fluke 8060A model with a NAMAS calibration (cert no. 57801) dated around four months before the tests were performed.

A 1000 pF capacitor was placed in series with the output of the FFT analyser in order to convert the voltage to a charge for the charge amplifier. The charge stored in the capacitor, Q , is easily determined if the capacitance, C , and the voltage across the capacitor, V , are known. Since the voltage across the capacitor is simply the output voltage of the FFT analyser, then for an input voltage of, say, 100 mV_{rms}:

$$C = \frac{Q}{V}$$

$$1000 \times 10^{-12} = \frac{Q}{0.1}$$

$$Q = 0.1 \times 10^3 \text{ pC}$$

Details of the Test Work

The Transducer Sensitivity (T) of the amplifier was initially set to 1×10^3 (pC/mechanical unit) and its Scale (S) set to unity (mechanical units/volt). Thus, given once again an input of 100 mV_{rms} and following on from equation 8., the Transducer Sensitivity gives 0.1 mechanical units and the Scale gives 0.1 V_{rms}. Therefore, if the amplifier is performing correctly, its output should be equal to the input. The frequency of the input voltage was set to 1 kHz and the filters of the charge amplifier were set to 0.1 Hz (high pass) and 10 kHz (low pass).

Five different input voltages were selected and, for each one, the values of both the input and the output voltage were noted from the multimeter. Following this, the Scale was changed to 10 to ensure this had no effect on accuracy. Thus, an output voltage of ten times the input voltage was expected. Another five input voltages were selected and the output noted. Results were inputted into an Excel spreadsheet and graphs produced.

In Stage Two, a random signal was fed to the charge amplifier. With the Scale reset to unity, results were expressed by the FFT analyser in the form of a transfer function (output voltage over input voltage). Thus a nominal value of one was expected.

Six runs were performed, each with varying settings of the filters and gains. These are listed below in table A3.3. In the last three runs the Scale was changed to 0.1 which gives an expected transfer function of 10.

RUN	Low Pass Filter (Hz)	High Pass Filter (Hz)	Trans Sensitivity (pC/mech unit)	Scale (mech unit/V)
1	10 k	0.1	1000	1
2	3 k	0.001	1000	1
3	1 k	LONG	1000	1
4	OFF	LONG	1000	0.1
5	30 k	LONG	1000	0.1
6	10 k	LONG	1000	0.1

Table A3.3: Settings Used for Stage Two of Charge Amplifier Calibration

Results of Stages One and Two

Table A3.4 below shows the results of stage one. The table lists the input and output voltages and the expected voltage (the product of the input voltage and the amplifier's gain). From these values the difference between the output signal and the expected value is derived and a mean value and standard deviation can also be calculated.

pC/unit	mV/unit out	Input Voltage	Output Signal	Calculated	Difference
1000	1000	0.0731	0.073	0.073	0.992
1000	1000	0.2197	0.218	0.220	0.991
1000	1000	0.4394	0.435	0.439	0.991
1000	1000	0.7325	0.726	0.733	0.991
1000	1000	0.9157	0.907	0.916	0.991
1000	10000	0.2198	2.179	2.198	0.991
1000	10000	0.1464	1.456	1.464	0.994
1000	10000	0.0731	0.728	0.731	0.996
1000	10000	0.0367	0.366	0.367	0.999

Std.Dev about mean	0.05	dB
Offset (Mean Error)	-0.06	dB

Table A3.4: Results of Stage One for Charge Amplifier Calibration

These results are also plotted in the form of expected values against output voltage (both of these parameters are logarithmic) and a trendline inserted through the points. This graph is given below in figure A3.9.

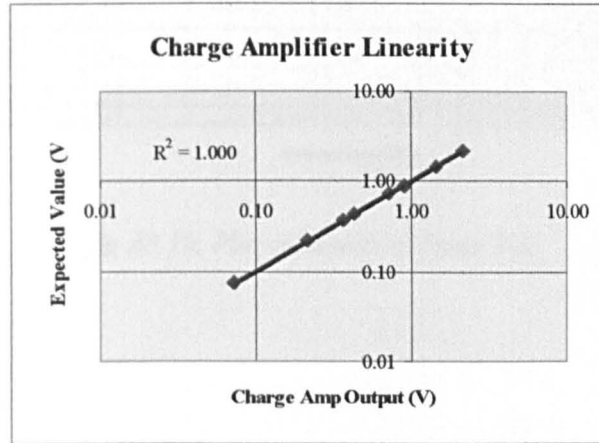


fig A3.9: Plot of Results of Stage One

Figure A3.10 below is a graph of the results of stage two and each of the six runs is plotted although this is not apparent as the results are often so similar. The magnitude of the transfer function is expressed in decibels and is calculated using the equation:

$$\text{Magnitude (dB)} = 20 \cdot \log\left(\frac{V_{out}}{V_{in}}\right) \quad \text{Eq (A3.4)}$$

Therefore, for a transfer function equal to unity the magnitude will be zero (dB) and for a transfer function of 10 the magnitude will be 20 (dB).

Charge Amplifier Filter Calibration

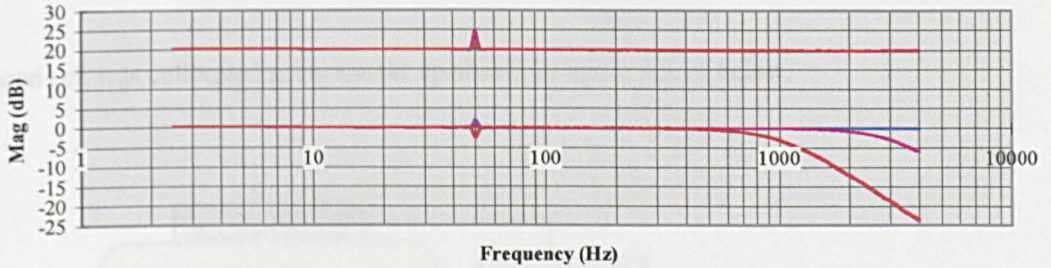


fig A3.10: Plot of Results of Stage Two

Discussion of Results

It seems clear that the charge amplifier is highly accurate within the tolerances of the calibration equipment given the low error and low variation as noted in table A3.4. Figure A3.9 indicates that the output of the charge amplifier is linearly proportional to its input in that the output remains equal to its input over a wide voltage range. This linearity is confirmed by the 'R²' value being unity.

Figure A3.10 shows that, in each case, the transfer function trace remains near zero up to cut-off frequency. Thus, the output from the charge amplifier closely matches the input signal. When the level of filtering is within the visible scale (up to 10 kHz) there is approximately a 3 dB fall at the cut-off frequency. This is evidence that the amplifier's filters are functioning correctly as it is common to design filters to do this (the filter's half power point). Given the degree of accuracy of the amplifier's filtering, it can be assumed that there was no influence of filtering during stage one of testing.

It can be seen that there is, for every run, a small peak at 50 Hz. This is no doubt due to noise the ac electrical source and it is assumed that this peak has no significant effect on the charge amplifier's operation.

A3.12: Calibration of the Load Cell

Referred to in section 3.4.3

The load cell was calibrated using the set up shown in figure A3.11 below.

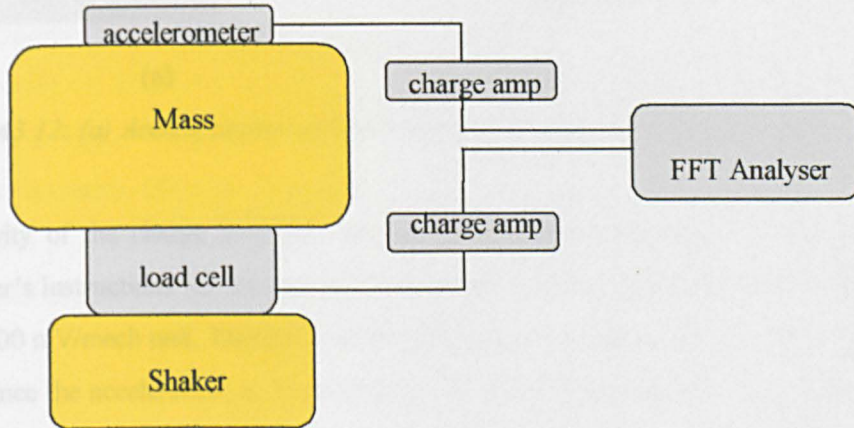
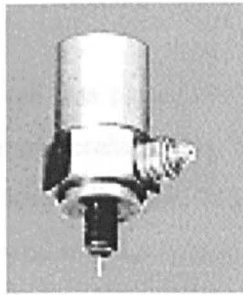


Fig A3.11: Set Up for Load Cell Calibration

Equipment

The shaker could generate a signal at a frequency of up to 100 kHz. The mass had a known value of 7.995 kg. Details of the FFT analyser were provided in section A3.11.

The accelerometer (type 4367) and its charge amplifier (type 2635) were both manufactured by Brüel & Kjær. They are shown below in figure A3.12 and their certificates of calibration can be found in appendix A3.13.



(a)



(b)

Fig A3.12: (a) Accelerometer and (b) Charge Amp Used During Calibration Test

The sensitivity of the charge amplifier for the accelerometer was set to 3.16 pC/m/s^2 as per manufacturer's instructions for when using the type 4367 accelerometer. The gain of the amplifier was set to 100 mV/mech unit . Therefore, if the 'mech unit' is acceleration, the gain is equal to 100 mV/ms^{-2} . Since the acceleration, a , is the ratio of the force, F , to the mass, M (equal to 7.995 kg neglecting the mass of the load cell and accelerometer), the output voltage from the charge amplifier, V_{out} , is readily obtained.

$$V_{out} = 100 \cdot a = \frac{100 \cdot F}{7.995} = 12.51 \cdot F \quad \text{Eq (A3.5)}$$

Therefore, in order to obtain a plot of force at the FFT analyser, the gain of this channel is set to $12.51 \text{ mV/engineering unit}$.

The sensitivity of the charge amplifier is set to the recommended value of 4.3 pC/N as per manufacturer's instructions for use with the type 9061A load cell. It's gain is also set to 100 mV/mech unit and, since the 'mech unit' is force then the gain is 100 mV/N . Thus, the gain of this channel of the FFT analyser is set to $100 \text{ mV/engineering unit}$.

Table A3.3. First Set of Measurements

Procedure

The load cell was placed on the shaker bed and on top of it was placed the known mass upon which was an accelerometer. With the shaker transmitting a signal at a frequency selected by the user, the load cell, mass and accelerometer collectively were assumed to be vibrating at that frequency and with a common value of transmitted force. The frequency was somewhat arbitrarily selected. However, so as not to violate the assumption of common frequency and force, no frequency above 1 kHz was chosen as individual components may have begun to act independently at higher frequencies. The FFT analyser measured the force of both the load cell and the accelerometer (through the charge amp) and these forces should be equal if each instrument was properly calibrated. At each of twelve selected frequencies the forces as measured by the load cell and the accelerometer were noted.

Results

The first eight results of the calibration tests on the load cell are shown below in table A3.5.

Frequency (Hz)	Load cell Force (N)	Accelerometer Force (N)	Ratio (load cell/accelerometer)
35	27.70	30.50	0.908
65	24.10	25.97	0.928
135	44.06	46.18	0.954
215	37.09	39.09	0.949
345	33.50	35.40	0.946
485	21.78	22.86	0.953
790	25.63	27.24	0.941
925	39.62	42.50	0.932
		Mean	0.946
		Standard Deviation	0.008
		Coeff Var (%)	0.88

Table A3.5: First Set of Results from Load Cell Calibration Test

From the above table it can be seen that there is an average error between the two sets of force results of about six percent. At this point the sensitivity of the charge amplifier for the load cell was changed to 4.04 which is six percent less than before. Table A3.6 shows the results using this value.

Frequency (Hz)	Load cell Force (N)	Accelerometer Force (N)	Ratio (load cell/accelerometer)
240	47.87	47.62	1.005
340	42.93	42.76	1.004
440	44.90	44.60	1.007
760	46.38	46.13	1.005
Mean			1.005
Standard Deviation			0.001
Coeff Var (%)			0.13

Table A3.6: Second Set of Results from Load Cell Calibration Test

The ratio of load cell force to accelerometer-based force as a function of frequency is plotted below in figure A3.13.

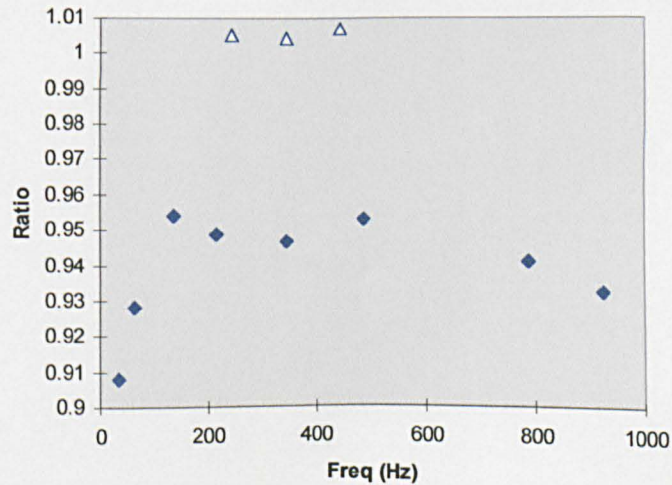


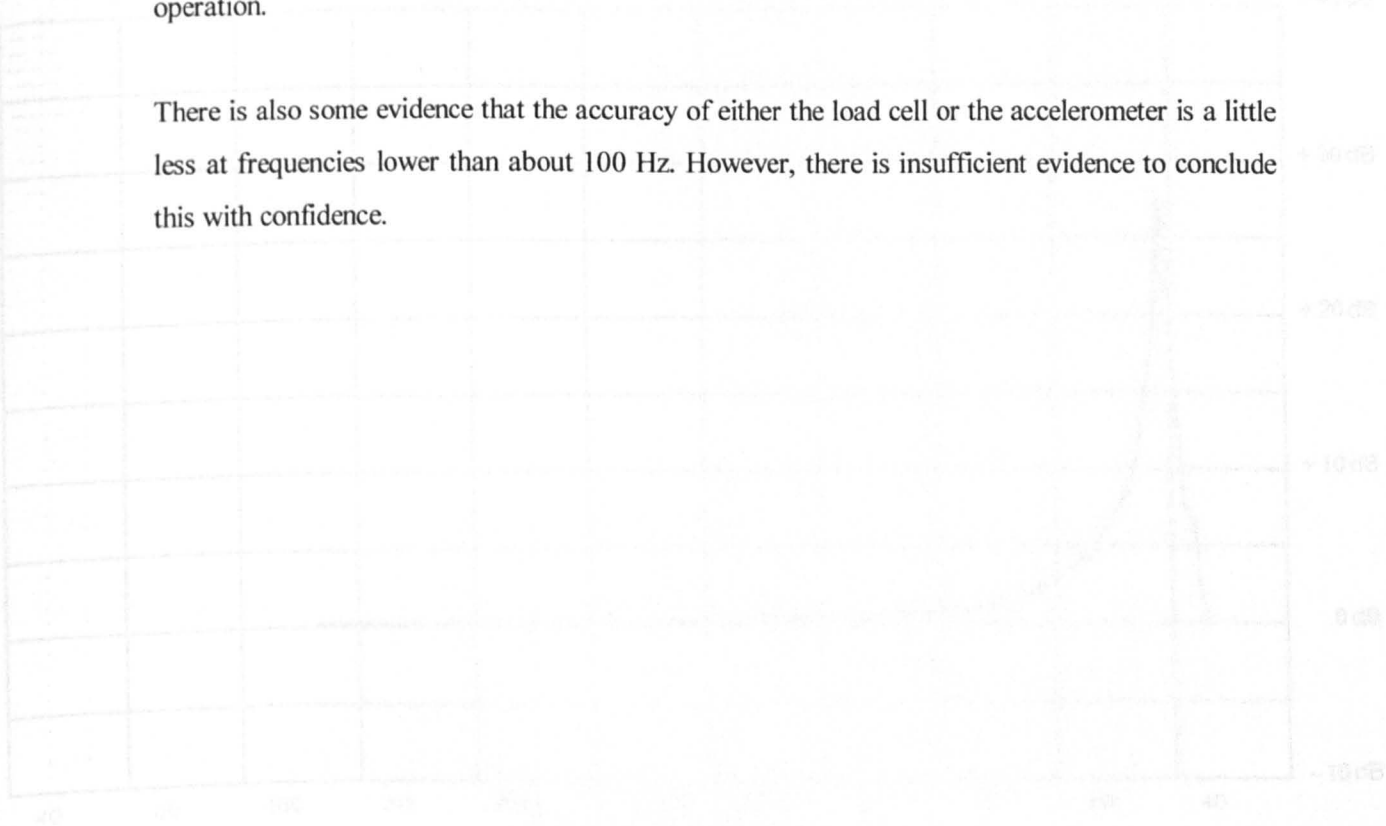
Fig A3.13: Ratio of Forces as a Function of Frequency

CERTIFICATE of CALIBRATION - 78720/5

Discussion of Results

It is clear that there is about a five percent difference between the forces derived from the accelerometer data and the load cell. When considering the low variation in results, the error would appear to be systematic in nature which can be demonstrated by reducing the sensitivity of the load cell as was done during the calibration work. However, it has not been shown which data set is in error, only that a difference exists. It could even be that error exists within both data sets. As both the load cell and the accelerometer and their associated charge amplifiers have been calibrated by their manufacturers, it is not possible to comment on the most likely source of error. It must suffice to state that the accuracy of the load cell is within five or six percent of its correct operation.

There is also some evidence that the accuracy of either the load cell or the accelerometer is a little less at frequencies lower than about 100 Hz. However, there is insufficient evidence to conclude this with confidence.



The Frequency Response is indicated with the instrument mounted on a 100 gram shaker.

Calibration Exciter Type 4230
Serial No. 789303

Accuracy: 100Hz to 30% of the accelerometer frequency range frequency $\times 1.05$

Calibration performed by [Signature]
Signature witnessed by [Signature]



COM 23/08

Brüel & Kjær

CERTIFICATE of CALIBRATION - 78720/5

The calibration is performed by comparison with:

Accelerometer Calibration Set Type 3506 8305
Serial no. 1033863

Accelerometer Type 4367
Serial No. 614226

Calibrated by SIRA Date OCT 19 97

Reference Sensitivity at 160Hz, 100 ms⁻² peak

a) Estimated uncertainty of comparison:
± % at 99% confidence level.

Charge Sensitivity 20.9 pC/g, or 2.14 pC/ms⁻²

b) Estimated uncertainty of Accelerometer Calibration Set Type 3506:
± % at 99% confidence level.

Voltage Sensitivity 16.5 mV/g, or 1.68 mV/ms⁻²

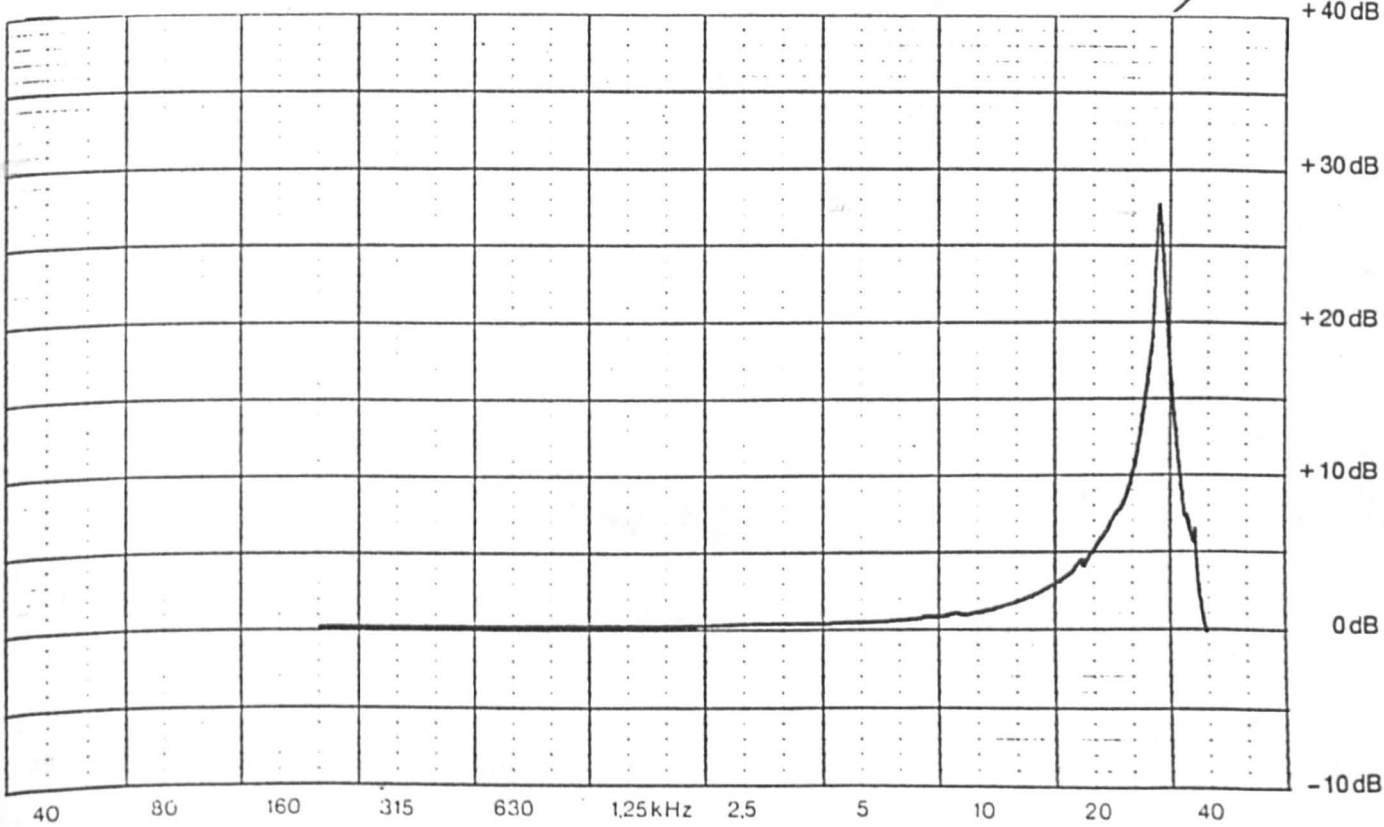
c) Absolute uncertainty:
 $\sqrt{a^2 + b^2} = \text{.....}$ % at 99% confidence level.

This calibration is traceable to: NATIONAL MEASUREMENT STANDARD

For **Mounted Resonant Frequency** and for **Frequency Response** relative to the **Reference Sensitivity**, see attached individual Frequency Response Curve.

Capacitance (including cable) 1262 pF

Input Capacitance of Pre-amplifier C_i = 90 pF



The **Frequency Response** is obtained with the accelerometer mounted on a 180 gram stainless steel block.

Condition of Test:

Calibration Exciter Type 4290
Serial No. 789505

Ambient Pressure: 1002 mbar
Temperature: 24 °C
Relative Humidity: 37 %
Date of Calibration: 3rd MARCH 1998

Accuracy: 200Hz to 30% of the accelerometers resonance frequency ± 1 dB

Calibration performed by [Signature]
Signature witnessed by [Signature]

XLVI

16

CERTIFICATE OF CALIBRATION



Issued by: Brüel & Kjær (A Division of Spectris (UK) Limited)

Date of issue: 30 MARCH 1998 Certificate number: 78720/2

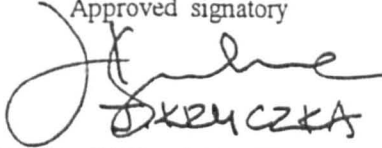
Brüel & Kjær 
A Division of Spectris (UK) Limited

Harrow Weald Lodge, 92, Uxbridge Road, Harrow, Middlesex HA3 6BZ
Telephone: 0181 954 2366 Fax: 0181 954 3729

Calibration Services

Page 1 of 6 pages

Approved signatory


D. KRYCZKA

Client: NATIONAL ENGINEERING LABORATORY
.....
.....
.....
.....
.....

Instrument **Charge Amplifier**
Type **2635** S/No: **1588592**
Manufacturer: Brüel & Kjær

Ambient conditions during calibration were:

Temperature **23** °C
Relative Humidity **31** %

V19

A3.14: Calculation of Initial Test Conditions
Referred to in section 3.5.3

The test rig, as it existed at this time, was limited in the maximum values of drop height and impact mass (and thus impact energy) that could be used for the test conditions. However, initial testing demonstrated that the values were sufficient to go well beyond collapse of the steel beam and so the impact testing could still be used to evaluate beam performance.

Two impact velocities were used within the testing. The higher velocity represents the maximum achievable with the given mass. The specifications used were:

Impact Velocity 1, v_1	=	8.0	m/s
Impact Velocity 2, v_2	=	9.75	m/s
Impact Mass, m	=	21.7	kg

The impact energy is easily derived from the relationship for kinetic energy (*k.e.*) to the impact mass of the striker and its velocity:

$$k.e. = \frac{mv_{1,2}^2}{2} \qquad \text{Eq (A3.10)}$$

The impact energy will be equal to the kinetic energy when impact velocity has been achieved. Therefore:

Impact Energy 1	=	695	J
Impact Energy 2	=	1035	J

Determining the height from which the striker must fall to achieve such an impact energy is also straightforward. A body that is held at some height, h , has a potential energy (*p.e.*) where:

$$p.e. = mgh \qquad \text{Eq (A3.11)}$$

Setting the potential energy equal to the impact energy and solving for h gives the drop height:

Drop Height 1	=	3.25	m
---------------	---	------	---

Drop Height 2 = 4.85 m

A3.15: Derivation of Velocity and Deflection data
Referred to in section 3.5.4

Figure A3.14 below shows a beam and the force, f_{beam} , acting upon it during impact by a mass, m , under acceleration, a .

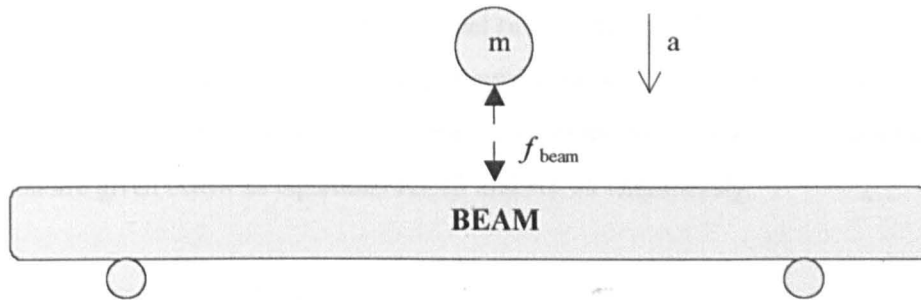


Fig A3.14: Forces Acting on Beam

Appendix A3.9 has shown that the force on the beam is the corrected force (accounting for the ratio of masses) measured by the load cell. The acceleration of the mass is given by:

$$a = \frac{f_{beam}}{m} \quad \text{Eq (A3.12)}$$

Note that the mass, m , is the total mass of the striker since the correction factor has been applied. The velocity, v , of the mass is given by:

$$\begin{aligned} v &= \int a \cdot dt = \int \left(\frac{f_{beam}}{m} \right) \cdot dt \\ &= \frac{1}{m} \int f_{beam} \cdot dt \end{aligned} \quad \text{Eq (A3.13)}$$

The displacement, δ , of the mass is given by:

$$\begin{aligned} \delta &= \int v \cdot dt \\ &= \frac{1}{m} \iint f_{beam} \cdot dt \cdot dt \end{aligned} \quad \text{Eq (A3.14)}$$

As the striker is in contact with the beam for virtually the whole of the impact event, the striker's velocity and displacement can be taken to be the beam's velocity and deflection at mid-span.

As can be seen in section __, the force plot is complicated and not easily represented by some mathematical function. Thus, integration of the force data must be by some numerical technique and this is done using the trapezoidal rule. In the Excel environment, formulas were applied to the spreadsheet cells to implement equations A3.13 and A3.14 using this rule. For cell $(i+1)$, where $i=1$ to n and n is the number of samples, the formulas for beam velocity and deflection are given below as equations A3.15 and A3.16 respectively.

$$v_{(i+1)} = v_{(i)} + TimeSize \times \left(\frac{P_{(i)} + P_{(i+1)}}{2M} \right) \quad Eq (A3.15)$$

$$\delta_{(i+1)} = \delta_{(i)} + TimeSize \times \left(\frac{v_{(i)} + v_{(i+1)}}{2} \right) \quad Eq (A3.16)$$

Integration methods other than the trapezoidal rule were tried, such as various forms of the Simpson's rule (varying in their complexity) but the difference was only marginal as can be seen in figure A3.15 below.

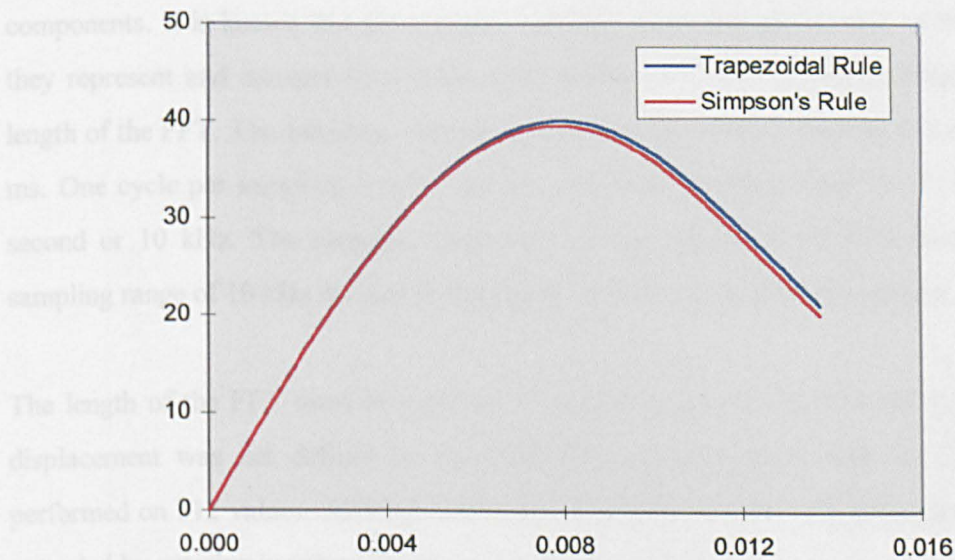


Fig A3.15: Comparison of Trapezoidal & Simpson's Rule

A3.16: Signal Filtering

Referred to in section 3.5.4

If the dynamic effects seen within the dynamic load data are not part of the structural response of the beams then it is desirable that they be removed and so some form of signal filtering is required. If the dynamic effects are at a higher frequency than the response of the specimen then filtering is simpler if it is carried out in the frequency domain.

Fourier analysis allows any signal to be represented by a sum of sinusoidal functions, the Fourier series, and filtering can then be achieved by removing those functions that are of a higher frequency. When computers are used for Fourier analysis the primary tool used to do this is the Discrete Fourier Transform (DFT) which involves discretization of the Fourier series. A number of efficient algorithms developed to compute the DFT have all been given the name 'Fast Fourier Transforms' or FFTs. The main advantage in using FFTs rather than DFTs is that the former has a much-improved processing speed.

Implementation of the FFT

It would be convenient if the whole filtering process could be performed within the Excel software. Excel v7.0 has an incorporated FFT data analysis tool that will transform a sequence of values to give a list of complex numbers that are related to the frequency components. It is known that the complex numbers generated are in order of the frequencies they represent and increase by a value equal to the ratio of the sampling frequency and the length of the FFT. The sampling interval used in the beam tests is the time size which was 0.1 ms. One cycle per sampling interval equates to a total sampling range of 10 000 cycles per second or 10 kHz. The sampling frequency, or step change in the FFT data, is the total sampling range of 10 kHz divided by the length of the FFT (usually 256 values).

The length of the FFT must be a power of two. If the whole impact event up to maximum displacement was not defined by the first 256 load data points then an FFT would be performed on 512 values. Although each data set consists of only 403 data points, it could be extended by entering in values based on a no-load condition.

Each value generated by the FFT corresponds to a frequency value which increases until the middle number in the list is reached which is the Nyquist, or critical, frequency. After this the numbers mirror the first half of the list except that they are the complex conjugate of the first half. The very first number in the list is simply a summation of all the numbers and is real as all the imaginary parts of the complex conjugates cancel each other out. It is known from theory that the Nyquist, or critical, frequency, f_c , is related to the sampling interval, Δ , in that:

$$f_c = \frac{1}{2\Delta} \quad \text{Eq (A3.17)}$$

Shannon's sampling theorem shows that no other frequency can be defined above the Nyquist frequency. For a sampling interval of 0.1 ms the critical frequency is therefore 5 KHz which is the middle number in the FFT data list.

Filtering the data can therefore be achieved by removing a middle band of the list of numbers and then applying the inverse Fast Fourier Transform (iFFT). The degree of filtering will depend on the width of this middle band and the issue becomes which degree to choose. Plotting filtered and unfiltered load and making a subjective balance between fluctuations removed and the correlation of filtered and unfiltered data could possibly justify the degree of filtering selected. Figure A3.16 below shows the effect of various degrees of filtering on the relationship of load to time.

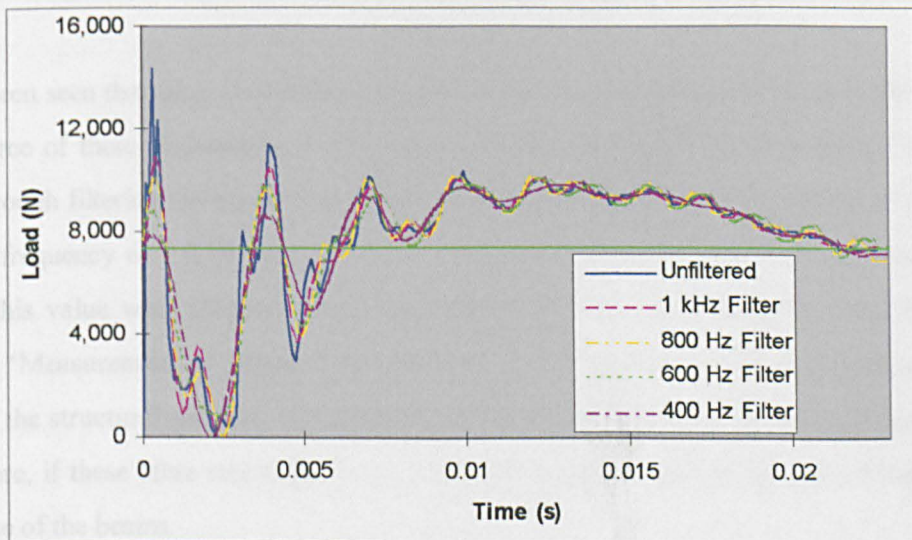


Fig A3.16: Effect of Filtering on the Relationship of Load to Time

It can be seen that, although a number of the load spikes have been removed in the filtered data, the large fluctuations still exist even at the highest levels of filtering. Therefore, either these fluctuations are due to the beams' vibration response in dynamic tests or the test rig and instrumentation is capable of producing very low frequency noise in the data.

It might be thought that a further criterion could involve the use of recalculating deflection from various degrees of filtered data and then making a comparison. However, even with considerable filtering, the derived deflection was found to vary by less than 1%. Figure A3.17 below shows the effect of various degrees of filtering on the relationship of deflection to time.

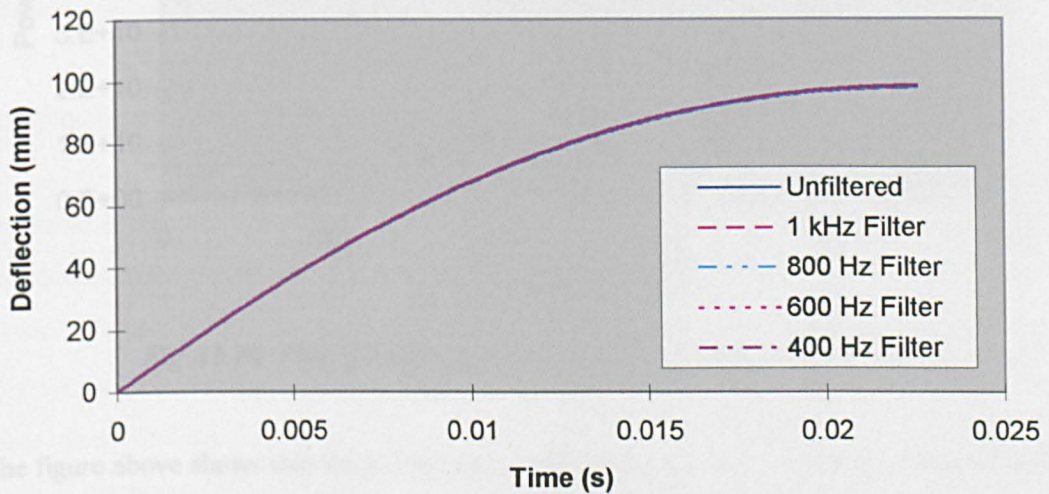


Fig A3.17: Effect of Filtering on the Relationship of Deflection to Time

It has been seen that large load fluctuations still exist even at the highest levels of filtering and the source of these fluctuations is at present unknown. It would not be desirable to remove data through filtering which represent the real structural behaviour of the beams. Therefore, a cut-off frequency of 1 KHz was selected for dynamic beam test data so that all frequencies above this value were removed. This is supported by other researchers (such as Birch and Jones ['Measurement of Impact Loads using a Laser Doppler Velocimeter']) as the upper limit of the structural response of specimens and below the frequency of test rig induced noise. Therefore, if these other researchers are correct, the load fluctuations are part of the dynamic response of the beams.

It is possible to plot the power at each frequency during a beam test. Power is defined as the square of the absolute magnitude of data at each frequency and is a measure of the contribution of each frequency. This plot, up to the cut-off frequency of 1 kHz, is shown below in figure A3.18. The plot is highly typical of all of the beam tests at either impact velocity.

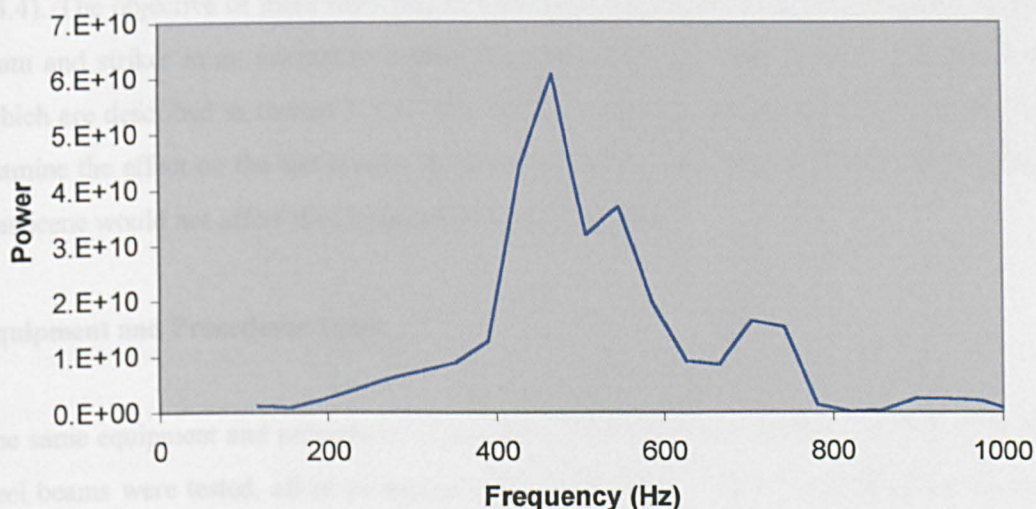


Fig A3.18: Plot of Power against Frequency During Impact Tests

The figure above shows that three frequency components, namely about 470, 550 and 700 Hz, are highly dominant in the load data and it is these frequencies that are mainly responsible for the load fluctuations. The value of around 470 Hz is particularly dominant. It should be noted that precise peak frequencies are not possible due to the resolution of the FFT data (about 40 Hz). These frequencies may represent vibrational modes of the beam under test conditions. If this could be verified then it would be known that the load fluctuations are indeed caused by the dynamic response of the beams.

The theory of modal testing relies on the assumption that the behaviour of the test structure is linear. If this ceases to be true, as for local deformation, then modal analysis becomes invalid. Yet, plots of power against frequency derived from different stages of the impact test in the time domain are highly consistent. This is the case even for the first 5 ms where only elastic behaviour exists. Therefore, it is supposed that the elastic modal response, if it gives rise to these load fluctuations, remains dominant throughout the impact test.

A3.17: Contact Tests on Beams

Referred to in section 3.5.5.

Introduction to Contact Tests

Impact tests, referred to as the contact tests, were carried out on steel beams with a different geometry (the same beam as used in the calibration of the test set up as described in section 3.4.4). The objective of these tests was to investigate the effect of the contact stiffness of the beam and striker in an attempt to explain the dynamic effects seen in all of the impact tests (which are described in section 3.5.5). The method used was to alter this contact stiffness and examine the effect on the test results. It was assumed that the inclusion of the polystyrene or plasticine would not affect the modal properties of the beam.

Equipment and Procedures Used

The same equipment and procedures were used as described in sections 3.5.2 and 3.5.3. Four steel beams were tested, all at an impact velocity of 8 m/s. The first was tested in the usual manner. Taped on to the top flange of the second beam, at mid-span, was a block of polystyrene (40 mm long, 20 mm wide and 18 mm thick). This was also done for the third beam except that the polystyrene block was 36 mm thick. On to the fourth beam was placed a block of plasticine (20 mm thick).

Results of Contact Tests

Figure A3.19 shows the results, for load against time, of the contact tests. No filtering has been performed on the load data. Two of the beams involved the addition of a block of polystyrene, each with a block of different thickness. However, it was found there was little difference between the two tests and only the results for the beam with the thicker block are shown in the figure below.

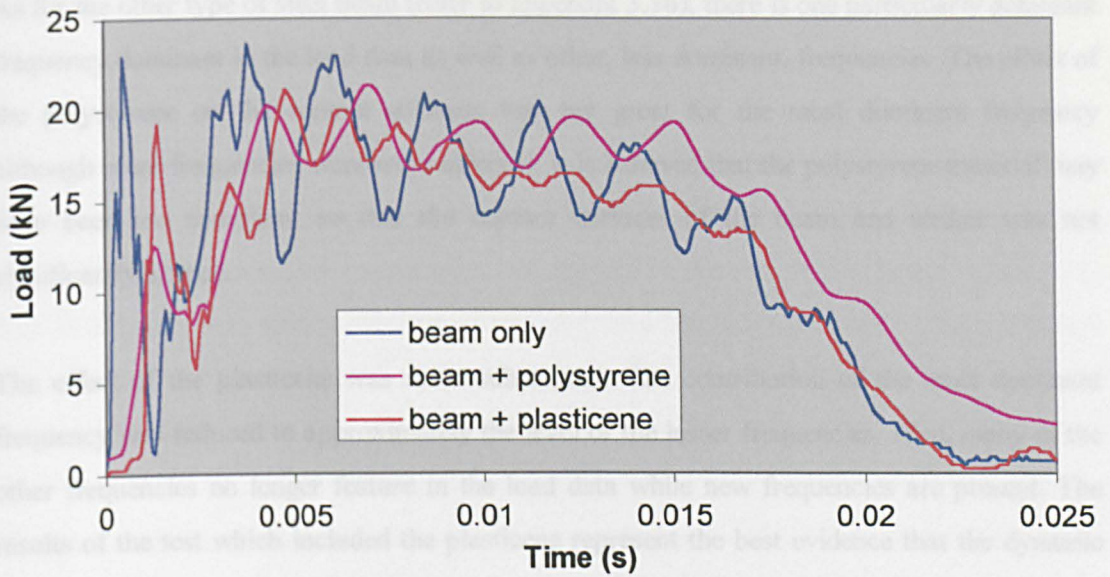


Fig A3.19: Plot of Load v Time for Contact Tests

The general elastic and collapse behaviour of the beam appears unaffected by the change in contact stiffness between the striker and beam. However, there is some change in the dynamic effects, in terms of their magnitude and frequency, that are present in the load data.

The FFT filtering procedure also allows identification of the frequencies of the dynamic effects and the contribution of each frequency. This process has been described in appendix 3.16. Figure A3.20 is a plot of the power against frequency for the contact test results.

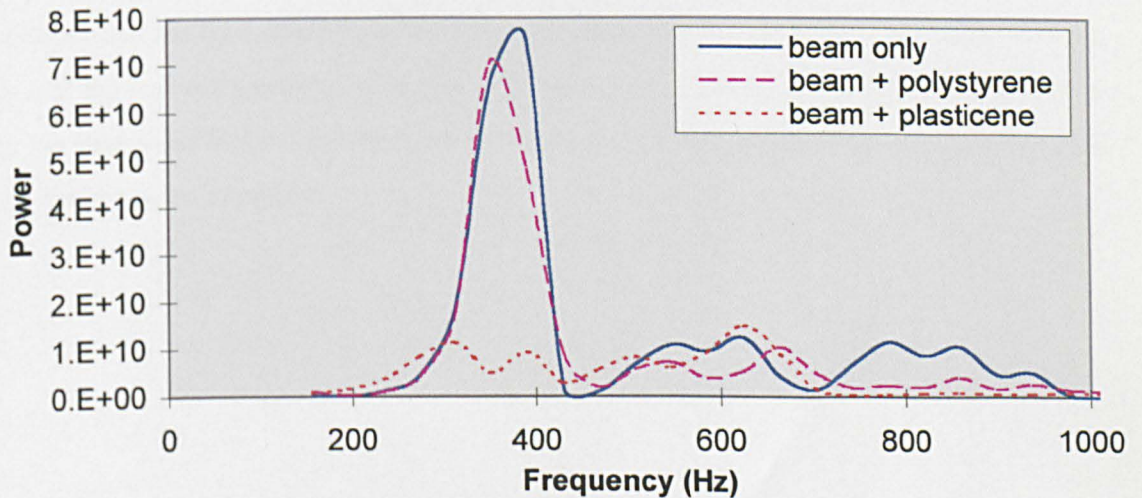


Fig A3.20: Plot of Power v Frequency for Contact Tests

As for the other type of steel beam (refer to appendix 3.16), there is one particularly dominant frequency dominant in the load data as well as other, less dominant, frequencies. The effect of the polystyrene on the contact stiffness was not great for the most dominant frequency although other frequencies were more affected. It is believed that the polystyrene material may have been too compliant so that the contact stiffness of the beam and striker was not significantly altered.

The effect of the plasticene was more substantial. The contribution of the most dominant frequency was reduced to approximately the level of the lesser frequencies. Also, many of the other frequencies no longer feature in the load data while new frequencies are present. The results of the test which included the plasticene represent the best evidence that the dynamic effects present in impact test results are a function of the contact stiffness of the beam and striker. However, more investigation is required in this area.

A3.18: Traces From the HSVC

Referred to in section 3.5.4

The video recordings were first downloaded to a VHS format and two copies made. It was fortunate that this was done as a technical fault developed with the HSV tape during downloading. The copies were made with only one test lost but the HSV tape is now unusable. The VHS tapes were used in determining the displacement but unfortunately during playback these tapes often 'jumped' one frame so that the value of displacement at the lost frame could not be determined.

The view scale factor was first calculated and this was done as follows: the video image of the distance from the marked interval at the beam's midpoint to the next interval was measured with a rule and compared with the actual distance. The actual distance was also checked with a rule. This was done for three arbitrary beams and an average taken.

For each specimen, the video recording was viewed and the frame just previous to the first frame showing displacement of the beam was taken as "time zero" and the frame number noted. The rule was then taped to the video monitor to restrain any movement and the video recording played one frame at a time (except for the frames lost). At each frame the displacement and the frame number were noted.

All these values were then entered into the Excel spreadsheet for the appropriate specimen ensuring that the time at which each value of displacement occurred was compatible with the time of the load cell generated data. The software was used to multiply the video displacement by the view scale factor. Displacements over time from both sources of the video and the load cell could now be compared.

A3.19: Other Values Obtained from Impact Testing

Referred to in section 3.5.5

Table A3.7 below lists some values of a more minor interest for each of the beams. Each of the headings of the table requires a brief explanation. Results of the beam tests show a general pattern and one aspect of this pattern is that there are always three peak loads and always at around the same time in each test. To make comparisons of beams in terms of peak loads at all meaningful, values for each of these peak loads, P_{peak} , are provided in the table.

The time taken to reach maximum deflection and energy absorption is included within the table (t_{max}). This will always be when the beam's velocity reaches zero (no further deflection and all of the impact energy absorbed). Values of maximum deflection, δ_{max} , and energy absorption, EA_{max} , are taken from the filtered data.

BEAM	$P_{peak\ 1}$		$P_{peak\ 2}$		$P_{peak\ 3}$		t_{max} (ms)	δ_{max} (mm)	EA_{max} (J)
	(kN)	(kN)	(kN)	(kN)	(kN)	(kN)			
	<i>unfil</i>	<i>filt</i>	<i>unfil</i>	<i>filt</i>	<i>unfil</i>	<i>filt</i>			
1 (8 m/s)	13.44	9.70	13.75	12.91	17.03	15.40	14.6	62	694
2 (8 m/s)	13.28	9.52	19.53	14.86	17.03	16.04	13.6	60	694
3 (9.75 m/s)	11.72	10.62	19.69	16.67	14.53	12.82	20.0	95	1031
4 (9.75 m/s)	11.09	11.46	19.06	17.21	14.69	12.82	20.9	97	1031

Table A3.7: Values Obtained from Testing

From the values above, the mean and standard deviation can be determined for each type of value. These statistical values are given below in table A3.8.

Impact Vel (m/s)	$P_{peak\ 1}$		$P_{peak\ 2}$		$P_{peak\ 3}$		δ_{max} (mm)	Ea_{max} (J)	No. of Spec.
	(kN)	(kN)	(kN)	(kN)	(kN)	(kN)			
	<i>unfil</i>	<i>filt</i>	<i>unfil</i>	<i>unfil</i>	<i>filt</i>	<i>unfil</i>			
8	13.36	9.61	16.64	13.89	17.03	15.72	61	694	2
	± 1%	± 1%	± 25%	± 10%	± 0%	± 3%	± 3%	± 0%	
9.75	11.41	11.04	19.38	16.94	14.61	12.82	96	1031	2
	± 4%	± 5%	± 2%	± 2%	± 1%	± 0%	± 2%	± 0%	

Table A3.8: Statistical Values Obtained from Test Results

A3.20: Details of Modal Testing

Referred to in section 3.6.1

Modal analysis allows the determination of a system's modal properties from its response to a given force excitation. While a free vibration analysis will ascertain the modal properties, such as the natural frequency and damping factor of the system, a modal analysis will provide the Frequency Response Function (FRF). However, there is a direct relationship between the system's modal characteristics and its frequency response and so one can be obtained from the other.

If only the response is measured, it is not possible to say whether a large response is due to a large excitation or to resonance and so the force is also measured. The most common methods of applying the force are by using a shaker or by hammer blow. A hammer impact generally gives a relatively flat force pulse over the frequency range up to some critical frequency. The value of this critical frequency can be controlled to some extent through the choice of material for the hammer tip.

Equipment

The modal analyses performed in this thesis were using freely supported beams with an excitation force provided by impact by a hammer. This force, and the beams' response to it, was measured using accelerometers. The system response was analysed using an FFT analyser.

Two types of beam were tested: a standard steel beam and a post-impact beam. The post-impact beam is a beam that has been used in a drop weight test and has deformed at mid-span so that the beam has a v-shape. The angle of deformation is approximately 22° from the horizontal. Each beam was suspended from the ceiling at one end only using a light elastic band, or bunjie [*bungee?*]. The bunjie has a very low natural frequency, which should not be close to any modes of the beam.

A Bruel and Kjaer piezoelectric accelerometer, type 4321 [*calibration certificate?*], was used to measure displacements. This was a tri-axial device and so the linear displacement could be

measured in all three axes. The accelerometer was bonded to the beam using super-glue. It has a mass of 55 g. The hammer was fitted with an accelerometer to measure the force of impact.

The accelerometers were connected to Bruel and Kjaer, type 2635, charge amplifiers which were described in appendix A3.12. Their calibration certificate can be found in appendix A3.13. These amplifiers were each set to the sensitivity of the appropriate accelerometer as specified by the manufacturer.

The signals of each accelerometer via their respective charge amplifier were inputted into a Hewlett Packard FFT analyser, type 35652B. The analyser is linked to a PC using its inherent software. The analyser calculates the transfer function of the output response (in terms of displacement, velocity or acceleration) and the input force within the frequency domain and this property is the FRF. Thus, although the input force varies with each hammer blow, the FRF accounts for this, as the output is proportional to the input.

A frequency range of up to 3200 Hz was selected. With 800 data points, this gave a frequency resolution of 4 Hz.

Procedure

The beam was marked at eleven intervals with each interval being 83.5 mm apart. This effectively separated the marks over the length of the beam with the sixth point at the beam's mid-span. A stud was glued to a point 200 mm from one end of the beam, at the centre of its top face, and the accelerometer could be attached to this stud. This location was close to the ninth interval marked on the beam.

Both the location of the intervals and of the accelerometer are arbitrary although the number of intervals determines the number of bending modes that can be derived. A minimum of three points is required to fit a curve that represents the first bending mode. Five points are required for the second mode, seven for the third mode and so on. Eleven intervals allow the first five bending modes to be obtained.

Any signals showing multiple impacts (bounce of the hammer) were rejected and the hammer strike at that location repeated until a satisfactory signal was obtained. If the strike was

satisfactory the traces were saved and the hammer strike moved to the next point along the beam. Once the sampling had been conducted at all the points, all the data was transferred to Excel.

Structural damping properties of the beams can be derived from the modal results using the 'half power' method. The sharpness of the response curve near resonance is an indication of the degree of damping in the system and is measured by the bandwidth, which is the width of the resonance peak at the half-power point. This is shown below in figure A3.21.

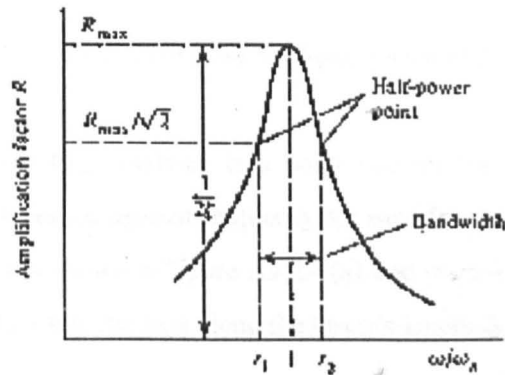


Fig A3.21: Illustration of Method for Calculating Damping Factor [bk 15]

The bandwidth is equal to the difference between r_1 and r_2 as defined in the above figure. The damping factor, ζ , is equal to half of this bandwidth.

Results

Firstly, the input force from the hammer was examined in the frequency domain to ensure that it was present over the whole frequency range of interest. This was found to be the case as is shown in figure A3.22 below.

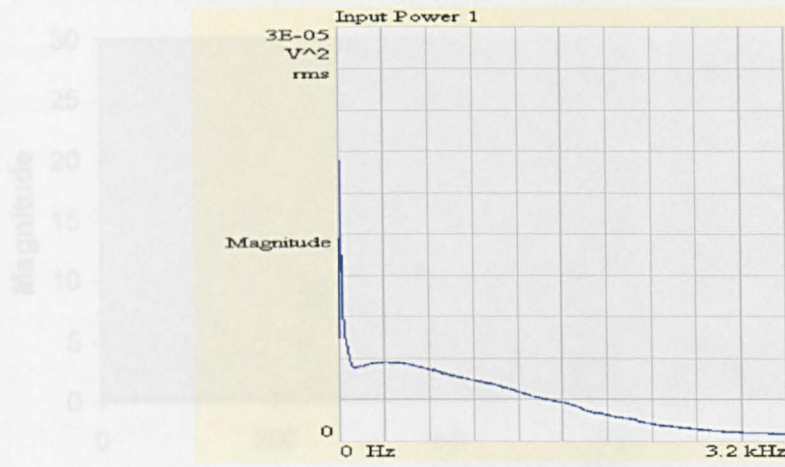


Fig A3.22: Frequency Plot for Input Force of Hammer

The FRF calculated by the FFT analyser is a polar number for each value of frequency. Plotting the magnitude component against frequency for each point along the beam reveals the resonant frequencies. This is shown in figure A3.23 (a) and (b) for points one and six of the standard beam respectively. Only the axis along the beam's length is considered.

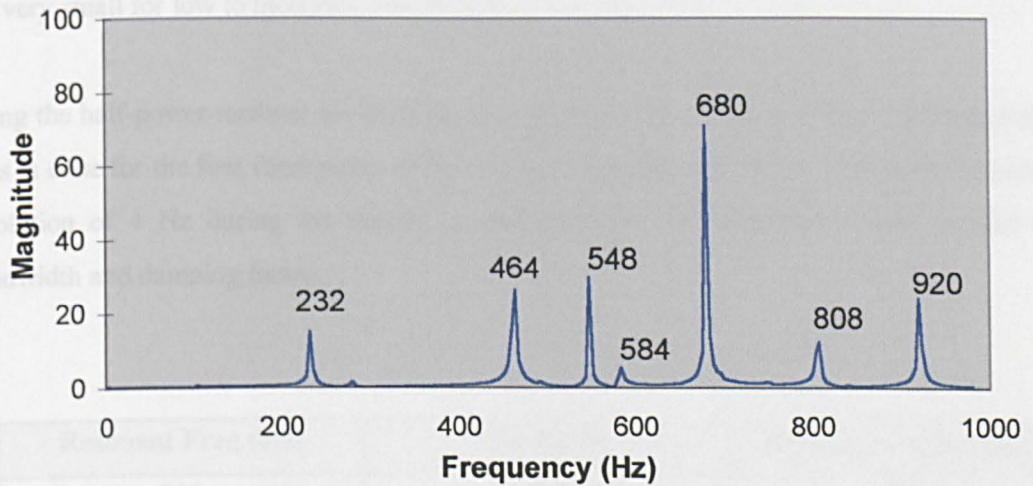


Fig A3.23: (a) Plot of FRF Magnitude against Frequency for Point One of Standard Beam

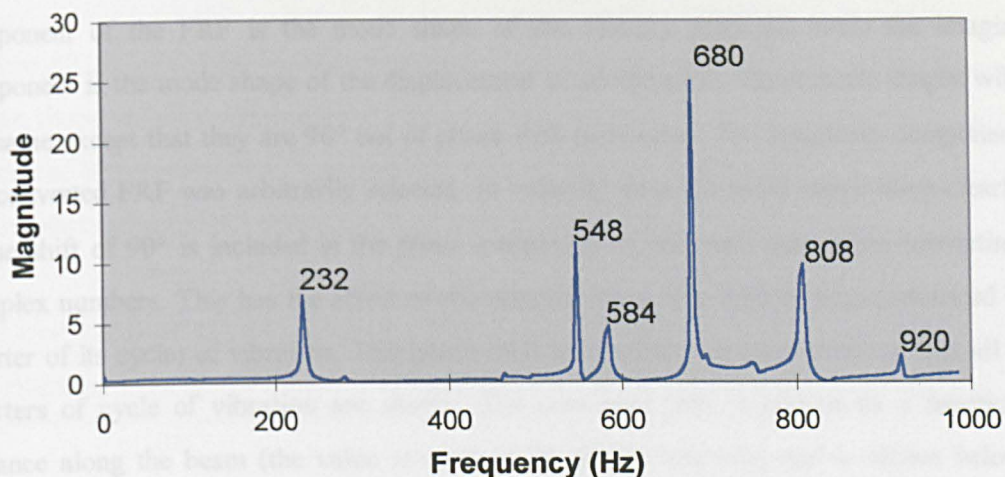


Fig A3.23: (b) Plot of FRF Magnitude against Frequency for Point Six of Standard Beam

For the axis along the beam's length, the pattern is highly consistent for each point in that the same frequencies will show high magnitudes of FRF. The exact magnitude will vary and occasionally a high magnitude common to other points will not be present at a particular point. For instance, in figure A3.23 (b) above, there is no high magnitude at 464 Hz, though it is present at many of the other points along the beam. For the other two axes, the magnitudes are very small for low to moderate frequencies.

Using the half-power method, the damping factor can be determined for these resonant peaks. This is done for the first three peaks of fig A3.23 (a) in table A3.9 below. Given the frequency resolution of 4 Hz during the testing, it was necessary to interpolate results to find the bandwidth and damping factor.

Resonant Freq (Hz)	Bandwidth	Damping Factor (%)
232	0.012	0.60
464	0.013	0.65
548	0.011	0.55
AVERAGE	0.012	0.60

Table A3.9: Damping Factor Calculated from Peak Frequencies

The mode shape of a particular resonant frequency can be derived from the FRF data. The data is first normalised in that every value was divided by the value at point one. Then the

data is converted from a polar number to a complex number. It is known that the real component of the FRF is the mode shape of the velocity response while the imaginary component is the mode shape of the displacement or acceleration. These mode shapes will be the same except that they are 90° out of phase with each other. The imaginary component of the converted FRF was arbitrarily selected. In order to show the mode shape more clearly, a phase shift of 90° is included in the phase component of the polar data when converting to complex numbers. This has the effect of showing the beam at a further stage (advanced by a quarter of its cycle) of vibration. This phase shift is repeated two more times so that all four quarters of cycle of vibration are shown. The converted data is plotted as a function of distance along the beam (the value at each of the eleven intervals) and is shown below in figure A3.24 (a) and (b) for the frequencies of 232 Hz and 464 Hz respectively for the standard beam. Again, only the axis along the beam's length has been considered.



Fig A3.24 (a) Complex FRF Data at 232 Hz for the standard beam

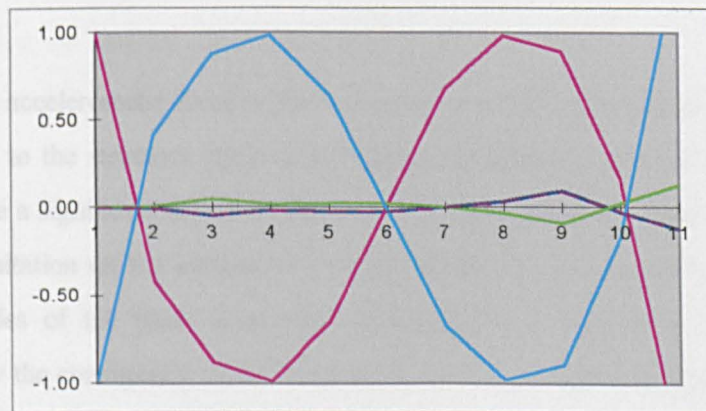


Fig A3.24 (b) Complex FRF Data at 464 Hz for the standard beam

Figure A3.24 (a) and (b) clearly show the first two bending modes for the standard beam. The mode shape at other frequencies is not so obvious. Table A3.10 below lists the vibrational modes of both types of beam determined from the testing. A description of the mode is also given where possible but often this cannot be ascertained.

Standard Beam: Resonant Frequency (Hz)	Post-Impact Beam: Resonant Frequency (Hz)	Description
104	-	-
232	224	Bending Mode 1
280	-	-
464	432	Bending Mode 2
548	548	-
584	584	-
680	684	-
696	812	-
808	840	-
920	904	-
1076	-	-
1120	1112	Bending Mode 3

Table A3.10: Resonant Frequencies of Standard and Post-Impacted Beam

Discussion

The mass of the accelerometer fixed to the beam may have had some influence on its response. How it is fixed to the structure (type of bonding or magnetic) is also of importance as the method can have a significant effect on the results obtained [book 13]. And the resolution of 4 Hz places a limitation on the accuracy of results. However, it is generally believed that the vibrational modes of the beam have been determined to a reasonable accuracy. This is demonstrated by the consistency of the frequencies showing a high magnitude of FRF at each point. When a particular point does not exhibit the high magnitude at a certain frequency seen at other points, it can always be shown that that point is a stationary node for the mode in

question. And it is known that it is not possible to excite a particular mode by applying the force to a stationary node of that mode.

It is assumed that for the two axes not along the beam's length, there is no mode to be measured in the low to moderate frequency range. Therefore, these axes are of little interest and will not be considered further.

Eleven observations made for the beams allow the first five bending modes to be obtained. It can be seen from table A3.10 that modes higher than the third are above 1 KHz and can be expected to have only a minor influence.

The half-power method gave an average damping factor of 0.6 % although the interpolation necessary to derive the value limits its accuracy. However, such a value seems reasonable since metals have typical values of around 1%.

While bending modes are easy to characterise, other types of modes are not so easy. This is because the test set up only allows the measurement of linear accelerations or displacements. To measure torsional modes, equipment measuring rotational acceleration would have to be used.

The FRF that is calculated, and consequently the modal shape, is derived from an output response normalised to the input force. Therefore, true deflections (or accelerations) from a particular input force cannot be determined from modal testing. Thus, the magnitude of force oscillations during an impact test could not be derived from modal data even if support conditions were the same.

Comparison of the standard and the post-impacted beam shows that there is a shift, generally to a lower frequency, in the modes of the post-impacted beam. This shift is not constant in value, or proportional, and there is often no shift at all. Also, three of the modes in the range considered no longer seem to be present. Two of these modes are at a low frequency and are potentially dominant in the beam's behaviour.

As the true deflections of each beam cannot be determined from modal test data, but rather the values are normalised, no comparison can be made of the deflections of the standard and the

post-impacted beam. However, mode shape plots for the post-impacted beam show that the deflections in the central region of the beam are proportionally smaller than at the beam's ends. This is evidence that the v-shape of the beam inhibits its deflection in the central region.



Figure 1.14 | *Illustrates Areas for V-shaped Geometry of Mid-Beam Cross-section*

Therefore, the flexural areas are calculated using:

where t is the uniform thickness of each individual arm, R is the mean radius of the beam, and θ is equal to 11° for a mean radius of 1 inch (2.54 cm) or a radius of 0.5 inch (1.27 cm).

A4.1: Determining the Values of y_1 and y_2

Referred to in section 4.1.4

Figure A4.1 shows the geometry of the beam at mid-span which has been simplified and separated into a number of individual areas. Symmetry about the mid-width has been used so that only one half of the beam is considered. The neutral axis is shown (*N.A.*) and the areas above and below the neutral axis are A_1 and A_2 respectively. The location of the neutral axis is as yet unknown though it is known that $A_1 = A_2$. The distance to the centroids of each area, y_1 and y_2 are also shown though their values are unknown.

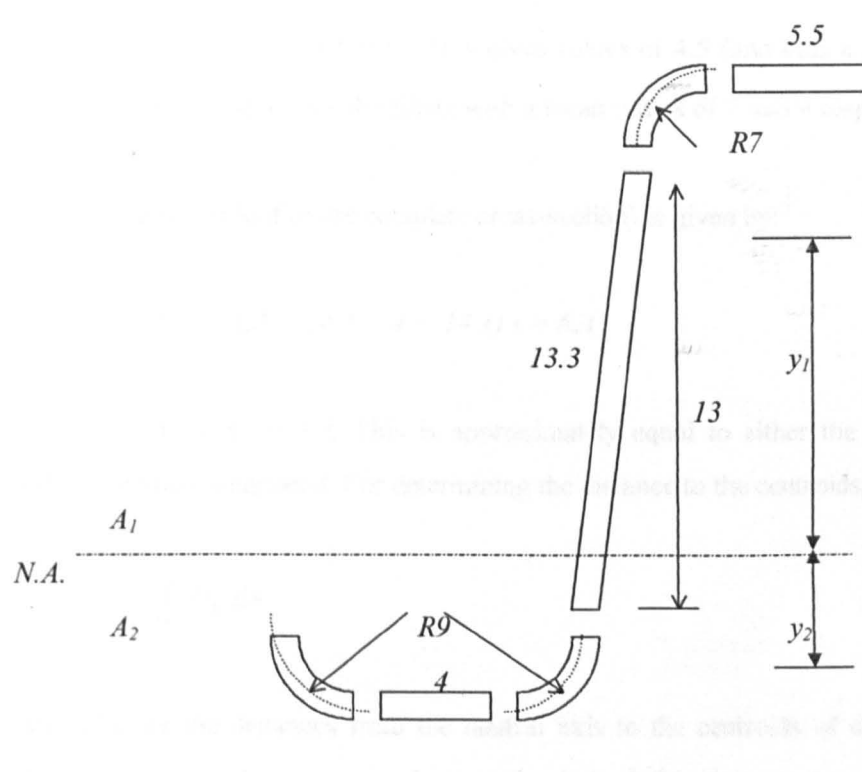


Fig A4.1: Individual Areas for Simplified Geometry of Mid-Span Cross-section

The areas of the fillets, $A_{fillets}$ are calculated using:

$$A_{fillet} = \frac{\pi}{2} R t \quad \text{Eq (A4.1)}$$

where t is the uniform thickness of each individual area and R is the mean radius of the fillet. Equation A4.1 is equal to $11t$ for a mean radius of 7 and $14.1t$ for a radius of 9. It is

necessary to know the distance to the centroid of each fillet. Figure A4.2 illustrates a fillet and shows the distances from the fillet's ends, \bar{x} and \bar{y} , to the centroid of the area.

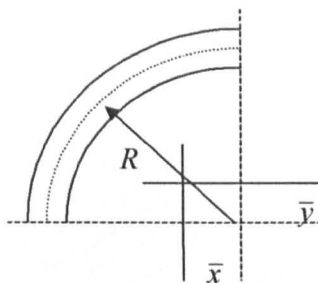


Fig A4.2: Illustration of a Single Fillet

It is known that $\bar{x} = \bar{y} = 0.636R$. This gives values of 4.5 (and thus a distance of 17.5 from the neutral axis) and 5.7 for the fillets with a mean radius of 7 and 9 respectively.

The total area (for half of the complete cross-section) is given by:

$$A = (5.5 + 11 + 13.3 + 14.1 + 4 + 14.1)t = 62t$$

Therefore, $A_1 = A_2 = 31t$. This is approximately equal to either the upper or lower three individual areas summated. For determining the distance to the centroids, it is known that:

$$A_{1,2} \cdot y_{1,2} = \int_A D_i \cdot dA$$

where D_i are the distances from the neutral axis to the centroids of each separate area. As these distances are known, y_1 and y_2 can be derived. For the area A_1 :

$$(5.5 + 11 + 13.3)t \cdot y_1 = (5.5 \times 20)t + (11 \times 17.5)t + (13.3 \times 6.5)t$$

This gives $y_1 = 13.05$. For the area A_2 :

$$(14.14 + 14.14 + 4)t \cdot y_2 = [(14.14 \times 5.7)t] \times 2 + (4 \times 9)t$$

Which gives $y_2 = 6.10$.

A4.2: Stressed Regions of Plates and Examples of Different Plates

Referred to in section 4.1.5

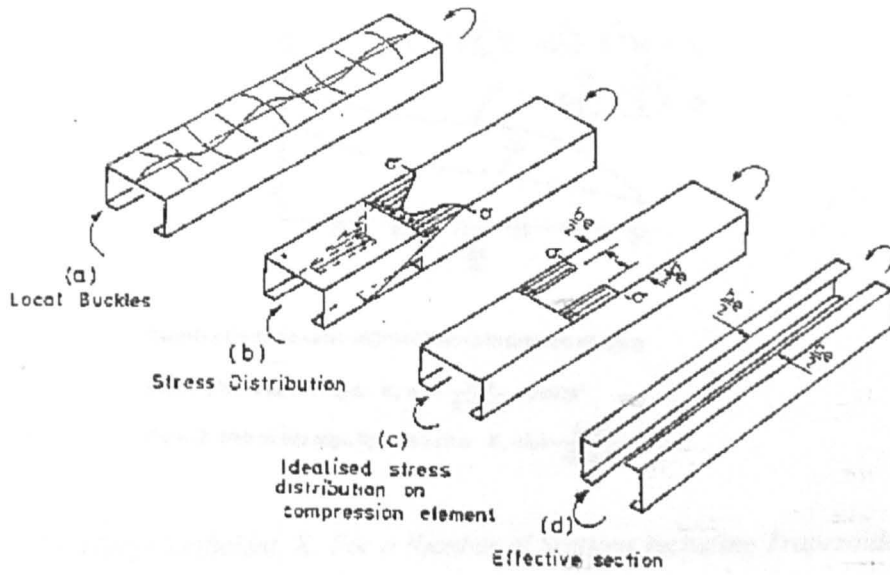


Fig A4.3: Lightly and Heavily Stressed Regions of a Plate

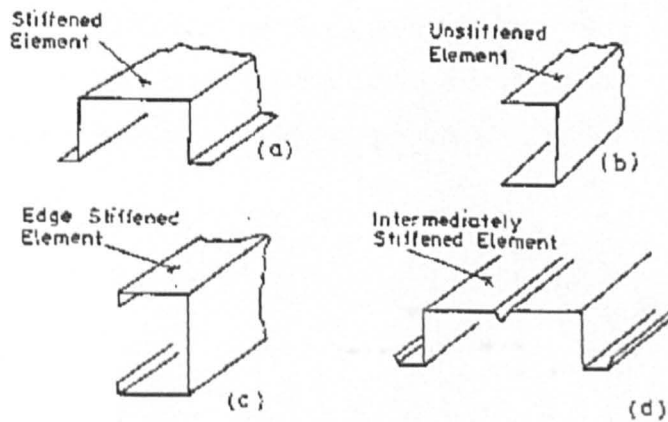
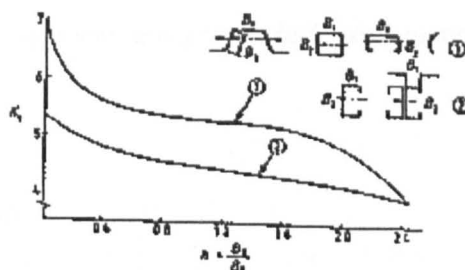


Fig A4.4: Stiffened and Unstiffened Plates

A4.3: Determining the buckling coefficient, K

Referred to in section 4.1.5



Buckling Coefficients for stiffened beam compression elements

Curve 1, Webs on two edges $K_1 = 7 - \frac{1.8h}{0.15+h} - 0.091A^2$

Curve 2, Web on one edge, lip on the other $K_1 = 5.4 - \frac{1.4h}{0.5+h} - 0.02h^2$

Fig A4.5: Buckling Coefficient, K , For a Number of Sections including Trapezoidal Section

A5.1: System and Specimen Bending During Tensile Testing

Referred to in section 5.1.4

The ASTM standard recommends that an evaluation of the degree of bending is made and an upper limit of five percent is set before the bending becomes unacceptable. For bending about the y -axis (in the direction of loading) both system-induced bending and specimen bending are defined in the standard and equations are given which are equations A5.1 and A5.2 below respectively.

$$B_y(\text{system}) = \frac{\varepsilon_{\text{ave}} - \varepsilon_2}{\varepsilon_{\text{ave}}} \times 100 \quad \text{Eq (A5.1)}$$

Where B_y is the percentage bending, ε_{ave} is the average of the strain gauge results and ε_2 is one of the longitudinal gauge readings (either gauge, ε_1 or ε_2 , can be used as the same value will result). The standard does not specify any particular strain or range with which to apply equation A5.1 other than that it should be at moderate strains, which are defined as greater than 0.1 %.

$$B_y(\text{specimen}) = \frac{|\varepsilon_1 - \varepsilon_2|}{|\varepsilon_1 + \varepsilon_2|} \quad \text{Eq (A5.2)}$$

For specimen bending, one value of bending should be determined at the mid-point of the strain range used to calculate the elastic modulus. However, it has been noticed that equation A5.2 is the same as equation A5.1 except for the multiplier of 100. Since, as stated in the standard:

$$\varepsilon_{\text{ave}} = \frac{\varepsilon_1 + \varepsilon_2}{2} \quad \text{Eq (A5.3)}$$

Then by substitution equation A5.3 into equation A5.1:

$$B_y(\text{system}) = \frac{\frac{\varepsilon_1 + \varepsilon_2 - 2\varepsilon_2}{2}}{\frac{\varepsilon_1 + \varepsilon_2}{2}} \times 100$$

$$= \frac{\varepsilon_1 - \varepsilon_2}{\varepsilon_1 + \varepsilon_2} \times 100$$

Eq (A5.4)

Thus, the system-induced bending is equal in magnitude to the specimen percentage bending multiplied by 100. It seems likely that the standard has made two mistakes. Firstly, there is no difference between specimen and system-induced bending as defined. Secondly, equation A5.2 should be multiplied by 100 (note that the equation is a ratio rather than a percentage) though this may be a mere typographical error. Therefore, bending was ascertained using equation A5.4 and this was done at the mid-point of the strain range used for the elastic modulus (i.e. 0.2 % strain).

A5.2: Correlation of Bending and Material Properties

Referred to in section 5.2.4

Figures A5.1 to A5.3 show the correlation between bending and the elastic modulus, ultimate compressive strength and ultimate compressive strain respectively.

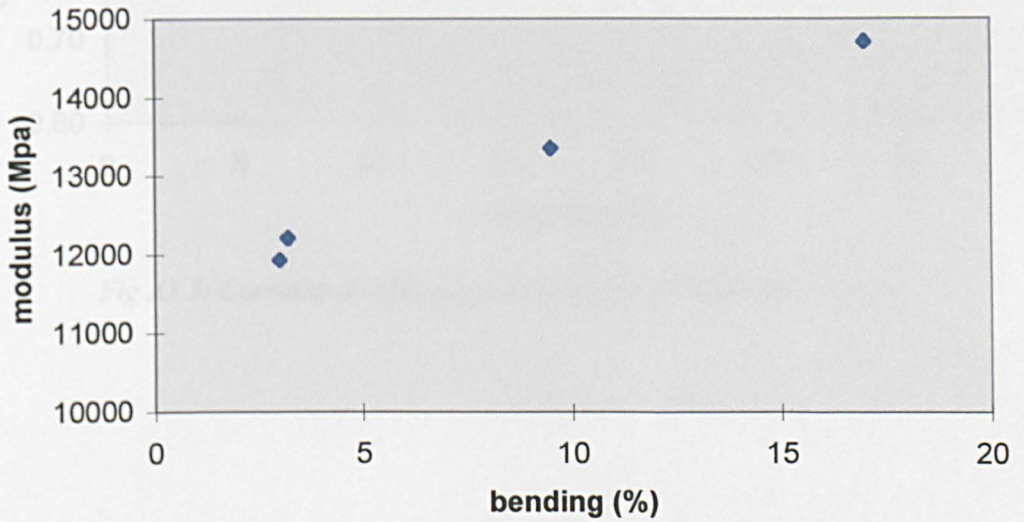


Fig A5.1: Correlation of Bending and Elastic Modulus

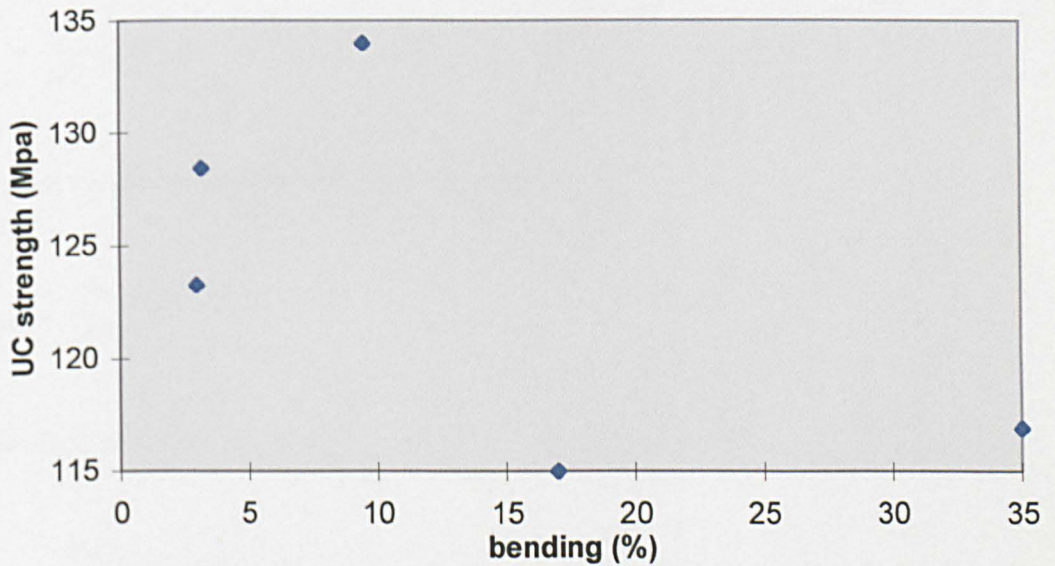


Fig A5.2: Correlation of Bending and Ultimate Compressive Strength

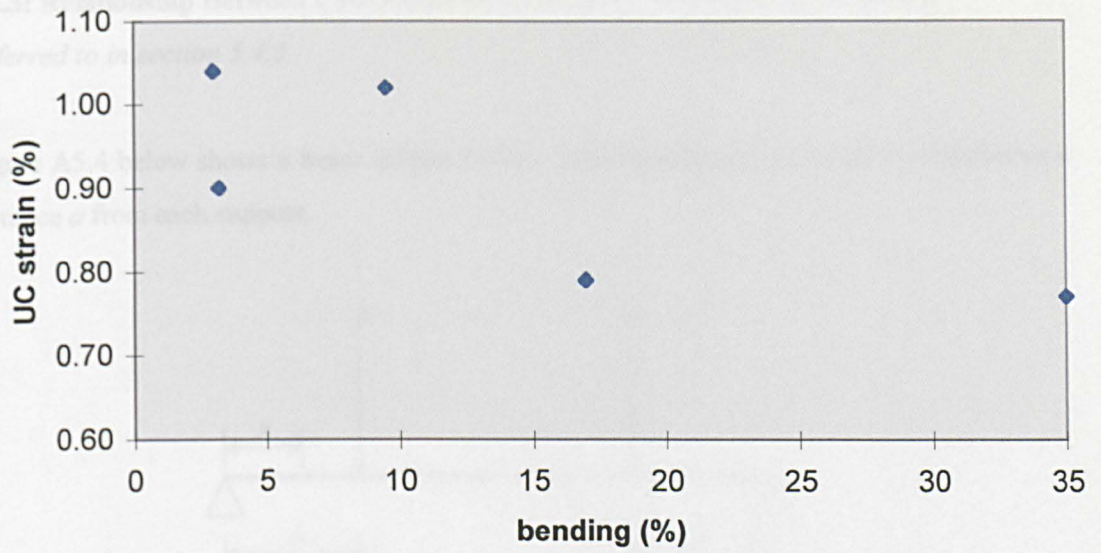


Fig A5.3: Correlation of Bending and Ultimate Compressive Strain

Fig A5.4: Specimen/Protein Model of a Cantilever Beam

It is known [4.1] that the deflection δ_x of a cantilever beam of length L (for $0 \leq x \leq L$) is given by:

$$\delta_x = \frac{-Px}{6EI} (3aL - 3x^2) - \frac{ax^3}{6EI}$$

and that the maximum deflection δ_{max} occurs at $x = a$:

$$\delta_{max} = \frac{-Pa}{24EI} (3L^2 - 4a^2)$$

Therefore, at $x = a$:

$$\delta_a = \frac{-Pa}{6EI} (3aL - 4a^2)$$

For $a = L/4$ as in the specimen shown, the deflection at a is:

A5.3: Relationship Between Cross-head Displacement and Mid-span Deflection

Referred to in section 5.4.3

Figure A5.4 below shows a beam subject to four-point bending where a load P is applied at a distance a from each support.

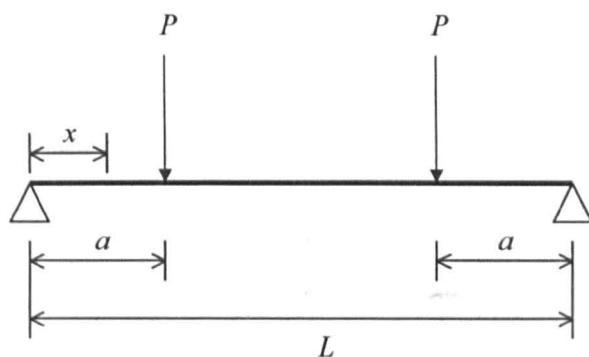


Fig A5.4: Specimen Profile During Four-Point Bending

It is known [4.1] that the deflection of the above beam, δ , at some point along the beam, x , (for $0 \leq x \leq a$) is given by:

$$\delta_x = \frac{-Px}{6EI} (3aL - 3a^2 - x^2)$$

and that the maximum deflection, δ_{\max} , is given by:

$$\delta_{\max} = \frac{Pa}{24EI} (3L^2 - 4a^2)$$

Therefore, at $x = a$:

$$\delta_a = \frac{-Pa}{6EI} (3aL - 4a^2)$$

For $a = L/4$ as in the coupon flexure tests, the ratio of the maximum deflection to the deflection at a is:

$$\frac{\delta_{\max}}{\delta_a} = \frac{\frac{P}{96EI} \left(3L^2 - \frac{L^2}{4} \right)}{\frac{-P}{24EI} \left(\frac{3L^2}{4} - \frac{L^2}{4} \right)}$$

$$= \frac{3L^2 - \frac{L^2}{4}}{-4 \left(\frac{3L^2}{4} - \frac{L^2}{4} \right)}$$

$$= \frac{L^2 \left(3 - \frac{1}{4} \right)}{L^2 (-2)}$$

$$= 1.375$$

The deflection at a represents the cross-head displacement and the maximum deflection occurs at mid-span. The relationship between the cross-head displacement (d_{cross}) and the mid-span deflection (d_{mid}) is therefore:

$$d_{\text{mid}} = 1.375 * d_{\text{cross}}$$

A6.1: Effect of Delamination on Bending Stiffness

Referred to in section 6.1.3

Consider the case where a simple coupon of rectangular cross-section is loaded in bending, which results in delamination at the mid-thickness of the coupon that spreads across the coupon's entire width and length. The coupon effectively becomes two separate parts of equal geometry. The coupon's cross-section before and after delamination is represented below in figure A6.1 (a) and (b) respectively.

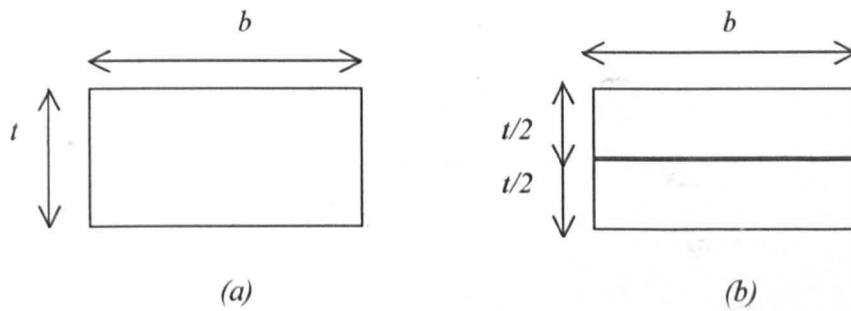


Fig 6.1: Cross-section of Coupon (a) Before and (b) After Delamination

The bending stiffness of the coupon is directly proportional to its second moment of area, I . Before delamination, the coupon has a second moment of area given by:

$$I = \frac{bt^3}{12} \quad \text{Eq (A6.1)}$$

After delamination, the coupon has a second moment of area given by:

$$I = 2 \times \frac{b \left(\frac{t}{2} \right)^3}{12}$$
$$= \frac{bt^3}{3} \quad \text{Eq (A6.2)}$$

Therefore, the coupon after delamination has only a quarter of the bending stiffness of the coupon before delamination.

The case given above, for reasons of simplicity, considers entire delamination at the mid-thickness of a coupon and represents the maximum loss in bending stiffness for delamination in one plane. More realistic cases, such as for the composite beam considered in this thesis, will not involve such a severe loss of stiffness but delamination must entail a drop in stiffness to some degree.

REFERENCES USED IN THESIS

Chapter One

- 1.1 Faith N (1997); 'Crash'
Boxtree, 1997
- 1.2 Nader R (1972); 'Unsafe - at any speed'
Grossman, USA, 1972
- 1.3 Green A P (1992); 'Design Methodology for Improving Side Impact performance of Passenger Cars'
FISITA Conf, Automotive Technology Serving Society, Inst Mech Engrs, 1992
- 1.4 Faerber E, Friedel, B and Glaeser, K P (1992); 'Development of the European Proposed Regulation for Side Impact Performance'
FISITA Conf, Automotive Technology Serving Society, Inst Mech Engrs, 1992
- 1.5 NHTSA (1997); 'NHTSA Plan for Achieving Harmonisation of US and European Side Impact Standards'
Report to Congress, Apr 1997
- 1.6 SACTAC Progress Reports 1 - 5 (1996 - 1998)
- 1.7 Wilson G, Wheel M and Lee W K (2000); 'Predicting the Deformation of Automotive Beams'
SAE 2000 conference, Detroit, 7 March 2000, paper no. 2000-01-0639

Chapter Two

Plastic Collapse of Beams

- 2.1 Moy S (1996); 'Plastic Methods for Steel and Concrete Structures'
MacMillan Press Ltd, 1996
- 2.2 Horne M R (1971); 'Plastic Theory of Structures'
Nelson, 1971
- 2.3 Haythornthwaite R M (1957); 'Beams with Full End Fixity'
Engineering, v183, p110-112, 1957
- 2.4 Lowe W T, Al-Hassani S T S and Johnson W (1972); 'Impact Behaviour of Small Scale Model Motor Coaches'
Proc Inst Mech Eng, v186, p409-419, 1972

- 2.5 Jones N (1989); 'Structural Impact'
Cambridge University press, 1989
- 2.6 Symonds P S (1967); Survey of Methods of Analysis for Plastic Deformation of Structures under Dynamic Loading'
Brown Uni Report, BU/NSRDC/1-67, 1967
- 2.7 Yu T X (1993); 'Elastic Effects in the Dynamic Plastic Response of Structures'
In 'Structural Crashworthiness and Failure', Jones N and Wierzbicki T (eds),
Elsavier Appl Science Publ, 1993
- 2.8 Samuelides E and Frieze P A (1984); 'Analytical and Numerical Simulation of Beams Subjected to Impact'
In 'Structural Impact and Crashworthiness', v2, Morton J (ed), Elsavier Appl Science Publ, 1984
- 2.9 Samuelides E and Frieze P A (1972); 'Strip Model Simulation for Low Energy Impacts on Flat Plated Structures'
Int Journ Mech Science, v25, p669, 1983
- 2.10 Hodge P G (1959); 'Plastic Analysis of Structures'
McGraw-Hill, 1959
- 2.11 Symonds P S (1967); Survey of Methods of Analysis for Plastic Deformation of Structures under Dynamic Loading'
Brown Uni Report, BU/NSRDC/1-67, 1967
- 2.12 Nonaka T (1967); 'Some Interaction Effects in a Problem of Plastic Beam Dynamics, Part 1-3'
Journ Appl Mech, v34, 3, p623-643, 1967
- 2.13 Shen W Q and Jones N (1991); 'A Comment on the Low Speed Impact of a Clamped Beam by a heavy Striker'
Mech Struct & Mach, v19, 4, p527-549, 1991
- 2.14 Symonds P S and Mentel T J (1958); 'Impulsive Loading of Plastic Beams with Axial Constraints'
Journ Mech & Physics of Solids, v6, p186-202, 1958
- 2.15 Symonds P S and Jones N (1971); 'Impulsive Loading of Fully Clamped Beams with Finite Plastic Deflections and Strain-rate Sensitivity'
Int Journ Mech Science, v14, p49-69, 1972
- 2.16 Humphreys J S (1965); 'Plastic deformation of Impulsively Loaded Straight Clamped Beams'

- Journ Appl Mech, v32, 1, p7-10, 1965
- 2.17 Marsh K J and Campbell J D (1963); 'The Effect of Strain Rate on the Post-yield Flow of Mild Steel'
Journ Mech Physics & Solids, v11, p49-63, 1963
- 2.18 Campbell J D and Cooper R H (1966); 'Yield and Flow of Low-carbon Steel at Medium Strain Rates'
Proc Conf on Physical Basis of yield & Fracture, Inst Physics & Physical Soc, London, p77-87, 1966
- 2.19 Marsh M G & McGregor I J (1999); 'The Axial Collapse Performance of Lightweight Steel Structures'
Mat Science & Eng, v12, p3-21, 1999
- 2.20 Cowper G R & Symonds P S (1957); 'Strain Hardening and Strain-Rate Effects in the Impact Loading of Cantilever Beams'
Brown Univ Report no. 28, Sep 1957
- 2.21 Jones N and Wierzbicki T (eds) (1983); 'Structural Crashworthiness'
Butterworth & Co. Publ Ltd, 1983
- 2.22 Rawlings B (1963); 'The Dynamic Behaviour of Mild Steel in Pure Flexure'
Proc Royal Soc London, series A, v290, p266, 1966
- 2.23 Aspen R J & Campbell J D (1966); 'The Effect of Loading Rate on the Elasto-Plastic Flexure of Steel Beams'
Proc Royal Soc London, series A, v275, p528-542, 1963
- 2.24 Youngdahl C K (1992); 'Optimum Approximate Modes of Strain-Hardening Beams'
Int Journ Impact Eng, v12, 2, 227-240, 1992
- 2.25 Youngdahl C K (1994); 'Approximation Method for the Dynamic response of Strain-Hardening Clamped Beams'
Int Journ Impact Eng, v15, 2, 101-118, 1994
- 2.26 Jones N (1971); 'A Theoretical Study of the Dynamic Plastic Behaviour of Beams and Plates with Finite-Deflections'
Int Journ Solids & Struct, v7, p1007-1029, 1971
- 2.27 Symonds P S and Providence R I (1953); 'Dynamic Load Characteristics in Plastic Bending of Beams'
Journ Appl Mech, p475-481, Dec 1953
- 2.28 Seiler J A and Symonds P S (1954); 'Plastic Deformation in Beams under

Structural Crashworthiness

(Full Review Given in Appendix 2.1)

- 2.28a Kecman D (1979); 'Bending Collapse of Rectangular and Square Section Tubes in Relation to the Bus Roll-Over Problem'
PhD Thesis, Cranfield Inst. Tech., 1979
- 2.28b Rhodes J and Harvey J M (1970); 'Design of Thin-Walled Beams'
Conf. Experim. Stress Anal in Design, Cambridge, 1970
- 2.28c Wah S C (1985); 'The Collapse behaviour of Thin-Walled Sections'
PhD Thesis, Strathclyde University, 1985
- 2.28d Ho T S (1986); 'A Study of the Impact Energy Absorption Capacity of Thin-Walled Sections'
MSc Thesis, Strathclyde University, 1986
- 2.29 Mamalis A G, Manolakos D E, Viegelaun G L and Baldoukas A K (1989);
'Deformation Characteristics of Crashworthy Thin-Walled Steel Tubes Subject to Bending'
Proc Instn Mech Engrs, v203, p411-417, 1989
- 2.30 Mamalis A G, Manolakos D E, Viegelaun G L and Baldoukas A K (1990);
'Bending of Fibre-Reinforced Composite Thin-Walled Tubes'
Composites, v21, 5, p431-438, Sep 1990
- 2.31 Mamalis A G, Manolakos D E and Demosthenous G A (1992); 'Crushing Behaviour of Thin-Walled, Non-Circular, Glass Fibre-Reinforced Composite Tubular Components Due to Bending'
Composites, v23, 6, p425-433, Nov 1992
- 2.32 Mamalis A G, Manolakos D E, Demosthenous G A and Ionnidis M B (1994); 'On the Bending of Automotive Fibre-Reinforced Composite Thin-Walled Structures'
Composites, v25, 1, p47-57, 1994
- 2.33 Cheon S S, Lee D G and Jeong K S (1997); 'Composite Side-Door Impact Beams for Passenger Cars'
Composite Structures, v38, 1-4, p229-239, 1997
- 2.34 Broughton W R, Nimmo W and Sims G D (1995); 'Flexural Failure in Composite Beam Structures'

3rd Int Conf on Deform & Fract of Composites, Uni of Surrey, p239-249, Mar 1995

- 2.35 Palmer D W, Bank L C and Gentry T R (1997); 'Simulation of Progressive Failure of Pultruded Composite Beams in Three Point Bending Using LS-DYNA3D'
Proc Int Composites Expo, session 14-c, p1-12, 1997

Composite Mechanics and Failure

- 2.36 Hsiao H M and Daniel I M (1999); 'Effect of Fibre Waviness on the high-Strain-Rate Behaviour of Composites'
Journ Thermoplastic Comp Mat, v12, p412-422, Sep 1999
- 2.37 Beardmore P and Johnson C F (1986); 'The Potential for Composites in Structural Automotive Applications'
Comp Science & Tech, v26, p251-281, 1986
- 2.38 Ashley S (1996); 'Composite Car Structures Pass the Crash Test'
Mechanical Engineering, Dec 1996
- 2.39 ASM International (1991); 'Composites - Engineering Materials Handbook'
ASM International, v1, 1991
- 2.40 Stowell E Z and Liu T S (1961); 'On the Mechanical Behaviour of Fibre Reinforced Crystalline Materials'
Journ Mech Physics & Solids, v9, p242
- 2.41 Waddoups M E (1968); 'Characterisation and Design of Composite Materials'
Comp Mat Workshop, Tsai S W *et al* (eds), Technomic Publ, p254-308, 1968
- 2.42 Hill R (1950); 'The Mathematical Theory of Plasticity'
Oxford Uni Press, 1950
- 2.43 Azzi V D and Tsai S W (1965); 'Anisotropic Strength of Composites'
Experimental Mech, v5, p286-288, 1965
- 2.44 Tsai S W and Wu E M (1971); 'A General Theory of Strength for Anisotropic Materials'
Journ Comp Mat, v5, p58-80, 1971
- 2.45 Narayanaswami R and Adelman H (1977); 'Evaluation of the tensor Polynomial and Hoffman Strength Theories for Composite Materials'
Journ Comp Mat, v11, p366, 1977
- 2.46 Hashin Z (1980); 'Failure Criteria for Unidirectional Fibre Composites'
Journ Appl Mech, v47, p329-334, 1980
- 2.47 Hart-Smith (1993); 'The Truncated Maximum Strain Composite Failure Model'
Composites, v24, 7, p587-591, 1993

- 2.48 Soni (1983); 'A Comparative Study of Failure Envelopes in Composite Laminates'
Journ Reinf Plastics & Comp, v2, p34-42, Jan 1983
- 2.49 Petit and Waddoups [r10 in C p236]
- 2.50 Ebeling T, Hiltner A, Baer E, Fraser I M and Orton M L (1997); 'Delamination Failure of a Woven Glass Fibre Composite'
Journ Comp Mat, v31, 13, p1318-1333, 1997
- 2.51 Hinton M, Kaddour A S, Soden P D (1999); 'Prediction of World-Wide Failure Theories, Part B: Some Experimental Comparisons'
5th Int Conf on Deform & Fract of Comp, London, Mar 1999

Testing Methods

- 2.52 Birch R S and Jones N (1990); 'Measurement of Impact Loads Using a Laser Doppler Velocimeter'
Proc Inst Mech Eng, v204, p1-8, 1990
- 2.53 Birch R S, Jones N and Jouri W S (1988); Performance Assessment of an Impact Rig'
Proc Inst Mech Eng, v202, p275-285, 1988
- 2.54 Money M W and Sims G D (1989); 'Calibration of Quartz Load Cells; An In-Situ Procedure for Instrumented Falling Weight Impact Machines'
Polymer Testing, v8, p429-442, 1989
- 2.55 Welsh J S and Adams D F (1997); 'Current Status of Compression Test Methods for Composite Materials'
SAMPE Journal, v33, 1, p35-43, Jan/Feb 1997
- 2.56 'Standard Test Method for Compressive properties of Rigid Plastics'
ASTM Standard D695-96, Amer Soc Testing & Mat, 1986
- 2.57 'Compressive Properties of Oriented Fibre-Resin Composites'
SACMA Recommended Method SRM1-88, Suppl Adv Comp Mat Assoc, 1989
- 2.58 'Standard Test Method for Compressive properties of Polymer Matrix Composite Materials with Unsupported Gage Section by Shear Loading'
ASTM Standard D3410/D3410M-95, Amer Soc Testing & Mat, 1995
- 2.59 Mathews F L and Haberle J G (1992); 'A New Method for Compression Testing'
Europ Conf on Comp Testing & Standardisation, Amsterdam, Sep 1992

- 2.60 Curtis P and Gates J (1992); 'An Improved Engineering Test Method for the Measurement of the Compressive Strength of Unidirectional Carbon Fibre Composites'
Europ Conf on Comp Testing & Standardisation, Amsterdam, Sep 1992
- 2.61 Finley G A and Adams D F (1995); 'An Analytical and Experimental Study of Unidirectional Composite Thickness-Tapered Compression Specimens'
Report no. UW-CMRG-R-95-101, Comp Mat Research Group, Uni of Wyoming, Jan 1995
- 2.62 Crasto A and Kim R (1992); Analysis of a Novel Compression Test Specimen: A Miniature Sandwich Beam'
Europ Conf on Comp Testing & Standardisation, Amsterdam, Sep 1992
- 2.63 McKelvie J, Jam M and Fort D (1995); 'Compression Testing of Damaged Graphite/Epoxy Composites'
3rd Int Conf on Deform & Fract of Composites, Uni of Surrey, p180-189, Mar 1995
- 2.64 Barker A J and Balasundaram V (1987); 'Compression Testing of Carbon Fibre-Reinforced Plastics Exposed to Humid Environments'
Composites, v18, 3, p217-226, July 1987
- 2.65 Mathews F L, Godwin E W and Rueda C (1989); 'Mechanical Testing and the Relevance of Standards'
Trans of Imech E, C387/016, 1989
- 2.66 Walrath D E and Adams D F (1983); 'The Iosipescu Shear Test as Applied to Composite Materials'
Experim Mech, v23, 1, p105-110, Mar 1983
- 2.67 Kellas S, Morton J and Jackson K E (1972); 'An Evaluation of the $\pm 45^\circ$ Tensile Test for the Determination of the In-plane Shear Strength of Composites'
Journ of Comp Mat, v6, p552, 1972
- 2.68 Iosipescu N (1967); 'New Accurate Procedure for Single Shear Testing of Metals'
Journ of Mat, v2, 3, p537-566, 1967
- 2.69 Adams D F and Walrath D E (1987); 'Further Development of the Iosipescu Shear Test Method'
Experim Mech, v27, 2, p113-119, 1987

- 2.70 'Standard Test Method for Shear Properties of Composite Materials by the V-Notched Beam Method'
ASTM Standard D5379/5379M-93, Amer Soc Testing & Mat, 1993
- 2.71 'Standard Test Method for Flexural Properties of Unreinforced and Reinforced Plastics and Electrical Insulating Material'
ASTM Standard D790/D790M-96a. Amer Soc Testing & Mat, 1997
- 2.72 Theobald D, McClurg J and Vaughan J G (1997); 'Comparison of Three-Point and Four-Point Flexural Bending Tests'
Proc of Int Comp Expo, session 5-B, 1997
- 2.73 Carlsson L A and Pipes R B, Eds (1989); 'Thermoplastic Composite Materials'
Elsevier Publ, Amsterdam, 1989
- 2.74 Tuttle M E (1989); 'Fundamental Strain-Gage Technology'
In Manual on Experimental Methods for Mechanical Testing of Composites, p17-26, Elsevier Publ, 1989

Chapter Three

- 3.1 Lee W K (1999); Private Conversation Discussing Test-work Carried out at NEL.
- 3.2 Buckley N (1997); 'The Instrumentation of an Impact Testing Rig'
BEng (Hons) Thesis, Uni of Strathclyde, 1997
- 3.3 Operators Manual for Gould Datasys 740 Digital Storage Oscilloscope
- 3.4 Kistler Instruments (1998); Private Conversation with Technical Support Staff
Discussing Calibration of Load Washers

Chapter Four

- 4.1 Young W C (1989); 'Roarke's Formulas for Stress and Strain'
McGraw-Hill Book Co, 1989
- 4.2 'Code of Practice for the Design of Cold Formed Steel Sections'
British Standard BS 5950: Part 5

- 4.3 Beards C F (1981); 'Vibration Analysis and Control System Dynamics'
Ellis Horwood Ltd, 1981

Chapter Five

- 5.1 'Standard Test Method for Tensile Properties of Polymer Matrix Composites'
ASTM Standard D3039/D3039M-95a, Amer Soc Testing & Mat, 1995
- 5.2 Auren B (2000); 'Determining Composite Structures' Bending Response from
Coupon Tests'
MEng (Hons) Thesis, Uni of Strathclyde, 2000
- 5.3 'Standard Test Method for In-Plane Shear Response of Polymer Matrix
Composite Materials by Tensile Test of a $\pm 45^\circ$ Laminate'
ASTM Standard D3518/D3518M-94, Amer Soc Testing & Mat, 1994

Chapter Seven

- 7.1 Callister W D (1995); 'Materials Science and Engineering'
John Wiley & Sons, 1995
- 7.2 ANSYS User's Manual
ANSYS Inc, 1997
- 7.3 LS-Dyna User's Manual
Livermore Software Tech Corp, May 1999

Appendix 2.1

- A2.1 Minorsky V U (1959); 'An Analysis of Ship Collisions with Reference to Protection
of Nuclear Power Plants'
Journ Ship Research, v3, 1, 1959
- A2.2 Pugsley A G (1960); 'The Crumpling of Tubular Structures Under Impact
Conditions'
Proc Symposium on Use of Aluminium in Railway Rolling Stock, p33, Inst Loco
Eng, The Aluminium Devlpment Assoc, London, 1960
- A2.3 Lin K H and Mase G T (1990); 'An Assessment of Add-on Energy Absorbing
Devices for Vehicle Crashworthiness'
Trans ASME, v112, p406-411, Oct 1990
- A2.4 'Structural Crashworthiness'

- Jones N and Wierzbicki T (eds), Butterworth & Co Ltd, 1983
- A2.5 Hull D (1991); 'A Unified Approach to Progressive Crushing of Fibre-Reinforced Composite Tubes'
Comp Science & Tech, v40, p377-421, 1991
- A2.6 Wierzbicki T and Abramowicz W (1983); 'On the Crushing Mechanics of Thin-Walled Structures'
Journ Appl Mech, v50, p727-734, Dec 1983
- A2.7 Thornton P H and Magee C L (1977); 'The Interplay of Geometric and Material Variables in Energy Absorption'
Journ Eng Mat Tech, Trans ASME, v99, p114, 1977
- A2.8 Magee C L and Thornton P H (1978); 'Design Considerations in Energy Absorption by Structural Collapse'
Trans SAE, v87, 2, p2041, 1978
- A2.9 Mahmood H F and Paluszny A (1982); 'Stability of Plate-Type Box Columns under Crush Loading'
Proc ASME, Winter Sessions in Computational Methods in Ground Transportation Vehicles, Phoenix, Arizona, 1982
- A2.10 Mahmood H F and Paluszny A (1981); 'Design of Thin Walled Columns for crash Energy Management - Their Strength and Mode of Collapse'
Trans SAE, v90, p4039, 1981
- A2.11 Reid S R, Reddy T Y and Gray M D (1986); 'Static and Dynamic Axial Crushing of Foam-filled Sheet Metal Tubes'
Int Journ Mech Sci, v28, 5, p295-322, 1986
- A2.12 Abramowicz W and Jones N (1984); 'Dynamic Axial Crushing of Square Tubes'
Int Journ Impact Eng, v2, 2, p179-208, 1984
- A2.13 Abramowicz W and Jones N (1984); 'Dynamic Axial Crushing of Circular Tubes'
Int Journ Impact Eng, v2, 3, p263-281, 1984
- A2.14 Birch R S and Jones N (1990); 'Dynamic and Static Axial Crushing of Axially Stiffened Cylindrical Shells'
Thin-Walled Structures, v9, p29-60, 1990
- A2.15 Jones N and Birch R S (1990); 'Dynamic and Static Axial Crushing of Axially Stiffened Square Shells'
Proc Inst Mech Eng, v204, p293-310, 1990
- A2.16 Thornton P H (1980); 'Energy Absorption by Foam Filled Structures'

SAE 1980 Conf, Detroit, Feb 1980

- A2.16a Kecman D (1979); 'Bending Collapse of Rectangular and Square Section Tubes in Relation to the Bus Roll-Over Problem'
PhD Thesis, Cranfield Inst. Tech., 1979
- A2.16b Rhodes J and Harvey J M (1970); 'Design of Thin-Walled Beams'
Conf. Experim. Stress Anal in Design, Cambridge, 1970
- A2.17 Mamalis A G, Manolakos D E, Viegelaun G L and Baldoukas A K (1989);
'Deformation Characteristics of Crashworthy Thin-Walled Steel Tubes Subject to Bending'
Proc Instn Mech Engrs, v203, p411-417, 1989
- A2.18 Price J N and Hull D (1987); 'Axial Crushing of Glass Fibre-Polyester Composite Cones'
Comp Science & Tech, v28, p211-230, 1987
- A2.19 Sigalas I, Kumosa M and Hull D (1991); 'Trigger Mechanisms in Energy Absorbing Glass Cloth/Epoxy Tubes'
Comp Science & Tech, v40, p265-287, 1991
- A2.20 Farley G L and Jones R M (1992); 'Analogy for the Effect of Material and Geometrical Variables on Energy Absorption Capability of Composite Tubes'
Journ Comp Mat, v26, 1, p79-89, 1992
- A2.21 Thornton P H, Harwood J J and Beardmore P (1985); 'Fibre-reinforced Plastic Composites for Energy Absorption Purposes'
Comp Science & Tech, v24, p275-298, 1985
- A2.22 Farley G L (1983); 'Energy Absorption of Composite Materials'
Journ Comp Mat, v17, p267-279, 1983
- A2.23 Mamalis A G, Manolakos D E, Demosthenous G A and Ionnidis M B (1996);
'The Static and Dynamic Axial Collapse of Fibreglass Composite Automotive Frame Rails'
Comp Structures, v34, p77-90, 1996
- A2.24 Czaplicki M J and Robertson R E (1991); 'Comparison of Bevel and Tulip Triggered Pultruded Tubes for Energy Absorption'
Comp Science & Tech, v40, p31-46, 1991
- A2.25 Thornton P H (1979); 'Energy Absorption in Composite Structures'
Journ Comp Mat, v13, p247-262, 1979

- A2.26 Schmueser D W and Wickliffe L E (1987); 'Impact Energy Absorption of Continuous Fibre Composite Tubes'
Trans ASME, v109, p72-77, Jan 1987
- A2.27 Farley G L (1991); 'The Effects of Crushing Speed on the Energy Absorption Capability of Composite Tubes'
Journ Comp Mat, v25, p1314-1329, 1991
- A2.28 Hamada H, Coppola J C, Hull D, Maekawa Z and Sato H (1992); 'Comparison of Energy Absorption of Carbon/Epoxy and Carbon/PEEK Composite Tubes'
Composites, v23, 4, p245-252, Jul 1992
- A2.29 Czaplicki M J, Robertson R E and Thornton P H (1990); 'Non-axial Crushing of E-Glass/Polyester Pultruded Tubes'
Journ Comp Mat, v24, p1077-1100, 1990
- A2.30 Mamalis A G, Manolakos D E, Viegelaan G L and Baldoukas A K (1990); 'Bending of Fibre-Reinforced Composite Thin-Walled Tubes'
Composites, v21, 5, p431-438, Sep 1990
- A2.31 Mamalis A G, Manolakos D E and Demosthenous G A (1992); 'Crushing Behaviour of Thin-Walled, Non-Circular, Glass Fibre-Reinforced Composite Tubular Components Due to Bending'
Composites, v23, 6, p425-433, Nov 1992
- A2.32 Mamalis A G, Manolakos D E, Demosthenous G A and Ionnidis M B (1994); 'On the Bending of Automotive Fibre-Reinforced Composite Thin-Walled Structures'
Composites, v25, 1, p47-57, 1994
- A2.33 Mamalis A G, Manolakos D E, Demosthenous G A and Ionnidis M B (1995); 'The Deformation Mechanism of Thin-walled Non-circular Composite Tubes subjected to Bending'
Comp Structures, v30, p131-146, 1995
- A2.34 Cheon S S, Lee D G and Jeong K S (1997); 'Composite Side-Door Impact Beams for Passenger Cars'
Composite Structures, v38, 1-4, p229-239, 1997
- A2.35 Broughton W R, Nimmo W and Sims G D (1995); 'Flexural Failure in Composite Beam Structures'
3rd Int Conf on Deform & Fract of Composites, Uni of Surrey, p239-249, Mar 1995
- A2.36 Palmer D W, Bank L C and Gentry T R (1997); 'Simulation of Progressive Failure of Pultruded Composite Beams in Three Point Bending Using LS-DYNA3D'

